



HAL
open science

Polyunsaturated phospholipids in large-scale membrane deformations induced by bacterial toxins

Meng-Chen Tsai

► **To cite this version:**

Meng-Chen Tsai. Polyunsaturated phospholipids in large-scale membrane deformations induced by bacterial toxins. Cellular Biology. Université Côte d'Azur, 2020. English. NNT : 2020COAZ6044 . tel-03506259

HAL Id: tel-03506259

<https://theses.hal.science/tel-03506259v1>

Submitted on 2 Jan 2022

HAL is a multi-disciplinary open access archive for the deposit and dissemination of scientific research documents, whether they are published or not. The documents may come from teaching and research institutions in France or abroad, or from public or private research centers.

L'archive ouverte pluridisciplinaire **HAL**, est destinée au dépôt et à la diffusion de documents scientifiques de niveau recherche, publiés ou non, émanant des établissements d'enseignement et de recherche français ou étrangers, des laboratoires publics ou privés.

THÈSE DE DOCTORAT

Les phospholipides polyinsaturés dans
les larges déformations membranaires
induites par les toxines bactériennes

Meng-Chen TSAI

Institut de Pharmacologie Moléculaire et Cellulaire, CNRS, UMR 7275

Présentée en vue de l'obtention
du grade de docteur en Sciences de la Vie et de la
Santé d'Université Côte d'Azur

Dirigée par : Hélène BARELLI
Co-encadrée par : Emmanuel LEMICHEZ

Soutenue le : 17 Décembre 2020

Devant le jury, composé de :
Ludger JOHANNES, DRE, Institut Curie
Gervaise LOIRAND, DR1, Université de Nantes
Jean-Baptiste MANNEVILLE, DR2, Institut Curie
Thierry FERREIRA, Maître de conférences,
Université de Poitiers, STIM – Directeur scientifique
ConicMeds Development
Emmanuel LEMICHEZ, DR1, Institut Pasteur
Hélène BARELLI, HDR, IPMC

Les phospholipides polyinsaturés dans les larges déformations membranaires induites par les toxines bactériennes

Jury :

Président du jury

Ludger JOHANNES, Directeur de Recherche Exceptionnelle - INSERM, Institut Curie, INSERM-U1143 /CNRS-UMR 3666

Rapporteurs

Gervaise LOIRAND, Directeur de Recherche - INSERM, Université de Nantes, UMR INSERM-1087/ CNRS- UMR 6291

Jean-Baptiste MANNEVILLE, Directeur de Recherche - CNRS, Institut Curie, Paris, CNRS-UMR 144

Examineur

Thierry FERREIRA, Maître de conférences, Université de Poitiers, STIM – Directeur Scientifique ConicMeds Development, Poitiers

Directeurs de Thèse

Hélène BARELLI, Chargée de Recherche - INSERM, HDR, IPMC CNRS-UMR 7275

Emmanuel LEMICHEZ, Directeur de Recherche - INSERM, Institut Pasteur, CNRS-UMR2001

Les phospholipides polyinsaturés dans les larges déformations membranaires induites par les toxines bactériennes

Résumé

La plupart des membranes cellulaires contiennent des phospholipides (PL) avec des chaînes acyles saturées et mono-insaturées. Cependant, les PL polyinsaturés (PUPL) sont des composants membranaires abondants dans certaines cellules spécialisées, notamment les neurones et les cellules endothéliales. Précédemment, nous avons montré que l'acide docosahexaénoïque (DHA), un acide gras polyinsaturé qui appartient à la famille des omega 3, réduisait le coût énergétique de la tubulation membranaire, facilitant ainsi la formation de vésicules dans les processus d'endocytose. Ici, nous étudions les effets du DHA dans les PL sur deux processus distincts d'invasion bactérienne ciblant les cellules endothéliales qui reposent soit sur l'inactivation de la RhoA GTPase, soit l'activation des Rho GTPases. Le premier processus est la formation de macroapertures transendothéliales (TEMs) ou tunnels, induits par une toxine bactérienne. Les TEMs représentent une nouvelle voie d'extravasation bactérienne dans les tissus à travers l'endothélium. Le second processus est l'invasion des cellules endothéliales par *Escherichia* pathogène extra-intestinal (ExPEC).

Nous avons modifié le profil lipidique des PL en terme de chaînes acylées dans les cellules endothéliales humaine de la veine ombilicale (HUVEC) par des régimes alimentaires à base d'acides gras définis. Dans des conditions de régime DHA où le pourcentage de DHA-PL à la membrane plasmique augmente, nous avons observé une augmentation de la fréquence d'ouverture des TEMs induits par l'exoenzyme C3 de *Clostridium botulinum* qui inactive la GTPase RhoA. L'effet facilitant la nucléation des TEMs est attribué à une diminution de l'épaisseur des cellules résultant de l'enrichissement en DHA-PL. Les TEMs dans un environnement enrichi en DHA-PL sont aussi plus petits et transitoires, montrant une densité plus élevée. Le produit de la taille maximale des TEMs par leur nombre reste pourtant constant, ce qui indique que la surface totale occupée par les TEM dans une cellule reste similaire. Notre étude montre donc une régulation homéostatique dans la cellule afin d'équilibrer la tension membranaire pour empêcher l'éclatement de la cellule induit par des toxines bactériennes.

Comme preuve plus large de l'importance des niveaux de PULP dans les membranes, nous avons découvert que l'augmentation du pourcentage de DHA-PL à la membrane plasmique réduit l'invasion des cellules endothéliales par une souche d'*E. coli* uropathogène, médiée par une toxine bactérienne activatrice des GTPases Rho. Dans l'ensemble, nos résultats mettent en lumière le rôle inhibiteur des PULP contenant du DHA sur les larges déformations

de la membrane plasmique provoquées par l'actine et induites par deux familles de toxines bactériennes, qui affectent la signalisation de la Rho GTPase pour permettre l'invasion des cellules ou des tissus par des bactéries pathogènes.

Mots clés: membrane, phospholipides polyinsaturés, invasion bactérienne, macro-ouverture transendothéliales, acide docosahexaénoïque, *E.coli* uropathogène

Polyunsaturated phospholipids in large-scale membrane deformations induced by bacterial toxins

Abstract

Most cellular membranes contain phospholipids (PL) with saturated and mono-unsaturated acyl chains. However, polyunsaturated PL (PUPL) are abundant membrane components in some specialized cells, notably neurons and endothelial cells. Previously, we showed that docosahexaenoic acid (DHA), a polyunsaturated fatty acid that belongs to the omega 3 family, reduced the energy cost for membrane tubulation, thereby facilitating vesicle formation in endocytosis processes. Here, we investigate the effects of DHA in PL on two distinct bacterial invasion processes in endothelial cells, which rely on either RhoA GTPase inactivation or the activation of Rho GTPases. The first process is bacterial-toxin induced formation of transendothelial cell macroapertures (TEMs) or tunnels, which represents a novel path for bacterial extravasation in tissues through the endothelium. The second process is extraintestinal pathogenic *Escherichia coli* (ExPEC) invasion of endothelial cells.

We modified the lipidic profile of PL in terms of acyl chains in Human Umbilical Vein Endothelial Cells (HUVEC) by defined fatty acid diets. Under DHA-diet conditions where the level of DHA-PL in the plasma membrane increased, we observed that the frequency of TEM openings increased in cells treated with the RhoA inactivating C3 exoenzyme from *Clostridium botulinum*. The facilitating effect on TEM nucleation was attributed to the thinner cell thickness resulting from DHA-PL enrichment. DHA-PL-enriched environment also triggered an increase of the density of TEMs that display smaller apertures and shorter lifetimes. The product of TEMs maximal size by their number remained constant, indicating the total area occupied by TEMs in a cell remains similar. We therefore show a homeostatic regulation in the host cell in order to balance the membrane tension to prevent cell rupture induced by bacterial toxins.

As a broader evidence of the importance of PULP-levels in membranes, we found that increase of DHA-PL at the plasma membrane reduced bacterial toxin-induced invasion of endothelial cells by uropathogenic *E. coli*. Altogether, our results shed light on the role of DHA-containing PUPL on actin-driven large-scale plasma membrane deformations triggered by two families of bacterial toxins, which jeopardize Rho GTPase signaling to allow cell or tissue invasion by pathogenic bacteria.

Keywords: membrane, polyunsaturated phospholipids, bacteria invasion, transendothelial cell macroaperture, docosahexaenoic acid

Acknowledgement

I thank both of my supervisors, H el ene Barelli and Emmanuel Lemichez for their support over the past four years. I was a stubborn student and they were always patience with me. Emmanuel worked closed with me in the first year of my PhD when he and the team taught me both the technical part and the critical thinking in science. The nutrition I was fed with allowed me to be more independent when the team moved to Paris and I was relocated to IPMC. Even, hundreds of kilometers away, we managed to write the draft of the manuscript together. I give you my appreciation from heart. In IPMC, H el ene continued to support me with her knowledge and kindness. I had a lot of frustration but she taught me a scientist has to be patience and determined. I am grateful to all the efforts she spent on me.

I appreciate Bruno Antonny for his broad knowledge in lipid biology which I hoped to learn a few percent from him. I thank him for all the discussion and his inputs in this project; furthermore, his sympathy and his wills to help all the time. He creates such a nice environment that I was allowed to be independent and surrounded by nice people who are friendly and wise.

I am grateful to all my colleagues who worked on polyunsaturated lipids, Macro Manni, Marion Tiberti, and Romain Gautier. Without them laying the foundation for the knowledge of polyunsaturated lipids, this project would not have come to the light. I thank the lipidomic platform in IPMC, especially Lucile Fleuriot, for their expertise in lipid analysis. Also, I will not forget Sophie Abelanet and Fr ed eric Brau for the numerous training and helps they offered.

I also appreciate my colleagues in bacterial toxin unit, Camille Morel, Serena Petracchini, and Amel Mettouchi, who helped with my experiments in the aspects of bacterial invasion. I thank Serena for working with me on CNF1 induced bacterial invasion. Camille, who also works on TEM, was always enthusiastic and thoughtful in giving her opinion and helping this project.

I am thankful to all the collaborators, David Gonzalez-Rodriguez, St ephane Dallongeville, and S ebastien Janel. St ephane developed a protocol which save a lot of my time on analyzing videos. S ebastien carried out a critical AFM experiment. David who was so bright to propose the physical model to explain our results.

This work will not be success without the warm environment created by my colleagues in IPMC. I thank Bruno Mesmin for his board knowledge and skills in cell biology and his kindness in the office. I thank Jo elle Bigay who did her best to keep the lab in order. Not to forget Amanda Patel and those delicious meals and snacks from her. Also, I thank David Kovacs, who is always intelligent and have good insight in science. I will not forget Melody

Subra for her kindness, Antoine Reynaud for his humor, and Ana Rita Dias Araujo for her thoughtfulness. At last, I thank Maud Magdeleine and Joël Polidori for their patience and constant helps to keep the lab running.

Last, I thank my family for their support and the courage they gave me through this journey. My friends from Signalife, with whom I shared happiness and sadness throughout these years, with whom I learned to live in this foreign country, with whom we defended our thesis during the Covid-19 pandemic. I give my deepest appreciation to Christian for his patience, sweetness, warm meals after a long day in the lab, and clean house. Last respect goes to my cat Tofu for her accompany and supervision in front of my PC.

Table of Contents

CHAPTER 1 POLYUNSATURATED PHOSPHOLIPIDS (PUPL)	15
1.1 PUPL: From chemical structure to physical properties	15
1.1.1 Cellular membranes	15
1.1.2 Lipid diversity in cellular membranes.....	17
1.1.3 Structure of PUPL membrane: MD simulation, X-ray, and NMR.....	19
1.1.4 Membrane deformation is facilitated in PUPL membrane.....	23
1.2 Metabolism of PUPL	27
1.2.1 Synthesis of saturated fatty acid.....	27
1.2.2 Introducing the double bonds to form unsaturated fatty acid	28
1.2.3 Transferring the fatty acid to PL	29
1.2.4 Acyltransferase for PUPL	31
1.3 Functions of PUPL in tissues	37
1.3.1 PUPL in retina.....	37
1.3.2 PUPL in brain.....	41
1.4 Functions of PUPL at the subcellular level	43
1.4.1 PUPL in endocytosis and synapse.....	43
CHAPTER 2 MEMBRANE CURVATURE: FROM LIPIDS TO PROTEINS	46
2.1 Membrane curvature formation	46
2.1.1 Lipid driven curvature formation.....	47
2.1.2 Proteins and membrane curvature.....	48
2.2 Behavior of PUPL on curved membrane.....	52
2.2.1 Composition of the plasma membrane.....	52
2.2.2 PUPL membrane deformation in asymmetric conditions	53
CHAPTER 3 BACTERIAL TOXINS INDUCED LARGE-SCALE MEMBRANE DEFORMATION	57
3.1 Rho family small GTPase	57
3.1.1 RhoA	59
3.1.2 Cdc42	60
3.1.3 Rac1.....	61
3.2 Rho GTPases and endothelium barrier function.....	62
3.2.1 Endothelial barrier functions.....	62
3.2.2 Nitric oxide (NO) signaling	62
3.2.3 Rho proteins and adherens junctions.....	63
3.3 Transendothelial cell macroaperture formation.....	64
3.3.1 Inducers for TEM opening: Toxins and RhoA inhibition.....	65

3.3.2 Stabilization of TEM and the physics behind	68
3.3.3 Effectors that stabilize TEM	71
3.3.4 Closure of TEM.....	73
3.3.5 Physiological consequence of TEM formations.....	74
3.4 Extra-intestinal pathogenic <i>E. coli</i> (ExPEC) invasion	75
3.4.1 Uropathogenic <i>E. coli</i> (UPEC).....	75
3.4.2 CNF1	76
THESIS OBJECTIVES	77
CHAPTER 4 MATERIALS AND METHODS.....	79
4.1 Reagents	79
4.2 Cell Culture, treatments, and transfection.....	79
4.3 Lipid extraction and lipidomic analysis	80
4.4 Video microscope.....	81
4.5 GPMV purification.....	81
4.6 Super-resolution stimulated emission depletion (STED) microscopy	82
4.7 Atomic force microscope measurement of TEM topology	82
4.8 ExPEC invasion	82
4.9 Statistical analysis.....	83
CHAPTER 5 RESULTS	84
5.1 Modulating lipid profile of HUVEC	84
5.1.1 Incorporation of DHA in total cell membranes.....	84
5.1.2 Incorporation of DHA at plasma membrane	87
5.1.3 Impact of Rho GTPases inhibition on FA incorporation.....	90
5.2 DHA promotes the formation of TEMs but inhibits their enlargement	91
5.2.1 Impact of DHA on TEM in a fixed cell population.....	91
5.2.2 Impact of DHA on TEM opening dynamics	93
5.2.3 Impact of DHA on TEM closure dynamics.....	96
5.2.4 Impact of DHA on TEM structures.....	98
5.3 Potential impact of FA-diets on actin recruitment to TEM	99
5.3.1 A second phase of TEM opening: resuming opening.....	99
5.4 DHA-enrichment reduced the invasion of ExPEC	104
CHAPTER 6 DISCUSSION.....	106
6.1 Where do the lipids go?	107
6.2 How does the TEM inducing toxin enter cells?.....	109
6.3 A possible effect from FA signaling?	109

6.4 Membrane tension and the expansion of TEM.....	110
6.5 Global bending rigidity and opening of TEM.....	112
6.6 Topology of TEM	114
6.7 Line tension and stabilization of TEM	115
REFERENCES.....	116
APPENDIX.....	130

List of Figures

Figure 1-1 Structure of eukaryotic cell.....	15
Figure 1-2 Fluid-mosaic model.....	16
Figure 1-3 Three major lipid families in eukaryotic membranes	17
Figure 1-4 DHA structures from computer modeling.....	20
Figure 1-5 Most common PUFAs in mammals	21
Figure 1-6 PUPL chain rotation and the energy cost.....	22
Figure 1-7 Membrane deformation by micropipette.....	23
Figure 1-8 Membrane deformation by optical tweezer.....	24
Figure 1-9 Molecular dynamics simulations of tube pulling from PUPL membrane.....	24
Figure 1-10 Bilayer thickness of natural or swapped phospholipids.....	26
Figure 1-11 Biosynthesis of saturated and unsaturated fatty acids	28
Figure 1-12 De novo and remodeling pathway of PL synthesis	30
Figure 1-13 Crystal structure of LPAAT from <i>T.maritima</i>	31
Figure 1-14 Phototransduction pathway in vertebrate	38
Figure 1-15 Conformational adaptation of rhodopsin in PUPL membrane.....	39
Figure 1-16 Phototransduction pathway in invertebrate.....	40
Figure 1-17 Endocytosis of synaptic vesicle	44
Figure 2-1 Membrane curvature and lipid packing defects	46
Figure 2-2 Intrinsic shape of phospholipids.....	48
Figure 2-3 Structure of amphipathic helix and ALPS motif.....	49
Figure 2-4 Structure of BAR domain proteins.....	50
Figure 2-5 Lipid composition of the inner or outer leaflet of the erythrocyte plasma membrane	53
Figure 2-6 Molecular dynamics simulations of tube pulling from asymmetric membrane.....	54
Figure 2-7 Shape of phospholipid in positive and negative membrane curvature.....	55
Figure 3-1 Structure and spatial-temporal regulation of Rho GTPases.....	58
Figure 3-2 Rho GTPases signaling pathway in regulating cell contractility	59
Figure 3-3 Signaling of nitric oxide between endothelial and smooth muscle cell	63
Figure 3-4 Induction of TEM formation by C3 toxin in HUVECs.....	65
Figure 3-5 Signaling pathway triggering TEM formation	66
Figure 3-6 Physical and cellular liquid dewetting models.....	69
Figure 3-7 Cytoskeleton structures around TEM.....	70
Figure 3-8 Topology of TEM measured by atomic force microscopy.....	71

Figure 3-9 Recruitment of I-BAR proteins around TEM	73
Figure 3-10 Invasion of UPEC is trigger by CNF1 toxin	76
Figure 5-1 Kinetics of fatty acids incorporation in HUVECs.....	85
Figure 5-2 Analysis of phospholipids in HUVEC submitted to OA or DHA diet	86
Figure 5-3 Lipidomic analysis of phospholipids from giant plasma membrane vesicle	89
Figure 5-4 Impacts of C3 and CNF1 toxin on cellular lipidome	90
Figure 5-5 Impact of fatty acid diets on TEM parameters.....	92
Figure 5-6 Impact of DHA enrichment on TEM opening frequency.....	94
Figure 5-7 Impact of DHA enrichment on TEM opening parameters	95
Figure 5-8 Impact of DHA enrichment on TEM closure parameters	97
Figure 5-9 Impact of DHA enrichment on TEM topology	98
Figure 5-10 Resume opening shows instability of TEM	100
Figure 5-11 Impact of DHA enrichment on actin recruitment.....	102
Figure 5-12 Impact of DHA enrichment on cell elasticity.....	103
Figure 5-13 Impact of DHA enrichment on ExPEC invasion.....	105
Figure 6-1 Summary of TEM formation in OA- and DHA-treated cells	107
Figure 6-2 Mechanism of membrane fusion.....	111
Figure 6-3 Mathematical modelling of TEM opening upon reducing membrane bending rigidity.....	112
Figure 6-4 Topology of TEM and membrane tube in OA and DHA membrane.....	114

List of tables

Table 1 The most common phospholipids.....	18
Table 2 The most common sphingolipids.....	19
Table 3. List of acyltransferases and their substrate selectivity.....	34
Table 4. Effect of FA diet on TEM parameters.....	93
Table 5 Increase in PL (%) compared to OA-treated cells.....	108

List of Abbreviations

AA	arachidonic acid
AGPAT	1-acylglycerol-3-phosphate O-acyltransferase
ALPS	amphipathic lipid packing sensor
AFM	atomic force microscope
ARP	Actin-Related Protein
BAR	Bin/Amphiphysin/Rvs
CNF1	cytotoxic necrotizing factor-1
DHA	docosahexaenoic acid
DG	diacylglycerol
EDIN	epidermal cell differentiation inhibitor
Epac	exchange protein directly activated by cAMP
eNOS	endothelial nitric oxide synthase
ET	edema toxin
ExPEC	extra-intestinal pathogenic <i>Escherichia coli</i>
FA	fatty acid(s)
GAP	GTPase-activating proteins
GDI	guanine nucleotide dissociation inhibitors
GEF	guanine nucleotide exchange factors
GPCR	G-protein coupled receptors
GPMV	giant plasma membrane vesicle
GTP	guanosine triphosphate
GUV	giant unilamellar vesicle
HUVEC	human umbilical vein endothelial cell
LBPA	lysobisphosphatidic acid
LPA	lyso-phosphatidic acid
LPAAT	lyso-phosphatidic acid acyltransferase
LPC	lyso-phosphatidylcholine
LPCAT	lyso-phosphatidylcholine acyltransferase
LPDS	lipoprotein depleted serum
LPE	lyso-phosphatidylethanolamine
LPEAT	lyso-phosphatidylethanolamine acyltransferase
LPI	lyso-phosphatidylinositol
LPIAT	lyso-phosphatidylinositol acyltransferase
LPL	lyso-phospholipid
LPLAT	lysophospholipid acyltransferase
LPS	lyso-phosphatidylserine
LIMK	LIM kinase
MBOAT	membrane bound O-acyltransferase
MD	molecular dynamics
mDia	mammalian Diaphanous-related
MI	metarhodopsin I
MII	metarhodopsin II
MLC	myosin light chain
MLCP	myosin light chain phosphatase
MLCK	myosin light chain kinase
MIM	missing in metastasis
MUPL	monounsaturated phospholipid
MUFA	monounsaturated fatty acid
NMDA	N-methyl-D-aspartate

NMIIa	non-muscle myosin IIA
NO	Nitric oxide
PA	phosphatidic acid
PC	phosphatidylcholine
PDE	phosphodiesterase
PE	phosphatidylethanolamine
PI	phosphatidylinositol
PL	phospholipid(s)
PS	phosphatidylserine
PIP	phosphatidylinositol bisphosphate
PUFA	polyunsaturated fatty acid(s)
PUPL	polyunsaturated phospholipid(s)
PKG	cGMP-dependent protein kinase
PKA	cAMP-dependent protein kinase
PLA ₂	phospholipase A2
PLC	phospholipase C
ROCK	Rho kinase
OA	oleic acid
sGC	nitric oxide-soluble guanylyl cyclase
SFA	saturated fatty acid
SM	sphingomyelin
SPL	saturated phospholipid(s)
STED	stimulated emission depletion
TEM	transendothelial cell macroaperture
TG	triacylglycerol
TRP	transient receptor potential
TRPV	transient receptor potential vanilloid
VE-cadherin	vascular endothelial (VE) cadherin
WASP	Wiskott–Aldrich syndrome protein
WAVE	WASP-like verprolin-homologous protein
UPEC	uropathogenic <i>Escherichia coli</i>
UTIs	urinary tract infections

Chapter 1 Polyunsaturated phospholipids (PUPL)

1.1 PUPL: From chemical structure to physical properties

PUPL are special lipids with interesting physical properties. Due to their chemical structures, they are highly dynamic and flexible. Therefore, they facilitate membrane deformation such as membrane protein conformational change, ion-channel opening, and endocytosis. In this chapter, we discuss how chemical structure of PUPL affect the physical properties of cellular membrane.

1.1.1 Cellular membranes

Cells are the fundamental building blocks of life. If we consider cell as a small house, then membrane is the wall of the house that separate inner and outer space. It blocks the entry and exit of polar materials, so as to contain molecules, generate membrane potential, prevent pathogens etc. Membrane wall also creates intracellular chambers, the organelles, to carry out specific cellular functions. Therefore, various biochemical reactions can occur in a tiny cell separately and simultaneously (**Figure 1.1**). The secretory pathway is one example. The nuclear membrane retains the genetic materials in the nucleus while RNAs are the messengers that pass through the nucleus pore to reach cytosol. RNAs are translated in ribosomes that are attached to ER. After being translated, proteins can be transported to Golgi apparatus, where various post-translational modification enzymes are abundant, for further processing. The secretory proteins are packed into vesicles nascent from *trans* Golgi membranes. As these vesicles travel and fuse with plasma membrane, secreted proteins are released and served as communicators from the cell to the outer environment.

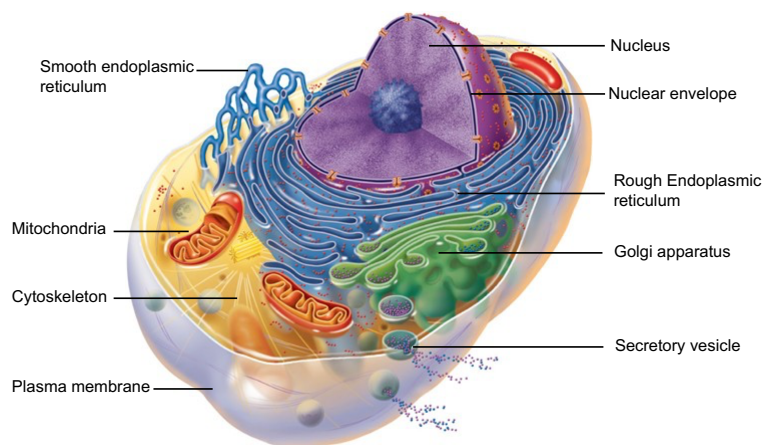


Figure 1-1 Structure of eukaryotic cell. Membrane is a barrier that separates the cell from the outer environment. Membrane proteins and vesicles are responsible for all the communications

between cell and environment. Internal membranes also enclose various organelles; thus, each organelle is dedicated to specific functions without interfering one another. Illustration extracted from Campbell Biology ©Pearson Education

Lipids are the bricks that compose membrane and are organized into a bilayer structure, where the polar head groups face aqueous medium, cytosol or external fluid, and the hydrophobic tails from the two monolayers face each other. In 1972, Singer and Nicolson proposed the fluid-mosaic membrane model, according to which proteins are integrated in or associated with the membrane bilayer by their non-polar residues (**Figure 1.2**). The lipid membrane has a fluid state, which acts as a 2-dimensional solution for protein diffusion (Nicolson, 2014; Singer and Nicolson, 1972). However, the lipid composition of the membrane is not uniform (Kobayashi and Menon, 2018). Owing to their fluid nature, lipids form transient nano-domain in response to stimulations to regulates cellular functions (Eggeling et al., 2009). Membrane bilayers compose a complexed network with proteins, including adhesion molecules, receptors, and cytoskeletons etc., to link the extracellular stimulation to cellular responses. In addition, the non-random complex interaction between membrane lipids, transmembrane proteins, cytoskeleton, and extracellular matrix forms are critical for distributions of membrane components (Nicolson, 2014). Owing to this complex interaction, the membrane barrier blocks the entry of most of the non-polar molecules but retains paths for communications with the extracellular environment.

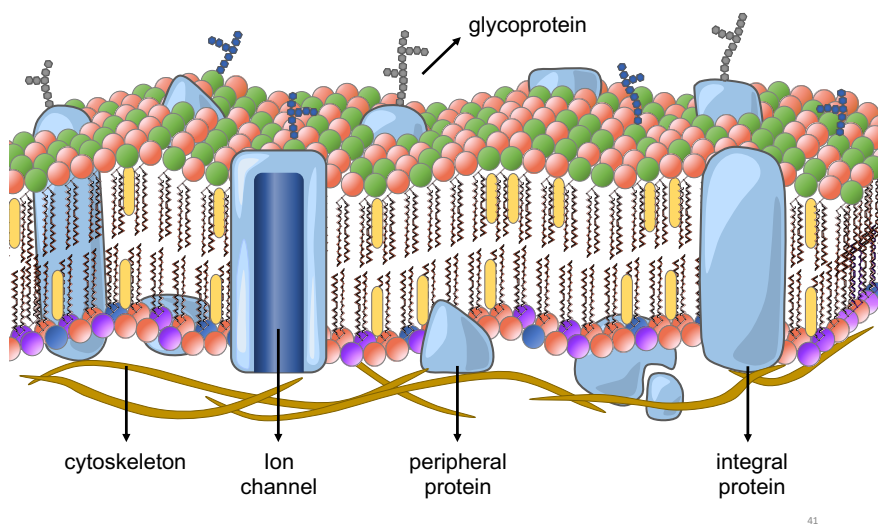


Figure 1.2. Fluid-mosaic model. Cellular membrane is composed of lipids and various proteins. Lipids are the matrix of the membrane and are fluid in physiological conditions. They form a bilayer, which polar heads face the water face and fatty acid tail cluster in bilayer center to

maintain the minimal energy required for thermodynamics. Proteins diffuse in the fluid lipid matrix. They either integrate in the membrane as transmembrane proteins, or associate with membrane as peripheral proteins.

1.1.2 Lipid diversity in cellular membranes

The cellular membranes are extremely complex not only due to variability of membrane proteins but also due to the lipid compositions. There are three major lipid families in eukaryotic membranes: glycerophospholipids, sphingolipids, and sterols (**Figure 1.3**). Combination of various polar groups and fatty acid chains generates highly diverse lipid chemical structures.

Glycerophospholipids or Phospholipids (PL) are composed of a glycerol backbone, a polar head group, and two acyl chains. The position of the three carbons of the glycerol backbone are designated as sn-1, sn-2, and sn-3. The polar group is attached to sn-3 position via a phosphodiester bond. The sn-1 and sn-2 carbons of glycerol are attached with fatty acids via ester bonds, creating the hydrophobic acyl chain part of the PL. (**Figure 1.3**).

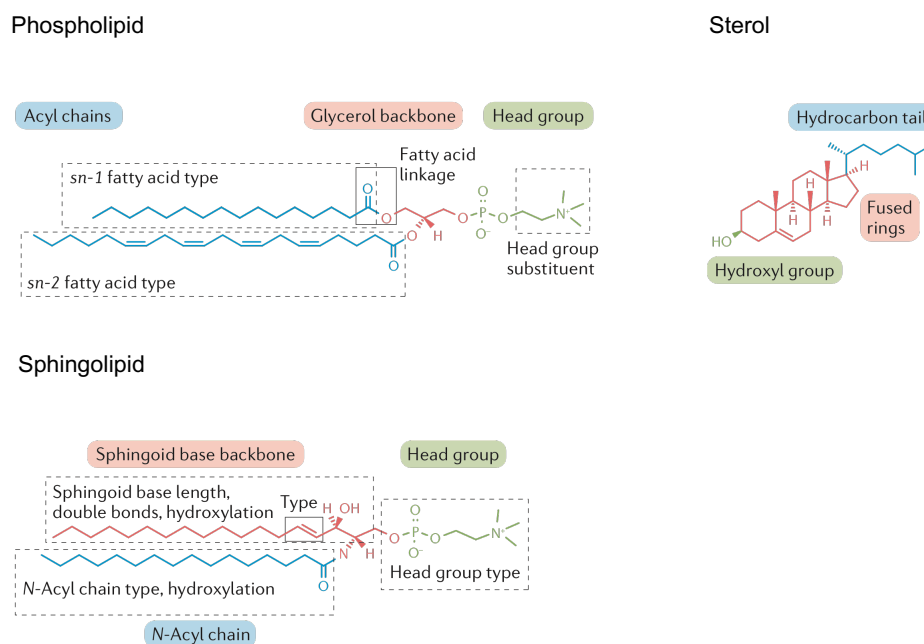
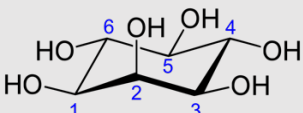


Figure 1.3. Three major lipid families in eukaryotic membranes. Phospholipid contains a glycerol backbone attached with a polar group and two fatty acyl chains. Sphingolipid contains a sphingoid base attached with a polar group and a fatty acyl chain. Sterol contains 4 fused carbon rings and a short hydrocarbon tail. Illustration extracted from (Harayama and Riezman, 2018).

The polar head groups define the lipid classes such as phosphatidylcholine (PC), phosphatidylethanolamine (PE), phosphatidylserine (PS) and phosphatidylinositol (PI), while the acyl chains define the lipid species. The combination of various polar groups and various acyl chains creates if not thousands, hundreds of lipid species.

PL are the most abundant lipids in mammalian membranes. They can be further divided into different classes by their polar group. The polar group contributes to the shape and defines the charge of the lipid, while the fatty acid chains influence the packing of the membrane. Polar groups are attached to glycerol via one negatively-charged phosphodiester bond. For example, a positively-charged polar group, choline, links to glycerol via phosphodiester bond creates zwitterionic phosphatidylcholine. PL are nominated as PX(A:B/C:D)nE in which PX represents the polar group of the PL, such as PC or PE. The A and C represent the number of carbons in the two acyl chains, while B and D represent the number of double bonds in the sn-1 and sn-2 acyl chain, respectively. Last, ωE (also nE) is the position of the first double bond counting from the methyl end. For example, PC(16:0/18:1) ω9 (or n9) contains a choline head group, one acyl chain with 16 carbons without double bond at sn-1 position while in sn-2 position an acyl chain with 18 carbons and 1 double bond at the 9th carbon. The most common PL classes are listed in **Table 1**.

Table 1 The most common phospholipids

Phospholipids	Formula of polar alcohol	PL net charge at pH7
Phosphatidic acid (PA)	-H	-1
Phosphatidylethanolamine (PE)	-CH ₂ - CH ₂ -NH ₃ ⁺	0
Phosphatidylcholine (PC)	-CH ₂ - CH ₂ -N ⁺ (CH ₃) ₃	0
Phosphatidylserine (PS)	-CH ₂ - CH(COO ⁻)- NH ₃ ⁺	-1
Phosphatidylglycerol (PG)	-CH ₂ - CH(OH)-CH ₂ -OH	-1
Phosphatidylinositol (PI)		-1

Sphingolipid is composed of a long-chain sphingoid base backbone, a fatty acid, and a polar head group. (**Figure 1.3**) The sphingoid base constitutes both a backbone and a hydrophobic tail. It is attached to another fatty acid chain and a polar group and it also contains a hydrocarbon tail that resembles one of the fatty acid in PL. Sphingolipid is named after its

polar head groups. Ceramide has a hydroxyl polar group and is the parent of all sphingolipids. Ceramide can further attach with other polar group such as phosphocholine or sugars to form sphingomyelin (SM) or glycosphingolipid. Sphingomyelin is present at the plasma membrane of animal cells and is abundant on the membranous myelin of neurons. Glycosphingolipids are present on the outer leaflet of the plasma membrane and are important for cell-cell interactions. The most common sphingolipids are listed in **Table 2**.

Table 2 The most common sphingolipids

Sphingolipids	Formula of polar alcohol
Ceramide	-H
Sphingomyelin	$-\text{PO}_3^- - \text{CH}_2 - \text{CH}_2 - \text{N}^+(\text{CH}_3)_3$
Glycosphingolipid	Glucose or Galactose
Ganglioside	Oligosaccharides

Sterols have an unconventional structure composed of 4 fused carbon rings, a minimal polar head group, and a short hydrocarbon tail. The most common sterol in mammals is cholesterol, which accounts for 30-50% of plasma membrane lipids (Gerl et al., 2012; van Meer et al., 2008). Cholesterol utilizes its head group and fused ring to contact with the head groups and fatty acid chains of PL respectively. Lack of rotation in the carbon ring makes sterol a rigid structure in membrane. Cholesterol is also the precursor of steroid hormones, vitamin D and bile salts.

1.1.3 Structure of PUPL membrane: MD simulation, X-ray, and NMR

Fatty acids (FA) are carboxylic acids with hydrocarbon chains containing 12-24 carbons. The carbons in the hydrocarbon chain are connected by single or double bonds. The carboxylic end is esterified with glycerol to form PL and the methyl end is extended in the bilayer. Saturated fatty acids (SFA) have only single bonds present in chain, making the number of hydrogen saturated. Monounsaturated fatty acids (MUFA) have only one double bond in the hydrocarbon chain. The most common MUFA is C18:1, in which the double bond is located at the middle (9th carbon, n9 or ω 9) of the hydrocarbon chain. Polyunsaturated fatty acids (PUFA) have from 2 to 6 double bonds. The most common PUFA are C20:4 and C22:6. C20:4 contains 4 double bonds from the 6th (omega-6, n-6 or ω 6) carbon counting from the methyl end while C22:6 contains 6 double bonds from the 3rd (omega-3, n3 or ω 3) carbon counting from the methyl end. In natural PL, sn-1 position is usually linked with a saturated acyl chain while sn-2 is usually linked with a mono- or polyunsaturated acyl chain. In this thesis, we define

monounsaturated phospholipid (MUPL) a phospholipid esterified with mono-unsaturated acyl chain(s). Polyunsaturated phospholipid (PUPL) is a phospholipid esterified with polyunsaturated acyl chain(s).

Membrane order

For a long time, researchers considered PUPL rigid due to the lack of rotation in the double bonds. However, various data has shown that PUPL membranes are disordered. NMR of PUPL membranes showed that increasing the unsaturation in sn-2 acyl chain reduced the order of the saturated sn-1 chain (Holte et al., 1995; Salmon et al., 1987). The probe 1,6-diphenyl-1,3,5-hexatriene is embedded in the membrane and sensitive to aqueous environment, thus it is used as a lipid order probe. Using 1,6-diphenyl-1,3,5-hexatriene, Mitchell and Litman demonstrated that membrane order decreased with the level of unsaturation, especially when both acyl chains were polyunsaturated (Mitchell and Litman, 1998a; Mitchell and Litman, 1998b). These observations led to two hypotheses: either that PUFA itself is less ordered, or the bulky PUFA decrease the order state of adjacent SFA.

Conformation: MD simulation, NMR, and X-ray

One of the first computer-based modeling of docosahexaenoic acid (DHA) molecules showed that DHA could have a twisted hairpin structure and two extended conformations, angle-iron shape and helical shape (Applegate and Glomset, 1986) (**Figure 1.4**). However, more and more structures were reported later on.

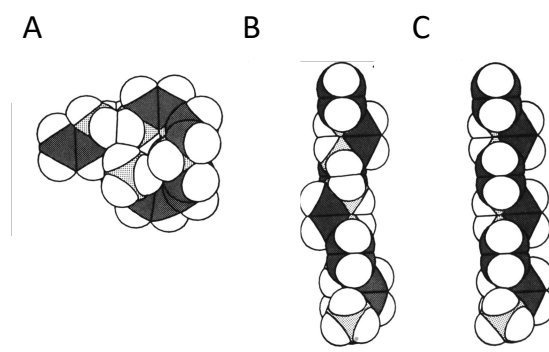


Figure 1.4. DHA structures from computer modeling. There were three C22:6 structures at low energy cost. (A) The hairpin structure, in which the carbons are twisted. (B) The helical structure, in which the 6 double bonds were projected from the methyl axis at 90° interval. (C) The angle-iron, in which the 6 double bonds were projected in two nearly perpendicular plans. Illustrations extracted from (Applegate and Glomset, 1986).

The double bonds in PUFA are never connected, they are always separated by single bonds in a pattern like -CH=CH-CH₂-CH=CH- (**Figure 1.5**). This unique chemistry, where a rigid double bond is flanked by rotating single bonds, creates an unique flexibility to the chain.

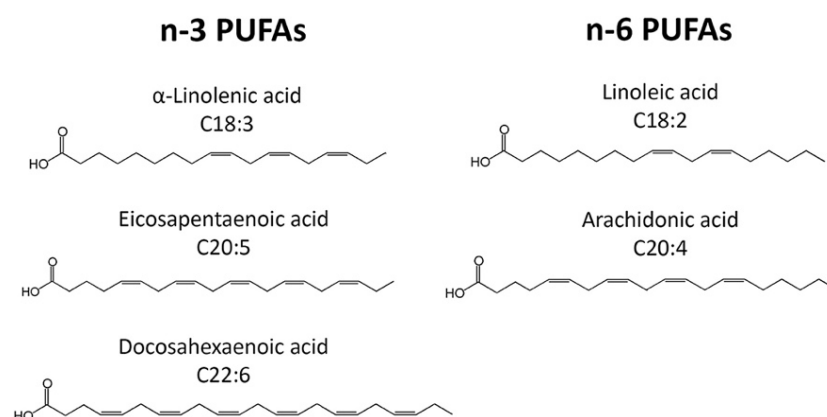


Figure 1.5. Most common PUFA in mammals. The double bonds in ω 3 PUFA starts from the 3rd carbon counting from the methyl group while the double bonds in ω 6 PUFA starts from the 6th carbon counting from the methyl group. Double bonds in PUFA are always flanked by single bonds.

Quantum mechanical calculation of PC(18:0/22:6) showed that the energy barrier for rotation of single-bond carbons in C22:6 chain was pretty low, even lower than that of C18:0 chain (**Figure 1.6A**)(Feller et al., 2002). The lowest energy state for C22:6 chain rotation was at $\pm 100^\circ$ dihedral angle (**Figure 1.6A**, solid line), whereas for C18:0 chain it was at $\pm 60^\circ$ (**Figure 1.6A**, dash line). The lowest rotation energy in C18:0 was higher than that of C22:6, indicating that C22:6 had less energy barrier to rotate. Apart from the angle-iron and helical conformations described by Applegate and Glomset, molecular dynamics (MD) simulation also identified several conformations where C22:6 was distorted or bent (**Figure 1.6B**)(Feller et al., 2002; Gawrisch et al., 2008).

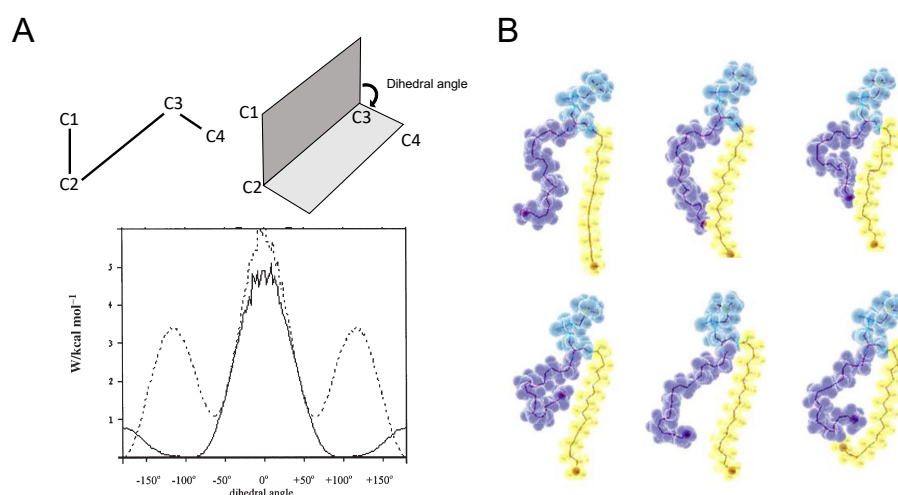


Figure 1.6. PUPL chain rotation and the energy cost. (A) Schematic view of dihedral angle along the hydrocarbon chain and the rotation energy of methylene carbons that separate alkene carbons in *sn*-2 C22:6 (solid line) and between methylene carbons in *sn*-1 C18:0 (dash line)(Feller et al., 2002). (B) Conformations of PC(18:0/22:6) in a lipid bilayer from MD simulation. The C22:6 is shown purple, C18:0 is shown in yellow, and glycerol is in blue. Illustrations extracted from (Gawrisch et al., 2008).

The structure of PUPL was studied intensively in the early 2000s by Gawrisch's and Brown's laboratories. NMR experiments on PC(18:0/22:6) showed that the methyl end of C22:6 underwent large and fast conformational changes. Moreover, NMR demonstrated that there was a gradient of disorder from carboxyl end to methyl end of C22:6, where the highest disorder was found (Eldho et al., 2003; Rajamoorthi et al., 2005). The X-ray scattering data also showed that in PC(18:0/22:6), C18:0 was stretched toward the bilayer center while C22:6 was shifted toward the water-lipid interface (Eldho et al., 2003; Rajamoorthi et al., 2005).

The structural studies and MD simulations on flat membrane bilayers showed that esterified PUFA chains are highly dynamics in transition between several conformations. The methyl carbons between double bonds could twist at low energy cost. While SFA is stretched toward the bilayer center, PUFA is distorted toward the water-lipid interface. Therefore, in PUPL membrane, *sn*-2 PUFA is disordered due to its fast-dynamic nature while *sn*-1 SFA is disordered due to the capacity to invade the vacancy created by PUFA torsion.

1.1.4 Membrane deformation is facilitated in PUPL membrane

For a long time, structural studies of PUPL were done on flat membranes. However, increase in FA chain flexibility should be more beneficial when membranes undergo deformations such as curvature formation. Increasing membrane disorder could make membranes more deformable and permeable.

The biochemical experiments on PUPL deformability started in 2000 when Evans's team used micropipette to apply tension on giant unilamellar vesicle (GUV) to deform membrane. The energy required to deform membrane depended on the membrane bending modulus. They measured a decrease in membrane bending modulus of PC(18:0/18:2) and PC(18:3/18:3) membrane compared to PC(18:0/18:1) (**Figure 1.7**) (Rawicz et al., 2000). Due to the unavailability of asymmetric PUPL lipids, they used mainly symmetric PUPL lipids that contains identical unsaturated chain in both sn-1 and sn-2 position. Moreover, highly unsaturated PUPL containing C20:4 or C22:6 chain was missing from the experiments.

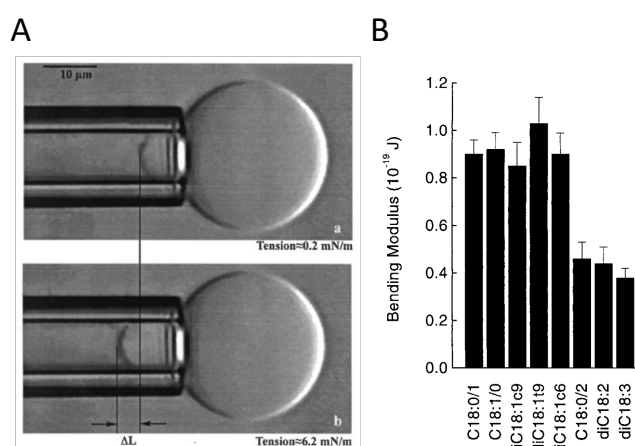


Figure 1.7. Membrane deformation by micropipette. (A) A micropipette was used to applied tension on GUV of different level of unsaturation. (B) Membrane bending modulus of different GUVs was calculated from the change in area. Illustrations extracted from (Rawicz et al., 2000).

Our lab (Bruno Antonny, IPMC) in collaboration with the lab of Bruno Goud (UMR144, Institute Curie) recently revised this concept. Pinot *et. al.*, pulled a 5-10 μ m tube with concanavalin A-coated optical tweezer from GUV made of PUPL (**Figure 1.8C**) or epithelial cells enriched in C22:6 (**Figure 1.8A-B**). They measured 2-fold reduction in both the force (F) that is needed to pull the tube and also the apparent radius of the tube (R). This allowed them to calculated membrane bending modulus (κ) and membrane tension (σ) from Helfrich's model: $\kappa = \frac{FR}{2\pi}$ and $\sigma = \frac{F}{4\pi R}$. They showed that the membrane bending modulus of PUPL membrane

was 4-fold smaller than MU-PL membrane while the membrane tension remained the same (Pinot et al., 2014).

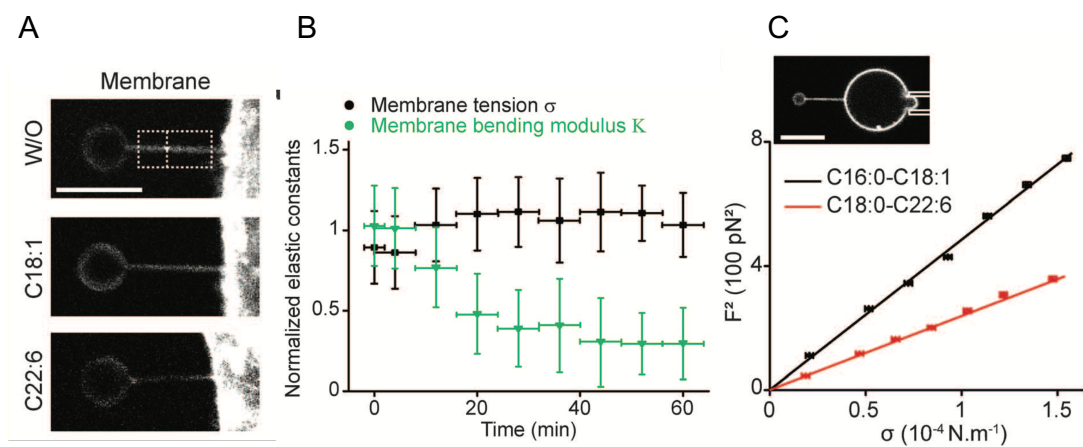


Figure 1.8. Membrane deformation by optical tweezer. (A) Experimental set up for measuring membrane deformation in cells. RPE1 cells were enriched in C18:1 or C22:6. A membrane tube was pulled from the membrane using optical tweezers. The force and radius of the tube was used to calculate membrane bending modulus in (B). (B) The evolution of membrane tension and bending modulus during the incubation of cells with C22:6. (C) Same experiment was done in GUV composed of 30% PE(16:0/18:1) or PE(18:0/C22:6). Illustrations extracted from (Pinot et al., 2014).

MD simulations of pulling tubes with constant force from membrane with different level of unsaturation showed that higher the unsaturation level was, faster and thinner the tube formed (Figure 1.9)(Manni et al., 2018; Pinot et al., 2014). MD simulations are in line with the biochemistry experiments which show that PUPL reduces the membrane bending modulus, thus it is easier to pull tube from PUPL membrane.

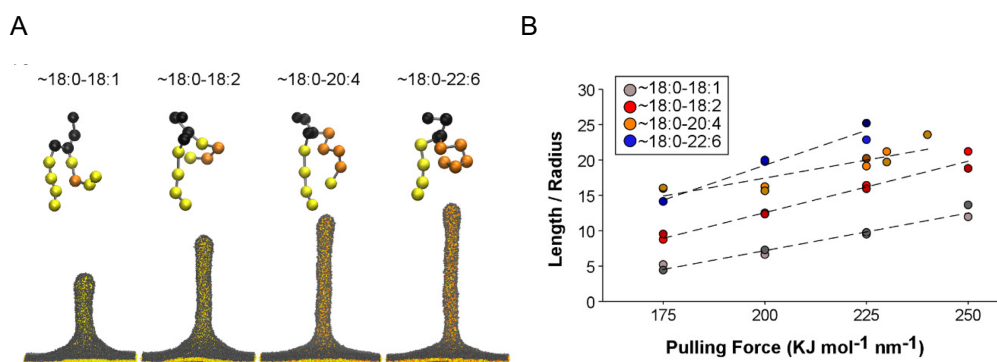


Figure 1.9. *Molecular dynamics simulations of tube pulling from PUPL membrane. (A) Snapshots at the same time of membranes containing the indicated PUPL pulled with a force of $200 \text{ KJ mol}^{-1}\text{nm}^{-1}$ in a coarse-grain MD simulation. (B) Correlation between the tube length/radius ratio and pulling force. Illustrations extracted from (Manni, et al. 2018).*

Here, our team and others extend the findings *in silico* to *in vitro* lipid models and *in vivo* cellular system. Increasing in lipid unsaturation makes membrane more flexible. The flexibility of membrane is beneficial to adapt membrane proteins, curvature, and fast membrane deformation. We will discuss more about the physiological significance of PUPL in Chapter 1.3 and 1.4.

Water permeability

Increase in water permeability of PUPL membrane was first described by Evans's team, when they applied hypotonic solution on GUV with micropipettes (Olbrich et al., 2000). Similar experiment was done recently using droplet interface bilayer (DIB), which two monolayer droplets were brought together and a bilayer was formed at the interface. Osmotic pressure was created due to the different salt concentration in the droplets, and water permeability was measured by the change in droplets volumes. Here, increasing the percentage of PUPL in membrane was correlated to higher water permeability (Foley et al., 2020). Using GUV with increasing level of unsaturation, our team also observed an increase in permeability to dithionite and water-soluble AlexaFluor. Moreover, MD simulations showed that water had higher probability of invading a PUPL bilayer compared to MUPL bilayer (Manni et al., 2018). The dynamics of PUPL membrane creates disorder FA organization and vacancy for water molecules to cross.

The importance of acyl chain asymmetry.

In 1968, Yabuuchi and O'Brien discovered that natural PL are usually asymmetric, with the sn-1 position bound with a saturated acyl chain and the sn-2 position bound with an unsaturated one (Yabuuchi and O'Brien, 1968). Two questions arise from this observation. Why having an asymmetry (one saturated and one unsaturated) combination of the two acyl chains in PL? Why unsaturated chain is situated in sn-2 position?

The impact of this striking asymmetry in acyl chain composition has been studied by Manni *et al.*, very recently in our lab. While having one PUFA chain is beneficial for membrane deformation, having 2 PUFA in the same time might create too much flexibility (Manni et al., 2018). Liposomes composed of symmetric PUPL, which contained 2 unsaturated chains, were

more disordered than natural asymmetric PUPL, which contained 1 unsaturated chain, as measured by lipid order probe, push-pull pyrene (Niko et al., 2016). Increasing in the lipid disorder resulted in higher dynamin activity, which drove the fission of vesicles and being critical for endocytosis, in symmetric PUPL membrane. Nevertheless, too much flexibility is problematic in terms of permeability. In symmetric PUPL GUV, permeability to dithionite and water-soluble Alexa Fluor was much higher than its asymmetric counterpart. MD simulations showed that membranes composed of symmetric PUPL were more permeable to water, suggesting a decrease in barrier function (Manni et al., 2018). Asymmetric PUPL generates membrane that are flexible but yet impermeable.

The importance of PUFA position: sn-1 and sn-2

In natural PUPL, PUFA chain is usually attached to sn-2 carbon. Interestingly, the 3 carbons of the glycerol of PL are slightly tilted, in which sn-2 carbon is higher than sn-1 carbon (Manni et al., 2018). Structural studies showed that sn-2 PUFA was shifted toward the bilayer surface, whereas sn-1 SFA was extended to the center of the bilayer. This indicates that the length of a PL is determined by the saturated chain in the lower sn-1 position. Swapping the position of SFA and PUFA between sn-1 to sn-2 position shifted SFA tail upward from bilayer center to the polar surface, making the bilayer thinner (**Figure 1.10**). However, the flexibility of PUPL did not seem to be affected by position swapping, since FA torsion and protrusion (the ability of acyl chain to twist) during tube formation remain similar (Manni et al., 2018).

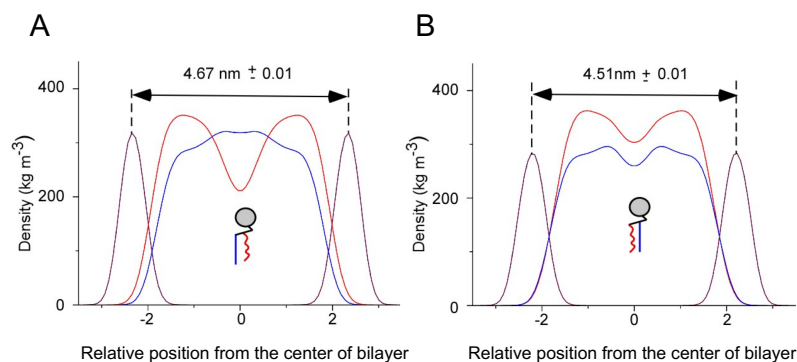


Figure 1.10. Density profile of polar group (purple line), saturated chain (blue line), and polyunsaturated chain (red line) across the lipid bilayers in natural PL (A) or swapped PL (B). The distance of the polar group between two bilayers is used to calculate the bilayer thickness. Illustrations extracted from (Manni, et al. 2018).

Another type of asymmetry in biological membrane is the asymmetry encountered between leaflets, which will be discussed in Chapter 2.2.

1.2 Metabolism of PUPL

The synthesis of PL is essential for any cell formation and maintenance. After being synthesized, FA can be incorporated into PL, the structural components of cellular membrane, through a series of enzymatic reactions. FA can also be converted to eicosanoids, which play roles in signaling. Furthermore, free FA act as agonists for ion channels. One of the challenges in studying PL is the difficulty to distinguish between effects of free FA on cell signaling from effect when FA are esterified to PL as membrane structure. This can be achieved by understanding the metabolic pathway of FA esterification. Defects from blocking the FA esterification to PL results from the lack of specific PL in membrane. Therefore, it reveals the impact of specific FA when it is incorporated to PL as a structural component of the membrane. For example, knocking down of the Lysophosphatidic Acid Acyltransferase 3 (LPAAT3), an acyltransferase specific for C22:6, reduced visual function (Shindou et al., 2017). This indicates that the present of PL containing C22:6 is critical for phototransduction. In this chapter, we describe the synthesis of PL and the physiological outcome of interfering this pathway.

1.2.1 Synthesis of saturated fatty acid

FA synthesis involves 4 repeated reactions carried out by different domains of the same enzyme, fatty acid synthase I (**Figure 1.11A**). FA are synthesized by adding 2 carbons from malonyl-CoA to the carboxyl terminus of the hydrocarbon chain. Before synthesis, acetyl-CoA and malonyl-CoA are attached covalently to the enzyme. The first step is condensation, in which the acetyl group is transferred to the malonyl group forming an acetoacyl group and a CO₂. Later on, the carbonyl group is reduced, hence forming a hydroxylacyl group. The hydroxyl group is then dehydrated, resulting in a *trans* double bond between the C2 and C3 carbons. The double bond is later reduced to form a saturated acyl group. This 4-step cycle continues by adding 2 carbons from malonyl-CoA in a time until reaching 16 carbons (Gunstone et al., 2007; Nelson et al., 2008).

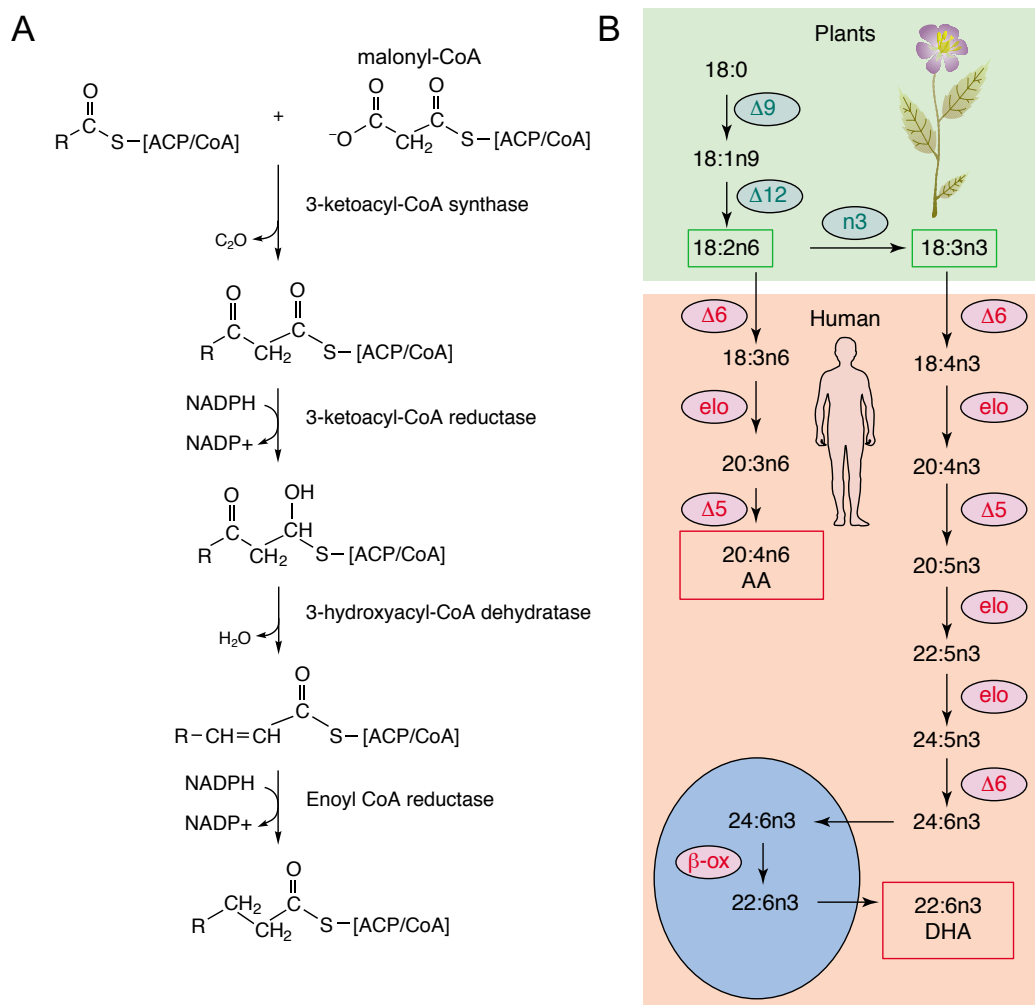


Figure 1.11. Biosynthesis of saturated and unsaturated fatty acids. (A) fatty acids are synthesized in a 4-step reaction using malonyl-CoA as carbons donor. This 4-step reaction repeats by adding 2 carbons in a time to create saturated fatty acids. (B) Double bonds are introduced into saturated fatty acids via series reactions of elongation and desaturation. Here, the fatty acids are presented as 18:1n-9, which n represents the ω number of FA. Illustrations extracted from (Wallis et al., 2002).

1.2.2 Introducing the double bonds to form unsaturated fatty acid

SFA can be further elongated and desaturated to give long chain PUFA (**Figure 1.10B**). Of note, unsaturated FA are designated by an ω (n) number, which is defined from the position of the first double bond counting from the methyl end. On the other hand, desaturases are designated by a Δ number, which gives the position of the double bond they introduce counting from the carboxyl end. C18:0 can be converted to C18:1 ω 9 by the Δ 9 desaturase, which

introduces a double bond between C9 and C10 from the carboxyl end. Addition of another double bond by a $\Delta 12$ desaturase at 12th carbons generates C18:2 $\omega 6$. From here, another double bond could be introduced at 15th carbon by $\Delta 15$ desaturase, forming C18:3 $\omega 3$. The $\Delta 12$ desaturase and $\Delta 15$ desaturase do not exist in mammals. Because mammals are incapable of synthesizing C18:3 $\omega 3$ and C18:2 $\omega 6$ PUFA, they must uptake these precursors from the diet (Wallis et al., 2002). However, further processing of C18:2 $\omega 6$ and C18:3 $\omega 3$ into longer and more unsaturated form can be performed by mammalian enzymes (**Figure 1.11B**).

C18:2 $\omega 6$ and C18:3 $\omega 3$ can be targeted by the same $\Delta 6$ desaturase, generating C18:3 $\omega 6$ and C18:4 $\omega 3$, respectively. They could be further elongated to C20:3 $\omega 6$ and C20:4 $\omega 3$ and targeted by $\Delta 5$ desaturase to create C20:4 $\omega 6$ and C20:5 $\omega 3$. The conversion to C22:6 is more complicated than just an elongation and a desaturation due to the lack of $\Delta 4$ desaturase activity in mammals. C20:5 $\omega 3$ has to go through 2 elongation reactions to form 24:5 $\omega 3$ and desaturated by $\Delta 6$ desaturase to C24:6 $\omega 3$. C24:6 then enters peroxisome or mitochondria for a round of β -oxidation to form C22:6 $\omega 3$ (Wallis et al., 2002).

1.2.3 Transferring the fatty acid to PL

Once PUFA is synthesized, it is incorporated into glycerol to form PUPL. There are two pathways to incorporate fatty acids into PL; one is the *de novo* pathway and the other is the remodeling pathway (**Figure 1.12**). All PL start from the *de novo* pathway, in which glycerol-3-phosphate is attached with an acyl-CoA by glycerol-3-phosphate acyltransferase (GPAT) to form lysophosphatidic acid (LPA). Then, another acyl-CoA is attached to LPA by LPA acyltransferase (LPAAT) to form phosphatidic acid (PA). PA is later converted to diacylglycerol or cytidine diphospho-diacylglycerol that can further be associated with different head groups to form different classes of PL.

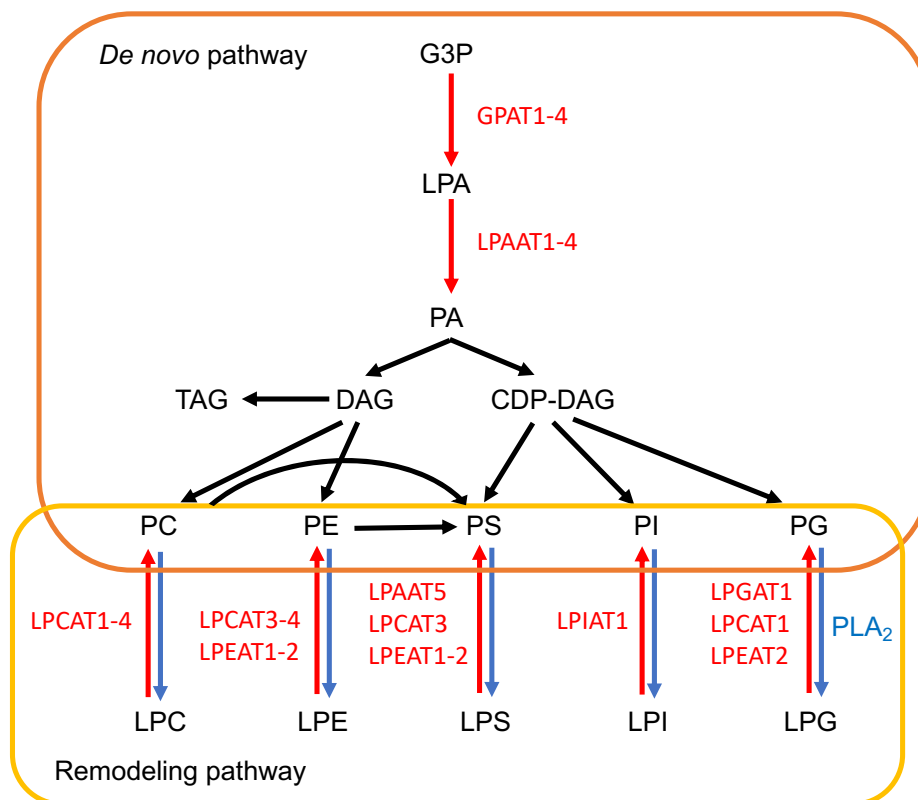


Figure 1.12 De novo and remodeling pathway of PL synthesis and the acyltransferases involved. Abbreviation: G3P, glycerol-3-phosphate; GPAT, glycerol-3-phosphate acyltransferase; PA, phosphatidic acid; LPAAT, lysophosphatidic acid acyltransferase; TAG, triacylglycerol; DAG, diacylglycerol; CDP-DAG, cytidine diphospho-diacylglycerol; PC, phosphatidylcholine; PE, phosphatidylethanolamine; PS, phosphatidylserine; PI, phosphatidylinositol. LPL, lyso-phospholipids. LPCAT, lyso-phosphatidylcholine acyltransferase; LPEAT, lyso-phosphatidylethanolamine acyltransferase; LPIAT, phosphatidylinositol; LPGAT, lyso-phosphatidylglycerol acyltransferase; PLA₂, phospholipase. Illustration updated from (Shindou and Shimizu, 2009).

The remodeling pathway is a coordinated action between phospholipase A₂ (PLA₂) and lysophospholipid acyltransferase (LPLAT). First, PLA₂ cleaves sn-2 acyl chain from PL, resulting in lysophospholipid (LPL), i.e. lyso-PC (LPC), lyso-PE (LPE), lyso-PS (LPS), and lyso-PI (LPI). Then, a new acyl chain is attached to LPL at the free sn-2 position by LPLAT. The combination of both *de novo* and remodeling pathway pave the way to a large diversity of PL (Harayama and Riezman, 2018; Shindou et al., 2013).

1.2.4 Acyltransferase for PUPL

Acyltransferases belongs to 1-acylglycerol-3-phosphate O-acyltransferase (AGPAT) and the membrane bound O-acyltransferase (MBOAT) families. There are 4 LPLATs identified in the MBOAT family (LPCAT3, LPCAT4, LPEAT1, LPIAT1), while the rest of LPLATs and LPAATs belong to the AGPAT family.

There are 4 conserved motifs in the AGPAT family, denoted as motif 1-4. Recently, the crystal structure of the bacterial LPAAT from *Thermotoga maritima* has been resolved (**Figure 1.13A**)(Robertson et al., 2017). Motif 1-3 are in close geometric proximity and create an active tunnel. The histidine in Motif 1 is the catalytic residue, in which it acts as a base to abstract a proton from LPA for nucleophilic attack. Motif 2 is adjacent to some basic residues that positioned to the negatively-charged acyl donor. Motif 3 stabilizes the binding between motif 1 and the LPA. Motif 4 acts as a cap for the active site. Interestingly, the hydrophobic tunnel fits perfectly a C16:0 chain. Changing the size of residue at the end of the tunnel changes the acyl chain selectivity of the enzyme. A two-helix motif is located at the N-terminus and associates with the membrane, making all the catalytic motifs on the same side of the membrane (**Figure 1.13B**). The conformation allows entry of soluble acyl-CoA from the cytosol and abstraction of LPA from the membrane bilayer (Robertson et al., 2017).

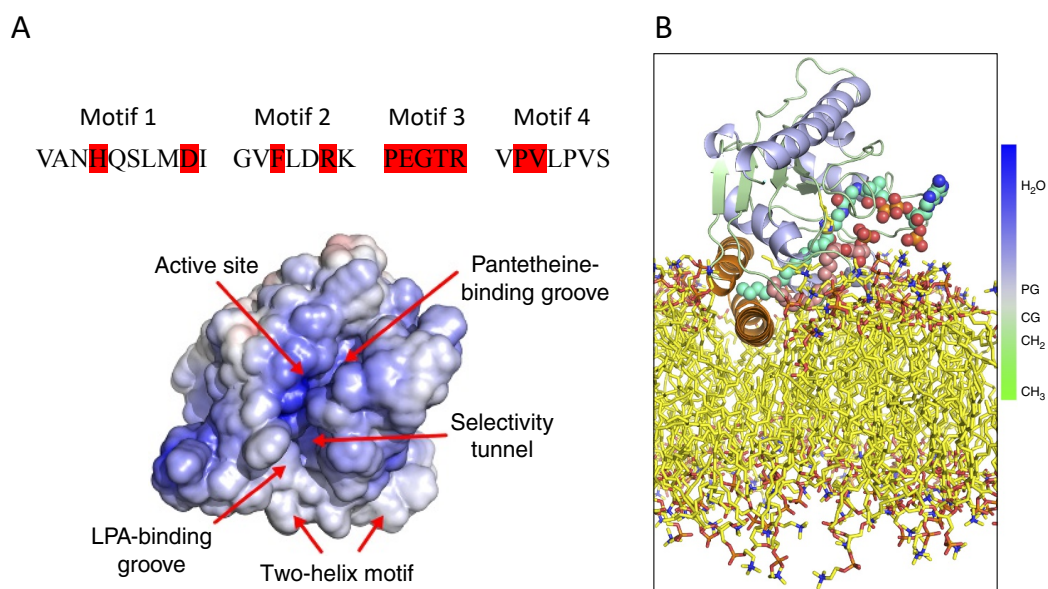


Figure 1.13. Crystal structure of LPAAT from *Thermotoga maritima*. (A) The sequence of 4 conserved AGPAT motifs and the structure of the protein. Conserved residues are marked in red. Motifs 1-3 are adjacent to each other and are embedded in an active site cleft. Range of red to blue color in the 3D structure represents negative to positive electrostatic potentials. (B)

The position of the protein to membrane bilayer. Two-helix motif binds and anchors to the membrane. The LPA-binding groove is close to the membrane while the acyl-CoA panthetheine-binding groove is faced toward the aqueous cytosol. Illustrations extracted from (Robertson et al., 2017).

On the other hand, the mammalian LPAAT1-4 were predicted to have 3-6 transmembrane domains, one of which was located between motif 1 and 2, resulting motif 1 on one side of the membrane and motif 2-3 on the other side (Yamashita et al., 2014; Zhukovsky et al., 2019). The functional relevance of this configuration is not clear. It might bring the 4 motifs in close proximity and allows substrate enter from both side of the membrane.

MBOAT family are multi-transmembrane proteins that do not have the classical AGPAT motifs. Human LPCAT3, LPCAT4, LPEAT1, and LPIAT1 were predicted to have respectively 10, 9, 9, and 6 transmembrane domains using HMMTOP server. Shindou et. al. compared the sequence of MBOAT family LPLATs and identified 4 functional motifs. Mutation on these motifs abolished acyltransferase activity (Shindou et al., 2009). A well conserved histidine among MBOAT family is localized to Motif B and is a putative catalytic residue. However, the functional roles of these motifs have not been investigated.

Acyltransferases have a fundamental role in both *de novo* and remodeling pathway. For a long time, remodeling pathway was considered the key for acyl chain asymmetry, according to which a SFA is located at the sn-1 position and a PUFA or MUFA is at the sn-2 position. Since remodeling pathway modified the acyl chain on the sn-2 positions, it should contribute to the unsaturated chain in PL. However, recent experiments from Harayama et. al showed that some PUPL are derived from the *de novo* pathway, whereas that some SPL and MUPL are derived from the remodeling pathway. The authors performed *in vitro* LPAAT or LPCAT activity assays using microsomes from cells overexpressing different LPAATs or LPCATs as the source of acyltransferases and incubated them with LPA or LPC and acyl-CoA. The ER-enriched microsome fractions from cells expressing LPAAT2 or LPAAT3 had higher selectivity in PC for C18:2 or C22:6, respectively. On the other hand, microsomes from LPCAT1 and LPCAT4 expressing cells preferred C16:0 and C18:1 as acyl donors, respectively. Therefore, SFA (C16:0) and MUFA (C18:1) are integrated in PC by LPCATs through the remodeling pathway and PUFA (C18:2 and C22:6) go through the *de novo* pathway via LPAATs (Harayama et al., 2014). However, how acyl chain diversity is established in other PL classes is still largely unknown.

Table 3 shows a list of acyltransferases and their substrate selectivity. In this thesis, we will focus on those acyltransferases with higher selectivity for PUFA. Acyltransferase is the key to incorporated fatty acids into PL. Understanding the functions of acyltransferases helps clarifying the dual roles between PUFA as signaling molecules or as structural membranes when esterified into PL. For example, the PUFA deficiency in *C.elegans* reduced touch sensation. This was also found in *mboat6* knockout worms, an acyltransferase that incorporates PUFA as PL, indicating the defect was contributed from the lack of PUPL in cellular membrane but not from signaling through free FA (Vásquez et al., 2014). We discuss the impact of PUPL on neuronal function further in Chapter 1.3.2.

Table 3. List of acyltransferases and their substrate selectivity

Acyltransferase	Other symbols	Acyl donor	Acyl receptor	Reference
LPCAT1	AGPAT9	16:0	LPC, LPG	(Harayama et al., 2014; Nakanishi et al., 2006)
LPCAT2	LysoPAFAT; AGPAT11	LPC 16:0, 18:1 PAF: 20:4	LPC, PAF	(Harayama et al., 2014; Shindou et al., 2007)
LPCAT3	MBOAT5	20:4 > 18:2	LPC, LPE, LPS	(Hashidate-Yoshida et al., 2015; Hishikawa et al., 2008)
LPCAT4	MBOAT2	18:1	LPC, LPE	(Harayama et al., 2014; Hishikawa et al., 2008)
LPAAT1	LPAAT α ; AGPAT1	16:0 > 14:0 > 18:2	LPA	(Hollenback et al., 2006)
LPAAT2	LPAAT β ; AGPAT2	18:1 > 14:0 = 16:0 = 18:2	LPA	(Hollenback et al., 2006)
LPAAT3	LPAAT γ ; AGPAT3	22:6 > 20:4 > 18:2	LPA, LPI, LPC	(Harayama et al., 2014; Koeberle et al., 2010; Koeberle et al., 2012)
LPAAT4	LPAAT δ ; AGPAT4	22:6 > 20:4 > 18:2 > 18:1	LPA	(Eto et al., 2014)
LPAAT5	LPAAT ϵ ; AGPAT5	18:1 > 20:4 = 16:0	LPA, LPE, LPC, LPI, LPS	(Prasad et al., 2011)
LPEAT1	MBOAT1	18:1	LPC, LPE	(Hishikawa et al., 2008)
LPEAT2	AGPAT7	18:0 > 18:1 > 16:0 > 20:4	LPE, LPG, LPS	(Cao et al., 2008)
LPIAT1	MBOAT7	20:4	LPI	(Lee et al., 2008)

LPCAT3 is highly expressed in proximal small intestine and liver (Hashidate-Yoshida et al., 2015). In *in vitro* LPCAT activity assay, the enzyme incorporates FA in LPC, LPE, and LPS as acyl chain acceptor. Having higher preference toward LPC, it was named LPCAT. It showed decreased acyl donor selectivity from C20:4, C18:2, to C18:3 but did not utilize C22:6. When using siRNA to knockdown LPCAT3 in cells, the level of total PC, PS, and PE decreased, especially those with C20:4 or C18:2 chain (Hishikawa et al., 2008).

Consistent with the *in vitro* assay, the knockout mice of LPCAT3 decreased greatly the in C20:4 containing PCs and PEs in almost all the tissues (Hashidate-Yoshida et al., 2015). Furthermore, TAG content was increased in both liver and intestine. These observations lead to a model in which the presence of PUPL in membrane facilitated TAG clustering and transfer. The enterocytes from small intestine lost their microvilli in LPCAT3 knockout mice. Thus, the lipids taken from the milk could not be transported as lipoproteins and accumulated as TAG in lipid droplets in the small intestine, resulting in hypoglycemia and neonatal death (Hashidate-Yoshida et al., 2015). These observations lead to a model in which the presence of PUPL in membrane facilitates TAG clustering and transferring. Altogether, these studies show that LPCAT incorporates C20:4 to PL and is important for TAG transport. The presence of C20:4-PL in intestine and liver is especially important due to the fact that these organs metabolize and store FA as TAG in lipoproteins.

LPAAT1 and **LPAAT2** have not been as well studied as other acyltransferases. LPAAT1 and LPAAT2 utilized LPA as acyl acceptor but the acyl donor selectivity is not clear. LPAAT activity assay using microsomes from Sf9 cells demonstrated that LPAAT1 showed gradient of selectivity from C16:0, C14:0, to C18:2 as acyl donor while LPAAT2 showed gradient of selectivity from C18:1, C14:0, C16:0, to C18:2 (Hollenback et al., 2006). On the other hand, using microsomes from CHO cells, Harayama *et al.* identified C18:2 as the preferred substrate of LPAAT1 and LPAAT2 (Harayama et al., 2014). The discrepancy might result from differences between the experimental system. Hollenback used insect cells and mM of substrates while Harayama used hamster cells and μ M of substrates. The acyl chain selectivity of LPAATs might depend on the cell type and the substrate concentration.

LPAAT3 is highly expressed in testis and retina, tissues where levels of PUPL are high. It utilizes C22:6 or C20:4 as acyl donor and LPA, LPC, or LPI as acyl acceptor *in vitro* (Harayama et al., 2014; Yuki et al., 2009). Cells overexpressing LPAAT3 incorporated C22:6 better than other LPAATs (Harayama et al., 2014).

LPAAT3 knockout contained less C22:6-PL but more C20:4-PL in the retina. Retina was known to have more than 50% C22:6 in its outer segments and C22:6 facilitates the

activation of rhodopsin, which is the key factor in visual transduction (see Chapter 1.3.1). Mass spectrometry imaging showed that C22:6-PL disappeared from the outer segment of retina in knockout mice at the advantage of C20:4-PL, resulting in reduction in visual function and abnormal retina layers (Shindou et al., 2017).

Mature sperms contain 20% of C22:6, especially in their tails (Connor et al., 1998; Lenzi et al., 2000). C22:6 in sperms is either supplied by the nurse cell, Sertoli cell, or is synthesized *de novo* by germ cells. Both Sertoli cells and mature spermatids express high level of LPAAT3 (Iizuka-Hishikawa et al., 2017; Koeberle et al., 2010; Koeberle et al., 2012). LPAAT3 knockout mice showed a dramatically reduced level of C22:6-PL in testis. Moreover, Sertoli cells failed to separate and release the mature sperms, thereby remaining wrapped around the head of sperms. LPAAT3 knockout mice had a reduced sperm number and reduced competence for fertilization (Iizuka-Hishikawa et al., 2017). Therefore, lack of C22:6 incorporation into membranes leads to male infertility.

LPAAT4 is highly expressed in brain and utilizes C22:6 and C20:4 as acyl donors *in vitro* (Eto et al., 2014). LPAAT4 knockout mice has impaired muscular and brain functions (Bradley et al., 2018; Bradley et al., 2017). Surprisingly, lipidomics of brain or muscles from LPAAT4 knockout mice did not show any reduction in neither ω 3-, ω 6-, nor C22:6-PL. LPAAT4 knockout brain had reduced level of total PC, PE, and PI, whereas the amount of PA, PS, and PG remained the same as wildtype. The acyl chain species were similar between wildtype and knockout brain except reduction in PL containing C22:4 chain (Bradley et al., 2017; Bradley et al., 2015). A similar trend was observed in muscle cells. LPAAT4 knockout muscle had increased level of PA and PE but the acyl chain species were similar to wildtype except for a decrease in PL containing C22:4 (Bradley et al., 2018; Bradley et al., 2015). However, the discrepancy might result from the redundancy between LPAATs. Indeed, loss of LPAAT4 in brain or muscles led to overexpression of other LPAATs (Bradley et al., 2018; Bradley et al., 2015). In addition, C22:4 was not included in the *in vitro* activity assays, thereby the selectivity of LPAAT4 toward C22:4 has not been compared with other fatty acids.

LPIAT1 utilized C20:4 or C22:5 as acyl donors and LPI as acyl receptor to synthesize PI (Lee et al., 2008). PI can be further phosphorylated to phosphatidylinositol phosphate (PIP). Cellular membrane contains little amounts of PIP, which is mainly involved in membrane-protein interactions and cell signaling. PI is usually coupled with a C20:4 chain. Loss of LPIAT1 in mice led to reduction in C20:4-PI, C20:4-PI-monophosphate (PIP), and C20:4-PI-bisphosphate (PIP₂) in the brain. LPIAT1 deficient mice delayed neuronal migration during

brain development, resulting in disordered cortical layers. Therefore, LPIAT1 deficient mice died within 4 weeks after birth (Lee et al., 2012).

In conclusion, the identification of the acyltransferases that are responsible for the acyl chain diversity in membrane phospholipids has started to reveal the functions of PUPL in cellular membranes. Free FA have short term effects as signaling molecules, such as eicosanoids, and long-term effects when incorporated into membrane as PL. Therefore, studying acyltransferases improves our understanding of the roles of various PUFA when esterified as acyl chain in phospholipids. PUPL incorporation in membranes appears particularly important in retina, testis, and brain, where membrane deformation is dominant. Rhodopsin in the retinal membrane undergoes fast conformational change. Adhesion molecules between Sertoli cells and spermatids require endocytosis in order to be removed. Synapses in brain rely on ultra-fast endocytosis for neuronal transduction. We discuss in detail the necessity of membrane flexibility in these particular cells in Chapter 1.3.

1.3 Functions of PUPL in tissues

Among mammalian cells and tissues, retina and brain have the highest amount of PUFA (Anderson et al., 1990). The rod outer segment membrane contains 40-50 % C22:6, which is incorporated into PC, PE, and PS (Martin et al., 2005; Stone et al., 1979). On the other hand, the gray matter contains 50 % of PUFA in PE and PS, among which half is C22:6 (O'Brien and Sampson, 1965).

The importance of PUFA in these tissues probably relies on its capacity to affect transmembrane proteins including G-protein Coupled Receptors (GPCR), such as rhodopsin, as well as voltage-gated ion channels, and other non-voltage-gated channels. In this chapter, we review the impacts of PUFA on these transmembrane proteins.

1.3.1 PUPL in retina

Rhodopsin is a GPCR located in the discs of the outer segment of rod cells. It is the first player of phototransduction, the pathway by which rod cells convert light into an electric signal (**Figure 1.14**). Rhodopsin is covalently bound to cis-retinal, a light sensitive chromophore. Upon light exposure, retinal is converted to its *trans* configuration and triggers rhodopsin to undergo conformational change from metarhodopsin I (MI) to metarhodopsin II (MII). MII binds and activates the heterotrimeric G protein transducin, by catalyzing the exchange of GDP to GTP. Once activated, the α subunit of transducin binds and activates a cGMP phosphodiesterase (PDE), which converts cGMP into GMP. cGMP is responsible for activating

cGMP-gated cation channels that depolarize membrane potential. As cGMP level decreases, cGMP-gated cation channels closes and the rod cells hyperpolarize (Yau and Hardie, 2009).

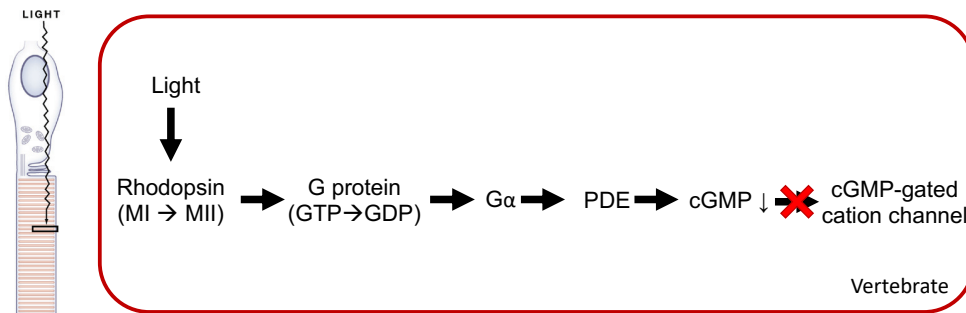


Figure 1.14. Phototransduction pathway in vertebrate. Light triggers conformational change of Rhodopsin which further activates the G protein, transducing. The α subunit of transducing activates cGMP phosphodiesterase (PDE) which converts cGMP to GMP, resulting in the inactivation of cGMP-gated ion channel. Illustration modified from (Yau and Hardie, 2009).

From a physical perspective, the conformational change of rhodopsin has to overcome the lateral pressure coming from the surrounding lipid bilayer (Gawrisch et al., 2008). In all-atom MD simulations of rhodopsin in retinal membrane, esterified C22:6 chains oriented themselves to reach maximum contact with the protein (**Figure 1.15**) (Feller et al., 2003; Pitman et al., 2005). A recent study compared the structure of various forms of rhodopsin in PE (18:0/22:6) membrane. When transiting from MI to a more elongated MII state, acyl chains change their conformation to display a more stretched shape. Moreover, comparing to C18:0, C22:6 chain penetrates deeper into rhodopsin (Salas-Estrada et al., 2018). These simulations show that a C22:6 containing membrane could favor the structural transition of rhodopsin, either by merely fitting to the rhodopsin conformation or by interacting with rhodopsin.

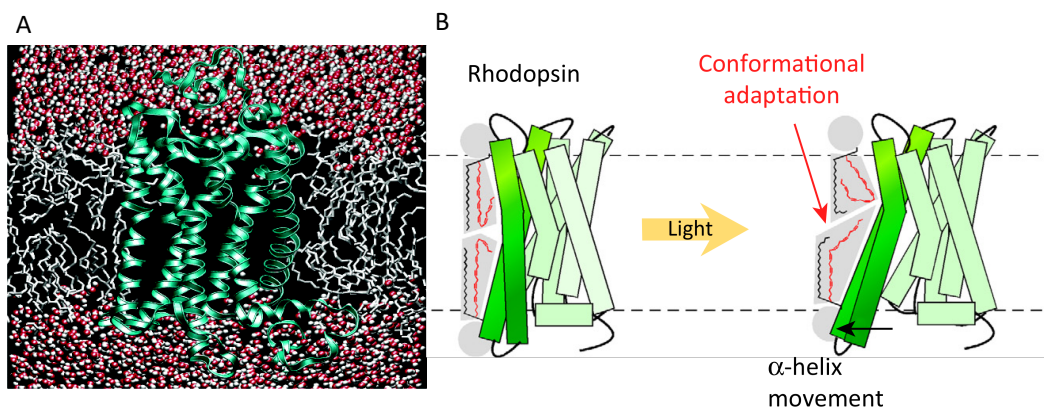


Figure 1.15. Conformational adaptation of rhodopsin in PUPL membrane. (A) All-atom molecular dynamic simulation of rhodopsin (green) in membrane with similar phospholipid (white) composition as retinal membrane. (B) Light stimulation leads to conformational change of rhodopsin, which is better adapted in PUPL membrane. Illustrations extracted from (Antonny et al., 2015; Feller et al., 2003).

The conformational change of rhodopsin from MI to MII is critical for its activation, and so is the coupling between MII and transducin. *In vitro* studies have been performed to reconstitute rhodopsin and transducin in liposomes of defined acyl chain composition. Compared to PC(18:0/18:1) vesicles, PC(18:0/22:6) containing vesicles promoted both MI-MII transition and MII-transducin coupling (Niu et al., 2001). A similar result was obtained from rhodopsin purified from rat reared with C22:6-rich diet (Niu et al., 2004). These biochemistry studies indicate that membranes containing C22:6-PL are beneficial for rhodopsin activation.

Lysophosphatidic acid acyltransferase 3 (LPAAT3) incorporates C22:6 into phospholipids. LPAAT3- knockout mice had shorter outer retina segment and disorganized retinal discs. Defects in the morphology corresponded to reduction in retina electrical activity, especially outer segment hyperpolarization, as measured by electro-retinogram. Here, Shindou et. al. showed that the presence of C22:6-PL in the membrane is critical for visual function (Shindou et al., 2017).

Invertebrate

Phototransduction in *Drosophila* is different from that occurring in mammals in two ways. (**Figure 1.16**) First the G protein activates phospholipase C (PLC) instead of PDE. Second, PLC hydrolyses phosphatidylinositol4,5-bisphosphate(PIP₂) to 1,4,5-trisphosphate and diacylglycerol. The hydrolysis of PIP₂ to diacylglycerol and inositol 1,4,5 trisphosphate reduces the size of the lipid, thereby generates imbalance of the membrane area. Reducing the membrane area in one leaflet creates a contraction force that gates the activation of ion channel (Hardie and Franze, 2012). Eventually, Transient Receptor Potential (TRP) channel is activated, allowing Ca²⁺ influx (Yau and Hardie, 2009).

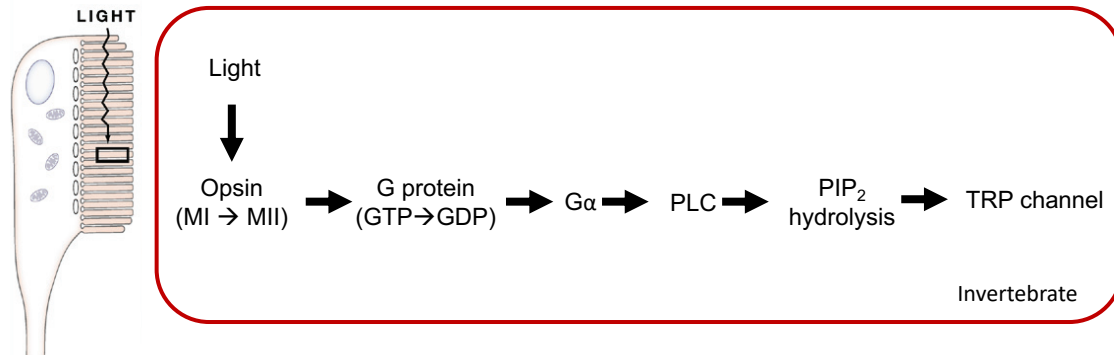


Figure 1.16. Phototransduction pathway in invertebrate. Opsin undergoes conformational transition upon light stimulation, resulting in the activation of downstream G proteins. The α subunit of the G protein activates phospholipase C (PLC) which catalyzes the hydrolysis of PIP_2 . PIP_2 hydrolysis generates a mechanical constriction of the membrane, resulting in the activation of Transient Receptor Potential (TRP) channel. Illustration modified from (Yau and Hardie, 2009).

Although different, phototransduction in fly and in mammal are both affected by PUPL. The lipidomic profile of *Drosophila* is less unsaturated than in mammals, notably because insect cells lack C22:6-containing lipids (Vrablik and Watts, 2013). However, phototransduction in fly is facilitated by the presence of PUPL in membranes. *In vivo* study of fly reared with low PUFA diet showed reduction in the speed of electrical light response at the cellular and animal levels. Supplementing the fly with single PUFA (i.e. C18:3) rescued the defect in phototransduction. The membrane contraction from PIP_2 hydrolysis is believed to mechanically gate the downstream TRP channel. AFM measured a slow and slight increase contractile force in photoreceptor membrane of fly reared with low PUFA diet. Also, when ectopically constructed the mechanical sensitive gramicidin channels on photoreceptor of low PUFA diet-reared fly, the activation of the channel was slower (Randall et al., 2015). Here, the authors showed that changing the diet of fly affects the mechanical property of the photoreceptor membrane, in which the transduction of force are slower and delays the phototransduction in fly.

Along the *Drosophila* phototransduction pathway, rhodopsin and TRP are the two factors that has been shown to be affected by PUFA. Rhodopsin is more active in PUPL membrane as described above. TRP in *Drosophila* photoreceptor can be directly activated by C18:3 after few seconds of free FA addition. Furthermore, it is gated also by mechanical force

generated by the lipid environment, i.e the hydrolysis of PIP₂ and transduction of force along the membrane (Chyb et al., 1999; Hardie and Franze, 2012).

1.3.2 PUPL in brain

The brain is enriched in PUPL. PUFA is involved in neuronal survival, neurogenesis, synaptic function, and cognition (Bazinet and Layé, 2014). In this chapter, we will discuss how PUFA regulates neuronal functions.

PUFA is uptake from the diet and transported to the brain. Mfsd2a is responsible for transporting LPC containing more than 14 carbons, notably C22:6, across the blood-brain barrier. Mfsd2a- knockout mice had a reduced amount of C22:6 in the brain but an increased amount of C20:4. Mfsd2a-KO mice also had a reduced brain size and neuron density at hippocampus, which correlated with impaired learning and memory capacity (Nguyen et al., 2014). Therefore, supplying brain with sufficient quantity of PUFA is essential for its proper functions. Another pathway for synthesizing C22:6-PL in brain is through the *de novo* pathway where lysophosphatidic acid acyltransferases (LPAATs) incorporate C22:6-CoA to LPA. LPAAT4 is highly expressed in brain and has preference toward C22:6-CoA (Eto et al., 2014). However, the role of this enzyme in brain is still under investigation.

Membrane creates barrier between cell and the outer matrix. Ion channels are multi-transmembrane proteins that allow ions to commute between membranes. There are several factors that could gate ion channels, such as voltage, ligands, or mechanical force. C22:6-PL is known to enrich at the synapse but in its free FA form is capable of affecting ion channel activity. Numerous voltage-gated ion channels could be modulated by PUFA in either positive or negative way, mostly through direct binding between PUFA and the channels. The binding of PUFA to these channels are rapid (seconds) and can be inhibited by mutating specific residues of the channels. Other type of ion channels, mostly mechanosensitive, rely on the membrane environment created by PUPL for activation. In this case, PL is viewed as a matrix that transduces the mechanical energy to the ion channels.

The direct interaction between PUFA and voltage-gated ion channels has been reviewed thoroughly in (Elinder and Liin, 2017). PUFA affects the activity of various voltage-gated ion channels including K⁺, Na⁺, Ca²⁺ and H⁺ channels. Depending on the channel families, the effects could be negative or positive. Here, we will discuss briefly a few examples of direct interaction between PUFA and K⁺ channel and focus later on those that are indirectly affected by the PUFA.

Voltage-gated K_v1 channels open and close rapidly, causing fast repolarization of the action potential in cardiac cells. Application of PUFA extracellularly blocked the activation of the channel in seconds. Moreover, only the PUFA but not its metabolites have the inhibitory function on $K_v1.5$, indicating an effect from direct binding (Honoré et al., 1994).

Voltage-gated K_v4 channels are another channel affected by PUFA. K_v4 channels contribute to most of the transient and voltage-dependent K^+ current in neuron and cardiac muscle. K_v4 channels can be heterologously expressed in *Xenopus* oocyte, which is a convenient model to record channel activity by patch clamp electrophysiology. PUFA with more than 2 double bonds, especially C20:4 and C22:6, inhibited K_v4 channels after few seconds of addition. PUFA reduced the peak outward current and increased the inactivation time course. Mutagenesis study showed that C20:4, but not its eicosanoid metabolites, binds reversely to K_v4 at an intracellular loop between the 4th and 5th transmembrane domain (Boland et al., 2009; Villarroel and Schwarz, 1996).

N-methyl-D-aspartate (NMDA) channels are glutamate-gated ion channels. Reconstitution of NMDA channel in liposomes showed that applying pressure on the liposome was sufficient to modify channel currents, indicating that membrane bilayer itself is enough to transmit mechanical energy without interacting with cytoskeleton. Interestingly, free C20:4 FA was capable of potentiating NMDA channel in this *in vitro* system, suggesting a direct impact from C20:4 (Kloda et al., 2007). Following studies investigated the capacity of different acyl chains in mechanical transduction.

Bacterial mechanosensitive small conductance (MscS) and large conductance (MscL) ion channels protect bacteria against hypo-osmotic shock. These two channels open in response to membrane pressure generated from osmotic stress. *In vitro* reconstitution of MscS or/and MscL in liposomes showed that these channels were sensitive to the thickness of bilayer (Nomura et al., 2012). Moreover, compared to MUPL liposomes, PUPL liposomes reduced the pressure dependence of MscS closure and MscL opening and closure. When reconstituted on PC/PE(18:3/18:3) liposomes, MscS fired less frequent, but once opened, it stabilized for a longer period of time. On the other hand, MscL opened and closed at a lower pressure (Ridone et al., 2018). This is the first *in vitro* evidence showing that MUPL and PUPL have different capacity in transducing/buffering membrane pressure.

In *Caenorhabditis elegans*, touch sensation is mediated by mechano-electrical transduction (MeT) channels, which are part of the degenerin/epithelial sodium channel family. *C. elegans* has well characterized pathways for *de novo* synthesis of PUPL and uptakes

exogenous PUFA from food. Genetically removing desaturase or elongase enables researchers to dissect the role of different PUFA in *C. elegans*. Genetically blocking PUFA synthesis in *C. elegans* reduced the touch response, which can be rescued by supplementing the worm with C20:4 but not other PUFA. In *C. elegans*, C20:4 is incorporated to PL by acyltransferase *mboa*. Knockdown of the acyltransferase *mboa* showed that incorporation of PUFA to PUPL was also important for touch response. The presence of PUPL on touch receptor neuron makes membrane more flexible as measured by AFM and generated a better environment for touch response (Vásquez et al., 2014).

Transient receptor potential vanilloid 4 (TRPV4) is another channel whose activation is facilitated due to the mechanical property of PUPL-enriched membrane. Rat TRPV4 were trans-genetically expressed in *C.elegans*. By genetically knockout the desaturase or elongase gene and dietary FA supplementation, Caires et al. demonstrated that the PUFA C20:5 and its eicosanoid derivatives (but not C22:6) modulated TRPV4 activity. The incorporation of FA in membrane PL was essential for TRPV4 since knockdown of the acyltransferase *mboa* inhibited TRPV4 activation. This positive effect might be due to an increase in membrane fluidity and decrease in bending rigidity as measured by AFM (Caires et al., 2017).

Altogether, these examples show that membrane alone is sufficient to transmit mechanic energy to mechanosensitive channels (Kloda et al., 2007; Ridone et al., 2018). PUPL membrane make a better matrix for mechanic force transduction and thus promotes mechanosensitive channels activation (Caires et al., 2017; Ridone et al., 2018; Vásquez et al., 2014). Together with structural studies, the flexibility of PUPL facilitates the transduction of mechanical force, which shifts the sensitivity of mechanosensitive ion channels (Koenig et al., 1997; Ridone et al., 2018).

1.4 Functions of PUPL at the subcellular level

1.4.1 PUPL in endocytosis and synapse

Another neuronal function affected by PUPL is synaptic transduction. There is a gradient of PUPL from neuron cell body to axon, where PUPL is enriched all along the axon until the synapse (Yang et al., 2012). Synaptic vesicles are small vesicles (40 nm in diameter), clustering at the presynaptic axon region. These vesicles contain neurotransmitters, which are released in the synaptic cleft upon stimulation. Synaptic vesicles are highly packed with proteins and enriched in PUPL, especially in PE and PS (Takamori et al., 2006). PUPL is

essential for synaptic vesicles formation. Deficiency in PUPL synthesis reduced the formation of synaptic vesicles at the neuromuscular junctions of *C. elegans*, resulting in reduced motility. This defect could be rescued by dietary supplementation of PUFA or by restoring PUFA synthesis in neurons (Lesa et al., 2003). Similar effects were also found in mouse neuron, in which supplementation of PUFA restored the synaptic vesicle lost due to serum starvation (Tixier-Vidal et al., 1986).

The release of neurotransmitter and recycling of synaptic vesicles require fast membrane deformation. The recycling of synaptic vesicles is a complicated process and several pathways are involved, including the clathrin-mediated endocytosis, kiss-and-run, ultrafast endocytosis and activity-dependent bulk endocytosis (Chanaday et al., 2019) (**Figure 1.17**). To our interest, the ultrafast endocytosis is a clathrin-independent pathway which occurs within 50 ms after stimulation. After membrane invagination, dynamin-endophilin complex promotes scission of endosome from the plasma membrane. The internalized endosome will later be reformed to synaptic vesicles by clathrin and AP2 (Watanabe et al., 2013a; Watanabe et al., 2013b; Watanabe et al., 2014).

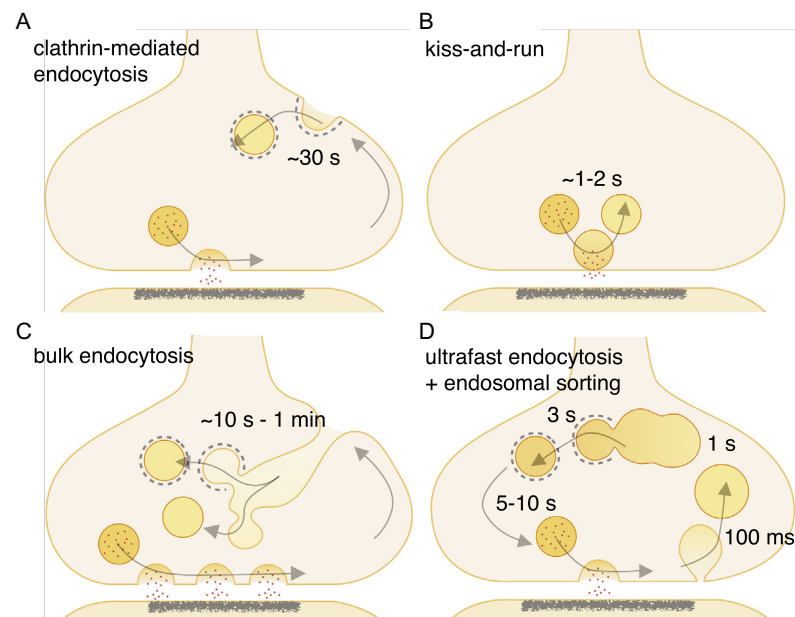


Figure 1.17. Endocytosis of synaptic vesicle. (A) The classical clathrin-mediated endocytosis is activated during low stimulation but is relatively slow (10-30s). (B) The kiss-and-run model (1-2 s) is when synaptic vesicles fuse with membrane temporally to release neurotransmitter and recycle back to the cell. (C) Activity-dependent bulk endocytosis (1-2 s) requires dynamin and actin to release the endosome and clathrin to reshape it to synaptic vesicles. (D) Ultrafast endocytosis (50 ms) is independent from clathrin but required dynamin

to release the endosome and clathrin to reform synaptic vesicles from endosome. Illustrations extracted from (Watanabe and Boucrot, 2017).

Dynamin-endophilin complex polymerizes to form a double spiral at the neck of endocytic vesicle and contract to trigger membrane fission. Pinot *et. al.*, have showed that when reconstituted *in vitro*, dynamin-endophilin had higher activity in fission on PUPL than MUPL liposomes (Pinot et al., 2014). Dynamin activity increases with the level of unsaturation in PL. MD simulations imposing a pulling force on membrane with different level of unsaturation showed that the more unsaturated the membrane was, the more deformable it was (Manni et al., 2018). Increase in membrane deformation upon PUPL enrichment could also be observed in cells. Cells that grew in PUFA-enriched medium showed a 4-fold reduced plasma membrane bending rigidity as measured by optical tweezers. In line with *in vitro* observation, cells enriched in PUPL had a 8-fold higher level of dynamin-dependent endocytosis (Pinot et al., 2014). Note, however, that a direct clue for the effect of polyunsaturated phospholipids on the speed of endocytosis for synaptic vesicle recycling *in vivo* is missing.

To sum, PUPL is enriched in neuron, notably to 70% of lipids at the synapse, and are probably essential for synaptic vesicle formation (Takamori et al., 2006). Factors involved in the synaptic vesicle endocytosis, including dynamin and endophilin, are more activated on PUPL membrane. The effect is probably due to the high deformability of PUPL.

Chapter 2 Membrane curvature: from lipids to proteins

Membrane deformation and membrane curvature are coupled. Cellular membranes are often curved at various degree and are constantly deformed into different shapes, *i.e.* filopodia, lamellipodia, phagocytosis, and endocytosis. Plasma membrane is flat, considering the size of mammalian cell ranges from 10-100 μm . However, endocytic vesicles, which are derived from the plasma membrane, are as small as 40-80 nm with very high curvature. How does such a dramatic change in topology occur?

2.1 Membrane curvature formation

Positive and negative curvatures are coupled together. As membrane curvature forms, the polar heads of PL in the convex side are more separated and gaps form in between (**Figure 2.1A, arrow**). We term this gaps as lipid packing defects which could be a binding site for membrane anchoring proteins. Geometrically, PL with large polar head groups (e.g. PI) fit better the positive curvature (convex side)(**Figure 2.1B**), reducing both the area of packing defects and exposure of hydrophobic acyl chains. On the negative curvature (concave side), the PL are more packed and compressed, in which PL with small head groups or single acyl chain (lysophospholipids) are favored.

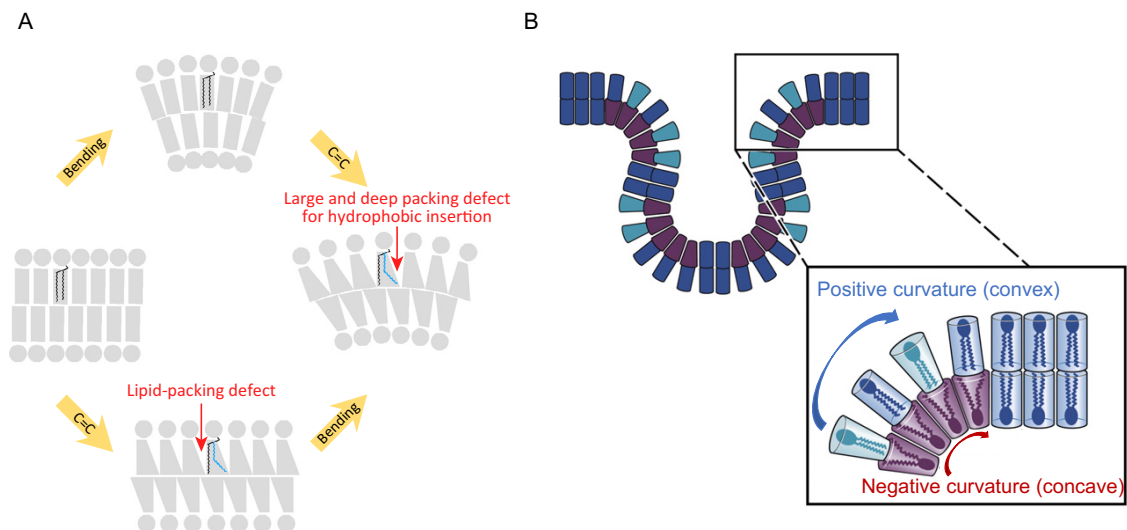


Figure 2.1. Membrane curvature and lipid packing defects. (A) Lipid packing defects on curved membrane. (B) Positive curvature locates in the convex side, where the head groups of PL separates to form gaps, the lipid packing defects. Negative curvature locates at the concave side, where head groups of PL are compressed. Illustration extracted from (Antonny et al., 2015; Peetla et al., 2013).

Membrane curvature forms due to intrinsic stress from the lipid bilayer or by external force applied. Intrinsic force comes from the packing of lipids which prevents the exposure of the hydrophobic tails to the aqueous environment. Another intrinsic source for membrane curvature is the insertion of membrane proteins that changes the area balance between the two bilayers. Furthermore, external conformation imposed by proteins could further shape the membrane. For example, clathrin polymerized into a curved structure that is essential for endocytic vesicle formation.

During bacterial invasion processes, several structures are generated in the plasma membranes. These structures involve large-scale membrane deformations and curvature formations. In this chapter, we are going to discuss about the basic driving force for membrane curvature formation and its functional consequences.

2.1.1 Lipid driven curvature formation

As mentioned in the Chapter 1.1, lipid composition of cellular membrane is diverse. Combination of different head groups and different acyl chains creates a diversity of PL with various shapes. Depending on the cross-section area of the head groups and acyl chains, lipids are categorized into cylinder, cone, and inverted cone shape (**Figure 2.2A**)(Cullis and De Kruijff, 1979). Cylindrical lipids, such as PC and PS, have similar cross section area between the head group and acyl chains, thereby intrinsically form flat bilayer. On the other hand, conical lipids, such as PE or PA, contain smaller head groups and favor negative curvature at zero bending stress (Frolov et al., 2011). In fact, PE (18:1/18:1) does not form stable lamella structure but rather a hexagonal phase at physiological conditions (**Figure 2.2B**). This hexagonal structure imposes a negative curvature at the polar heads of PL (Cullis and De Kruijff, 1979). Inverse conical lipids have a bulky head group such as PI, or have single hydrophobic tail such as LPL (**Figure 2.2C**). Owing the larger cross-section area ratio, inverted conical lipids favor positive curvature at zero bending stress (Cullis and De Kruijff, 1979; Frolov et al., 2011).

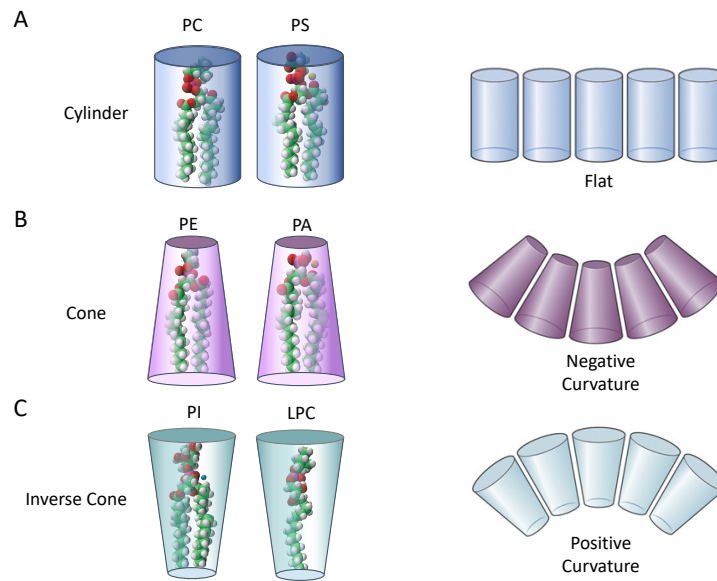


Figure 2.2. *Intrinsic shape of phospholipids. PL are categorized into (A) cylinder, (B) cone, (C) inverted cone shape according to the area ratio of their head groups and acyl chains. Illustrations modified from (Peetla et al., 2013).*

Combination of different PL creates membranes that fit different conformations and curvatures at low energy cost. Therefore, the size range of cellular organelles are wide, from as large as plasma membrane (10-100 μm), nuclear membrane (5 μm), mitochondria (0.5-10 μm), ER tubules (30-100 nm in diameter) until synaptic vesicles (30-40 nm).

2.1.2 Proteins and membrane curvature

Proteins can further shape the membrane. During cellular processes, proteins shape the membrane into specific curvature which downstream molecules sense and react with these membranes of distinct shapes. There are several mechanisms how proteins can interfere with membrane. Insertion of protein domain/motifs will change the area balance between the two leaflets, increasing the area at the side of insertion. Therefore, membrane curves away from the side of insertion. Another example is the crescent-shaped Bin/Amphiphysin/Rvs (BAR) domain proteins that bind membrane through their concave surface, imposing a positive curvature on the membrane. Coat proteins assemble into a spheroid structure and enclose membrane as vesicles. In addition, the B subunit of Shiga toxin binds to glycolipids, Gb3, of the host membrane, leading to local compressing of lipids area and generation of negative curvature (Römer et al., 2007; Watkins et al., 2019).

In this chapter, we discuss some of the principal mechanism of membrane curvature formation induced by proteins.

Membrane protein insertion: transmembrane protein and amphipathic helix

Amphipathic helix contains hydrophobic and polar residues that decorate at the opposite side of the α -helix, creating a hydrophobic surface and a hydrophilic surface (**Figure 2.3**). The amphipathic nature of the helix enables it to insert deeply in the membrane. The polar residues of the helix form electrostatic interaction with the polar head groups of the PL, while the hydrophobic residues face the fatty acyl chains (Drin and Antonny, 2010).

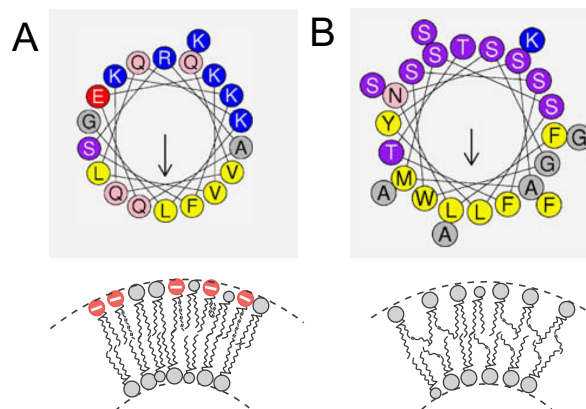


Figure 2.3. Structure of amphipathic helix and ALPS motif. (A) The structure of the amphipathic helix from BRAP/Bin2. The amphipathic helix contains hydrophobic residues (yellow) on one side and charged residues (red and blue) on the other side, making it sensitive to the charge of membrane. (B) The ALPS motif of ArfGAP1. The ALPS motif contains hydrophobic residue (yellow) on one side and uncharged polar residues (purple and pink) on the other, making it sensitive to membrane packing defects. Color code for helical residues: yellow, hydrophobic; purple, serine and threonine; blue, cationic; red, anionic. Illustrations extracted from (Antonny, 2011; Drin and Antonny, 2010).

Depending on the composition of the residues, amphipathic helix has different preference for the membrane composition and curvature. The amphipathic helix of BRAP/Bin2 contains positively-charged residues on the polar side, making it prefers binding with negatively-charged membrane regardless of the membrane curvature (**Figure 2.3A**)(Fernandes et al., 2008). On the other hand, the amphipathic helix of Arf-GAP1 contains mostly uncharged polar residues on the hydrophilic surface (**Figure 2.3B**). We termed this type of peptide Amphipathic Lipid Packing Sensor (ALPS). Since ALPS does not contain charged residue to

form electrostatic interactions with lipids, it relies solely on the hydrophobic interaction for membrane binding. Therefore, ALPS prefers deeper lipid packing defect where the hydrophobic surface can be embedded. High positive membrane curvature exposes the hydrophobic acyl chains, creating higher packing defects. Indeed, Arf-GAP1 preferably binds to liposomes as small as 36 nm as compare to bigger ones (Drin et al., 2007).

Insertion of multiple amphipathic helices in one leaflet of the membrane increase the area of the monolayer. Therefore, the membrane bends away from the insertion site. For example, when incubating with liposomes, epsin deformed liposomes into tubules of 19 nm diameter. Mutating the hydrophobic residues on the amphipathic helix of Epsin reduced or abolished the membrane tubulation (Ford et al., 2002).

Bin/Amphiphysin/Rvs (BAR) domain proteins

BAR domain has intrinsic crescent shape that fits and imposes membrane curvature. BAR family protein is composed of 3 helices that forms homo- or hetero-dimers (Qualmann et al., 2011). Depending on the angles of dimerization, the BAR proteins cover a range of curvature. The classical BAR domain dimers at a bigger angle (30°) embracing a curvature of 15-17 nm diameter (Qualmann et al., 2011). On the other hand, the F-BAR subfamily dimers at a lower angle (10°) embracing a curvature of 110-130 nm diameter (**Figure 2.4A**)(Henne et al., 2007). There are positively-charged residues on the concave side of the banana-shaped dimers, interacting electrostatically with negatively-charged PL, such as PS and PI (**Figure 2.4B**)(Peter et al., 2004). BAR dimers align tip-to-tip as oligomers that further form lattices structure on the membrane surface (**Figure 2.4C**)(Frost et al., 2008). These lattice structures further impose positive curvature on the membrane. When incubating with liposomes, BAR protein deforms membrane into tube at nanometer scale (Ford et al., 2002; Peter et al., 2004).

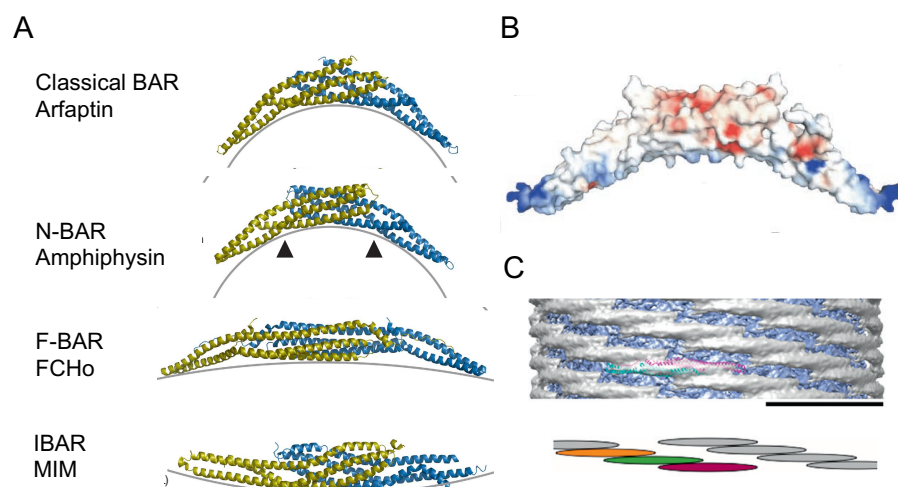


Figure 2.4. Structures of BAR domain proteins. (A) Different subfamilies of the BAR proteins in their dimerization states. There are 3 helices from each monomer (blue and green) that form crescent-shaped structures. N-BAR proteins contain amphipathic helix at the N-terminal (black arrow head) (B) Electrostatic map of the BAR domain, Amphiphysin. Positive residues (blue) at the concave face interacts with the negatively-charged residues. (red = -10 kTe^{-1} , blue = $+10 \text{ kTe}^{-1}$) (C) BAR protein aligns tip-to-tip as lattices. Illustrations extracted from (Frost et al., 2008; Peter et al., 2004; Qualmann et al., 2011)

The inverse-BAR (I-BAR) domain contains positively-charged residues on its convex side rather than on concave side. Furthermore, instead of having a banana shape, I-BAR proteins have a zeppelin-shaped structure (**Figure 2.4A**). As a result, I-BAR imposes negative curvature to membranes. I-BAR proteins trigger negative membrane curvature both *in vitro*, when incubate with GUVs, and *in vivo*, when overexpress in cells (Saarikangas et al., 2009). There are 5 proteins identified in I-BAR subfamily: IRSp53, MIM, ABBA, IRTKS, and FLJ22582. I-BAR proteins contain additional domains that modulate actin recruitment or binding (Zhao et al., 2011). Notably, all I-BAR proteins contain a WH2 domain that bind to globular actin (Lin et al., 2005; Zhao et al., 2011). In addition, IRSp53, IRTKS, and FLJ22582 contain a SH3 domain that interacts with numerous actin regulators and builds a scaffold network, including N-WASP, WAVE, mDia1, and actin (Lim et al., 2008). Through this scaffold, I-BAR proteins promote actin polymerization and regulates actins at filopodia and lamellipodia *in vivo* (Zhao et al., 2011).

Some BAR proteins have additional membrane binding motif or domain that enables membrane binding regardless of the curvature. The N-BAR subfamily contains an amphipathic helix at its N-terminal. Surprisingly, the N-BAR protein, Amphiphysin, binds to liposomes regardless of the size. Removal of the amphipathic helices unmasks the curvature sensing capacity of the BAR domain of Amphiphysin, in which it prefers binding to small liposomes (Peter et al., 2004). Likewise, F-BAR protein, Fcho2, binds to liposomes without size preference. Reducing the membrane binding by mutating the first BAR helix gained the protein membrane sensing capacity, in which it preferred larger liposomes (Henne et al., 2007).

The BAR domain proteins not only sense but also generate membrane curvature. As discussed, the angle of dimerization determines the intrinsic curvature of BAR proteins, i.e. higher curvature for classical BAR (Amphiphysin) and low curvature for F-BAR (Fcho2). In the case of strong membrane binding, i.e. due to the amphipathic helices, BAR proteins bind membrane regardless of the curvature and impose curvature on membrane according to BAR's

intrinsic structure. In case of weak membrane binding, i.e. mutation or removal of amphipathic helices, BAR proteins sense the membrane curvature according to its intrinsic curvature.

There are numerous membranous organelles and structures with various degree of membrane curvature within cells (Harayama and Riezman, 2018). The curvature specific for each organelle results from the intrinsic shapes of PL they contain and the external stress applied from the membrane proteins. The composition, shape, and curvature of a membrane is a hallmark for protein bindings. Different level of membrane curvature attracts different effector proteins and result in different biological events. For example, the cis golgin GMAP-210 captures small and monounsaturated vesicles via its ALPS motif (Magdeleine et al., 2016). This allows selectivity targeting of transport vesicles to specific organelles filtering through their size and lipid composition.

2.2 Behavior of PUPL on curved membrane

Even though plasma membrane itself is relatively flat, there are several nano-scale structures derived from the plasma membrane, including protrusions, invaginations and vesicles. Of no doubt proteins play a major role in shaping these nanoscale structure. However, what has been ignored for a long time is that the lipid composition of the plasma membrane might also facilitate these deformation processes. In this chapter, we focus on the asymmetric lipid composition of the plasma membrane and its facilitative effects on membrane deformation and curvature formation.

2.2.1 Composition of the plasma membrane

Plasma membrane are asymmetric in the composition of the inner and outer membrane leaflet. The studies in plasma membrane asymmetry were firstly done in erythrocyte, in which plasma membrane is the only membranous structure. Treating the cells with phospholipase A2 (PLA2) and sphingomyelinase digests the outer leaflet of the membranes, allowing researchers to understand the detailed lipid composition between the two leaflets. The inner leaflet of the plasma membrane is enriched in PE and PS while the outer leaflet is enriched with sphingomyelin and PC (Verkleij et al., 1973).

A recent lipidomic analysis of erythrocyte treated with PLA2 or sphingomyelinase revealed more detail on the acyl chains composition of PL in the two plasma membrane leaflets (Lorent et al., 2020). The outer leaflet is composed of mostly of 40% PC and 50% SM (**Figure 2.5A**). Among the PL in the outer leaflets, only 40% are polyunsaturated i.e. containing at least 2 or more double bonds (**Figure 2.5B**). Given the fact that SM is highly saturated, the majority

of the PUPL in the outer leaflet are PC. The inner leaflet has a complete different lipid landscape, containing 23% PC, 41% PE, and 28% PS (**Figure 2.5A**). In the inner leaflets, more than 75% of the PL are polyunsaturated, in which the majority of the PUPL are PE and PS (**Figure 2.5B**) (Lorent et al., 2020). Plasma membrane is asymmetric in terms of lipid unsaturation, i.e. the inner leaflet is more unsaturated than the outer.

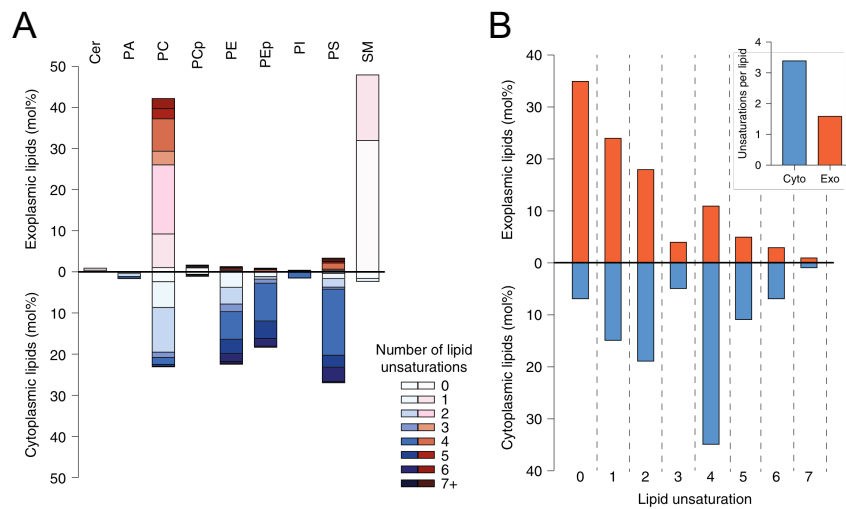


Figure 2.5. Lipid composition of the inner or outer leaflet of the erythrocyte plasma membrane. (A) Lipid classes and double bonds distribution of the outer (upper panel) and inner leaflet (lower panel). (B) Number of double bonds present in the lipids of the outer (upper panel) and inner leaflet (lower panel). Illustration extracted from (Lorent et al., 2020).

2.2.2 PUPL membrane deformation in asymmetric conditions

Maintaining lipid asymmetry is energy costly. Why does mother nature keep such asymmetry? What could compensate the energy cost to maintain lipid asymmetry? An explanation we proposed is that PUPL, when present in the inner leaflet, facilitate membrane deformation as well as they are on both leaflets.

We discussed in the previous chapter that PUPL promote membrane tubulation. MD simulations pulling tubes from PUPL membrane require less energy than from MUPL membrane (Manni et al., 2018; Pinot et al., 2014). Our team revised this concept with an asymmetric membrane in which PUPL was in one of the leaflets and MUPL was in the other (Tiberti et al., 2020). Tiberti *et. al.*, pulled the membrane with the same force to generate a tube from either side (**Figure 2.6A**). When PUPL is in the convex side (positive curvature), the tube is longer than on the concave side (negative curvature) after the same period of pulling (**Figure 2.6B**, red and blue). In fact, the tube is as long as when PUPL is present in both leaflets (**Figure**

2.6B, red and black). On the contrary, when PUPL is in the concave side, the speed of invagination is as slow as a symmetric MUPL membrane, leading in both cases to a shorter tube (**Figure 2.6B**, blue and gray). Having PUPL on the convex side, i.e. the side with positive curvature, has the same effect on tubulation as when PUPL is on both leaflets (Tiberti et al., 2020).

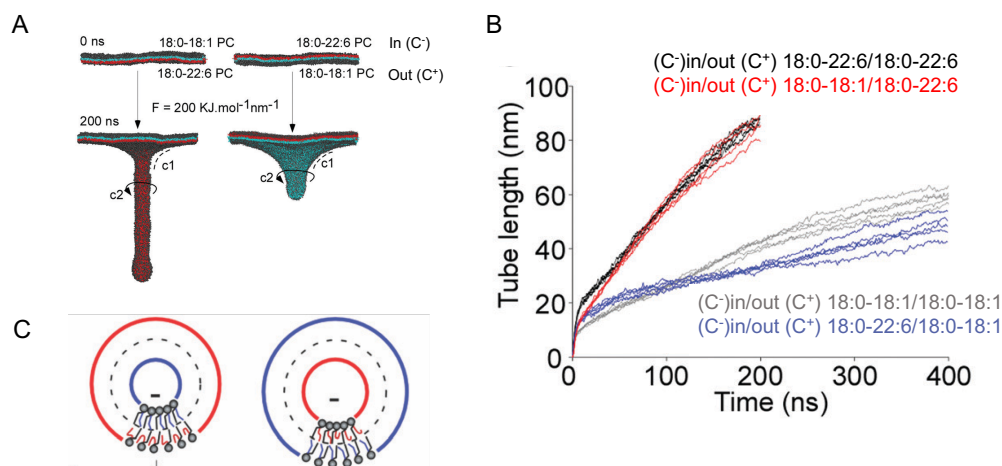


Figure 2.6. Molecular dynamics simulations of tube pulling from asymmetric membrane. (A) Screenshot of asymmetric membrane during pulling simulations. Color code: red, PC(18:0/22:6); blue, PC(18:0/18:1). (B) The elongation of the tube length during pulling simulations. The composition of the leaflet inside (in; concave side; C^- , negative curvature) or outside (out; convex side; C^+ , positive curvature) the tube was as indicated. Color code: black, symmetric PUPL; gray, symmetric MUPL; red asymmetric PUPL inner; blue, asymmetric PUPL outer. (C) Schematic view of the inner and outer leaflets of the tube in relation with the shape of lipids. Illustrations extracted from (Tiberti et al., 2020).

During vesiculation, inner leaflet of the plasma membrane encounters positive curvatures while the outer leaflet faces negative curvature. In addition, PUPL has beneficial effects on membrane tubulation when present on the side of positive curvature. As discussed above, conical lipids fit the geometry of negative curvatures and inverted conical lipids fit positive curvatures. Therefore, it will be beneficial to have inverted conical lipids in the inner leaflet and conical lipids in the outer leaflet of the plasma membrane during endocytosis (**Figure 2.6C**). In this case, what is the shape of PUPL? Why is PUPL beneficial to positive curvature formation?

Tiberti, *et. al.*, measured the area per lipids in the inner (concave side; negative curvature) and outer leaflets (convex side; positive curvature) of the asymmetric membrane

during tubulation. The area of the concave side is the same regardless of the unsaturation, demonstrating that MUPL and PUPL have the same level of compression at negative curvature. On the convex side (positive PC curvature), the area of lipids is larger at PUPL membrane than MUPL membrane, indicating that the lipids are more dispersed. This was consistent with our MD simulations showing that a positively-curved PUPL membrane contains more shallow packing defects as compare to MUML membrane (Pinot et al., 2014).

They projected all the lipids on the membrane tube together to have a geometric shape (**Figure 2.7A**). The shape of lipids in the concave side is similar between MUPL and PUPL. However, unsaturated acyl chains of PUPL in the convex side is able to invade the water-lipid interface, occupying the vicinity forms between polar heads due to the positive curvature. The flexibility of the acyl chain is owing to the low energy cost of rotation that allows it to move along the z direction (**Figure 2.7B-C**). Therefore, PUPL does not have a specific shape but rather adapts its shape to the environment owing to the flexibility of the acyl chains. (Tiberti et al., 2020)

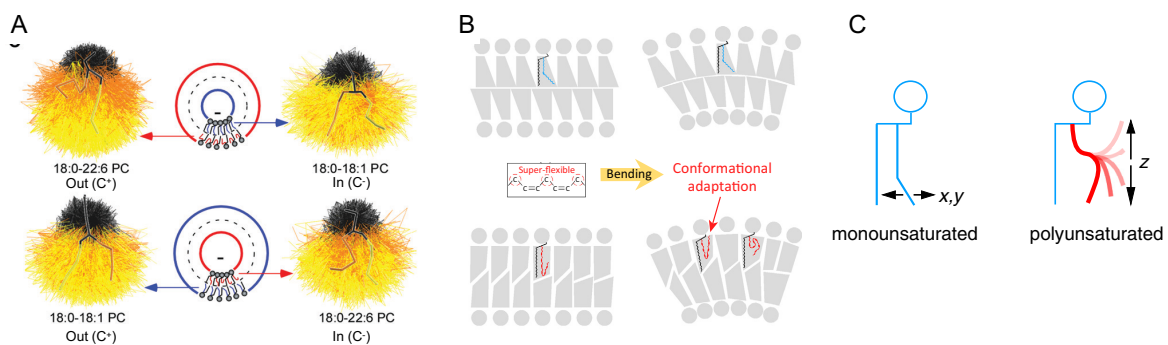


Figure 2.7. Shape of phospholipid in positive and negative membrane curvature. (A) The shape of lipids in leaflet inside (in; concave side; C⁻, negative curvature) or outside (out; convex side; C⁺, positive curvature) the tube. Color code: black, head groups; yellow, sn-1 18:0; orange, sn-2 18:1 or 22:6. (B-D) The unsaturated acyl chain can move along the z-axis, thereby fitting the conformation of the membrane. Illustrations extracted from (Antonny et al., 2015; Barelli and Antonny, 2016; Tiberti et al., 2020)

Having an asymmetric plasma membrane is not just a strategy to have rigid external membrane that serves as a barrier and a fluid internal membrane for signaling and trafficking. Presence of PUPL in the inner leaflet is sufficient to reduce the energy cost for membrane tubulation. There are various membrane deformations occurring at the plasma membrane, such as endocytosis and exocytosis, that could be facilitated by PL unsaturation (Tanguy et al., 2020).

Considering the density of synaptic vesicles is as many as 200 vesicles per μm^2 in nerve terminals and they undergo an ultra-fast endocytosis within 50 ms upon stimulation, there is no doubt that PUPL is indispensable in synaptic junctions (Pinot et al., 2014; Watanabe et al., 2013b; Zhang et al., 1998)

In this chapter, we discussed about the curvature formed on the plasma membrane and how PUPL could affect them. Apart from the intrinsic curvature that forms due to the nature of lipids and proteins, external stimuli could also invoke membrane curvature. Next chapter, we will discuss how bacteria interferes with the host cells to form various routes for invasion.

Chapter 3 Bacterial toxins induced large-scale membrane deformation

In this thesis, we focus on two bacterial invasion processes that involve either the formation of transendothelial cell macroaperture (TEM) tunnels for translocation of *Staphylococcus aureus* in tissues or the formation of large macropinocytic-like vacuoles containing extra-intestinal strains of pathogenic *Escherichia coli* (ExPEC) for invasion of endothelial or epithelial cells. These two modes of bacterial invasion are regulated by bacterial toxins that modulate the activity of a subset of Rho family small GTPases. In this chapter, we discuss about the family of small Rho GTPases and how bacterial toxins affect their functions.

3.1 Rho family small GTPase

Rho GTPases are regulators of the cytoskeleton (Heasman and Ridley, 2008; Hodge and Ridley, 2016). Their activity was mostly found to affect actin assembly. They promote the polymerization and bundling of actin filaments in various cellular processes, including cell adhesion, migration, polarity, and phagocytosis. Their activity is tightly regulated. Major Rho GTPases can bind and hydrolyze the guanosine triphosphate (GTP). Therefore, they switch between an active GTP-bound conformation and an inactive GDP-bound conformation. Rho GTPases contain a P-loop that interacts with β and γ phosphate of the guanine nucleotide, and switch I and switch II motifs that undergo conformational change upon GDP/GTP nucleotide exchange (**Figure 3.1A**). In RhoA, Thr 37 and Gly 63 in the switch I and switch II motifs respectively form hydrogen bonds with the γ -phosphate from GTP (**Figure 3.1B**). Therefore, switching between GTP and GDP binding induces conformational changes of the switch regions of the GTPases, which represents the trigger for effector bindings (Gasper and Wittinghofer, 2019; Hakoshima et al., 2003).

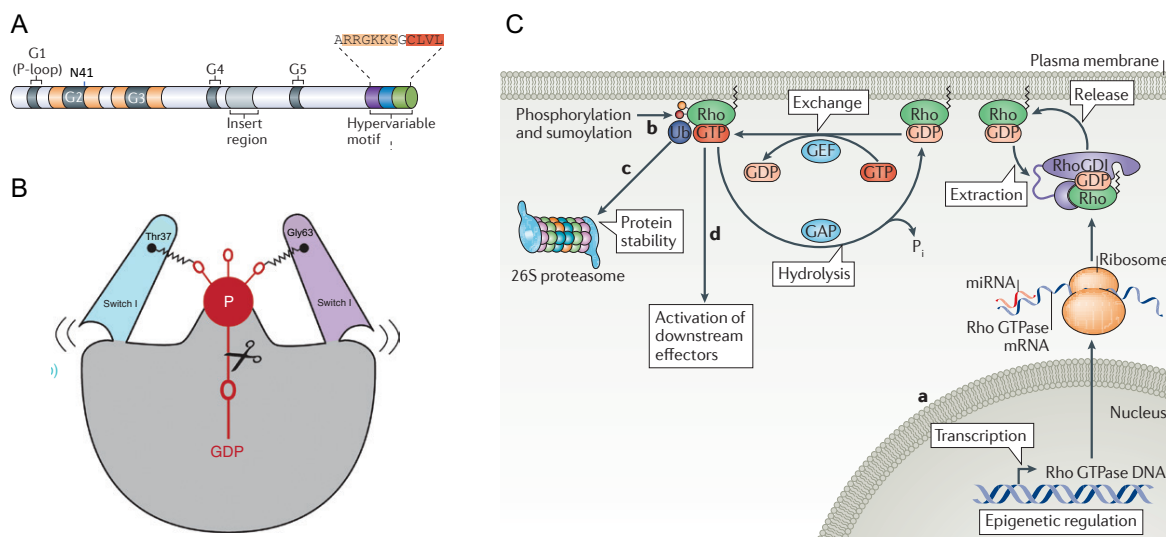


Figure 3.1. *Structure and spatial-temporal regulation of Rho GTPases. (A) Domain architecture of Rho GTPase. G1 is the P-loop motif that interacts with guanine. G2 and G3 are the switch motifs that undergo conformational change upon GDP-nucleotide exchange by GTP. The asn41, located in the switch I motif can be mono-ADP-ribosylated by bacterial toxins. (B) Representation of the switch mechanisms. switch I and II form hydrogen bonds with the γ phosphate of GTP. Upon GTP hydrolysis, the interactions are lost and switch I and II change their conformations (Gasper and Wittinghofer, 2019). (C) The regulation of Rho. The Guanine Exchange Factors (GEFs) promote GTPase activation while the GTPase Activating Proteins (GAPs) facilitate their inactivation. The guanine dissociation inhibitors (GDIs) sequester Rho GTPases into the cytosol preventing them from binding to effectors. In addition, Rho GTPase stability is regulated by ubiquitin-mediated proteasomal degradation (Hodge and Ridley, 2016). Illustrations adapted from (Gasper and Wittinghofer, 2019; Hodge and Ridley, 2016).*

The activity of small GTPases is regulated by Guanine Nucleotide Exchange Factors (GEFs) and GTPase-Activating Proteins (GAPs). GEFs catalyze the exchange of GDP for GTP, therefore activate Rho GTPases. GAPs enhance the GTPase intrinsic activity of Rho, thereby inactivating their signaling functions. In addition, Guanine Nucleotide Dissociation Inhibitors (GDIs) prevent the nucleotide exchange by sequestering Rho GTPases in the cytosol (**Figure 3.1 C**) (Hodge and Ridley, 2016).

There are more than 20 Rho family members, of which RhoA, Rac1, and Cdc42 are the most studied ones. The classical view of Rho GTPase came from microinjections of the active mutants of RhoA, Rac1, or Cdc42, which induced formation of stress fiber, lamellipodia, or filopodia, respectively (Nobes and Hall, 1995; Ridley and Hall, 1992; Ridley et al., 1992). However, recent studies suggest the actin organization is more complicated and involves coordinated actions between different Rho GTPases.

Upon activation, Rho GTPases interact at the membrane with a spectrum of effectors to trigger their downstream functions for cytoskeleton remodeling. Here we are going to review some of the main Rho GTPases, their effectors, and cellular functions (**Figure 3.2**).

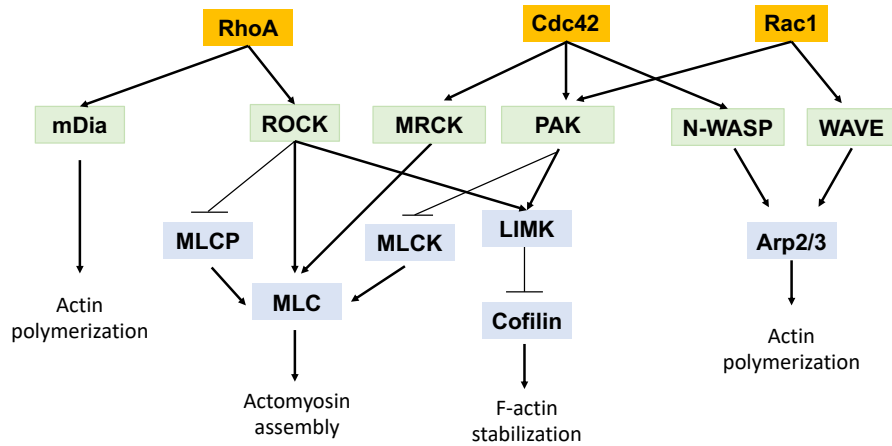


Figure 3.2. Rho GTPases signaling pathway in regulating cell contractility. Abbreviations: mDia, mammalian Diaphanous-related formin; ROCK, Rho kinase; MRCK, myotonic dystrophy kinase-related cdc42-binding kinases; PAK, p21-activated kinases; N-WASP, N-Wiskott–Aldrich syndrome protein (N-WASP); WAVE, WASP-like verprolin-homologous protein; MLC, myosin light chain; MLCP, myosin light chain phosphatase; MLCK, myosin light chain kinase; LIMK, LIM kinase; ARP2/3, actin related protein 2/3 complex.

3.1.1 RhoA

Microinjection of a GTPase-dead permanently activated mutant form of RhoA induced stress fiber and cell contractility (Ridley and Hall, 1992). Once activated, RhoA can bind to its effector Rho kinase (ROCK)1/2, which phosphorylate the myosin binding subunit (MYPT) of myosin light chain phosphatase (MLCP), resulting in its inactivation (Kimura et al., 1996). Myosin binds and cross-links F-actin into actomyosin bundle, which forms structures such as stress fiber and thereby promotes the formation of focal adhesion complexes. Inactivation of MLCP by ROCKs leads to elevated level of phosphorylated MLC and their cross-linking with actin filaments (Vicente-Manzanares et al., 2009). In addition, ROCKs also phosphorylate MLC directly, leading to its activation (Amano et al., 1996; Totsukawa et al., 2000). ROCKs also phosphorylate LIM kinases (LIMK) 1/2 which in turn phosphorylate and inhibit cofilin (Riento and Ridley, 2003). Cofilin is an actin severing protein that depolymerizes actin filaments. Reduction of cofilin activity increases the number of actin filaments. Another effector for RhoA is mammalian Diaphanous-related (mDia) formin, which nucleates and elongates straight actin filaments. Formin contains a FH2 domain that binds the actin filament while a FH1 domain grabs profilin, which associates with globular actin (Chesarone et al.,

2010). Therefore, activation of Rho promotes actin polymerization and bundling, leading to enhanced actomyosin cytoskeleton contractility.

RhoA, RhoB, and RhoC share 85% sequence identity with major difference in their C-terminal membrane binding motifs. As a result, RhoA and RhoC attach to the plasma membrane while RhoB binds to endosomal membrane (Adamson et al., 1992). Even though sharing similar sequence and effectors, Rho isoforms have different cellular functions. RhoA controls cell contractility as discussed above and is a critical regulator of cell cycle progression. This illustrates the importance of Rho GTPases in coordinating cytoskeleton structures with cell fate. RhoB seems to control late stages of vesicular trafficking. RhoC regulates cell spreading and lamellipodia through the formin, FMNL3 (Vega et al., 2011).

3.1.2 Cdc42

Microinjection of an active mutant of Cdc42 induced filopodia formation (Nobes and Hall, 1995). To induce actin reorganization, active Cdc42 interacts with N-Wiskott–Aldrich syndrome protein (N-WASP), releasing C-terminal of N-WASP for interaction with Actin-Related Proteins (Arp) 2/3 complex. Arp2/3 complex catalyzes actin nucleation and polymerization from an existing actin filament, creating a branched dendritic actin network. Once binding with N-WASP, Arp2 and Arp3 are brought in close proximity to nucleate actin polymerization. This is facilitated by the WH2 domain of N-WASP that grabs globular actin (Goley and Welch, 2006). All together, they form a supply chain for actin polymerization.

Cdc42 signals through the activation of different protein kinases. The p21-activated kinases (PAK) protein family are other important effectors of Cdc42. This family of kinase comprises 6 members. PAKs are Ser/Thr kinases with numerous protein substrates. MLC kinase (MLCK) is one of the substrate of PAK. Phosphorylation of MLCK reduces its activity, decreasing and inhibiting actin cross-linking. PAKs also phosphorylate LIMK, which inhibits cofilin activity and stabilize actin filaments (Hanna and El-Sibai, 2013). Another Cdc42 effector is myotonic dystrophy kinase-related cdc42-binding kinases (MRCK), which phosphorylates and activates MLC (Bishop and Hall, 2000).

Cdc42 also regulates migratory polarity in cells through interacting with the PAR complex (Etienne-Manneville and Hall, 2002). Once activated, Cdc42 and Rac1 bind to PAR6, which further complexes with PAR3 and PKC ζ . This complex regulates cellular polarity in various aspects, such as basolateral polarity in MDCK cells (Joberty et al., 2000). Furthermore, PKC ζ binds to Smurf1, a E3 ubiquitin ligase, at cell protrusions. This allows Smurf1 to target

RhoA for ubiquitin-dependent proteasomal degradation, reducing locally the activity of RhoA at protrusion, where Cdc42 and Rac1 activity are more dominant (Wang et al., 2003).

3.1.3 Rac1

Microinjection of a constitutively active GTPase-deficient mutant of Rac1 induced lamellipodia formation (Ridley et al., 1992). Active Rac1 binds to WASP-like verprolin-homologous protein (WAVE). WAVE on one hand binds to globular actin through profilin, and on the other hand binds to Arp2/3 complex. Similar to N-WASP, WAVE activates Arp2/3 while providing it materials for actin polymerization. Like Cdc42, Rac1 also interacts with PAK1/2/3 that could further regulate actin remodeling (Bishop and Hall, 2000). Active Rac1 localizes to the leading edge of lamellipodia (Machacek et al., 2009). Depletion of Rac1 inhibits lamellipodia formations (Tan et al., 2008b; Wells et al., 2004), while a local enrichment of active Rac1 is sufficient to induce lamellipodia formation (Wu et al., 2009). These indicates that Rac1 plays a central role in lamellipodia formation, though Rac1 is not the sole Rho member in generating membrane ruffles.

In order for cells to migrate, the leading edge protrudes while the rear end retracts. This process is regulated by the local activation and inactivation of Rho GTPases. Biosensors of active Rho GTPases reveal their spatial and temporal subcellular activation. All three Rho GTPases are activated at the leading edge of migrating cells (Machacek et al., 2009). Active RhoA locates both to the leading edge of lamellipodia and the retraction rear (Pertz et al., 2006). In fibroblast, RhoA is activated simultaneously at the leading edge of migrating cells, while Cdc42 and Rac1 follow with 40s delay (Machacek et al., 2009). This indicates that the formation of lamellipodia is a coordinated work between different Rho GTPases. RhoA seems to initiate the actin polymerization at the front end of the migrating cells, while Rac1 and Cdc42 involve in reinforcing adherens junctions (Machacek et al., 2009).

3.2 Rho GTPases and endothelium barrier function

Blood vessel is the major path for transporting essential nutrients throughout the body. It is no wonder that bacteria take the advantage of circulation system as a highway for their dissemination in whole body. Furthermore, interfering with the barrier function of endothelia allows bacteria to distribute from the vessels to underlying tissues. Endothelial cells form the lining of the vessel lumen which separates blood from tissues thereby been a major target of pathogenic bacteria and their toxins (Lemichez et al., 2010).

3.2.1 Endothelial barrier functions

The endothelial tissues are lining the interior lumen of vessels forming a semi-permeable barrier. Endothelium barrier controls the exchange of gas and small molecules, while blocking the passage of big ones. Pathogens, such as bacteria, are blocked by the endothelial barrier. However, there are two major ways pathogens interfere protective functions of endothelium. One is through the disruption of intercellular junctions and the other is through the corruption of intracellular integrity.

The permeability of endothelial cells is regulated by cell-cell junctions that hold adjacent cells. There are two major types of intercellular junctions between endothelial cells: tight junctions and adherens junctions. In adherens junction, the dominant cell-cell junctions in endothelial cells, vascular endothelial (VE) cadherin binds to neighboring cells through homophilic interactions while connecting with intracellular F-actin via catenins. Tight junctions are formed via homophilic interactions between claudins or occludins that hold the neighboring cells together and are linked to actin cytoskeleton via zonula occludins. Cell-cell junctions are closely associated with cortical actin network, thereby being susceptible to intracellular tension that retains the cell contractility or extracellular shear forces. Therefore, Rho GTPases are key regulators of endothelial permeability. Actin cytoskeleton regulates cell-cell junctions by generating centripetal tensions or modifying the stability of adhesion complexes.

3.2.2 Nitric oxide (NO) signaling

NO is an important signaling regulator of cardiovascular functions, especial in vascular tone and blood clotting. It governs the vascular smooth muscle relaxation and thereby regulates vascular tension. NO is synthesized by endothelial nitric oxide synthase (eNOS) in endothelial cells (**Figure 3.3**). This lipophilic gaseous molecule diffuses freely across cellular membrane to the vascular smooth muscles, where it activates the nitric oxide-soluble guanylyl cyclase (sGC) (Komarova et al., 2017). The sGC synthesizes cyclic guanosine monophosphate (cGMP),

which activates cGMP-dependent protein kinase (PKG). PKG phosphorylates RhoA leading to its inactivation, thereby reducing actomyosin contractility of the vascular smooth muscle to achieve vasodilation (Rolli-Derkinderen et al., 2005).

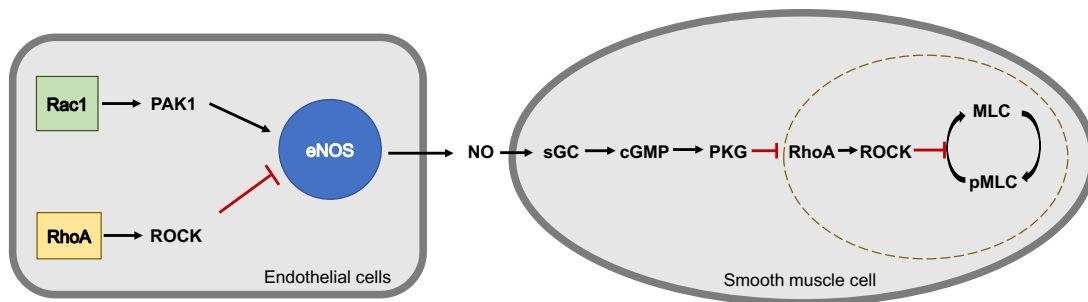


Figure 3.3. Signaling of nitric oxide between endothelial and vascular smooth muscle cell. Abbreviations: ROCK, Rho kinase; PAK, p21-activated kinases; eNOS, endothelial nitric oxide synthase; MLC, myosin light chain. sGC, nitric oxide-soluble guanylyl cyclase; cGMP, cyclic guanosine monophosphate; PKG, cGMP-dependent protein kinase. Illustration modified from (Loirand and Pacaud, 2010).

NO remains a path for crosstalking between endothelial cells and smooth muscle cells. The expression of eNOS is positively regulated by Rac1 but negatively regulated by RhoA in endothelial cells. Activation of Rac1 increases the stability of eNOS mRNA (Laufs and Liao, 1998). On the contrary, RhoA reduced both the expression and stability of eNOS mRNA (Sawada et al., 2008). Therefore, RhoA activation leads to increase in vascular tone while RacA has an opposite effect.

3.2.3 Rho proteins and adherens junctions

The balance of Rho GTPases activity is important to maintain endothelial barrier function. At the basal condition, ROCK activates myosin at the cell-cell junction and stabilizes adherens junctions, which activity is essential for endothelial barrier functions (Amerongen et al., 2007). Thrombin is a well-known factor that increases endothelium permeability. Thrombin activates RhoA GTPase, which in turn increases the actomyosin contractility via ROCKs (Wojciak-Stothard and Ridley, 2002). ROCKs activate myosin, leading to the formation of actomyosin stress fibers. Therefore, myosin activity is relocated from cell-cell junctions to the stress fibers. Furthermore, actomyosin contractility generates a centripetal tension

counteracting with the cell-cell adhesion (Moy et al., 1996). In this case, VE-cadherin dissociates from catenin and junctions disassemble, thereby increasing the permeability (Rabiet et al., 1996).

Rac1 and Cdc42 counteract the function of RhoA by stabilizing adherens junctions formation. First of all, Rac1 counteracts RhoA activity by relocating p190RhoGAP to adherens junctions where it inactivates locally the RhoA activity (Wildenberg et al., 2006). Moreover, both Rac1 and Cdc42 are required for adherens junctions functions. During the adherens junctions formation, p120 catenin activates Rac1 and Cdc42 via binding to their GEF, Vav2 (Noren et al., 2000). In coordination, VE-cadherin also activates Rac1 through another GEF, Tiam (Lampugnani et al., 2002). Depletion of either Cdc42 or Rac1 in endothelial cells results in a loss of cell-cell junctions and increased endothelial permeability (Barry et al., 2015; Tan et al., 2008a).

In the following chapters, we discuss how bacteria interfere with host cell Rho signaling to reduce intracellular permeability of endothelial cells to achieve their dissemination.

3.3 Transendothelial cell macroaperture formation

Transendothelial cell macroaperture (TEM) tunnels are induced by several bacterial toxins likely forming a path for extravasation of pathogenic bacteria through the endothelium barrier (**Figure 3.4**). It was first noticed by our team (Emmanuel Lemichez, Institut Pasteur) in 2006 (Boyer et al., 2006) and has been studied intensively ever since. TEM is induced by toxins secreted by several pathogenic bacteria, including *Staphylococcus aureus*, *Clostridium botulinum*, *Bacillus anthracis*, and *Bordetella pertussis* (Boyer et al., 2006; Maddugoda et al., 2011). Via inhibiting RhoA or increasing cyclic-AMP signaling pathway, TEMs-inducing toxins reduce actomyosin contractility in human umbilical vein endothelial cell (HUVEC) and other cell types. Therefore, endothelial cells spread, leading to a spontaneous opening of large transcellular tunnels (5-10 μm in radius). TEMs form labile openings. During the opening of TEMs, cells recruit effectors along the edge of the tunnel to build a rigid actin cable that encircles TEMs and restricts TEM widening. TEMs are resealed by either a lamellipodia-like membrane wave or a purse-string contraction phenomenon.

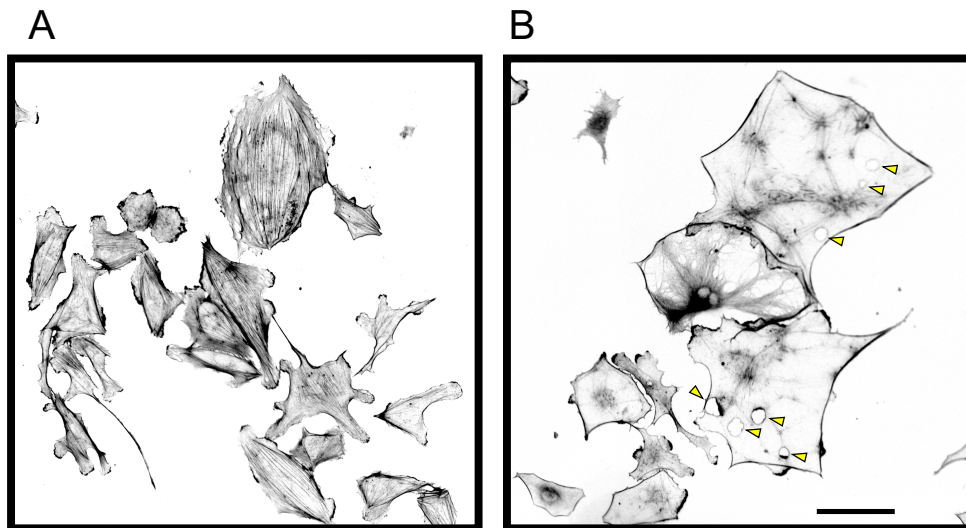


Figure 3.4. Induction of TEM (arrow heads) formation by C3 toxin in HUVECs. Phalloidin staining of control cells (A) and cells treated with C3 exotoxin from *C. botulinum* (B). Scale bar = 100 μ m.

In this chapter, we discuss the molecular mechanism of TEM opening, stabilization, and closure.

3.3.1 Inducers for TEM opening: Toxins and RhoA inhibition

ADP-ribosylating toxins

There are several toxins that can induce the opening of TEMs through different signaling pathways (**Figure 3.5**). The C3 exoenzyme from *C. botulinum* and Epidermal Cell Differentiation Inhibitors A/B/C (EDIN-A/B/C) from *S. aureus* catalyze the mono-ADP-ribosylation of RhoA on Asn-41 and RhoB, C isoforms to a lower extent (Wilde et al., 2003). Asn-41 is localized in the switch I region of Rho proteins. This region undergoes conformational changes between the active and inactive states. ADP-ribosylation does not affect the nucleotide binding or hydrolysis but relocates the Rho GTPases in the cytosol, where they are tightly sequestered with GDI proteins (Aktories and Just, 2005). As discussed, RhoA regulates actomyosin contractility through ROCK. Inhibition of RhoA in HUVECs leads to the disassembly of stress fibers and spreading of cells (**Figure 3.4**). In addition, TEM can be induced either by RNAi-targeted depletion of RhoA or ROCK inhibition by Y27632 although with lower efficacy (Boyer et al., 2006).

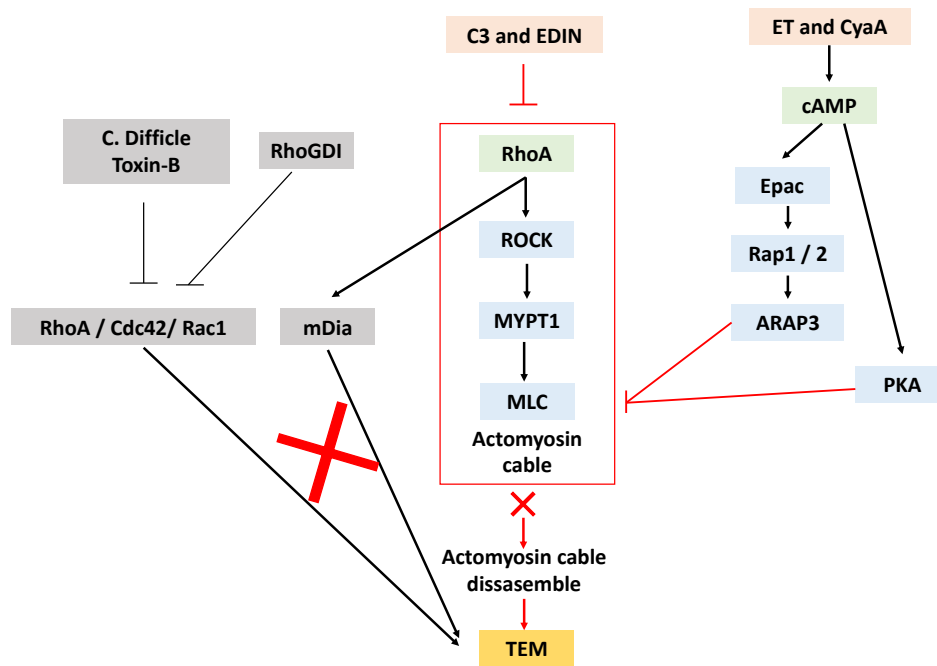


Figure 3.5. Signaling pathway triggering TEM formation. Color cod: pink, toxins; green, direct targets of the toxin; blue, proteins involved in toxin-induced signaling pathway; gray, proteins that do not induce TEM. Note that toxin-A and B from *C. difficile* although they induce RhoA inactivation and also induce the inactivation of Rac1 and Cdc42 thereby triggering a rounding and detachment of cells.

Adenylate cyclase toxins

Another family of TEM-inducing toxins are the adenylate cyclases, edema toxin (ET) from *B. anthracis* and CyaA toxin from *B. pertussis* (**Figure 3.5**). Anthrax toxin contains three components: the protective antigen, edema factor, and lethal factor. Contrary to EDIN and the C3 exoenzymes, these toxins inject their enzymatic component with high efficacy in host cells. The protective antigen recognizes capillary morphogenesis protein 2 (CMG2)/tumor endothelial marker 8 (TEM8) receptors and the lipoprotein receptor-related protein 6 (LRP6) co-receptor on host cell membranes (Bann, 2012). Following its binding, the protective antigen undergoes proteolytic cleavage and later assembles into a donut-shape prepore on the host membrane, offering binding sites for one to three molecules of either edema factor or lethal factor. This hepta/octamerization of protective antigen induces the mono-ubiquitination of the TEM8 receptors as signal triggering their internalization into endocytic vesicles (Abrami et al., 2006). When endocytosed into acidic endosome, the prepore undergoes conformational change

and forms a membrane spanning pore, through which edema factor and lethal factor translocate into the cytoplasm of the host cells (Bann, 2012).

The edema factor couples with protective antigen as edema toxin (ET), an adenylate cyclase, resulting in the production of cAMP. Elevated level of cAMP leads to the activation of cAMP-activated protein kinase A (PKA). PKA has several substrate in cells, including RhoA (Howe, 2004). PKA phosphorylates RhoA at Ser188, increasing its interaction with RhoGDI thereby being sequestered into the cytosol (Lang et al., 1996). In HUVEC cells PKA does not inactivate RhoA directly (Maddugoda et al., 2011). In this cell type, cAMP rather inhibits actomyosin contraction via dephosphorylation of MLC. Another effector downstream of cAMP is Exchange Protein Directly Activated by cAMP (Epac), a GEF for small GTPase Rap 1 and Rap2. Like Rho GTPase, Rap is regulated through its GTP and GDP exchange to switch between active to inactive forms. Rap controls cell adhesion and migration via binding to its effectors, Afadin (AF-6) and integrin (Bos, 2005). Rap also interacts with ARAP3, a RhoGAP, to promote RhoA inactivation (Krugmann et al., 2004). Pharmacological activation of Epac led to the disassembly of stress fibers in endothelial cells and opening of a few TEMs of small size (Cullere et al., 2005; Maddugoda et al., 2011).

Apart from bacterial toxins, pharmacological or RNAi-based interferences with actomyosin contractility can induce the opening of TEMs (**Figure 3.5**). Inhibiting actin polymerization with low dose of cytochalasin D or latrunculin B for a short period of time can induce TEM formation (Boyer et al., 2006). Direct inhibiting of RhoA by siRNA or blocking ROCK activity with Y27632 also induced TEMs. Importantly, treatment of cells with cAMP analog also triggered TEM formation, thereby indicating that TEM can be induced by cell signaling. More specifically, both PKA-specific cAMP analog, 6-Bnz-cAMP, and Epac-specific cAMP analog, 8-CPT-cAMP, induced TEM (Maddugoda et al., 2011). On the other hand, cAMP antagonist, PKA inhibitor, or dominant negative form of Rap1 all blocked ET-induced TEM formation. Interestingly, in collaboration with the team of Daniel Fletcher, Ng *et al.*, found that application of mechanical force by atomic force microscope (AFM) was sufficient to induce TEM of small size (Ng et al., 2017). They used AFM tip to apply progressive mechanical force on the cell and found the average force to induce TEM was 39 nN. These TEMs were relatively small (0.6 μm in radius) and transient. The AFM-induced TEM resembles leucocyte diapedesis processes in which leucocytes produce protrusion or invadopodia generating a force at 94 nN, which allows leucocyte to invade and migrate through the endothelial cells (Labernadie et al., 2014). In conclusion, the mechanical force required to induce TEM is comparable to the protrusion force generated by leukocyte during diapedesis.

TEMs form due to the reduction of actomyosin contractility. TEM inducing toxins disassemble F-actin network, resulting in a spreading of cell estimated to 1.5 fold (Maddugoda et al., 2011). Excessive amount of F-actin accumulates at the periphery of the cells, which might be the driving force for cell spreading (Boyer et al., 2006; Maddugoda et al., 2011). Our unpublished data show that ablation of actin cables at the cell periphery by laser nano-surgery leads to induction of C-shape retractions. In line with this, loss of actomyosin reduces cell contractility, which in turns promote cell spreading and formation of C-shape or TEM in mouse embryonic fibroblasts (Cai et al., 2010). Spreading of the cells generates a membrane tension along the cell surface, which is believed to be the driving force for pore extension. As a consequence of C3 exoenzyme action, cells are 1.5-fold larger, 1.4-fold thinner, and 30-fold softer, likely making them prone to plasma membrane fusion events that generate transcellular openings (Maddugoda et al., 2011; Ng et al., 2017).

3.3.2 Stabilization of TEM and the physics behind

The dynamics of TEM is driven by an opposing effect between bacteria and host cells. Bacterial toxins trigger a first physical process of membrane nucleation and pore extension while the host cell reacts for stabilization and closure of the pore. The nucleation of the membrane and extension of the pore likely result from the spreading of cells as discussed. After TEM opening, cells organize, in a time dependent manner, a thick and rigid actin cable around TEMs to stop their widening.

The opening of TEMs resembles the liquid dewetting process in which a viscous liquid film is forced to spread on a non-wettable surface, resulting in nucleation and growth of dry patches (**Figure 3.6A**) (Gonzalez-Rodriguez et al., 2012; Maddugoda et al., 2011). Similar to the liquid dewetting process, TEMs open when cells are forced to spread due to the lack of actomyosin contractility, leading to increased membrane tension which is the driving force for TEM nucleation and growth. The extension of TEM is limited by the building of a line tension that works against TEM enlargement. There are several contributions to line tension (**Figure 3.6B**). Once, a TEM opens, the membrane tension is released locally due to the reduction in cell area (Gonzalez-Rodriguez et al., 2012). Second, as TEMs open, the membrane needs to deform from a flat conformation to curved rim along TEMs. Therefore, the line tension is contributed by the energy cost for bending the membrane and actin cortex along TEMs. Increasing the global bending rigidity of the cell shall increase the line tension (Gonzalez-Rodriguez et al., 2012). Third, as TEMs form, cell recruits proteins to build a stiff actin cable

that restricts TEM widening (**Figure 3.6A**). Deficiency in recruiting actin cable formation leads to indefinite opening of TEM (Stefani et al., 2017).

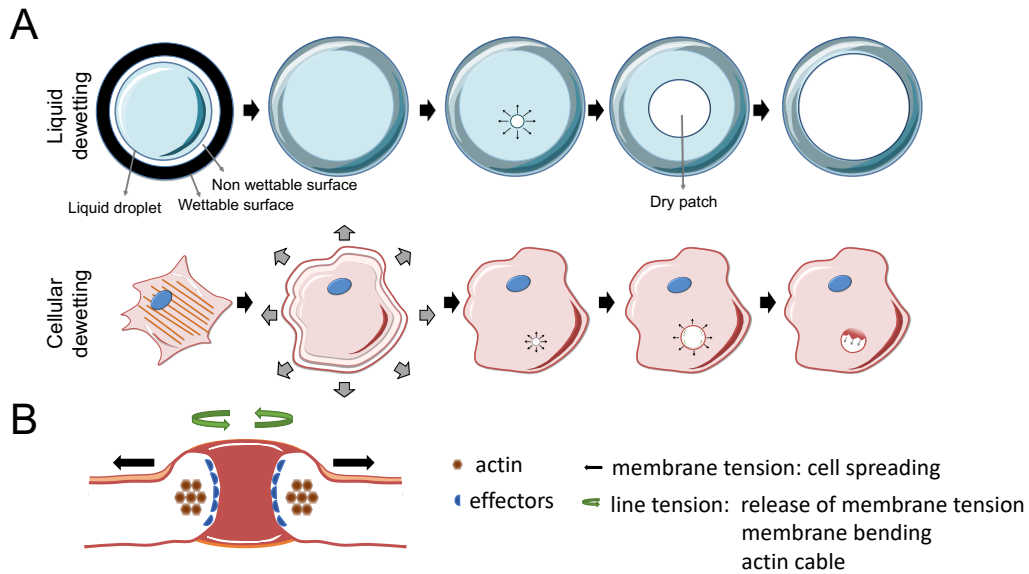


Figure 3.6. Physical and cellular liquid dewetting models. (A) Progression of a physical liquid dewetting and cellular dewetting. Liquid dewetting describes a drop of viscous liquid is forced to spread on non-wettable surface and dry patches grow. Cellular dewetting is when cell spreads in response of the toxin treatment and TEMs nucleate and grow up to a maximal size. (B) The driving forces for TEM opening is the membrane tension arose from cell spreading. The restriction force of TEM opening is the line tension that attribute from the energy cost for bending membrane and by building of actin cables.

We have proven this with a laser that ablated the actin cables around TEMs, either globally or locally, and initiated a second widening (**Figure 3.7B**)(Stefani et al., 2017). This has proven that the actomyosin cables around TEM are the main figure to restrict TEM widening. Once the building of actin cables is strong enough to balance the membrane tension, TEM stabilized. Moreover, this actomyosin cable is not a contractile structure, considering that its length remains constant before and after ablation (Stefani et al., 2017).

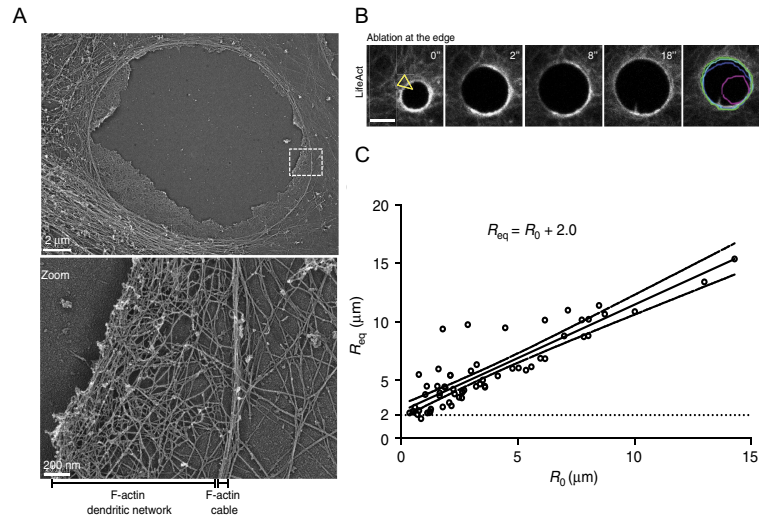


Figure 3.7. Cytoskeleton structures around TEM. (A) A platinum replica electron micrograph of TEM show two types of actin structures: a thick actin cable and a branched dendritic network. (B) Laser ablation of TEM at the actin cables (C) Graph shows linear curve fitting of initial radius (R_0) and equilibrium radius (R_{eq}) after laser ablation. Scale bar, 5 μm . Illustrations extracted from (Stefani et al., 2017).

Interestingly, after the laser ablation, the second stabilization was reached when new actin filaments were recruited to replenish the fracture, typically in 10 seconds (Stefani et al., 2017). We noticed that TEM enlargement after laser ablation was independent of the initial radius. Rather, the equilibrium TEM radius (R_{eq}) was the initial radius (R_0) plus a constant value of 2 μm (**Figure 3.7C**) (Stefani et al., 2017). This constant ΔR (2 μm) suggests that the building of new cables is independent of the R_0 . Therefore, it is not through bending of the existing actin cables which is dependent on the length of initial cable. Nor it is through the sweep-motion collection of F-actins, in which TEM sweeps through the region and collects molecules at its rim, during TEM reopening. Our experimental data fit the mathematical model implying that the building of a new line tension is through a mechanism that recruits F-actin at a constant rate along the edge of TEMs. We calculated that the line tension at a stabilized TEM after laser ablation was around 500 pN. Further reducing this tension to 200 pN led to indefinite TEM opening. Indeed, interfering with actin cable formation by non-muscle myosin IIA (NMIIa) depletion led to indefinite opening of TEM after ablation (Stefani et al., 2017).

3.3.3 Effectors that stabilize TEM

NMIIa bundles actin cables around TEMs to restrict their opening. The next question is by which molecules or mechanisms the actin is recruited and build actomyosin cables. As discussed in Chapter 2.1, membrane curvature could be a cue for protein recruitment. Our team collaborated with the team of Frank Lafont (Institut Pasteur, Lille) to study the topology of TEM by AFM. Maddugoda *et al.*, identified a higher ridge (115 nm) at TEM border compared to the surrounding area (53 nm) (Figure 3.8A-B), resulting in a structure composed of both positive and negative membrane curvature in the inner leaflet of the plasma membrane (Figure 3.8C) (Maddugoda et al., 2011). Positive curvature aligns along the perimeter (xy-axis) of the tunnel. The level of positive curvature inversely correlates to the diameter of the tunnel, which decreases as TEM opens. Negative curvature aligns along the z-axis of the ridge. The level of negative curvature inversely correlates to the height of the ridge. Therefore, dynamics of membrane curvature during opening of TEMs might attract different effectors at different stages.

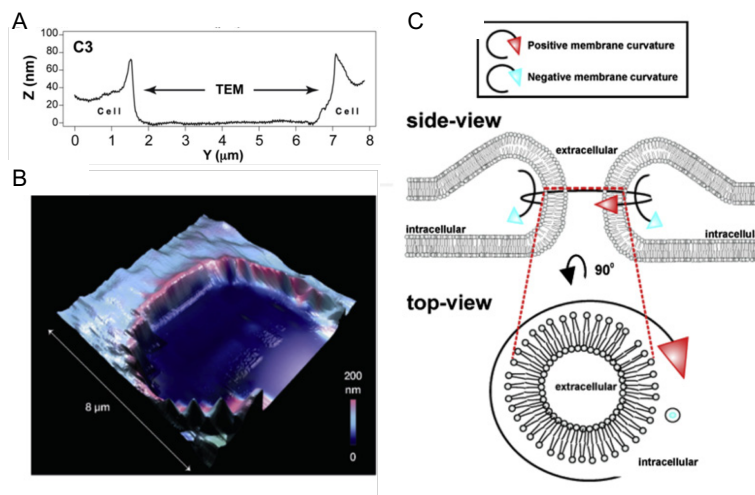


Figure 3.8. Topology of TEM measured by atomic force microscopy. (A) Representation of an AFM profile of TEM. (B) 3D topographic image of a TEM (C) Schematic presentation of lateral and top view of TEM. Red and blue arrow indicate positive curvature encircle the TEM perimeter and negative curvature along the TEM z axis. Illustrations extracted from (Maddugoda et al., 2011).

Ezrin, radixin and moesin are proteins that bridge F-actin and membrane. They bind to membrane through the N-terminal FERM domain and F-actin through the C-terminal domain. Our team identified that Ezrin localized to the edge of TEMs. Depletion of Ezrin but not radixin

and moesin increased the size of TEMs, due to the thinner actin cables formed around TEMs (Stefani et al., 2017).

The FERM domain of Ezrin binds to PI(4, 5)P₂ (Tsai et al., 2018). When inactivated, the N- and C- terminals fold into an auto-inhibitory conformation. Binding with PIP₂ allows Ezrin to be phosphorylated by its kinase, LOK (Pelaseyed et al., 2017). Phosphorylation releases Ezrin from its closed configuration (Fievet et al., 2004) for subsequent F-actin and effectors binding. Indeed, Ezrin does not entirely rely on PI(4, 5)P₂ binding to target to the membrane *in vivo*. Mutating the PI(4, 5)P₂ binding residues of full-length Ezrin led to its translocation from the plasma membrane to cytosol. However, the PI(4, 5)P₂-binding defected mutant of N-terminal Ezrin domain still localized to the plasma membrane (Fievet et al., 2004). This indicates that in the absence of autoinhibition, i.e. removal of the C-terminal domain, Ezrin could translocate to membrane regardless of PI(4, 5)P₂. Therefore, the key factor that blocks the membrane targeting of wildtype Ezrin is the autoinhibition but not the presence of PI(4, 5)P₂.

We collaborated with the team of Patricia Bassereau to study how Ezrin translocates to membrane (Tsai et al., 2018). Full-length Ezrin and the phosphomimetic mutant (T567D), only bound to giant unilamellar vesicles (GUV) containing PI(4, 5)P₂ *in vitro*. Ezrin T567D was even recruited to nano-tube, a positive curvature, pulling from the GUV. However, in the presence of I-BAR proteins, both Ezrin wildtype and T567D bound to GUV without PIP₂ (Tsai et al., 2018). Furthermore, both Ezrin wildtype and T567D were enriched at I-BAR induced invagination, a negative membrane curvature. Therefore, Ezrin itself binds to membrane through PIP₂. Phosphorylation enables Ezrin to sense positive curvatures on PIP₂ containing membrane. The membrane targeting of Ezrin partly relied on its interacting partners, such as I-BAR, that help binding to non PIP₂ membrane, even negative curvatures (Tsai et al., 2018).

I-BAR proteins, MIM and ABBA, are found to localized to TEM but seems to be involved in the closure of TEM with low effect on line tension (Maddugoda et al., 2011). This will be discussed further soon.

I participated in another part of the investigation in identifying potential effector, formin. Considering formin is one of the few protein family that catalyzes actin nucleation, it is a possible that formin is responsible for actin cables around TEM. However, we did not detect the recruitment of mDia1, a member of the formin family, to the edge of TEMs (Stefani et al., 2017). Neither did the formin inhibitor, SMIFH2, increased the size of TEMs. Rather, SMIFH2 reduced the TEM size to half, suggesting an impact on the spreading or/and adhesion of the cells.

3.3.4 Closure of TEM

After TEMs stabilize, they progressively undergo closure via two different phenomenon: a lamellipodia-like membrane wave or a purse-string constriction. Maddugoda *et al.*, have identified I-BAR proteins, MIM and ABBA, localized to TEM edges (**Figure 3.9 A**)(Maddugoda *et al.*, 2011). Compared to other I-BAR proteins, MIM and ABBA contain a N-terminal amphipathic helix that facilitate their localization to TEMs (**Figure 3.9B-C**). MIM and ABBA might use amphipathic helix to bind to positive membrane curvature at the beginning of TEM opening. A targeting of MIM I-BAR at the edge was observed already at 500 ms. As TEM progress, positive membrane curvature reduces and MIM and ABBA switch to utilize I-BAR domain for membrane binding and promote accumulation of PIP₂ (Saarikangas *et al.*, 2009). This hypothesis is strengthened by the fact that MIM-I-BAR is recruited to TEM few hundred milliseconds after TEM opens.

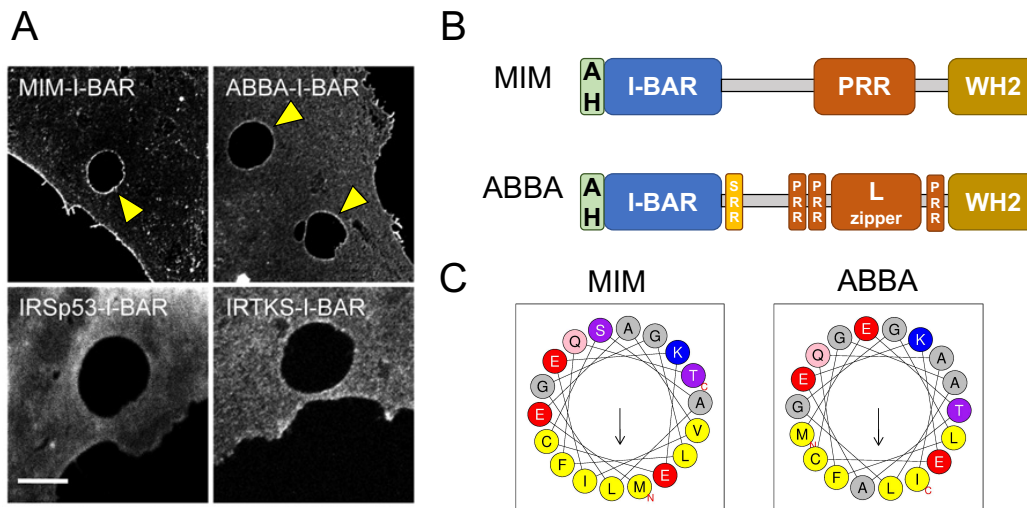


Figure 3.9. Recruitment of I-BAR proteins (arrow heads) around TEM. (A) The recruitment of GFP tagged I-BAR domains to TEM. Scale bar, 10 μ m. Illustrations extracted from (Maddugoda *et al.*, 2011). (B) The structure of MIM and ABBA. Modified from (Zhao *et al.*, 2011). AH, amphipathic helix; PRR, proline-rich region; SSR, serine-rich region; WH2, WASP-homology 2; L zipper, Leucine zipper. (C) The amphipathic helices of MIM and ABBA predicted by Heliquest server.

MIM triggers membrane protrusion, through recruiting Arp2/3 complex, to close TEM. Knockdown of MIM blocked the recruitment of Arp2/3. Therefore, lamellipodia-like membrane wave was not observed around TEM and the closure of TEM was strongly perturbed, increasing the population of cell with TEMs. However, the formation of actin cable around

TEM was not affected in cells knockdown of MIM or Arp2/3. On the other hand, overexpressing of MIM induced actin wave that close TEM before reaching a stable state (Maddugoda et al., 2011). Therefore, it cannot be excluded that MIM plays a minor role in the control of line tension that limit the speed of opening. Consistent with this idea, MIM knockdown led to TEMs of bigger size.

3.3.5 Physiological consequence of TEM formations

When treated with EDIN, HUVEC monolayers and arterial endothelium developed apertures as well increased permeability (Boyer et al., 2006). Treating the HUVEC monolayer with EDIN toxin induced TEM formation, though at a lower occupancy compare to disperse cell culture. However, the formation of TEMs was coupled with increase monolayer permeability. In addition, both EDIN toxin and *S. aureus* containing an EDIN-encoding gene induced TEMs on aortic endothelium *ex vivo* (**Figure 3.10A**). Furthermore, *S. aureus* was found in close proximity to endothelium basement membrane exposed due to the formation of TEMs (**Figure 3.10B**). Furthermore, injection of mice with either EDIN or Edema toxin increased vascular permeability (Boyer et al., 2006).

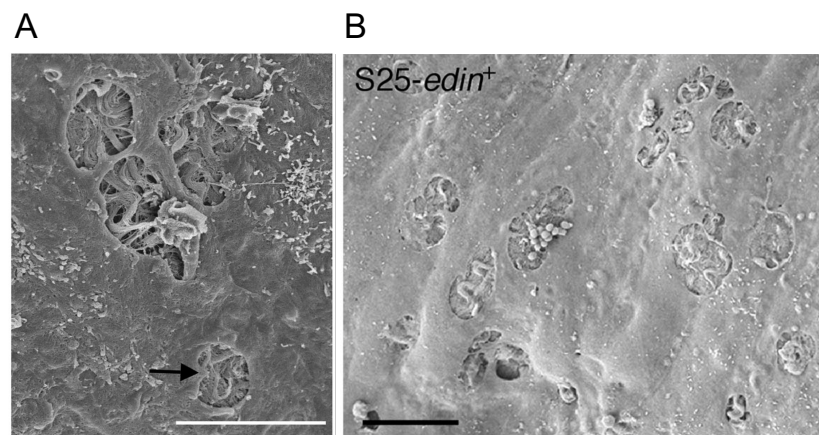


Figure 3.10. Macroaperture formation on aortic endothelium. (A) Electron micrographs show the formation of macroaperture induced by EDIN toxin on aortic endothelium. (B) Electron micrographs show the formation of macroaperture induced by *S. aureus* expressing EDIN toxin. Scale bars, 10 μm . Illustrations extracted from (Boyer et. al., 2006).

Little is known about the correlation between EDIN and *S. aureus* infection, except EDIN being a prevalent factor that is often identified from clinical patients (Czech et al., 2001; Munro et al., 2010). On the other hand, Anthrax toxin is the main virulent factor for *B. anthracis*. Removal of either components (protective antigen, edema factor, or lethal factor) reduced the

LD₅₀ of *B. anthracis* (Pezard et al., 1991). Importantly, depletion of edema factor or lethal factor attenuates the bacteria-induced vascular permeability (Guichard et al., 2010).

TEMs induced by bacterial toxins resembles to the formation of endothelial pores during leukocyte diapedesis, in which leukocyte transmigrates through the endothelium. Leukocytes exert force via their invading protrusions on endothelial cells to induced the formation of pores on endothelium (Yeh et al., 2018). The endothelial pores were encircled with actin structures from endothelial cells and their sizes are tightly regulated to prevent vascular leakage during leukocyte transmigration (Heemskerk et al., 2016). The endothelial pores induced by leukocyte share similarity with TEMs induced by bacterial toxins: (1.) they are both encircled by actomyosin bundles to regulate their sizes (2.) They are both few μm in diameter (3.) They are both transient (few mins) structure on endothelial cells. (4.) They both can be induced by mechanical force at nN scale. Therefore, studies on the dynamics of TEM could provide more insights on the formation of endothelial pores during leukocyte diapedesis.

3.4 Extra-intestinal pathogenic *E. coli* (ExPEC) invasion

3.4.1 Uropathogenic *E. coli* (UPEC)

Urinary tract infections affect one third of the women in US (Foxman, 2002). Uropathogenic *E. coli* (UPEC), which refer to extra-intestinal pathogenic *E. coli* (ExPEC) isolated from urinary tract infections (UTIs), are causative agents of 85% of UTIs and also responsible of neonatal meningitis (Ronald, 2002). About one third of UPEC secrete the Cytotoxic Necrotizing Factor-1 (CNF1) toxin (**Figure 3.11**) (Landraud et al., 2000). CNF1 is a potent inducer of inflammatory responses through its capacity to hijack Rho proteins. Most of UPEC express type I pili, a 7 nm helical rod tipped by FimH adhesin that recognizes highly mannosylated beta-1 integrins from host cells (Eto et al., 2007). CNF1 is able to promote the invasion of cells by *E. coli* in a beta-1 integrin-dependent manner (Visvikis et al., 2011). UPEC invasion promotes the formation of bacterial reservoir and confers bacteria higher capacity to resist to medical treatments (Mysorekar and Hultgren, 2006). Therefore, understanding the invasion process of UPEC and studying the potential prevention strategy are important.

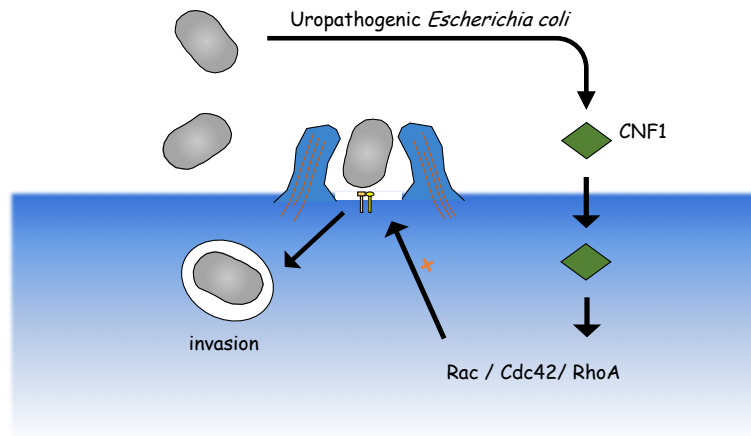


Figure 3.11. Invasion of uropathogenic *E. coli* is triggered by CNF1 toxin. CNF1 deamidates and locks Rho GTPases in their active conformation. This constitute activation targets Rho GTPases for ubiquitination and subsequently proteasome-mediated degradation.

3.4.2 CNF1

The invasive process of UPEC is highly promoted by CNF1 toxin (Visvikis et al., 2011). CNF1 deamidates a specific glutamine residue to glutamic acid in the switch II motif of Rho GTPases, i.e. Rho, Rac, and Cdc42. This blocks the intrinsic and GAP-regulated GTPase activity of Rho GTPases, locking them in their active states and sensitizing Rho GTPases to ubiquitination and degradation by the proteasome (Doye et al., 2002). Therefore, CNF1 induced a transient activation of Rho GTPases that peaks at 2 hours due to progressive cellular depletion of Rho proteins (Doye et al., 2002). Both activation and inactivation of Rho GTPase are important for cell invasion by UPEC. Blocking the proteasomal degradation by inhibitor or over-expression of wildtype Rac1 reduced CNF1 mediated UPEC invasion (Doye et al., 2002). Additionally, knockdown Rac1 also reduced CNF1-mediated UPEC invasion (Visvikis et al., 2011). Indeed, the maximum UPEC invasion correspond to the inactivation phase of Rho GTPase depending cell types (Doye et al., 2002). It is still not clear whether ubiquitin-mediated proteasomal degradation of Rho represent a refine mechanism exploited by CNF1 or a host reaction to the CNF1 action.

Thesis Objectives

Modern western diets shift our consumption of oil. We consume more vegetable oil and meat but less fish, i.e. more saturated fat and cholesterol at the expense of polyunsaturated fat. However, increasing animal and clinical studies show that PUFA improves the memory/learning and also cardiac functions (Shahidi and Ambigaipalan, 2018). There are even commercial products claiming to be enriched in ω -3 and ω -6 fatty acids. Yet, little is known about the cellular functions of PUFA.

Our team and others have uncovered that PUPL reduce the energy cost for membrane deformation, thus the vesicle trafficking is facilitated (Feller et al., 2002; Pinot et al., 2014). PUPL also serves as a matrix for transducing mechanical force on the membrane, therefore light and touch sensation are elevated (Caires et al., 2017; Ridone et al., 2018). Nevertheless, these are local impacts of PUPL. How can we expand our knowledge of PUPL in different aspects of cellular functions?

In this thesis, we ask a simple question: does PUPL controls large scale membrane deformation during bacterial invasion processes?

Bacteria induce membrane deformations at the much larger scale than membrane trafficking associated processes. Here we turn to the study of two system of invasion triggered by bacterial toxins that hijack host Rho GTPase signaling in bidirectional ways. We focused on RhoA inactivation by ExoC3 from *C. botulinum* that leads to the opening of large transcellular tunnels, here referred to as transendothelial cell macroapertures (TEM). Formation of TEMs has been linked to bacterial extravasation through the endothelium to the underneath tissues and vascular leakages (Boyer et al., 2006; Maddugoda et al., 2011). Indeed, the endothelium plays a key role in separating the blood borne bacteria during septicemia from host tissues therefore being a major target of invasive bacteria. Considering that vascular endothelial cell is one of the first cell type exposed to dietary changes, it is a perfect model for our study. We performed complementary studies on another system that involves Rho GTPase activation for enhanced invasion of endothelial cells by ExPEC, which can trigger meningitis in childhood. Again, invasion of cells by micrometer objects such as bacteria involves large-scale membrane deformation.

Most of the natural phospholipids are asymmetric with one saturated and one unsaturated chain. We studied oleic acid (OA, C18:1) as a control and docosahexaenoic acid (DHA, C22:6) as a represent for PUFA in this project. OA is the most abundant unsaturated FA, and DHA is the most polyunsaturated FA containing 22 carbons and 6 double bonds starting from the ω 3 (n3) position. By comparing the effects of OA and DHA on these two

pathways of bacterial invasion, we thought to uncover the role of PUPIL in large scale membrane deformations induced by bacteria toxins.

Chapter 4 Materials and Methods

4.1 Reagents

LifeAct-GFP-pCMV plasmid was purchased from Ibidi. GFP-Actin expressing plasmid was clone previously in the lab using pCMV-RFP-actin (E. Fuchs, The Rockefeller University, New York) as template (Boyer et al., 2006). The desired fragment was digested with XhoI-ApaI and ligated into pEGFP-C1. Antibodies used in this study were mouse anti-Na⁺/K⁺ ATPase (Santa Cruz), Annexin II (BD Transduction Laboratories), Calregulin (Santa Cruz), ERGIC 54 (Santa Cruz), and LAMP1 (BD Transduction Laboratories), and sheep anti-TGN46 (BioRad). Secondary Alexa Fluor-conjugated antibodies were from ThermoFisher and secondary peroxidase-conjugated antibodies were from Jackson ImmunoResearch. For immunofluorescence, hoechst 33342 and Alexa-fluor conjugated phalloidin were purchased from ThermoFisher. For STED imaging, Star635-phalloidin was purchased from Abberior. C3 toxin was purified as described (Boyer et al., 2006) by our colleague, Camille Morel (Institut Pasteur, CNRS-UMR2001).

OA and DHA fatty acids (Sigma-Aldrich) were conjugated with fatty acid-free BSA (Sigma-Aldrich). Fatty acids were dissolved in warm (60°C) 200 mM NaOH and conjugated with BSA at the molar ratio of 5:1. The FA-BSA was aliquoted and filled with argon to minimalized oxidation. Lipoprotein depleted serum (LPDS) were prepared as described (Renaud et al., 1982). Fetal bovine serum was loaded with NaBr to increase density to 1.21 g/ml followed by ultracentrifugation at 220,000g at 10°C for 48 hours in a Beckman Ti70 rotor. After centrifugation, a greasy layer containing lipoproteins appeared on the top of the tube was removed and the subnatant was centrifuged again at 220,000g at 10°C for 24 hours to remove the remaining lipoprotein. Later the serum was dialyzed intensively with Earle buffer (115 mM NaCl, 5.4 mM KCl, 1.8 mM CaCl₂, 0.8 mM MgSO₄, 5 mM Hepes, pH 7.4) in 14 kD cut-off dialysis membrane (Spectrum) for 72 hours and the buffer was refreshed for at least 5 times.

4.2 Cell Culture, treatments, and transfection

HUVEC were isolated from umbilical cords collected at Hospital l'Archet (Nice, France) as described (Baudin et al., 2007). In brief, umbilical cords were rinsed with HBSS followed by injection and incubation with 0.325 g/L collagenase for 30 minutes. Later, HUVECs were collected by centrifugation and incubated with Endothelial growth medium-2 (Lonza) supplemented with SingleQuots growth factors (Lonza). Cells were washed and supplemented with fresh medium until confluent, when the cells were frozen in medium containing 50% FBS

and 10% DMSO. For routine uses, HUVEC were culture in Human Endothelial SFM (Gibco) supplemented with 20% FBS, 20 ng/ml FGF (PeproTech), 10 ng/ml EGF (PeproTech), 1 µg/ml Heparin (Sigma-Aldrich), and Zellshield (Minerva-Biolabs) in a humid incubator at 37°C supplied with 5% CO₂. Electroporation was used for DNA transfection in HUVEC as described (Doye et al., 2006). HUVEC cells were trypsinized and suspended in Ingenio Solution (Mirus) containing the target DHA DNA (10 g per 10⁶ cells) in a 4-mm cuvette (CellProjects). Then, cells were electroporated at 300 V, 450 µF, one pulse by GenePulser electroporator (BioRad).

To enriched HUVECs with OA or DHA, cells were washed twice with PBS and lipid starved in LPDS medium (Human endothelial SFM, 20% LPDS, 20 ng/ml FGF, 10 ng/ml EGF, 1 µg/ml Heparin, and Zellshield) overnight with or without 50 µg/ml C3 toxin as indicated. Before experiments, cells were supplemented with 125 µM FA-BSA for 6 hr.

4.3 Lipid extraction and lipidomic analysis

Lipidomic analysis were performed in mass spectrometry platform in IPMC by Lucile Fleuriot. A modified Bligh and Dyer (Bligh and Dyer, 1959) was used for lipid extraction. The cell pellet from 1 million cells was collected in an eppendorf and 200 µL of water was added. After vortexing (30s), the sample was transferred in a glass tube containing 500 µL of methanol and 250 µL of chloroform. The mixture was vortexed for 30s and centrifuged (2500 rpm, 4°C, 10 minutes). Then, 300 µL of the organic phase was collected in a new glass tube and dried under a stream of nitrogen. The dried extract was resuspended in 60 µL of methanol/chloroform 1:1 (v/v) and transferred in an injection vial. The extraction protocol for purified cell pellet is the same as the one aforementioned in which every volume is divided by two.

Reverse phase liquid chromatography was selected for separation with an UPLC system (Ultimate 3000, ThermoFisher). Lipid extracts were separated on an Accucore C18 150x2.1, 2.5µm column (ThermoFisher) operated at 400 µl/ minutes flow rate. The injection volume was 3 µL. Eluent solutions were ACN/H₂O 50/50 (V/V) containing 10mM ammonium formate and 0.1% formic acid (solvent A) and IPA/ACN/H₂O 88/10/2 (V/V) containing 2mM ammonium formate and 0.02% formic acid (solvent B). The step gradient of elution was in %B: 0.0 minutes, 35%; 4.0 minutes, 60%; 8.0 minutes, 70%; 16.0 minutes, 85%; 25.0 minutes, 97%. The UPLC system was coupled with a Q-exactive Mass Spectrometer (thermofisher, CA); equipped with a heated electrospray ionization (HESI) probe. This spectrometer was controlled by Xcalibur software and operated in electrospray positive mode.

Data were acquired with dd-MS2 mode at a resolution of 70 000 for MS and 35 000 for MS2 (200 m/z) and a normalized collision energy (NCE) of 25 and 30 eV. Data were

reprocessed using Lipid Search 4.1.16 (ThermoFisher). The product search mode was used and the identification was based on the accurate mass of precursor ions and MS2 spectral pattern.

Due to the lack of internal standards, relative quantification was performed to compare the ratio of lipids species in each lipid class. The obtained mass peak area was normalized to the sum of total peak areas within each lipid class to calculate the relative ratio of different lipid species. To compare the fold change of lipid classes in different treatment, the sums of each lipid class were normalized to the sum of all the phospholipids, considering the total quantity of phospholipids should be constant regardless of the treatments. Then, this ratio was normalized to that of the control condition (FBS-treated or OA-treated as indicated). The GPMV enrichment was calculated by normalizing this ratio to that of total cell membrane.

4.4 Video microscope

HUVECs were electroporated with LifeAct-GFP-pCMV as described above and seeded on gelatin coated polymer coverslip dish (Ibidi). After recovering for 24 hours from transfection, cells were lipid starved as in LPDS containing medium overnight. OA-BSA and DHA-BSA were added to the cells to the final concentration at 125 μ M for 6 hours prior to video recording. Cells were supplemented with 25 mM HEPES (pH 7.4) and recorded on a 37°C heated stage of Nikon Ti inverted microscope using Ultraview spinning disk confocal system (Perkin Elmer). For the TEM opening, images were taken every 10 seconds for 1 hour. For TEM closure, images were taken every minute for 3 hour to avoid phototoxicity and bleaching during the acquisition. Acquired videos were analyzed by an ICY based automatic protocol. Acquired videos were analyzed by an ICY based automatic protocol.

4.5 GPMV purification

Cells were enriched with OA or DHA as described above followed by induction of GPMV as described (Sezgin et al., 2012). Cells were washed with GPMV buffer (10 mM HEPES, 150 mM NaCl, 2 mM CaCl₂, pH 7.4) twice and incubated with GPMV buffer containing 25 mM PFA and 2 mM DTT for 1 hour. Blebs were formed and released as GPMVs. Supernatant was collected and centrifuged at 100 g for 5 minutes to remove cell debris. Supernatant containing GPMVs was centrifuged in Beckman Type 70 Ti rotor at 20,000 g at 4 °C for 1 hr. GPMVs appeared as a transparent pellet and was collected for lipidomic analysis or western blot. For western blot, GPMV was lysed in Leammli buffer (50 mM Tris pH 7.4, EDTA 5mM, 2% SDS) and protein concentration was determined with BCA assay kit (Thermo Fisher) using BSA suspended in Leammli buffer as standard. GPMV lysate was adjusted to the

same protein quantity. Glycerol, β -mercaptoethanol, and bromophenol blue were added to final concentration of 10%, 5% and 0.004%. Protein samples were analyzed by SDS-PAGE western blot.

4.6 Super-resolution stimulated emission depletion (STED) microscopy

Cells were grown on H1.5 glass coverslips coated with 10 μ g/ml fibronectin. After treatment, cells were fixed with 4% PFA/0.1% glutaraldehyde for 15 minutes at room temperature. Cells were washed with PBS, quenched in 50 mM NH_4Cl for 15 minutes followed by permeabilizing in IF buffer (PBS/0.05% saponin/0.2 % BSA) for 30 minutes. Later, the cells were stained with 1 μ M Star635-phalloidin (Abberior) for 1 hr followed by 3 washes with IF buffer for 5 minutes and a final wash in H_2O . The cells were mounted in Mount Solid Antifade (Abberior) following manufacturer's instruction. Stimulated Emission Depletion (STED) imaging was performed by TCS STED SP8 (Leica) using a APO 93X/1.3 motCORR lens. The excitation laser was at 633 nm and pulse depletion laser at 775 nm. STED images were deconvolved using Huygens with 5 iterations.

4.7 Atomic force microscope measurement of TEM topology

AFM experiments were performed by our collaborator Sébastien JANEL from Institut Pasteur, Lille. AFM were carried out on a JPK NanoWizardIII mounted on a Zeiss Axio Observer.Z1. For elasticity measurements PFQNM-LC-A-Cal cantilevers (Bruker) were used with the SNAP calibration method. The AFM was operated in QI mode on the cytoplasmic region of living cells to record a 10 μm^2 , 20x20 pixels map of force curves with 2 μ m ramp length, 200 pN force trigger and 50 $\mu\text{m/s}$ tip velocity. Force maps were computed using in-house software (pyAF) for the fitting of the indentation up to 40 nm using Hertz model. For height measurements of TEMs Olympus AC40 cantilevers were used with the SADER calibration method. A QI map of 150x150 pixels bigger than the size of the TEM was recorded on formalin-fixed cells with an 800-nm ramp and 100 $\mu\text{m/s}$ tip velocity. We then computed the zero-force topography by determining the point of contact, and drew several profiles across the TEM to measure its diameter and the height of the cell at the border. This was all performed on the JPK analysis software.

4.8 ExPEC invasion

ExPEC invasion assay was performed as described (Doye et al., 2002). In brief, HUVECs were seeded on 12-well plates, lipid starved, and enriched with OA or BSA as described above except

DMEM medium was used instead of human endothelial SFM. After 4 hours of FA enrichment, cells were treated with 10^{-9} M CNF1 for 2.5 hr. ExPEC (strain UT189) was then added to the cells at the ratio of 100:1 and internalization were facilitated by centrifuging at 1000g for 20 minutes followed by incubation at 37°C for 10 minutes. For UPEC attachment, cells were washed intensively 3 times with PBS and lysed in PBS/0.1% triton to release the bacteria. ExPEC was cultured in serial dilution and counted for at least 3 dilutions on LB ampicillin 100 µg/ml plates. For entry, cells were treated with 50 µg/ml gentamycin for 30 minutes at 37°C followed by washed, lysed, and cultured of ExPEC on LB ampicillin 100 µg/ml plate.

4.9 Statistical analysis.

Data are showed as the medium \pm s.e.m. unless otherwise indicated. Data were analyzed with unpaired and two-tailed Mann-Whitney test unless otherwise indicated. P-value for *P<0.05, **P<0.01, ***P<0.001 and ****P<0.0001 were considered statistically significant. The statistical software used was Prism 8 (GraphPad Software, San Diego, CA, USA).

Chapter 5 Results

The acyl chains of PUPL are flexible and deformable, thereby adapting various conformations. In this thesis, we investigated the impact of higher membrane polyunsaturation on two bacterial invasion processes through inactivating Rho GTPases. The formation of TEM is driven by the reduced actomyosin contractility due to RhoA inhibition and stabilized by line tension contributed by cellular cytoskeleton. The invasion of ExPEC requires transient activation and subsequent degradation of Rho GTPase. Both processes involve large-scale membrane deformations in which PUPL might have an impact.

5.1 Modulating lipid profile of HUVEC

We began from asking whether primary human umbilical vein endothelial cells (HUVEC) constituted a good model to modulate acyl chains composition of PL such as PC, PE, and PS. Notably if HUVECs incorporate exogenous monounsaturated and polyunsaturated FA, such as OA and DHA, into PL as structural components of cellular membrane. OA contains 18 carbons and 1 double bond at ω 9 position and is the most abundant unsaturated FA in cellular membranes (Harayama and Riezman, 2018), thereby it was used as a control for FA enrichment. For highly unsaturated FA, we made use of DHA, which is a ω 3 FA containing 22 carbons and 6 double bonds.

5.1.1 Incorporation of DHA in total cell membranes

In culture medium, lipids are contributed from serum in which FA are stored as triacylglycerol in lipoprotein or as non-esterified FA in albumin. To enrich HUVECs with specific FA, we pre-cultured cells with lipoprotein-depleted serum (LPDS) for 16 hours to limit lipid intake from cells. Then, we supplemented cells with OA or DHA in complex with BSA (**Figure 5.1A**). Eventually, we analyzed the lipid profiles of cells by MS/MS in collaboration with IPMC lipidomic facility. We first examined the kinetics of FA incorporation at different time points. At the first hour, both OA and DHA were incorporated into cells as triacylglycerol (TG) (**Figure 5.1B**). This was consistent with the fact that excess of FA is stored in lipid droplet as triacylglycerol. Later on, exogenous FA gradually incorporated into PL, reaching a plateau for DHA in PC at 6 hours of incubation (**Figure 5.1C**). Notably, PC and PE were the two PL classes that were more susceptible to DHA enrichment with increase by 20% and 15%, respectively (**Figure 5.1 C-D**). On the contrary, DHA had modest incorporation in PS and PI by less than 5% (**Figure 5.1 E-F**). Owing to the fact that DHA incorporation in PC, the most

abundant PL in cellular membrane, reached a maximum at 6 hours (**Figure 5.1C**), we focused on comparing the cellular lipid profile at this time point.

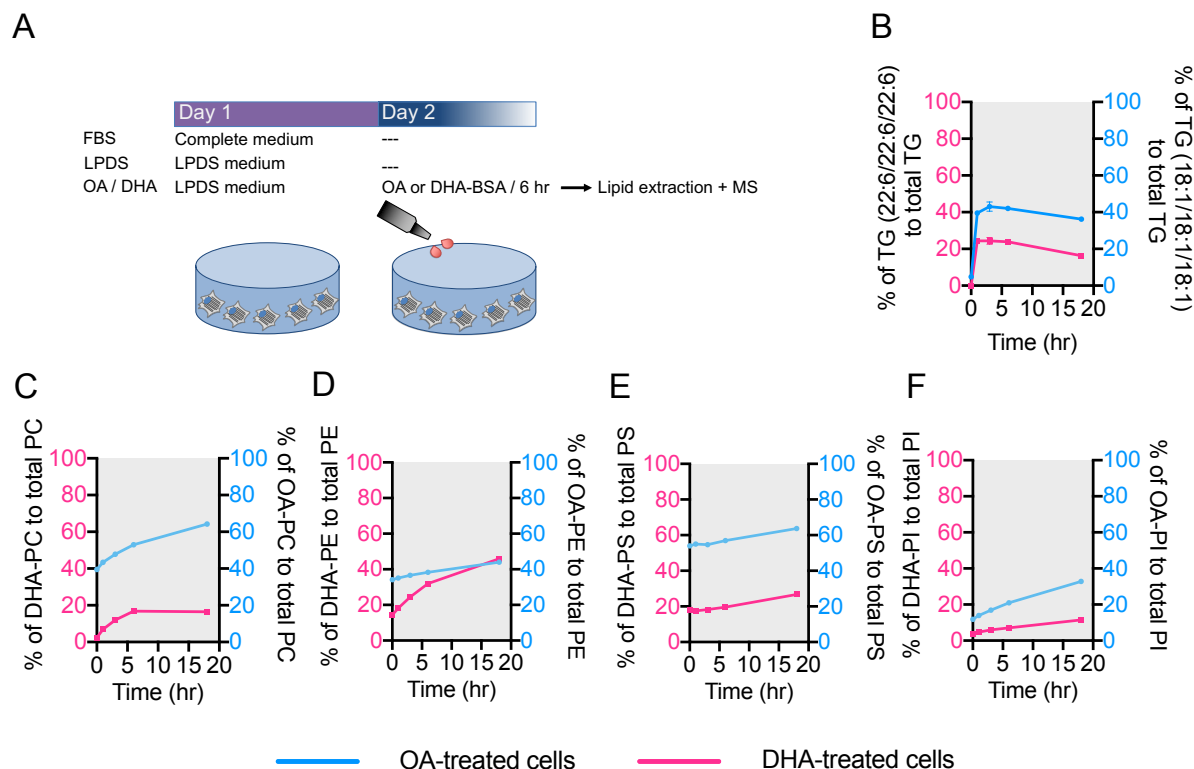


Figure 5.1. Kinetics of fatty acids incorporation in HUVECs. **(A)** Experimental workflow. HUVEC cells are grown in normal culture conditions (FBS), lipid-starved (LPDS), followed by enrichment with OA or DHA for 6 hours (OA- or DHA-treated) **(B)** The kinetics of FA incorporation into TG(18:1/18:1/18:1) in OA-treated cells (blue line) and FA incorporation into TG(22:6/22:6/22:6) in DHA-treated cells (pink line). **(C-F)** The kinetics of FA and incorporation into different lipid classes: phosphatidylcholine (PC, **C**), phosphatidylethanolamine (PE, **D**), phosphatidylserine (PS, **E**) and phosphatidylinositol (PI, **F**) during OA- or DHA-treatment. Data show means \pm SEM; $n=3$ / experiments; 3 experiments.

We compared the lipid profiles of HUVEC under different culture conditions, i.e. normal culture conditions (FBS), lipid-starved (LPDS), followed by enrichment with OA or DHA for 6 hours (OA- or DHA-treated). We first verified if the ratio of different PL classes varied between our culture conditions. To achieve this, we normalized the sum of each PL classes to the sum of all the PL to obtain the relative ratio of each PL classes. Then, we compared the relative abundance of each PL class between culture conditions by normalizing

them to that of FBS conditions. Except a 25% decrease in PE in DHA-treated cells, we observed no major difference in the ratio between PL classes in our culture conditions (**Figure 5.2A**).

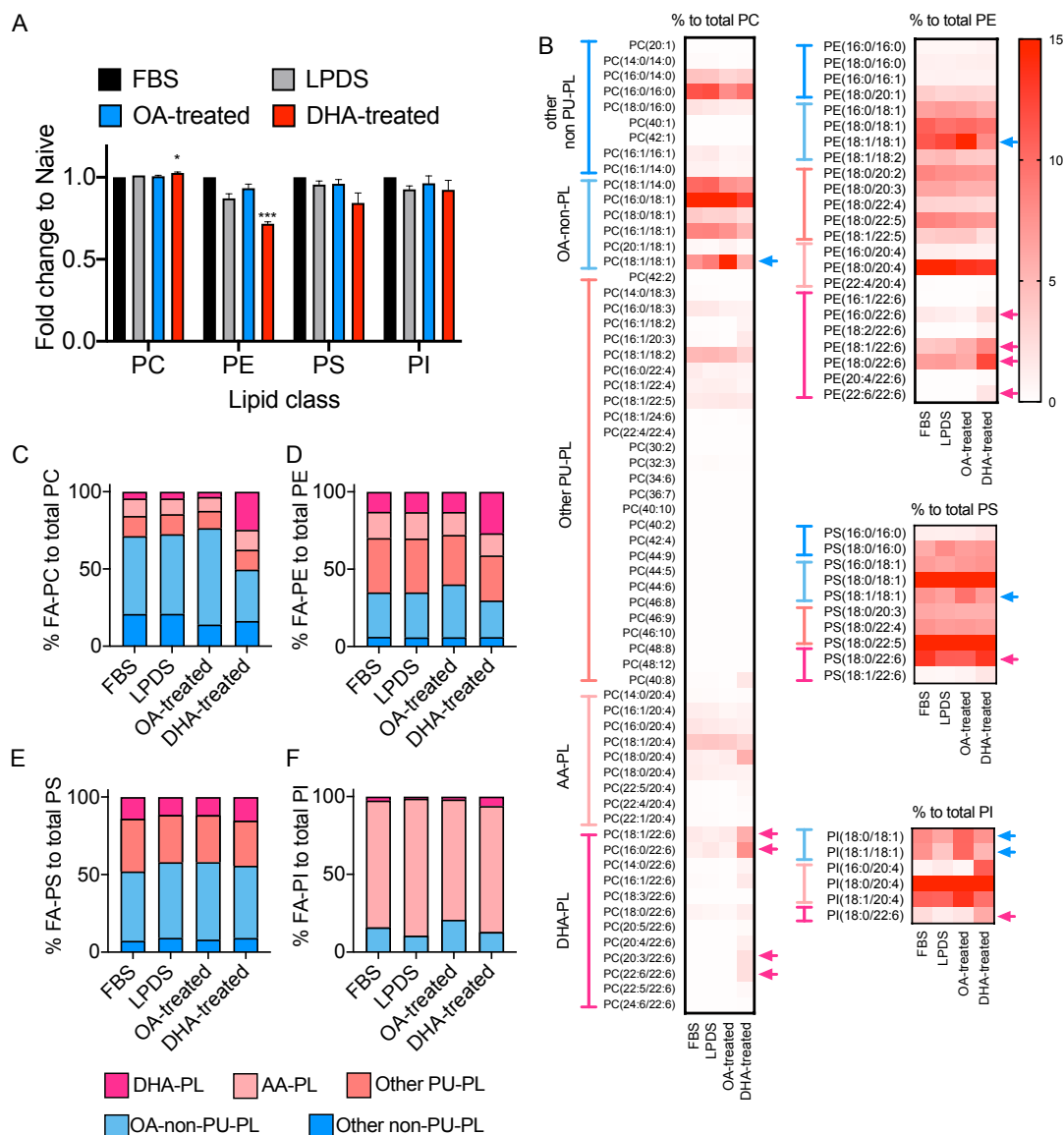


Figure 5.2. Analysis of phospholipids in HUVEC submitted to oleic acid (OA) versus docosahexaenoic acid (DHA). (A) Global fold change of phosphatidyl choline (PC), ethanolamine (PE), serine (PS) and inositol (PI) from HUVEC submitted to OA- or DHA-diet for 6 hours compared to FBS-cultured HUVEC. Two-way ANOVA was used to analyze the significance between each condition to FBS control. Data were significant with $*p < 0.05$ and $***p < 0.001$. (B) Lipidic profiles comparison of the different PL classes: PC, PE, PS and PI upon OA-diet or DHA-diet compared to controls (FBS and LPDS). Values were normalized individually to the sum of each PL classes. (C) PL species distribution regarding their number of double bonds (level of unsaturation): from zero to 6 double bonds as illustrated in Figure

5.2B. AA and DHA contain respectively 4 and 6 double bonds. LPDS, lipoprotein-depleted serum. (A-C) Data show means \pm SEM; $n > 3$ / experiments; 3 experiments.

We further analyzed all the PL species with various acyl chains compositions and calculated their relative abundance in each PL classes (**Figure 5.2B**). We noticed that the PL profiles of cells cultured in FBS and LPDS conditions were highly similar, indicating that lipid starvation with LPDS did not affect a specific PL species. Second, OA was often incorporated as symmetric PL containing two C18:1 chains, such as PC(18:1/18:1) and PE(18:1/18:1) (**Figure 5.2B**, blue arrow head). Interestingly, DHA was incorporated into a wide range of PL, most notably PC(16:0/22:6) and PE(18:0/22:6) (**Figure 5.2B**, pink arrow head). To evaluate the global FA incorporation in each PL classes, PL were divided according to their most unsaturated acyl chain, ranging from 0 to 6 double bonds as depicted in Figure 5.2B. Note that OA incorporated as PL containing 1 double bond while DHA incorporated as PL with 6 double bonds. Exogenous OA and DHA mainly incorporated into PC and PE. After DHA enrichment, DHA-PC increased greatly by 22 % at the expense of saturated or monounsaturated PC, mostly those that contained OA chain (**Figure 5.2C**). On the other hand, OA incorporation was less efficient, probably because OA-PL are already very abundant in HUVECs. Indeed, OA-PC increased by 11% at the expense of saturated PC (7%) and polyunsaturated PC (4%)(**Figure 5.2C**). As a consequence, the level of polyunsaturated PC remained similar between LPDS- and OA-treated cells at around 25% while it showed a 2-fold increase to 50% in DHA-treated cells. For PE, DHA-PE increased by 14% in DHA-treated cells while OA-PE increased by 5% in OA-treated cells, leading to 70% and 60% of polyunsaturated PE content respectively in the two FA diets (**Figure 5.2C**). On the contrary, exogenous DHA and OA barely incorporated as PS and PI (**Figure 5.2C**).

We concluded that OA-treated cells have a similar level of unsaturated PL to cells submitted to FBS and LPDS and constitute a better control than HUVECs submitted to sole lipid deprivation like LPDS condition. Further, our data show that HUVEC incorporates efficiently exogenous PUFA into PL in cellular membranes, thus is an excellent model for lipid research.

5.1.2 Incorporation of DHA at plasma membrane

We then wanted to confirm if the exogenously supplied FA could reach the plasma membrane. We produced Giant Plasma Membrane Vesicles (GPMVs) as a way to isolate plasma membrane. GPMVs are blebs formed at the plasma membrane by the action of

vesiculation reagents such as formaldehyde and DTT or N-ethylmaleimide (**Figure 5.3A**). GPMVs have been shown to share plasma membrane characteristics and are used commonly in lipid research (Sezgin et al., 2012). We verified that GPMV fraction was enriched in plasma membrane markers, Na⁺/K⁺ ATPase and Annexin V, while being devoid of markers of intracellular organelles (**Figure 5.3B**). Next, we performed MS/MS analysis of lipids extracted from GPMVs derived from OA- or DHA-treated cells. We normalized the relative ratio of each lipid classes in GPMVs to that of total cellular membranes, thereby getting a lipid enrichment index. GPMVs were enriched in SM and PS, the lipids that are known to be present in the plasma membrane, while been largely deprived of diacylglycerol and lysobisphosphatidic acid (LBPA), which are localized in ER and late endosomes (**Figure 5.3C**). We also observed a slight exclusion of PE from GPMV fractions, which was described as an artefact to be due to the cross-linking of PE with the membrane proteins (Levental et al., 2011). Therefore, lipid extraction efficiency for PE was reduced in GPMV fractions. This characterization confirmed that GPMVs are good representatives of plasma membrane compartment both in term of proteins and lipids.

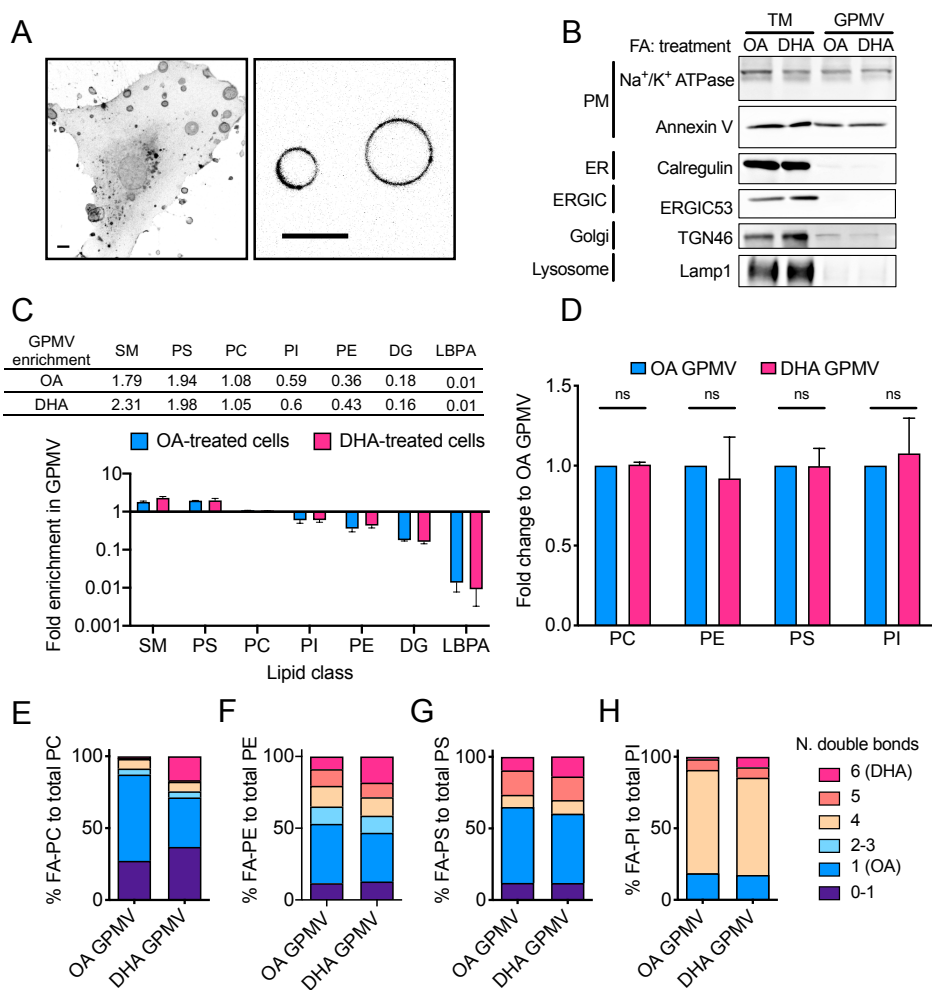


Figure 5.3. Lipidomic analysis of phospholipids from Giant Plasma Membrane Vesicle (GPMV). (A) 3D-projection of WGA-Alexa488 labeled GPMVs (left, arrow head) and FM4-64 labelled GPMVs (right) from HUVEC. Scale bars 10 μ m. (B) Western blot of total membrane (TM) and GPMV using different organelles markers. Plasma membrane (PM) marker: Na⁺/K⁺ ATPase and Annexin V, Endoplasmic reticulum (ER) marker: Calregulin, ER-Golgi intermediate compartment (ERGIC) marker: ERGIC53, Golgi complex marker: Trans-Golgi Network 46 (TGN46), Lysosome marker: Lysosomal-associated membrane protein 1 (LAMP1). (C) Lipidomic analyses of GPMVs from OA- or DHA-treated cells. Lipid classes enrichment in GPMVs is calculated by dividing the relative content of each lipid class in GPMVs by those of total membranes. Value bigger than 1 indicate that lipids are enriched in GPMVs, value smaller than 1 indicate that lipids are excluded from GPMVs. SM, sphingomyelin; PC, phosphatidylcholine; PE, phosphatidylethanolamine; PS, phosphatidylserine; PI, phosphatidylinositol; DG, diacylglycerol; LBPA, lysobisphosphatidic acid. (D) Fold change of different PL classes in DHA-treated cells compared with OA-treated cells. Data were analyzed with two-way ANOVA and no significance, ns, was found. (E-H) PL species distribution regarding their number of double bonds (level of unsaturation): from zero to 6 double bonds as illustrated in Figure 5.2C. AA and DHA contain respectively 4 and 6 double bonds. (C-E) Data show means \pm SEM; n>3 / experiments; 3 experiments.

We compared the relative quantity of each PL classes between OA- and DHA-treated cells. The ratio of all PL classes in the plasma membrane remained unchanged between OA- and DHA-treated cells (**Figure 5.3D**). To determine levels of incorporation of exogenously supplemented FA, we categorized PL of GPMVs by the number of double bonds in their FA chains as described above. Mirror to what we obtained from total cell membranes, DHA-treated cells displayed an elevated level of DHA-containing PC and PE but not PS and PI (**Figure 5.3E-H**). The quantity of DHA-PC was 10-fold higher in GPMVs of DHA-treated cells (17 %) as compared to OA-treated cells (1.6%)(**Figure 5.3E**). Likewise, quantity of DHA-PE was 2-fold higher in DHA-treated cells (18%) as compared to OA-treated cells (9%)(**Figure 5.3F**). Therefore, comparing the GPMVs from OA- or DHA-treated cells, level of polyunsaturated PC increased from 13% to 29% while polyunsaturated PE increased from 47% to 53% (**Figure 5.3E-F**). Here, we showed that exogenous supplementation of DHA in lipid starved cells is incorporated in PL of cellular membrane comprising plasma membrane.

5.1.3 Impact of Rho GTPases inhibition on FA incorporation

Our next goal was to challenge FA-enriched HUVEC with bacterial toxins, C3 or CNF1, which induce TEM formation and ExPEC invasion, respectively. The C3 exoenzyme and CNF1 toxin interfere with Rho signaling pathways and could potentially impact FA incorporation. Therefore, we first examined OA- and DHA-incorporation in C3 or CNF1 intoxicated cells. We found that the kinetics of either OA or DHA incorporation were similar between control and C3-treated HUVECs in all the PL classes (**Figure 5.4A-D**). As a consequence, the ratios of PL with various acyl chains in control cells C3-treated cells are comparable (**Figure 5.4E-F**). We further determined the lipid profile of cells subjected to CNF1 toxin which activates Rho GTPases. Cells treated with CNF1 presented similar acyl chains profiles than non-intoxicated cells (**Figure 5.4E-F**). We concluded that Rho GTPases-targeting C3 and CNF1 toxins have no effect on FA incorporation.

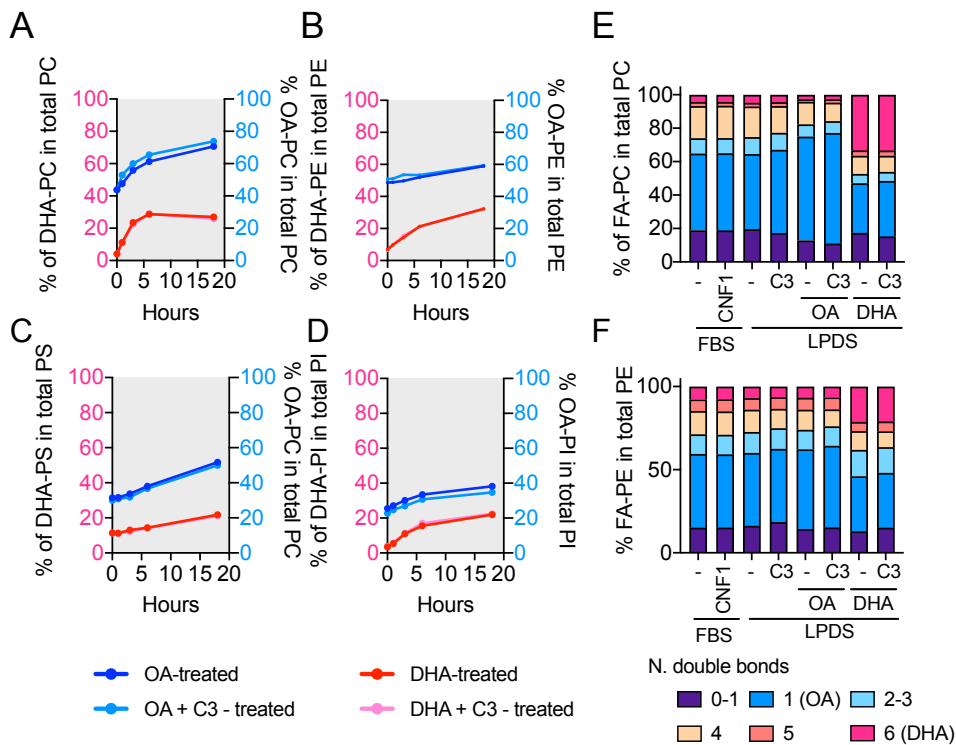


Figure 5.4. Impacts of C3 and CNF1 toxin on cellular lipidome. (**A-D**) The kinetics of DHA or OA incorporation into different lipid classes: PC, PE, PS, and PI in the absence or presence of C3 toxin. Data show means \pm SEM; $n > 3$ / experiments; 1 experiments. (**E-F**) PL species distribution regarding their number of double bonds (level of unsaturation): from zero to 6 double bonds as illustrated in Figure 5.2C. AA and DHA contain respectively 4 and 6 double bonds.

Here, we did a comprehensive lipidomic analysis of HUVEC cells subjected to different culture conditions. The exogenous OA and DHA incorporate first in triacylglycerols and are later found in PL, especially in PC and PE. HUVECs are more susceptible to incorporate PUFA than MUFA which is already quite abundant in the cell. Importantly, exogenous FA reach the plasma membrane. The DHA enrichment does not change the ratio between PL classes at the plasma membrane while it increases the unsaturation of acyl chains. Here, we show that HUVEC is an excellent cellular model for PL modulation. Furthermore, treatment of neither C3 nor CNF1 toxin affects the lipidome of cells.

5.2 DHA promotes the formation of TEMs but inhibits their enlargement

5.2.1 Impact of DHA on TEM in a fixed cell population

At this stage, we began to challenge the OA-enriched or DHA-enriched HUVEC with C3 toxin to induce TEM formation. We first confirmed, by immunofluorescence on fixed cells, that stress fibers were disrupted in C3-treated cells (**Figure 5.5 A**). Disruption of stress fibers indicated that cell contractility was reduced, thereby the cells spread. We thus measured the area of cells as quantitative parameter of cell spreading. Without C3 toxin, the size of OA- and DHA-treated cells were around $5000 \mu\text{m}^2$ with no significant difference (**Figure 5.5 B**). With the presence of C3 toxin, both OA- and DHA-treated cells spread 1.2-fold to $6000 \mu\text{m}^2$ at similar levels. Next, we quantified the percentage of cells with TEM at a fixed timing in both FA conditions. We observed that 25% of the C3-treated cells developed TEMs with no differences between OA- and DHA-treated cells (**Figure 5.5 C**). Interestingly, among this 25% of the TEM⁺ cells, DHA treatment slightly increased the number of TEMs per cell by 1.4-fold as compared to OA treatment, i.e. 3.5 ± 0.3 TEMs and 2.5 ± 0.1 TEMs per DHA- and OA-treated cells, respectively (**Figure 5.5 E**). Furthermore, the size of TEMs was 1.6-fold smaller in DHA-treated cells (median, $5.6 \mu\text{m}^2$; 95% CI, $5.1\text{-}6.4 \mu\text{m}^2$) as compared to OA-treated cells (median, $9.9 \mu\text{m}^2$; 95% CI, $8.4\text{-}12.2 \mu\text{m}^2$) (**Figure 5.5 F**). Therefore, we here establish that DHA-enrichment increases the density of TEMs in the cells while reducing their size. A complete summary of impacts of FA diet on TEM parameters is listed in **Table 4** and will be discussed in detail in the following section.

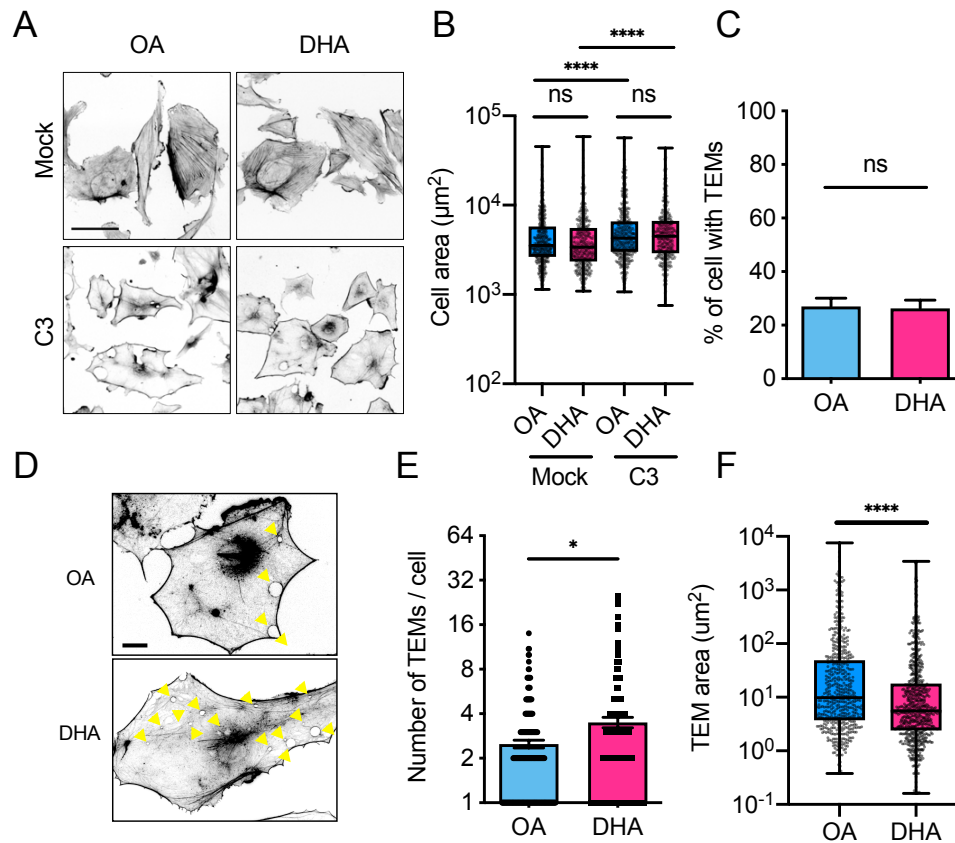


Figure 5.5. Impact of fatty acid diets on TEM parameters. (A-F) HUVEC are treated with C3 exoenzyme or without (mock) for 16 hours in prior to 6 hours of fatty acid diet (OA or DHA) as sole source of exogenously added lipids. (A) FITC-phalloidin staining of HUVEC in mock, OA or DHA conditions. Scale bar 100 µm. (B) Cell area of cells on OA- or DHA-diet. Data show median ± max to min from one experiment; cells > 450 / experiments; 2 experiments. (C) Percentage of HUVEC with at least one TEM in OA or DHA conditions. Data show means ± SEM; cells > 200 / experiments; 3 experiments. (D) Representative FITC-phalloidin staining of OA or DHA-treated cells intoxicated with C3 toxins. Scale bar 20 µm. (E) Number of TEMs per cell under OA- or DHA-diet. Data show median ± max to min of >100 cells from 2 independent experiments (> 50 cells/ experiment). (F) Graph shows median values of TEM area in fixed cells treated with either OA or DHA. Data show median ± max to min of > 450 TEMs from 3 independent experiments (>40 cells/ experiments). (B, C, E and F) Data were analyzed with nonparametric Mann-Whitney test and are significant with * $p < 0.05$, **** $p < 0.0001$ or not significant, ns.

Table 4. Effect of FA diet on TEM parameters

	OA	DHA	Statistics
Cell area (μm^2)	6330 \pm 271	6003 \pm 251	ns
Cell thickness (nm)	190 \pm 6	164 \pm 6	**
% of cells with TEMs	27 \pm 3	26 \pm 3	ns
Number of TEMs/cell	2.5 \pm 0.1	3.5 \pm 0.3	*
TEM frequency (TEMs/hour)	8.9 \pm 1.4	19.3 \pm 3.2	**
TEM max size (μm^2) ^a	37.4 (27.6-59.4)	25.4 (21.2-28.6)	*
Opening time (sec)	179 \pm 21	162 \pm 23	ns
Initial opening speed ($\mu\text{m}^2/\text{sec}$) ^a	0.47 (0.35-0.95)	0.39 (0.29-0.54)	ns
Late opening speed ($\mu\text{m}^2/\text{sec}$) ^a	0.38 (0.22-0.61)	0.27 (0.14-0.37)	*
Latency phase (min)	7.3 \pm 0.6	5.3 \pm 0.4	*
Closure time (min)	16.3 \pm 1.4	11.1 \pm 0.8	**
Closure speed ($\mu\text{m}^2/\text{sec}$) ^a	4.3 (3.4-6.1)	2.7 (2.1-3.3)	***
Life time (min)	42.0 \pm 4.0	24.6 \pm 1.8	***
Data show the means \pm SEM; data were analyzed by Mann-Whitney test			
^a data show the median (95% CI, upper-lower)			
ns, not significant; *p<0.05, **p<0.01, ****p<0.0001			

5.2.2 Impact of DHA on TEM opening dynamics

Considering that TEMs are dynamic structures, we thought to know if changing the unsaturation of membrane PL could have an impact on their kinetics. Using LifeAct-GFP as a probe, we were able to monitor the opening and closure of TEMs in live cells (**Figure 5.6A**). We recorded the TEM opening events in more than 20 cells (**Figure 5.6B**) and found that the frequency of TEM opening was 2-fold higher in DHA-treated cells (19.3 \pm 3.2 TEMs/hour) as compared to OA-treated cells (8.9 \pm 1.4 TEMs/hour)(**Figure 5.6C**). We further noticed that the turnover rate of TEM, i.e. the lifetime of a TEM from its opening to complete closure, was 2-fold shorter in DHA-treated cells (24.6 \pm 1.8 min) as compared to OA-treated cells (42.0 \pm 4.0 min) (**Figure 5.6D**). This established that DHA-enriched cells have a higher TEM opening frequency with shorter TEM lifetime and was in adequacy with higher number of TEMs in fixed DHA-treated cells. The number of TEMs in a cell should be the product of TEM lifetime and their opening frequency. Our data on reduced TEM lifetime explains the modest reduction in the number of TEMs in DHA treated cells while having high TEM opening frequency.

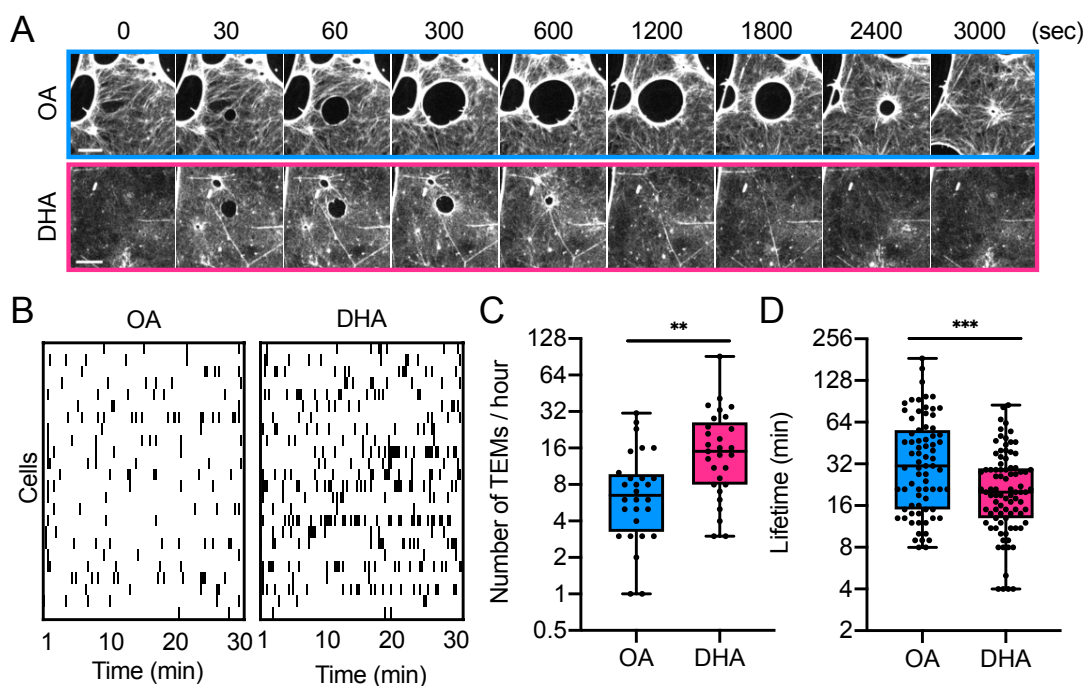


Figure 5.6. Impact of DHA enrichment on TEM opening frequency. (A) Time-lapse images of TEM opening dynamics in OA- or DHA-fed cells using LifeAct-GFP as label. Scale bars 10 μm . (B-C) Frequency of TEM opening events per cell in cells treated with ExoC3 and fed with either OA or DHA. (B) Each row on the Y-axis of the diagram pinpoints all the opening events of TEM in a single cell, each black bar is an individual opening event. (C) Graph shows total number of TEM opening events per cell in an hour. Data show are median \pm max to min; $n > 28$ cells from 28 independent experiments. (D) Graph shows the distribution of values of TEM opening lifetimes measured for each TEM. Data show are median \pm max to min, $n > 75$ TEMs from > 8 independent experiments. (C-D) Data were analyzed with nonparametric Mann-Whitney test and are significant with $**p < 0.01$ or $***p < 0.001$.

We then asked whether PUPL enrichment affects the kinetics of TEM opening. The opening of TEM is driven by the membrane tension due to the spreading of cells. We have described previously that the opening phase takes about two minutes (Maddugoda et al., 2011). Therefore, we recorded live cell images every 10 seconds using LifeAct-GFP to visualize TEMs (Figure 5.7A). We analyzed the size of TEM in our video recording using a custom-made Icy program developed by our collaborators, Stéphane Dallongeville, from the team of Jean-Christophe Olivo-Marin (UMR3691, Institut Pasteur, Paris) (Figure 5.7B). We measured the size of more than 70 TEMs and derived the evolution of TEM median size over time (Figure 5.7C). We noticed that 11% of the TEMs in OA-treated cells and 3% TEM in DHA treated

cells resumed their growth after the first stabilization to reach a second opening phase. Here we only discuss the opening of TEMs until their first stabilization and the secondary opening is discussed in the next chapter. The kinetics of TEM opening in OA- and DHA-treated cells showed great differences. First, we measured similar initial opening speed of TEM between 10-20 seconds after opening in OA- (median, $0.47 \mu\text{m}^2\text{s}^{-1}$; 95% CI, $0.35\text{-}0.95 \mu\text{m}^2\text{s}^{-1}$) and DHA-treated cells (median, $0.39 \mu\text{m}^2\text{s}^{-1}$; 95% CI, $0.29\text{-}0.54 \mu\text{m}^2\text{s}^{-1}$)(**Figure 5.7C and D**). However, later opening speed between 20-70 seconds was altered between TEMs from OA- and DHA-treated cells. The DHA diet (median, $0.27 \mu\text{m}^2\text{s}^{-1}$; 95% CI, $0.14\text{-}0.37 \mu\text{m}^2\text{s}^{-1}$) reduced the late opening speed by 1.4-fold as compared to OA diet (median, $0.38 \mu\text{m}^2\text{s}^{-1}$; 95% CI, $0.22\text{-}0.61 \mu\text{m}^2\text{s}^{-1}$)(**Figure 5.7E**).

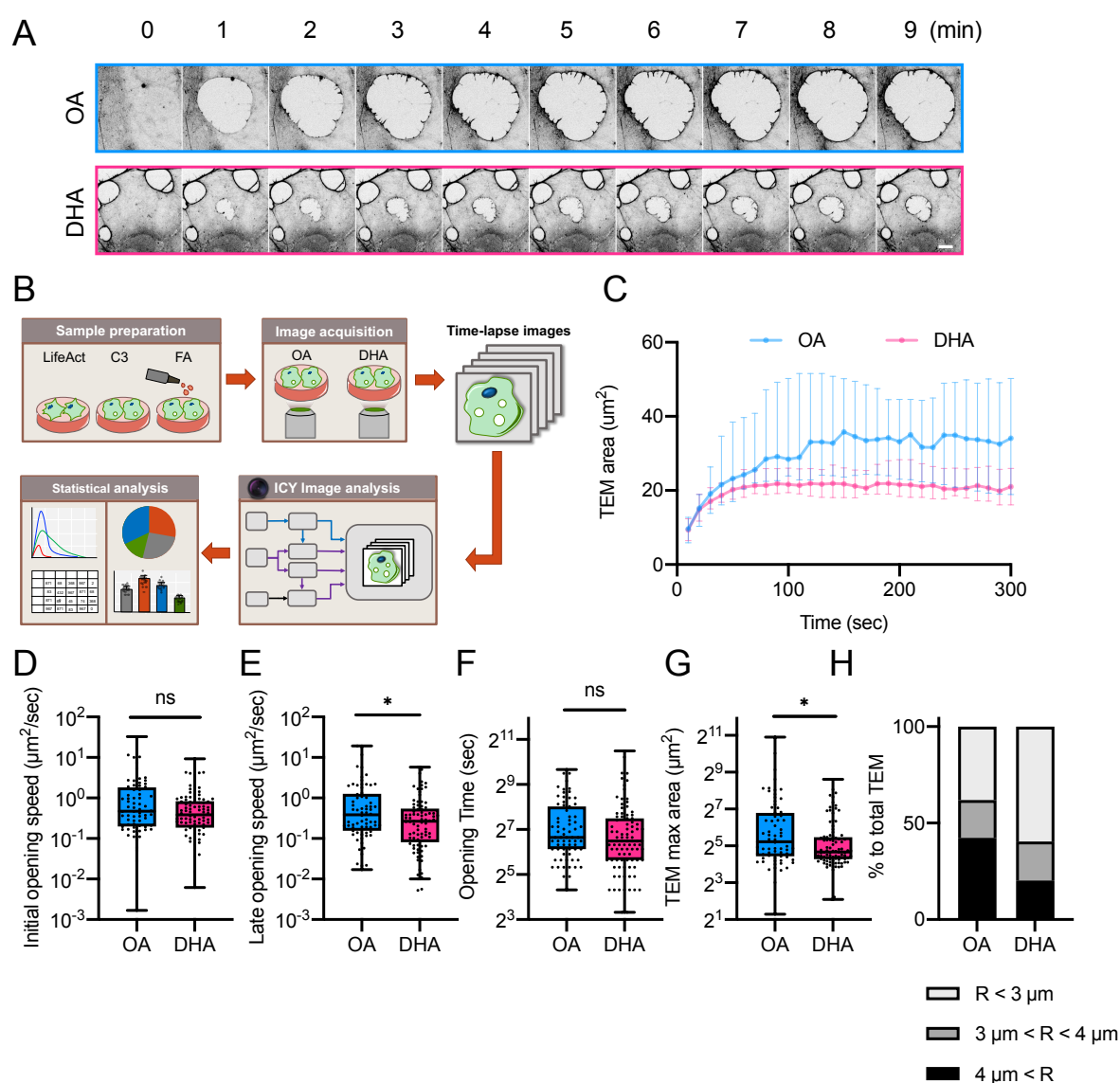


Figure 5.7. Impact of DHA enrichment on TEM opening parameters. (A) Time-lapse images of TEM opening dynamics in OA- or DHA-fed cells using *LifAct-GFP* as label. Scale bars $10 \mu\text{m}$.

(B) *Experimental workflow.* Cells were transfected with LifeAct-GFP, treated with LPDS and C3 toxin, followed by OA- or DHA-BSA diet for 6 hours. The dynamics of each TEM was recorded by spinning disk confocal microscope and was analyzed through custom made ICY-based protocol. **(C)** Graph shows the evolution of TEM median size \pm 95% CI. **(D)** Graph shows distribution of initial opening speed of TEM between 10-20 seconds. Data show median \pm max to min, $n > 68$ TEMs for each condition from 28 independent experiments. **(E)** Graph shows distribution of late opening speed of TEM between 20-70 seconds. Data show median \pm max to min, $n > 70$ TEMs for each condition from 28 independent experiments. **(F)** The opening time is the duration from which TEM opens until it reaches the 95% of maximum size. Data are median \pm max to min; $n > 71$ TEMs from 28 independent experiments. **(G)** The maximum size of TEM. Data are median \pm max to min; $n > 71$ TEMs from 28 independent experiments. **(H)** TEM maximum size was distributed in 3 classes: radius $< 3 \mu\text{m}$, $3 \mu\text{m} < \text{radius} < 4 \mu\text{m}$, radius $> 4 \mu\text{m}$. (D-G) Data are analyzed with nonparametric Mann-Whitney statistical test and are significant with $*p < 0.05$ or not significant, ns.

We have shown in the previous publication that the line tension increases as a function of time (Stefani et al., 2017), which is equivalent to the time required to build actin cables around TEM. Therefore, we analyzed for each TEM the duration to reach its maximum size in cells subjected to OA or DHA diets. The opening time was similar between OA- and DHA-treated cells (179 ± 21 sec vs 162 ± 23 sec) (**Figure 5.7F**). The maximum TEM area corresponds to the product of opening time by the speed. Since DHA-treated cells had slower opening speed, it should have smaller TEM size. Indeed, we measured that the maximum TEM area that was 1.5-fold smaller under DHA treatment (median, $25 \mu\text{m}^2$; 95% CI, $21\text{-}29 \mu\text{m}^2$) as compared to OA treatment (median, $37 \mu\text{m}^2$; 95% CI, $28\text{-}59 \mu\text{m}^2$) (**Figure 5.7G**). We categorized TEM by their maximum area and found that DHA-treated cells shifted by 20% to higher density of small TEMs (radius $< 3 \mu\text{m}$) at the expense of big ones (radius $> 4 \mu\text{m}$) as compared to OA-treated cells (**Figure 5.7H**). In conclusion, DHA enrichment shifts the dynamics of TEM, in which TEM opens at a lower speed and results in smaller TEM area. In addition, the time that is required to build the actin cables remains the same between OA- and DHA-treated cells.

5.2.3 Impact of DHA on TEM closure dynamics

We turned to the analysis of TEM closure kinetics in the presence of either OA and DHA-diets. To capture the entire cycle of TEM, we recorded time-lapses videos for 3 hours

(**Figure 5.8A**). We reduced interval to one image every minute to avoid photobleaching and phototoxicity. As described previously, TEMs are closed by two different mechanisms: lamellopodia-like membrane wave or purse-string actin bundle. We observed that 25% of TEMs closure involved membrane waves and 75% of TEMs closed by purse-string mechanism. No difference was observed between OA- or DHA-treated cells in terms of closure mechanism. To simplify the system, we analyzed TEM closure kinetics regardless of the closure mechanisms. We analyzed the closure of TEMs from their stabilization (90% of maximum size) to 20% size, period in which the slope corresponding to the speed of closure is linear (**Figure 5.8B**). Mirrored to the opening kinetics, TEMs from DHA-treated cells (median, $2.7 \mu\text{m}^2\text{min}^{-1}$; 95% CI $2.2\text{-}3.3 \mu\text{m}^2\text{min}^{-1}$) had 1.6-fold lower closure speed as compared to OA-treated cells (median, $4.3 \mu\text{m}^2\text{min}^{-1}$; 95% CI $3.4\text{-}6.1 \mu\text{m}^2\text{min}^{-1}$) (**Figure 5.8B**). Furthermore, the closure time was slightly but significantly shorter in DHA-treated cells ($11.1 \pm 0.8 \text{ min}$) as compared to OA-treated cells ($16.3 \pm 1.4 \text{ min}$) (**Figure 5.8C**). The parameters that we obtained for TEM closure dynamics matched perfectly to the observed TEM size in OA- and DHA-treated cells. The TEMs in DHA-treated cells are smaller and are closed with a slower speed in a reduced duration as compared to OA-treated cells.

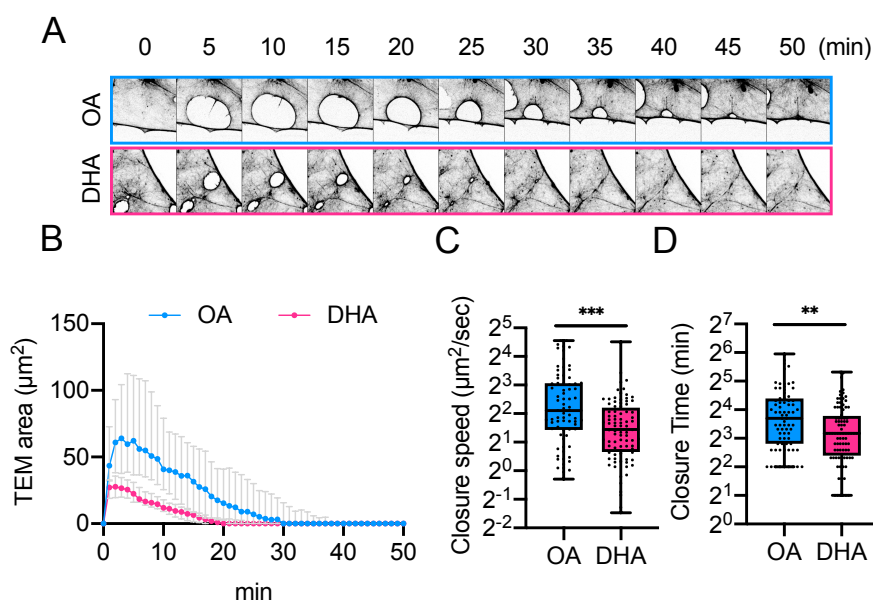


Figure 5.8. Impact of DHA enrichment on TEM closure parameters (A) Time-lapse images of TEM opening dynamics in OA- or DHA-fed cells using LifeAct-GFP as label. (B) Graph shows the evolution of TEM mean size \pm SEM. (C) The speed of TEM closing from 90% to 20% of the max size. Data are median \pm max to min; $n > 75$ TEMs from 8 independent experiments. (D) The time of TEM closing from 90% to 20% of the max size. Data are median \pm max to min; $n >$

75 TEMs from 8 independent experiments. (C-D) Data are analyzed with nonparametric Mann-Whitney statistical test and significant with $**p < 0.01$ and $***p < 0.001$.

5.2.4 Impact of DHA on TEM structures

Topology of TEM is an important criterion for recruiting proteins and membrane fusion. We showed TEMs are not a flat structure but have elevated rim at their borders (Maddugoda et al., 2011). Considering DHA membrane is more deformable, TEM might have different topology as compared to OA membrane. In collaboration with Sébastien Janel and Frank Lafont (UMR8204, Pasteur Institute, Lille), we measured the thickness of TEM borders with zero-force AFM. We chose specially TEMs at the very beginning of opening, i.e. before the formation of actin ring. At the initial stage of TEM opening, before actin is recruited, the height of the TEM border is dependent on the cortical active network: the cytosol and the plasma membrane. Later, F-actin accumulates at the TEM border as thick cables and contributes to TEM thickness. In DHA-enriched cells, the TEM border without actin was thinner as compared to OA-enriched cells (243 ± 14 nm vs 294 ± 14 nm) (**Figure 5.9A**). Meanwhile, the cell thickness at the periphery of TEM was also thinner in DHA-treated cells (164 ± 6 nm) as compared to OA (190 ± 6 nm) (**Figure 5.9B**), leading to a higher curvature at the TEM border. The curvature was 1.2-fold higher in DHA treated cells ($8.8 \pm 0.4 \mu\text{m}^{-1}$) as compared to OA-treated cells ($7.2 \pm 0.3 \mu\text{m}^{-1}$) (**Figure 5.9C**). Here, we show that, comparing to OA-enriched cells, DHA-enriched cells are thinner, generating a higher curvature at the TEM border.

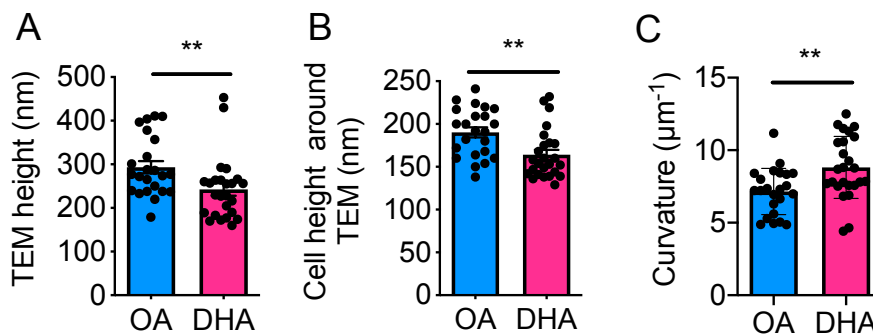


Figure 5.9. Impact of DHA enrichment on TEM topology. The cell thickness around TEM (A) and thickness of TEM border (B) were measured by AFM using zero-force topology. (C) Curvature around TEMs was calculated from TEM height. (A-C) Data show means \pm SEM; $n = 23$ TEMs. Data are analyzed with nonparametric Mann-Whitney statistical test and significant with $**p < 0.01$.

We conclude that, enrichment of cell with DHA-PL increases the frequency of TEM opening as compared to OA-enriched cells. However, TEMs open at a slower speed and reach a reduced maximal size upon DHA-diet. These smaller TEMs are closed at a slower speed during a shorter period of time. Finally, DHA enrichment shifts the shape of TEM to a thinner and more curved structure.

5.3 Potential impact of FA-diets on actin recruitment to TEM

5.3.1 A second phase of TEM opening: resuming opening

We noticed some of TEMs presented a secondary opening 103 seconds after their first stabilization, termed resume opening (**Figure 5.10A**). The resume opening began locally at a punctuate site of the TEM, leading to pear-shaped or multi-circular TEM (**Figure 5.10B**). This resume opening resembled our previous experiments when we severed the actin with laser (as discussed in chapter 3) (Stefani et al., 2017). We recorded the changes in TEM radius during resume growth in both OA- and DHA-treated cells (**Figure 5.10C-D**). However, OA- and DHA-treated cells were affected differently by resume growth. The population of TEM that develops resume opening was 4-fold less in DHA condition (3%) as compared to OA condition (11%) (**Figure 5.10F**). Second, the increment in TEM radius (ΔR) after the resume opening was smaller in DHA-treated cells ($1.5 \pm 0.5 \mu\text{m}$ versus $2.6 \pm 0.5 \mu\text{m}$) (**Figure 5.10G**). However, since TEMs from DHA-treated cells rarely resumed their opening, we did not obtain sufficient sample number for statistical analysis. Third, the resume opening speed was 2-fold slower in DHA-treated cells as compared to OA-treated cells with no statistical significance (**Figure 5.10H**). This was consistent with the opening kinetics showing that TEMs have slower opening speed in DHA-treated cells. Last, we have reported previously that ΔR was independent of the initial TEM radius (R_0) but a function of time (Stefani et al., 2017). Therefore, using laser to ablate TEM, we measured a constant increase in radius which was equal to $2 \mu\text{m}$. In OA-treated cells, the correlation in TEM radius before (R_0) and after (R_{eq}) the resume opening was linear with the trend that $R_{\text{eq}} = R_0 + 2.4 \mu\text{m}$. This fit perfectly with our laser ablation experiment. On the other hand, the correlation of radius in DHA-treated cells was $R_{\text{eq}} = R_0 + 1.1 \mu\text{m}$, suggesting that TEM resumed open to a lesser extent. In conclusion, in DHA-treated cells, there are limited population of TEMs undergo resume growth. Further, in DHA-enriched cells, TEM resumes its growth at a slower speed thereby it opens for a smaller size as compared to OA-treated cell

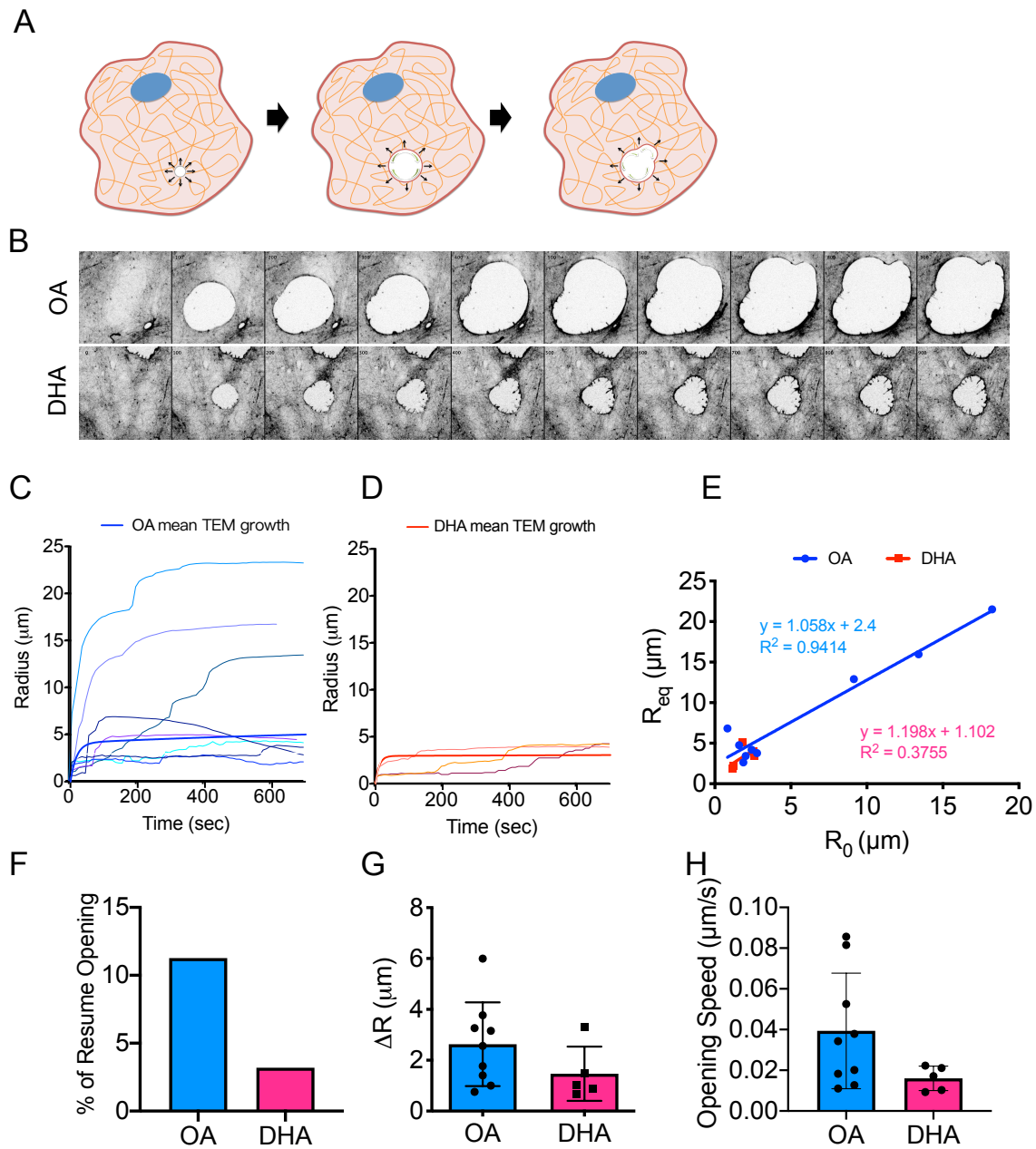


Figure 5.10. Resume opening shows instability of TEM. (A) Scheme of resume opening that TEM breaks locally and undergoes a second phase of opening (B) Time-lapse images of TEM resume opening dynamics in OA- or DHA-fed cells using LifeAct-GFP as label. (C-D) The evolution of TEM size over the period of recording in OA- (C) or DHA- (D) treated cells. (E) The correlation of TEM radius before (R_0) and after resume opening (R_{eq}) (F) The percentage TEM that undergo resume opening. Data show % of resume opening in all the recordings; $n > 71$ TEMs. (G) Graph show mean difference in TEM radius (ΔR) before and after resume opening. (H) The speed of resume opening. (G-H) Data show means \pm SEM; $n > 5$ TEMs.

We observed a limited population of TEM developing resume opening in DHA-treated cells. This might arise from two reasons: (1) the actin stabilizes faster in DHA-treated cells as compared to OA-treated cell (2) the driving force of TEM opening (membrane tension) is smaller in DHA-treated cells as compared to OA-treated cell. As we measured similar area of cells, which indicates the level of spreading should be similar, we assume the membrane tension comparable between the two diets. Therefore, we further tested if the building of line tension is different between OA- and DHA-enriched cells.

Actin structures around TEM

Using super-resolution stimulated emission depletion (STED) microscopy, we were able to observe different actin structures at nanometer scale in C3 intoxicated cells (**Figure 5.11A**). Importantly, there were a thick actin bundle encircled the perimeter of TEM and a lamellipodia-like actin network invaded the pore. The actin structures observed by super-resolution microscope were similar to what we have seen by electron microscopy (Stefani et al., 2017). After TEM opens, actin is recruited to the TEM edge and assemble as actomyosin cable to restrict TEM widening (as discussed in chapter 3). We tested whether the *de novo* actin recruitment is different between the FA treatments. Again, we used LifeAct-GFP as a probe for actin and acquired live-time images every 10 seconds (**Figure 5.11B**) to capture the actin recruitment during TEM opening. Actin was recruited to TEM in a halftime of 140 seconds with no differences between OA and DHA treatments (**Figure 5.11E**). Furthermore, we used florescence recovery after photobleaching (FRAP) to study the dynamic of existing actin cables around TEM. We bleached the entire actin ring and recorded the recovery of GFP-actin (**Figure 5.11C**). The turnover rate of actin cable around TEM was slow. Only 50% of actin was renewed after 300 seconds of recovery with no apparent difference between OA- and DHA-treated cells (**Figure 5.11F**). It was consistent with previous report that actin stress fiber is stable and had limited recovery after 300 seconds of bleaching (Hotulainen and Lappalainen, 2006). On the contrary, lamellipodia-like actin wave was highly dynamics with recovery halftime of 15s (**Figure 5.11D and G**). However, we did not observe differences in lamellipodia-like actin recovery between OA and DHA conditions. Therefore, we showed that the two actin structures around TEM have different dynamics. The actin cable is relatively stable with long turnover rate while the lamellipodia is dynamics with short turnover rate. However, PUPL enrichment does not affect the dynamics of neither actin structures.

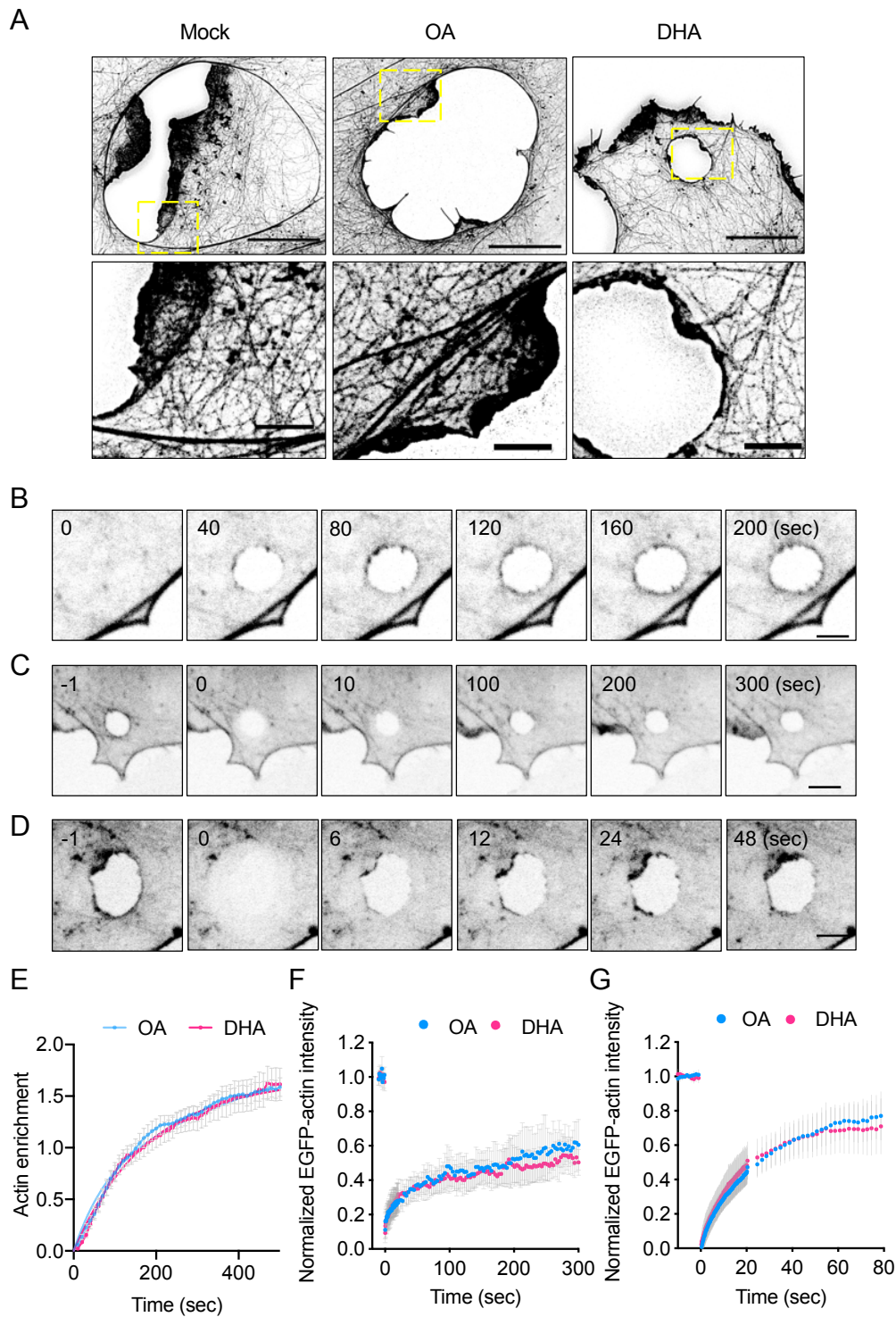


Figure 5.11. Impact of DHA enrichment on actin recruitment. (A) Super-resolution image of phalloidin staining in C3 intoxicated cells treated with OA or DHA. (B) The de novo recruitment of actin during TEM opening, Images show signal of LifeAct-GFP. (C-D) fluorescence recovery after photobleaching (FRAP) of GFP-actin around TEM. (E) The de novo recruitment of actin during TEM opening. Data are means \pm SEM; $n = 22$ TEMs (F) Recovery of actin cable around TEM after photobleaching. Actin signal around TEM are normalized to

prebleached state. Data are means \pm SEM; n = 5 TEMs (G) Recovery of lamellipodia-like actin network around TEM after photobleaching. Data are means \pm SEM; n = 10 TEMs.

The elasticity of the cells depends mainly on the actin cortex. We have previously shown that cell elasticity reduced in response to RhoA inhibition (Ng et al., 2017). To identify a potential impact of DHA enrichment on cortical elasticity, we measured the elasticity of cell subjected to different FA diets using AFM (**Figure 5.12A**). In the absence of toxin, we measured no difference in cell elasticity between OA- and DHA-treated cells (**Figure 5.12B and C**). In the presence of C3 toxin, the cell elasticity reduced 1.7-fold without significant difference between OA- and DHA-treated cells (**Figure 5.12C**). Here we showed that, HUVEC cells enriched in PUPPL does not affect the actin, including actin recruitment to TEM, the stability of actin ring around TEMs, and the elasticity of actin cortex.

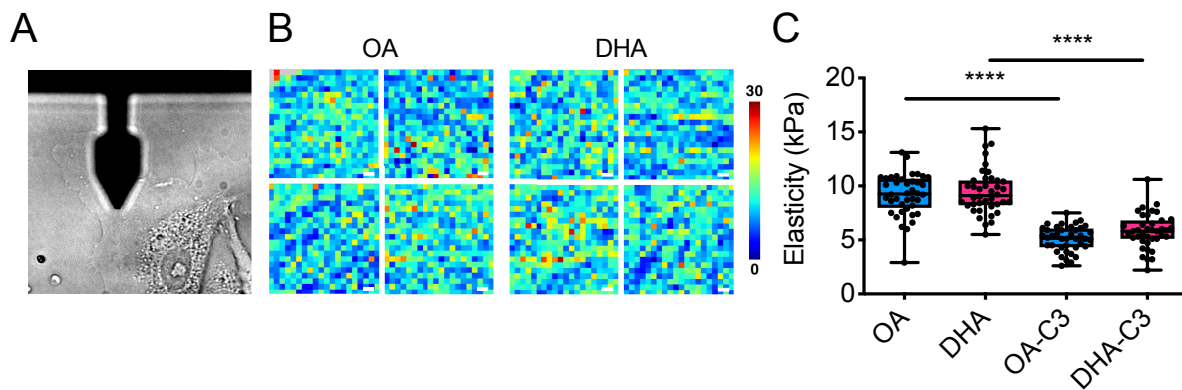


Figure 5.12. *Impact of DHA enrichment on cell elasticity. (A) Cell elasticity was measured by scanning the OA- and DHA-treated cells with 200 pN force by AFM. (B) Heatmap of cell elasticity on OA- and DHA-treated cells. Each square corresponds to area of 10 μm^2 from individual cells. (C) Cell elasticity measured by AFM. Data are means \pm SEM; n = 40 TEM from 3 independent experiments. Data are analyzed with one-way ANOVA and significant with **** $p < 0.0001$.*

5.4 DHA-enrichment reduced the invasion of ExPEC

To expand our study to a broader aspect of bacteria invasion, we investigated another bacterial invasion process that also perturbed Rho GTPases of host cell: the invasion of extra-intestinal pathogenic *E.coli* (ExPEC). The invasion of ExPEC is another example of how bacteria hijacks the Rho GTPase. The invasion of ExPEC is highly promoted by CNF1 toxin which activates Rho GTPases, resulting in their activation and subsequent proteasomal degradation. I collaborated with my colleague, Serena Petracchini (Pasteur Institute, Paris), to study the invasion of ExPEC using gentamicin protection assay. The principle of this assay is that gentamicin kills only the extracellular bacteria but not the internalized ones. Therefore, the bacteria that is resistant to gentamicin is the internalized population (**Figure 5.13A**). We pretreated HUVEC cells with OA- or DHA-diet followed by CNF1 prior incubating with bacteria for 30 minutes. Then, the extracellular bacteria were killed with gentamicin (**Figure 5.13B**). We obtained similar level of bacteria attached on host cells treated with OA and DHA (**Figure 5.13C**). This ruled out any possible impact of the diets on bacteria-host receptor recognition. The invasion of ExPEC was limited in the absence of CNF1 toxin. We did not detect significant difference between OA- and DHA-enriched cells in the absence of CNF1. However, ExPEC invasion was greatly promoted by CNF1. In this condition, we observed a 2.6-fold reduce in ExPEC invasion in DHA-treated cells as compared to OA-treated cells (**Figure 5.13D**). One possibility is that DHA inhibits the actions of CNF1, thereby reduces bacteria entry. We verified that the CNF1-mediated Rac1 degradation by proteasome was similar between the OA- and DHA-treated cells (**Figure 5.13E**). Therefore, comparing to OA treatment, DHA enrichment does not affect the susceptibility to CNF1 toxin nor the recognition of ExPEC to cellular receptor. However, the invasion processes of ExPEC was largely reduced when cells were enriched with DHA.

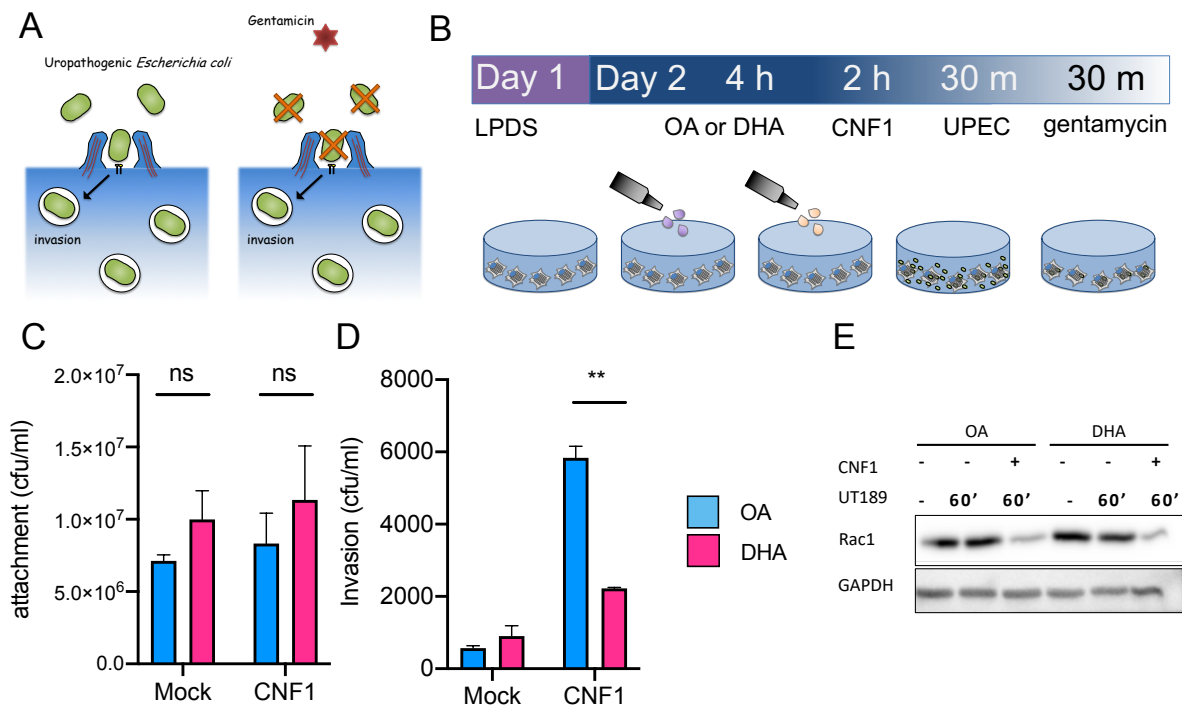


Figure 5.13. Impact of DHA enrichment on ExPEC invasion. (A) Measuring the ExPEC invasion by gentamicin protection assay. (B) Workflow of gentamicin protection assay. (C) The attachment of ExPEC to cell surface after 30 min of incubation. (D) The invasion of ExPEC into HUVEC measured by gentamicin protection assay. (C-D) Data are means \pm SEM from 1 experiment was shown out of 2 independent experiments; $n = 3$ replicates. Data are analyzed with student t test and significant with $**p < 0.01$ or not significant, ns. (E) Western blot of cells subjected to CNF1 followed by ExPEC (strain UT189) incubation. The degradation of Rac1 is confirmed with specific antibody.

Chapter 6 Discussion

We find that HUVEC is an excellent model for increasing DHA acyl chain content of phospholipids without affecting the respective ratio of phospholipid classes in the plasma membrane. HUVEC uptakes efficiently PUFA supplemented in the medium and incorporated them into phospholipids of cellular membranes, notably plasma membrane. Under such conditions, we are able to investigate the impact of DHA enrichment on the dynamics of formation of TEMs, tunnels that induced by a RhoA inhibitory toxin from bacteria. DHA-enriched cells have higher capacity to form TEMs compared to OA enrichment, *i.e.* higher frequency of TEM opening, which can be explained by the shorter distance between the apical and basal membrane (**Figure 6.1**). DHA has a facilitating effect on membrane fusion to nucleate TEMs probably due to a more proximal distance between the apical and basal membrane. This novel effect on membrane fusion provides interesting property for DHA in addition to its previously established role in facilitating membrane fission triggered by dynamin and endophilin (Pinot et al., 2014). Further, we observed a homeostatic mechanism from the cells to counteract high TEM nucleation rate in DHA-treated cells to prevent bursting. Though, TEMs open at higher frequency in DHA-enriched cells, they are more transient and smaller in size as compared to OA-enriched cells, leading to the same total TEMs area in both conditions.

Interestingly, the curvature around TEM is higher in DHA-treated cells. Membrane curvature might be determinant for the recruitment of curvature sensor proteins. However, we did not observe any apparent change in actin recruitment, dynamics, nor cell elasticity. Though, a potential impact of DHA on protein recruitment at early stage of TEM opening cannot be excluded, since TEMs in DHA-enriched cells have more stable opening. At the end, the small TEMs in DHA-enriched cell close at a slower speed but over a shorter period of time given the smaller size of TEMs.

We expand our finding on TEM formation to another bacterial invasion process that involves modulation of Rho family GTPase activities: the invasion of ExPEC. The invasion process of ExPEC is a strategy of bacteria to escape from medical treatments, *i.e.* antibiotics. Cells enriched with DHA are more resistant to ExPEC invasion. Though we lack molecular mechanism linking the change from membrane polyunsaturation to the macropinocytic-like invasive process of ExPEC. Our result shows interestingly that changing the diet of lipids could shift the susceptibility of endothelial cells against pathogenic bacteria.

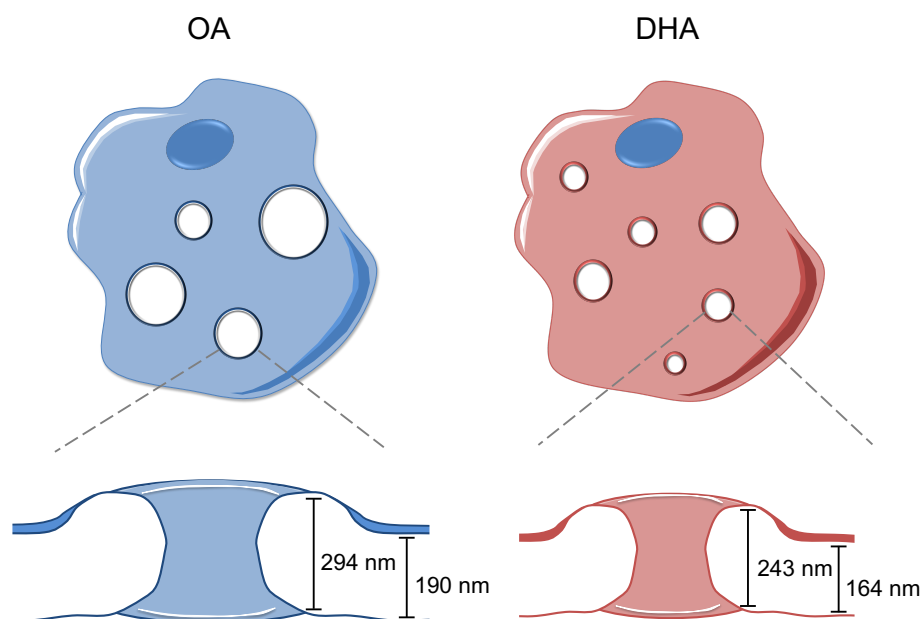


Figure 6.1. Summary of TEM formation in OA- and DHA-treated cells. TEMs in DHA-treated cells are numerous but smaller. DHA-treated cells have thinner cell and TEM border. In addition, TEMs in DHA-treated cells are more transient than in OA-treated cells.

6.1 Where do the lipids go?

Exogenous FA complexed to the protein carrier, BSA, are taken up by cells via passive diffusion across plasma membrane or via transporters, such as CD36. Once internalized, FA are converted into acyl-CoA by long-chain acyl-CoA synthetases (ACSLs), which locate mainly in ER and mitochondria (Mashek and Coleman, 2006). Later, the acyl-CoA is esterified to PL or triacylglycerol by acyltransferases, which mainly locate in ER. The triacylglycerol is stored in lipid droplets, which form rapidly after addition of exogenous FA (Rohwedder et al., 2014). In our case, triacylglycerol formed and reached a plateau within 1 hour of incubation with FA in HUVEC (**Figure 5.1**). On the other hand, acyl-CoA is also used to build PL, and then transported to various organelles via ER-membrane contact sites or vesicular trafficking. We have shown here that exogenous DHA can be found at the end in the PL of the plasma membrane. The increase in PUPL and DHA-PL in total membrane and GPMV are listed in **Table 5**. Furthermore, inhibition of RhoA does not interfere with the incorporation of exogenous fatty acids in PL, indicating that the entire process of PL metabolism is independent from RhoA.

Table 5 Increase in PL (%) compared to OA-treated cells

	PUPL		DHA-PL	
	TM	GPMV	TM	GPMV
PC	27	16	23	15
PE	10	6	14	9
PS	2	5	4	5
PI	8	1	4	6

*TM, total membrane; GPMV, giant plasma membrane vesicle; PC, phosphatidylcholine; PE, phosphatidylethanolamine; PS, phosphatidylserine; PI, phosphatidylinositol.

Here we performed relative quantification of lipid profiles using MS/MS, in which we analyzed the relative abundance of each PL class separately. Without standards to quantify properly each species, we were not able to obtain the ratio between PL classes, considering MS are more sensitive to PC than other PL. However, based on our preliminary thin layer chromatography data that the total membranes in HUVEC are composed of 38%, 46%, 9%, and 7% of PC, PE, PS, and PI respectively. Using this ratio, we can estimate that DHA-treatment increases the level of DHA-PL from 9% to 24% in total membranes. In addition, based on the published ratio of PL classes in mammalian cell plasma membrane, we can roughly assume that DHA treatment increases the level of DHA-PL from 6 to 16% at the plasma membrane (Lorent et al., 2020; Lorizate et al., 2013; van Meer et al., 2008). This estimation is comparable to the 8% increase when incubating leukocyte with 20 μ M of BSA-DHA for 4 days (Levental et al., 2016) while we incubated endothelial cells with 125 μ M BSA-DHA for 6 hours.

The next question is: do the PUPL locate in the outer or inner leaflet? Our lipidomic data of GPMV could not distinguish lipids between the two leaflets. Even if we could have digested the outer leaflets of GPMV with PLA or sphingomyelinase, it was reported that GPMV lost its lipid asymmetric and was scrambled (Lorizate et al., 2013). We can only estimate roughly the location of PUPL on plasma membrane based on the PL composition of each leaflet established in erythrocyte (Lorent et al., 2020). Though this ratio might vary between cell types, majority of PC in erythrocyte is in the outer leaflet and large majority of PE and PS are in the inner leaflet. In our system DHA incorporates mainly in PC and PE. Therefore, we assume that the exogenous PUPL reaches both leaflets of the plasma membrane. This reasoning of plasma membrane asymmetry will be important to understand the topology of TEM that we will discuss in the next chapter.

6.2 How does the TEM inducing toxin enter cells?

EDIN can enter passively into cells after secretion by *S. aureus* and get released into phagocytic vacuoles containing the bacterium (Molinari et al., 2006). In the second scenario, *S. aureus* first attaches to the host cells and enters into endosome like vacuoles. This may foster the delivery of toxin into the cell cytosol by preventing it from dilution in the medium.

C3 exoenzyme (ExoC3) has been referred as a RhoA inhibitor for decades. Incubation with high concentration of C3 (μM) for long period of time (12-24 hours) is required to induce morphological changes. C3 lacks known ligand recognition domain/motifs, thus little is known about how it enters cells except it is through a clathrin-, actin-, cholesterol-independent but dynamin dependent pathway (Rohrbeck and Just, 2017). Our team has shown that DHA promotes dynamin-dependent endocytosis (Pinot et al., 2014). However, in our experiments, we incubate C3 exotoxin 16 hours prior to DHA treatment. The C3 toxin has entered cells before fatty acid enrichment. Even if DHA promote the entry of toxin at late stage, it should have a promotive impact on either TEM formation or UPEC invasion, which is opposed to what we have observed. The fact that OA and DHA condition have the same percentage of cells displaying TEM and have no significant difference of actin cable disruptions indicate that both FA have no impact on C3 intoxication process. Furthermore, the level of intoxication can be verified by measuring RhoA ADP-ribosylation in the FA-treated conditions.

6.3 A possible effect from FA signaling?

The concentration of fatty acids in the serum is around $500 \mu\text{M}$ (Abdelmagid et al., 2015). Upon fish-oil supplementation, the level of $\omega 3$ -FA increases up to 10% of total FA in the serum (Lundström et al., 2013), i.e., $50 \mu\text{M}$. We used $125 \mu\text{M}$ of FA in complex with BSA at the ratio of 5:1, which is of the same order of the physiological condition.

As discussed in Chapter 1, FA could incorporate into PL as structural components of membrane or function as signaling molecules. In this study, we are not able to distinguish the two effects. However, signaling through FA occurs rapidly, for example within few seconds for ion channel modulations. Furthermore, we did not observe differences in TEM size between 1 and 3 hours after incubating with FA (data not shown). A control experiment for this study is to block the incorporation of DHA by downregulating acyltransferase during FA incubation. In this case, we will see solely the effect of FA as signaling molecule rather than structural

component of cellular membrane. Studies has shown that downregulation of acyltransferases expression reduced the level of certain PUPL in specific organs. LPAAT3 knockout mice has lower level of DHA-PL in testis and retina (Iizuka-Hishikawa et al., 2017; Shindou et al., 2017). LPAAT3 and LPAAT4 are the two acyltransferases that use C22:6 as a substrate (Eto et al., 2014; Yuki et al., 2009). In HUVEC cells, LPAAT3 expressed at much higher level than LPAAT4 (data not shown). We presume that LPAAT3 is the acyltransferase for incorporating C22:6 in HUVEC. When targeting LPAAT3 with siRNA in HUVEC cells, the mRNA level of LPAAT3 dramatically decreased but the total level of PUPL only reduced slightly (data not shown). We assumed this was a compensatory effect by other acyltransferases or a long turnover rate of the LPAAT3. For example, in LPAAT4 knockout mice, the expression of other acyltransferases increased. An alternative is to generate LPAAT3 knockout HUVEC by CRISPR, though HUVEC is not adapted for clonal selection due to its primary cell status. However, there are some strategies involving co-targeting enzymes with CRISPR that avoid the clonal selection thus shortens the CRISPR process (Liao et al., 2015). Another mirror experiment we can do for this study is to enrich the cells with PUPL by overexpression of acyltransferases. For example, overexpression of LPCAT1 increased the level of its enzymatic products (Morita et al., 2013). By such way, we can bypass the FA supplementation which flood the cells with specific FA. Anyway, a comprehensive analysis on signaling pathway upon FA enrichment could be done by western blot.

6.4 Membrane tension and the expansion of TEM

The opening of TEM requires fusion of the apical and basal membrane. The exact mechanism of membrane fusion and fission is still unclear, and it is possible that several mechanisms co-exist in cells depending on the proteins involved. The most accepted mechanism of membrane fusion is through an intermediate hemifusion stage, in which the two proximal leaflets merge locally (**Figure 6.2A**) and eventually form a pore of few nanometers in diameter. Hereafter, the pore has to expand to a size comparable to a vesicle or a cell, depending on the biological content, to complete the fusion process. In the case of cell-cell fusion, the pore expansion continues through the diameter of the cell (**Figure 6.2B**) (Kozlov and Chernomordik, 2015).

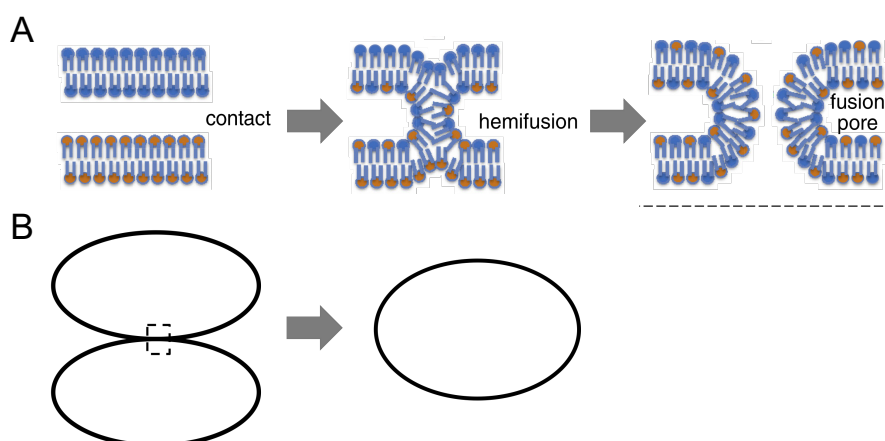


Figure 6.2. Mechanism of membrane fusion. (A) Membrane fusion occurs through a series of steps. First, the proximal leaflet from the two bilayers merge to form hemi-fusion structure. Then, the distal leaflets fuse to generate a pore at nanometer scale. (B) To complete the fusion process, for example cell fusion, the pore has to expand to the size of the cells. Illustration extracted from (Kozlov and Chernomordik, 2015).

Endothelial membrane fused in response to RhoA inhibitions that removes actomyosin cables between the apical and basal membranes. One can imagine that two membranes have higher chance to fuse as there are less objects (F-actin) in between. Further, in response to reduced actomyosin contractility, cells spread and result in a thinner cell thickness. Reduction in the distance between the two membranes also increases the probability for membrane to undulate and contact. Further, application of mechanical force that brings two membranes in contact is sufficient to trigger membrane fusion and TEM formation (Ng et al., 2017).

In our case, DHA supplementation increases the frequency of TEM opening, i.e. membrane fusion. We might either affect the formation of hemifusion intermediate or the expansion of pore. *In vitro*, dynamin and endophilin have higher GTPase activity on DHA-PL membranes, resulting in fission of liposomes. In cells, the dynamin-dependent endocytosis is increased by 8-fold in DHA-enriched cell (Pinot et al., 2014). However, the molecular mechanism of how DHA promotes fusion and fission events is still unclear. One can imagine that two flexible membrane in closer proximity will have higher chance to undulate and contact. Further, flexibility of the acyl chain might reduce the energy cost for bridging proximal leaflets to form hemifusion intermediate. To this end, it is very likely that DHA enrichment increases the chance of the initial membrane contact and fusion during TEM formation.

On the other hand, TEM has to expand from a nanometer pore to a larger size to be detected by our system. This process depends on the membrane tension that pulls the pore apart (Kozlov and Chernomordik, 2015). OA- and DHA-treated cells have comparable cell spreading. As spreading generates membrane tension for TEM extension, we assume that the membrane tension is comparable between OA and DHA condition. This assumption is strengthened by our observation that OA and DHA-treated cells have similar initial opening speed, which should be correlated to the pulling force. Therefore, we conclude that the second phase of membrane fusion (**Figure 6.2B**), i.e. the expansion of pores, should not be affected by DHA enrichment.

6.5 Global bending rigidity and opening of TEM

Our team showed that when pulling a nanotube from membrane with optical tweezers, OA membrane or DHA membrane have similar membrane tension. Nevertheless, the membrane bending rigidity is decreased by 4-fold in DHA membrane compared to OA membrane (Pinot et al., 2014). The opening of TEM is governed by physical forces around, including the bending rigidity of the membrane and the attached cortex. If the membrane is more deformable it requires less energy to bend a membrane rim during TEM opening. In our case, smaller bending rigidity of DHA membrane should have increased the size of TEM. Indeed, our collaborator David Gonzalez-Rodriguez (Université de Lorraine, Metz) modeled the evolution of TEM size in decreased membrane bending rigidity according to our physical model (**Figure 6.3**)(Gonzalez-Rodriguez et al., 2012). The size of TEM should increase by at least 2-fold when membrane bending rigidity is reduced to 4-fold. This prediction is complete opposite to the reduction of TEM the size observed experimentally. Therefore, we conclude there are factors other than membrane bending rigidity are affected in DHA-treated cells.

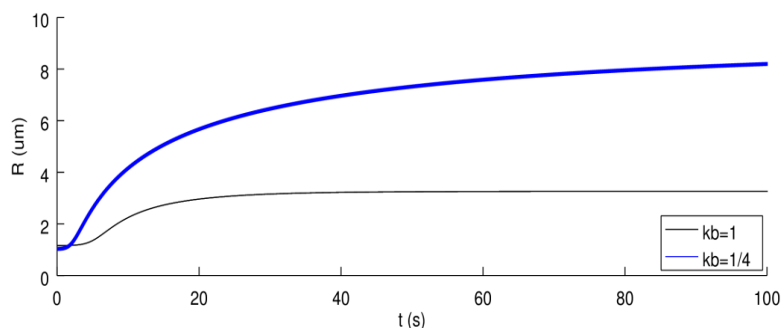


Figure 6.3. Mathematical modelling of TEM opening upon reducing membrane bending rigidity. The model is based on two cases with identical parameters except for the membrane

bending rigidity: $40 k_B T$ for the reference case (black lines) and $10 k_B T$ for the second case (blue line). The plot shows that the cell with a smaller membrane bending rigidity opens up to a larger radius, and continues opening up for a longer time. Illustrated by David Gonzalez-Rodriguez.

We should note that the bending rigidity in the two contexts is different. In the case of optical tweezer pulling tubes of nanometer scale from plasma membrane or GUV, the membrane bending rigidity is contributed solely from membrane due to the lack of actin structures in the tube. In the case, of TEM formation, the global bending rigidity corresponds to the energy cost to bend the matrix along TEM, including the membrane and the cortical actin network as seen by super-resolution microscopy (**Figure 5.11A**). As we measured similar cells elasticity, i.e. unaffected cortical actin, the bending rigidity contributed from cortex should be similar between OA- and DHA-treated cells. Importantly, the energy required to bend a membrane is at the scale of pN (Sandre et al., 1999) while energy exerted by stress fiber is at nN scale (Gonzalez-Rodriguez et al., 2012; Soiné et al., 2015; Stefani et al., 2017). The contribution of actin explained the unexpected results on TEM size upon reducing membrane bending rigidity.

We should notice that the membrane tension is released after TEM opens and the total cells surface reduces according to Helfrich's law (Gonzalez-Rodriguez et al., 2012; Helfrich, 1973). Considering there are multiple TEMs open simultaneously in a cell. The release of membrane tension corresponds to the sum of all the TEM area. This can be modeled by the equation 4 in Gonzalez-Rodriguez et al. We calculated the total TEM area in OA- and DHA-treated cells by multiplying number of TEMs in a cell by the median TEM size in fixed cells (Table 4). Interestingly, we obtained similar total TEM area in OA and DHA-treated cells, i.e. $24 \mu\text{m}^2$ for OA and $22 \mu\text{m}^2$ for DHA. This suggested a homeostatic mechanism in balancing the membrane tension by the formation of TEM.

Though we measured a 2-fold higher frequency in TEM opening, the increase in the number of TEMs per cells is modest (1.4 fold) in DHA-treated cell. This is explained by a shorter TEM cycle in DHA-treated cells, which compensates the increased TEM nucleation rate. Further, we observed a smaller TEM size, which further compensates the increased number of TEMs per cells. Eventually, the total area occupied by TEMs is similar between OA and DHA-treated cells. As membrane tension increases in response to toxin, TEMs open to release the tension. As DHA membrane favors TEMs nucleation at a higher frequency, tension is release more frequent and TEMs are not allowed to grow to a bigger size. In case of large

TEMs opening (OA condition), membrane tension is release so as less TEM are allowed to open. This is a homeostatic state regulated by the host cell to prevent tear force, due to high membrane tension, or to prevent cell bursting due to the excessive growing of TEMs (Rolando et al., 2009).

6.6 Topology of TEM

We showed that the thickness of TEM border is shorter in DHA-treated cells than OA-treated cells, resulting in 1.2-fold increase in negative membrane curvature along the z axis of TEM (**Figure 6.4A and B**). Interestingly, similar topology was also seen in MD simulations of tube pulling from OA- and DHA-membrane (Manni et al., 2018; Tiberti et al., 2020). The negative curvature at the base of the membrane tube (**Figure 6.4C and D**, arrow) shares similar topology to the negative curvature along the TEM z axis (**Figure 6.4A and B**, arrow). The curvature at the base of the tube is 1.8-fold smaller in DHA membrane than OA membrane (Tiberti et al., 2020). As discussed in chapter 2, membrane curvature could be a cue to attract proteins with curvature sensing motifs, such as BAR proteins and ALPS motifs. Depletion of I-BAR protein MIM leads to TEMs of bigger size indicating that it contributes, although is not essential, to the line tension that oppose membrane tension during the opening phase (Gonzalez-Rodriguez et al., 2012). We will discuss in the following some potential impact on proteins recruitments due to DHA enrichment.

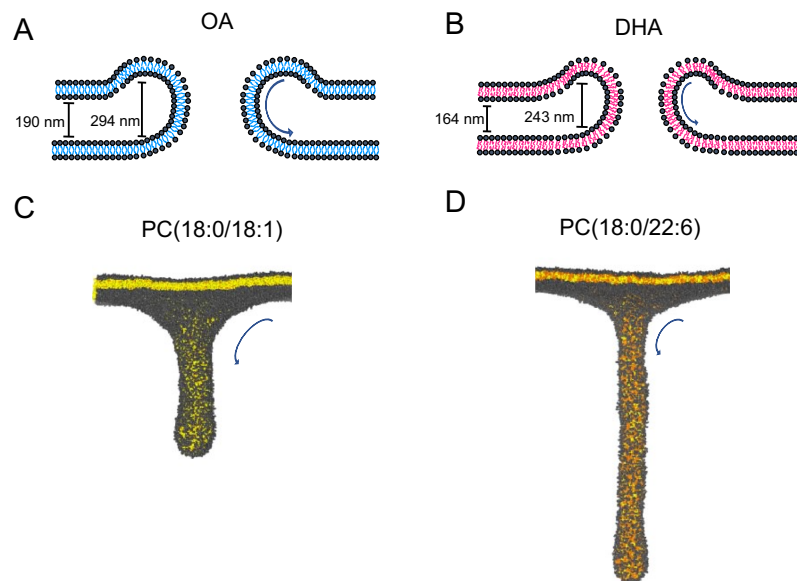


Figure 6.4. Topology of TEM and membrane tube in OA and DHA membrane. (A-B) Lateral view of TEM in OA and DHA-treated cells. The thickness of TEM are shorter in DHA condition

thus the membrane curvature (arrow) are higher. (C-D) MD simulations pulling membrane composed of either PC(18:0/18:1) or PC(18:0/22:6) with $200 \text{ KJ}\cdot\text{mol}^{-1}\text{nm}^{-1}$ force for 200 ns .

6.7 Line tension and stabilization of TEM

The line tension is built from the proteins that is recruited to encircle TEM. We calculated that the minimal line tension requires to stabilize a TEM is 300 pN (Stefani et al., 2017) while the tension generated by a stress fiber is at nN scale. Therefore, little amount of actin is sufficient to stabilize TEM. We showed the absence of detectable variation in actin recruitment between OA- and DHA-treated cells with various approaches using fluorescence microscope (**Figure 5.11**). However, there are some limitation in our experiments. First, we are not sure if the amount of actin that is sufficient to stabilize TEM widening is within the detectable range. Second, we are not sure if proteins upstream of actin are affected or not. For example, MIM recruitment to TEM edges can be visualized at 282 ms after its opening while actin is recruited in hundreds of seconds (**Figure 5.11F** and Maddugoda et. al.). MIM belongs to the I-BAR family but is capable of binding positively-curved membrane, owing to its amphipathic helix, thereby inducing tubules within GUVs. DHA facilitates the formation of positively curve membrane during membrane tubulation (Tiberti et al., 2020). Moreover, curved DHA membrane contains larger shallow packing defects which allow binding of membrane anchoring proteins (Pinot et al., 2014). Based on our AFM analysis, the TEM structure has higher negative curvature at the cytosolic surface in DHA-treated cells (**Figure 5.9**). We had tried to record the dynamics of MIM recruitment during TEM opening.

Furthermore, there are structural proteins other than actin that could be potential contributors for line tension. For example, the Septin family proteins polymerize as string and bundle. Septins family contains 4 subgroups. One proteins from each group is required to form octamer which further forms filaments. Septins has been shown to preferably bind to positive curvature of $2 \mu\text{m}^{-1}$ but is also capable of binding negative curvatures (Beber et al., 2019; Bridges et al., 2016). We found that Septins are recruited to the edge of TEM (data not shown). It would be interesting to test the kinetics of Septins recruitment to TEM in OA- or DHA-treated cells. However, one should note that overexpressed Septins in cells form insoluble aggregates. Septin filaments are stable structures with long turn over, thus the overexpressed Septins incorporate with only 50% endogenous Septins filaments after 3 days of expression (Sellin et al., 2011). Therefore, it is critical to generate stable cell line that expressed Septins at low level.

References

- Abdelmagid, S.A., S.E. Clarke, D.E. Nielsen, A. Badawi, A. El-Soheby, D.M. Mutch, and D.W.L. Ma. 2015. Comprehensive profiling of plasma fatty acid concentrations in young healthy Canadian adults. *PloS one*. 10:e0116195-e0116195.
- Abrami, L., S.H. Leppla, and F.G. van der Goot. 2006. Receptor palmitoylation and ubiquitination regulate anthrax toxin endocytosis. *Journal of Cell Biology*. 172:309-320.
- Adamson, P., H.F. Paterson, and A. Hall. 1992. Intracellular localization of the P21rho proteins. *The Journal of cell biology*. 119:617-627.
- Aktories, K., and I. Just. 2005. Clostridial Rho-Inhibiting Protein Toxins. In *Bacterial Virulence Factors and Rho GTPases*. P. Boquet and E. Lemichez, editors. Springer Berlin Heidelberg, Berlin, Heidelberg. 113-145.
- Amano, M., M. Ito, K. Kimura, Y. Fukata, K. Chihara, T. Nakano, Y. Matsuura, and K. Kaibuchi. 1996. Phosphorylation and Activation of Myosin by Rho-associated Kinase (Rho-kinase). *Journal of Biological Chemistry*. 271:20246-20249.
- Amerongen, G.P.v.N., C.M.L. Beckers, I.D. Achekar, S. Zeeman, R.J.P. Musters, and V.W.M.v. Hinsbergh. 2007. Involvement of Rho Kinase in Endothelial Barrier Maintenance. *Arteriosclerosis, Thrombosis, and Vascular Biology*. 27:2332-2339.
- Anderson, G.J., W.E. Connor, and J.D. Corliss. 1990. Docosahexaenoic Acid Is the Preferred Dietary n-3 Fatty Acid for the Development of the Brain and Retina. *Pediatric Research*. 27:89-97.
- Antony, B. 2011. Mechanisms of membrane curvature sensing. *Annu Rev Biochem*. 80:101-123.
- Antony, B., S. Vanni, H. Shindou, and T. Ferreira. 2015. From zero to six double bonds: phospholipid unsaturation and organelle function. *Trends in Cell Biology*. 25:427-436.
- Applegate, K.R., and J.A. Glomset. 1986. Computer-based modeling of the conformation and packing properties of docosahexaenoic acid. *Journal of Lipid Research*. 27:658-680.
- Bann, J.G. 2012. Anthrax toxin protective antigen--insights into molecular switching from prepore to pore. *Protein Sci*. 21:1-12.
- Barelli, H., and B. Antony. 2016. Lipid unsaturation and organelle dynamics. *Current Opinion in Cell Biology*. 41:25-32.
- Barry, D.M., K. Xu, S.M. Meadows, Y. Zheng, P.R. Norden, G.E. Davis, and O. Cleaver. 2015. Cdc42 is required for cytoskeletal support of endothelial cell adhesion during blood vessel formation in mice. *Development*. 142:3058.
- Baudin, B., A. Bruneel, N. Bosselut, and M. Vaubourdoille. 2007. A protocol for isolation and culture of human umbilical vein endothelial cells. *Nature Protocols*. 2:481-485.
- Bazinet, R.P., and S. Layé. 2014. Polyunsaturated fatty acids and their metabolites in brain function and disease. *Nature Reviews Neuroscience*. 15:771-785.
- Beber, A., C. Taveneau, M. Nania, F.-C. Tsai, A. Di Cicco, P. Bassereau, D. Lévy, J.T. Cabral, H. Isambert, S. Mangenot, and A. Bertin. 2019. Membrane reshaping by micrometric curvature sensitive septin filaments. *Nature Communications*. 10:420.
- Bishop, A.L., and A. Hall. 2000. Rho GTPases and their effector proteins. *Biochemical Journal*. 348:241-255.
- Bligh, E.G., and W.J. Dyer. 1959. A RAPID METHOD OF TOTAL LIPID EXTRACTION AND PURIFICATION. *Canadian Journal of Biochemistry and Physiology*. 37:911-917.

- Boland, L.M., M.M. Drzewiecki, G. Timoney, and E. Casey. 2009. Inhibitory effects of polyunsaturated fatty acids on Kv4/KChIP potassium channels. *American Journal of Physiology-Cell Physiology*. 296:C1003-C1014.
- Bos, J.L. 2005. Linking Rap to cell adhesion. *Current Opinion in Cell Biology*. 17:123-128.
- Boyer, L., A. Doye, M. Rolando, G. Flatau, P. Munro, P. Gounon, R. Clément, C. Pulcini, M.R. Popoff, A. Mettouchi, L. Landraud, O. Dussurget, and E. Lemichez. 2006. Induction of transient macroapertures in endothelial cells through RhoA inhibition by *Staphylococcus aureus* factors. *The Journal of Cell Biology*. 173:809-819.
- Bradley, R.M., D. Bloemberg, J.J. Aristizabal Henao, A. Hashemi, A.S. Mitchell, V.A. Fajardo, C. Bellissimo, E.B. Mardian, E. Bombardier, M.F. Paré, K.A. Moes, K.D. Stark, A.R. Tupling, J. Quadrilatero, and R.E. Duncan. 2018. Lpaat δ /Agpat4 deficiency impairs maximal force contractility in soleus and alters fibre type in extensor digitorum longus muscle. *Biochimica et biophysica acta. Molecular and cell biology of lipids*. 1863:700-711.
- Bradley, R.M., E.B. Mardian, D. Bloemberg, J.J. Aristizabal Henao, A.S. Mitchell, P.M. Marvyn, K.A. Moes, K.D. Stark, J. Quadrilatero, and R.E. Duncan. 2017. Mice Deficient in lysophosphatidic acid acyltransferase delta (Lpaat δ)/acylglycerophosphate acyltransferase 4 (Agpat4) Have Impaired Learning and Memory. *Molecular and Cellular Biology*. 37:e00245-00217.
- Bradley, R.M., P.M. Marvyn, J.J. Aristizabal Henao, E.B. Mardian, S. George, M.G. Aucoin, K.D. Stark, and R.E. Duncan. 2015. Acylglycerophosphate acyltransferase 4 (AGPAT4) is a mitochondrial lysophosphatidic acid acyltransferase that regulates brain phosphatidylcholine, phosphatidylethanolamine, and phosphatidylinositol levels. *Biochimica et Biophysica Acta (BBA) - Molecular and Cell Biology of Lipids*. 1851:1566-1576.
- Bridges, A.A., M.S. Jentsch, P.W. Oakes, P. Occhipinti, and A.S. Gladfelter. 2016. Micron-scale plasma membrane curvature is recognized by the septin cytoskeleton. *The Journal of Cell Biology*. 213:23.
- Cai, Y., O. Rossier, N.C. Gauthier, N. Biais, M.-A. Fardin, X. Zhang, L.W. Miller, B. Ladoux, V.W. Cornish, and M.P. Sheetz. 2010. Cytoskeletal coherence requires myosin-IIA contractility. *Journal of Cell Science*. 123:413-423.
- Caires, R., F.J. Sierra-Valdez, J.R.M. Millet, J.D. Herwig, E. Roan, V. Vásquez, and J.F. Cordero-Morales. 2017. Omega-3 Fatty Acids Modulate TRPV4 Function through Plasma Membrane Remodeling. *Cell Reports*. 21:246-258.
- Cao, J., D. Shan, T. Revett, D. Li, L. Wu, W. Liu, J.F. Tobin, and R.E. Gimeno. 2008. Molecular Identification of a Novel Mammalian Brain Isoform of Acyl-CoA:Lysophospholipid Acyltransferase with Prominent Ethanolamine Lysophospholipid Acylating Activity, LPEAT2. *Journal of Biological Chemistry*. 283:19049-19057.
- Chanaday, N.L., M.A. Cousin, I. Milosevic, S. Watanabe, and J.R. Morgan. 2019. The Synaptic Vesicle Cycle Revisited: New Insights into the Modes and Mechanisms. *The Journal of Neuroscience*. 39:8209-8216.
- Chesarone, M.A., A.G. DuPage, and B.L. Goode. 2010. Unleashing formins to remodel the actin and microtubule cytoskeletons. *Nature Reviews Molecular Cell Biology*. 11:62-74.
- Chyb, S., P. Raghu, and R.C. Hardie. 1999. Polyunsaturated fatty acids activate the *Drosophila* light-sensitive channels TRP and TRPL. *Nature*. 397:255-259.

- Connor, W.E., D.S. Lin, D.P. Wolf, and M. Alexander. 1998. Uneven distribution of desmosterol and docosahexaenoic acid in the heads and tails of monkey sperm. *Journal of Lipid Research*. 39:1404-1411.
- Cullere, X., S.K. Shaw, L. Andersson, J. Hirahashi, F.W. Luscinikas, and T.N. Mayadas. 2005. Regulation of vascular endothelial barrier function by Epac, a cAMP-activated exchange factor for Rap GTPase. *Blood*. 105:1950-1955.
- Cullis, P.R., and B. De Kruijff. 1979. Lipid polymorphism and the functional roles of lipids in biological membranes. *Biochimica et Biophysica Acta (BBA) - Reviews on Biomembranes*. 559:399-420.
- Czech, A., T. Yamaguchi, L. Bader, S. Linder, K. Kaminski, M. Sugai, and M. Aepfelbacher. 2001. Prevalence of Rho-Inactivating Epidermal Cell Differentiation Inhibitor Toxins in Clinical Staphylococcus aureus Isolates. *The Journal of Infectious Diseases*. 184:785-788.
- Doye, A., L. Boyer, A. Mettouchi, and E. Lemichez. 2006. Ubiquitin-Mediated Proteasomal Degradation of Rho Proteins by the CNF1 Toxin. *In Methods in Enzymology*. Vol. 406. Academic Press. 447-456.
- Doye, A., A. Mettouchi, G. Bossis, R. Clément, C. Buisson-Touati, G. Flatau, L. Gagnoux, M. Piechaczyk, P. Boquet, and E. Lemichez. 2002. CNF1 Exploits the Ubiquitin-Proteasome Machinery to Restrict Rho GTPase Activation for Bacterial Host Cell Invasion. *Cell*. 111:553-564.
- Drin, G., and B. Antonny. 2010. Amphipathic helices and membrane curvature. *FEBS Letters*. 584:1840-1847.
- Drin, G., J.-F. Casella, R. Gautier, T. Boehmer, T.U. Schwartz, and B. Antonny. 2007. A general amphipathic α -helical motif for sensing membrane curvature. *Nature Structural & Molecular Biology*. 14:138-146.
- Eggeling, C., C. Ringemann, R. Medda, G. Schwarzmann, K. Sandhoff, S. Polyakova, V.N. Belov, B. Hein, C. von Middendorff, A. Schönle, and S.W. Hell. 2009. Direct observation of the nanoscale dynamics of membrane lipids in a living cell. *Nature*. 457:1159-1162.
- Eldho, N.V., S.E. Feller, S. Tristram-Nagle, I.V. Polozov, and K. Gawrisch. 2003. Polyunsaturated docosahexaenoic vs docosapentaenoic acid differences in lipid matrix properties from the loss of one double bond. *Journal of the American Chemical Society*. 125:6409-6421.
- Elinder, F., and S. Liin. 2017. Actions and mechanisms of polyunsaturated fatty acids on voltage-gated ion channels. *Frontiers in Physiology*. 8.
- Etienne-Manneville, S., and A. Hall. 2002. Rho GTPases in cell biology. *Nature*. 420:629-635.
- Eto, D.S., T.A. Jones, J.L. Sundsbak, and M.A. Mulvey. 2007. Integrin-Mediated Host Cell Invasion by Type 1-Piliated Uropathogenic Escherichia coli. *PLOS Pathogens*. 3:e100.
- Eto, M., H. Shindou, and T. Shimizu. 2014. A novel lysophosphatidic acid acyltransferase enzyme (LPAAT4) with a possible role for incorporating docosahexaenoic acid into brain glycerophospholipids. *Biochemical and Biophysical Research Communications*. 443:718-724.
- Feller, S.E., K. Gawrisch, and A.D. MacKerell. 2002. Polyunsaturated Fatty Acids in Lipid Bilayers: Intrinsic and Environmental Contributions to Their Unique Physical Properties. *Journal of the American Chemical Society*. 124:318-326.

- Feller, S.E., K. Gawrisch, and T.B. Woolf. 2003. Rhodopsin Exhibits a Preference for Solvation by Polyunsaturated Docosohexaenoic Acid. *Journal of the American Chemical Society*. 125:4434-4435.
- Fernandes, F., L.M.S. Loura, F.J. Chichón, J.L. Carrascosa, A. Fedorov, and M. Prieto. 2008. Role of Helix 0 of the N-BAR Domain in Membrane Curvature Generation. *Biophysical Journal*. 94:3065-3073.
- Fievet, B.T., A. Gautreau, C. Roy, L. Del Maestro, P. Mangeat, D. Louvard, and M. Arpin. 2004. Phosphoinositide binding and phosphorylation act sequentially in the activation mechanism of ezrin. *Journal of Cell Biology*. 164:653-659.
- Foley, S., E. Miller, S. Braziel, and S. Lee. 2020. Molecular organization in mixed SOPC and SDPC model membranes: Water permeability studies of polyunsaturated lipid bilayers. *Biochimica et Biophysica Acta (BBA) - Biomembranes*. 1862:183365.
- Ford, M.G.J., I.G. Mills, B.J. Peter, Y. Vallis, G.J.K. Praefcke, P.R. Evans, and H.T. McMahon. 2002. Curvature of clathrin-coated pits driven by epsin. *Nature*. 419:361-366.
- Foxman, B. 2002. Epidemiology of urinary tract infections: incidence, morbidity, and economic costs. *The American Journal of Medicine*. 113:5-13.
- Frolov, V.A., A.V. Shnyrova, and J. Zimmerberg. 2011. Lipid polymorphisms and membrane shape. *Cold Spring Harbor perspectives in biology*. 3:a004747-a004747.
- Frost, A., R. Perera, A. Roux, K. Spasov, O. Destaing, E.H. Egelman, P. De Camilli, and V.M. Unger. 2008. Structural Basis of Membrane Invagination by F-BAR Domains. *Cell*. 132:807-817.
- Gasper, R., and F. Wittinghofer. 2019. The Ras switch in structural and historical perspective. *Biological chemistry*. 401:143-163.
- Gawrisch, K., O. Soubias, and M. Mihailescu. 2008. Insights from biophysical studies on the role of polyunsaturated fatty acids for function of G-protein coupled membrane receptors. *Prostaglandins, Leukotrienes and Essential Fatty Acids*. 79:131-134.
- Gerl, M.J., J.L. Sampaio, S. Urban, L. Kalvodova, J.-M. Verbavatz, B. Binnington, D. Lindemann, C.A. Lingwood, A. Shevchenko, C. Schroeder, and K. Simons. 2012. Quantitative analysis of the lipidomes of the influenza virus envelope and MDCK cell apical membrane. *The Journal of cell biology*. 196:213-221.
- Goley, E.D., and M.D. Welch. 2006. The ARP2/3 complex: an actin nucleator comes of age. *Nature Reviews Molecular Cell Biology*. 7:713-726.
- Gonzalez-Rodriguez, D., M.P. Maddugoda, C. Stefani, S. Janel, F. Lafont, D. Cuvelier, E. Lemichez, and F. Brochard-Wyart. 2012. Cellular Dewetting: Opening of Macroapertures in Endothelial Cells. *Physical Review Letters*. 108:218105.
- Guichard, A., S.M. McGillivray, B. Cruz-Moreno, N.M. van Sorge, V. Nizet, and E. Bier. 2010. Anthrax toxins cooperatively inhibit endocytic recycling by the Rab11/Sec15 exocyst. *Nature*. 467:854-858.
- Gunstone, F.D., J.L. Harwood, and A.J. Dijkstra. 2007. The lipid handbook with CD-ROM. CRC Press, Boca Raton, FL.
- Hakoshima, T., T. Shimizu, and R. Maesaki. 2003. Structural Basis of the Rho GTPase Signaling. *The Journal of Biochemistry*. 134:327-331.
- Hanna, S., and M. El-Sibai. 2013. Signaling networks of Rho GTPases in cell motility. *Cellular Signalling*. 25:1955-1961.
- Harayama, T., M. Eto, H. Shindou, Y. Kita, E. Otsubo, D. Hishikawa, S. Ishii, K. Sakimura, M. Mishina, and T. Shimizu. 2014. Lysophospholipid Acyltransferases Mediate

- Phosphatidylcholine Diversification to Achieve the Physical Properties Required In Vivo. *Cell Metabolism*. 20:295-305.
- Harayama, T., and H. Riezman. 2018. Understanding the diversity of membrane lipid composition. *Nature Reviews Molecular Cell Biology*. 19:281-296.
- Hardie, R.C., and K. Franze. 2012. Photomechanical responses in Drosophila photoreceptors. *Science*. 338:260-263.
- Hashidate-Yoshida, T., T. Harayama, D. Hishikawa, R. Morimoto, F. Hamano, S.M. Tokuoka, M. Eto, M. Tamura-Nakano, R. Yanobu-Takanashi, Y. Mukumoto, H. Kiyonari, T. Okamura, Y. Kita, H. Shindou, and T. Shimizu. 2015. Fatty acid remodeling by LPCAT3 enriches arachidonate in phospholipid membranes and regulates triglyceride transport. *eLife*. 4:e06328.
- Heasman, S.J., and A.J. Ridley. 2008. Mammalian Rho GTPases: new insights into their functions from in vivo studies. *Nature Reviews Molecular Cell Biology*. 9:690-701.
- Heemskerk, N., L. Schimmel, C. Oort, J. van Rijssel, T. Yin, B. Ma, J. van Unen, B. Pitter, S. Huvneers, J. Goedhart, Y. Wu, E. Montanez, A. Woodfin, and J.D. van Buul. 2016. F-actin-rich contractile endothelial pores prevent vascular leakage during leukocyte diapedesis through local RhoA signalling. *Nature Communications*. 7:10493.
- Helfrich, W. 1973. Elastic properties of lipid bilayers: theory and possible experiments. *Zeitschrift fur Naturforschung. Teil C: Biochemie, Biophysik, Biologie, Virologie*. 28:693-703.
- Henne, W.M., H.M. Kent, M.G.J. Ford, B.G. Hegde, O. Daumke, P.J.G. Butler, R. Mittal, R. Langen, P.R. Evans, and H.T. McMahon. 2007. Structure and Analysis of FCHO2 F-BAR Domain: A Dimerizing and Membrane Recruitment Module that Effects Membrane Curvature. *Structure*. 15:839-852.
- Hishikawa, D., H. Shindou, S. Kobayashi, H. Nakanishi, R. Taguchi, and T. Shimizu. 2008. Discovery of a lysophospholipid acyltransferase family essential for membrane asymmetry and diversity. *Proceedings of the National Academy of Sciences*. 105:2830-2835.
- Hodge, R.G., and A.J. Ridley. 2016. Regulating Rho GTPases and their regulators. *Nature Reviews Molecular Cell Biology*. 17:496-510.
- Hollenback, D., L. Bonham, L. Law, E. Rossnagle, L. Romero, H. Carew, C.K. Tompkins, D.W. Leung, J.W. Singer, and T. White. 2006. Substrate specificity of lysophosphatidic acid acyltransferase β —evidence from membrane and whole cell assays. *Journal of Lipid Research*. 47:593-604.
- Holte, L.L., S.A. Peter, T.M. Sinnwell, and K. Gawrisch. 1995. ^2H nuclear magnetic resonance order parameter profiles suggest a change of molecular shape for phosphatidylcholines containing a polyunsaturated acyl chain. *Biophysical Journal*. 68:2396-2403.
- Honoré, E., J. Barhanin, B. Attali, F. Lesage, and M. Lazdunski. 1994. External blockade of the major cardiac delayed-rectifier K^+ channel (Kv1.5) by polyunsaturated fatty acids. *Proceedings of the National Academy of Sciences*. 91:1937.
- Hotulainen, P., and P. Lappalainen. 2006. Stress fibers are generated by two distinct actin assembly mechanisms in motile cells. *The Journal of cell biology*. 173:383-394.
- Howe, A.K. 2004. Regulation of actin-based cell migration by cAMP/PKA. *Biochimica et Biophysica Acta (BBA) - Molecular Cell Research*. 1692:159-174.
- Iizuka-Hishikawa, Y., D. Hishikawa, J. Sasaki, K. Takubo, M. Goto, K. Nagata, H. Nakanishi, H. Shindou, T. Okamura, C. Ito, K. Toshimori, T. Sasaki, and T. Shimizu. 2017.

- Lysophosphatidic acid acyltransferase 3 tunes the membrane status of germ cells by incorporating docosahexaenoic acid during spermatogenesis. *J Biol Chem.* 292:12065-12076.
- Joberty, G., C. Petersen, L. Gao, and I.G. Macara. 2000. The cell-polarity protein Par6 links Par3 and atypical protein kinase C to Cdc42. *Nature Cell Biology.* 2:531-539.
- Kimura, K., M. Ito, M. Amano, K. Chihara, Y. Fukata, M. Nakafuku, B. Yamamori, J. Feng, T. Nakano, K. Okawa, A. Iwamatsu, and K. Kaibuchi. 1996. Regulation of Myosin Phosphatase by Rho and Rho-Associated Kinase (Rho-Kinase). *Science.* 273:245.
- Kloda, A., L. Lua, R. Hall, D.J. Adams, and B. Martinac. 2007. Liposome reconstitution and modulation of recombinant N-methyl-d-aspartate receptor channels by membrane stretch. *Proceedings of the National Academy of Sciences.* 104:1540-1545.
- Kobayashi, T., and A.K. Menon. 2018. Transbilayer lipid asymmetry. *Current Biology.* 28:R386-R391.
- Koeberle, A., H. Shindou, T. Harayama, and T. Shimizu. 2010. Role of lysophosphatidic acid acyltransferase 3 for the supply of highly polyunsaturated fatty acids in TM4 Sertoli cells. *FASEB journal : official publication of the Federation of American Societies for Experimental Biology.* 24:4929-4938.
- Koeberle, A., H. Shindou, T. Harayama, K. Yuki, and T. Shimizu. 2012. Polyunsaturated fatty acids are incorporated into maturing male mouse germ cells by lysophosphatidic acid acyltransferase 3. *The FASEB Journal.* 26:169-180.
- Koenig, B.W., H.H. Strey, and K. Gawrisch. 1997. Membrane lateral compressibility determined by NMR and x-ray diffraction: effect of acyl chain polyunsaturation. *Biophys J.* 73:1954-1966.
- Komarova, Y.A., K. Kruse, D. Mehta, and A.B. Malik. 2017. Protein Interactions at Endothelial Junctions and Signaling Mechanisms Regulating Endothelial Permeability. *Circ Res.* 120:179-206.
- Kozlov, M.M., and L.V. Chernomordik. 2015. Membrane tension and membrane fusion. *Curr Opin Struct Biol.* 33:61-67.
- Krugmann, S., R. Williams, L. Stephens, and P.T. Hawkins. 2004. ARAP3 Is a PI3K- and Rap-Regulated GAP for RhoA. *Current Biology.* 14:1380-1384.
- Labernadie, A., A. Bouissou, P. Delobelle, S. Balor, R. Voituriez, A. Proag, I. Fourquaux, C. Thibault, C. Vieu, R. Poincloux, G.M. Charrière, and I. Maridonneau-Parini. 2014. Protrusion force microscopy reveals oscillatory force generation and mechanosensing activity of human macrophage podosomes. *Nature Communications.* 5:5343.
- Lampugnani, M.G., A. Zanetti, F. Breviario, G. Balconi, F. Orsenigo, M. Corada, R. Spagnuolo, M. Betson, V. Braga, and E. Dejana. 2002. VE-cadherin regulates endothelial actin activating Rac and increasing membrane association of Tiam. *Molecular biology of the cell.* 13:1175-1189.
- Landraud, L., M. Gauthier, T. Fosse, and P. Boquet. 2000. Frequency of Escherichia coli strains producing the cytotoxic necrotizing factor (CNF1) in nosocomial urinary tract infections. *Letters in applied microbiology.* 30:213-216.
- Lang, P., F. Gesbert, M. Delespine-Carmagnat, R. Stancou, M. Pouchelet, and J. Bertoglio. 1996. Protein kinase A phosphorylation of RhoA mediates the morphological and functional effects of cyclic AMP in cytotoxic lymphocytes. *The EMBO Journal.* 15:510-519.

- Laufs, U., and J.K. Liao. 1998. Post-transcriptional Regulation of Endothelial Nitric Oxide Synthase mRNA Stability by Rho GTPase. *Journal of Biological Chemistry*. 273:24266-24271.
- Lee, H.-C., T. Inoue, R. Imae, N. Kono, S. Shirae, S. Matsuda, K. Gengyo-Ando, S. Mitani, and H. Arai. 2008. Caenorhabditis elegans mboa-7, a Member of the MBOAT Family, Is Required for Selective Incorporation of Polyunsaturated Fatty Acids into Phosphatidylinositol. *Molecular Biology of the Cell*. 19:1174-1184.
- Lee, H.-C., T. Inoue, J. Sasaki, T. Kubo, S. Matsuda, Y. Nakasaki, M. Hattori, F. Tanaka, O. Udagawa, N. Kono, T. Itoh, H. Ogiso, R. Taguchi, M. Arita, T. Sasaki, and H. Arai. 2012. LPIAT1 regulates arachidonic acid content in phosphatidylinositol and is required for cortical lamination in mice. *Molecular Biology of the Cell*. 23:4689-4700.
- Lemichez, E., M. Lecuit, X. Nassif, and S. Bourdoulous. 2010. Breaking the wall: targeting of the endothelium by pathogenic bacteria. *Nat Rev Micro*. 8:93-104.
- Lenzi, A., L. Gandini, V. Maresca, R. Rago, P. Sgrò, F. Dondero, and M. Picardo. 2000. Fatty acid composition of spermatozoa and immature germ cells. *Molecular Human Reproduction*. 6:226-231.
- Lesca, G.M., M. Palfreyman, D.H. Hall, M.T. Clandinin, C. Rudolph, E.M. Jorgensen, and G. Schiavo. 2003. Long chain polyunsaturated fatty acids are required for efficient neurotransmission in *C. elegans*. *Journal of Cell Science*. 116:4965-4975.
- Levental, I., M. Grzybek, and K. Simons. 2011. Raft domains of variable properties and compositions in plasma membrane vesicles. *Proceedings of the National Academy of Sciences*. 108:11411-11416.
- Levental, K.R., J.H. Lorent, X. Lin, A.D. Skinkle, M.A. Surma, E.A. Stockenbojer, A.A. Gorfe, and I. Levental. 2016. Polyunsaturated Lipids Regulate Membrane Domain Stability by Tuning Membrane Order. *Biophysical Journal*. 110:1800-1810.
- Liao, S., M. Tammaro, and H. Yan. 2015. Enriching CRISPR-Cas9 targeted cells by co-targeting the HPRT gene. *Nucleic acids research*. 43:e134.
- Lim, K.B., W. Bu, W.I. Goh, E. Koh, S.H. Ong, T. Pawson, T. Sudhaharan, and S. Ahmed. 2008. The Cdc42 Effector IRSp53 Generates Filopodia by Coupling Membrane Protrusion with Actin Dynamics. *Journal of Biological Chemistry*. 283:20454-20472.
- Lin, J., J. Liu, Y. Wang, J. Zhu, K. Zhou, N. Smith, and X. Zhan. 2005. Differential regulation of cortactin and N-WASP-mediated actin polymerization by missing in metastasis (MIM) protein. *Oncogene*. 24:2059-2066.
- Loirand, G., and P. Pacaud. 2010. The role of Rho protein signaling in hypertension. *Nature Reviews Cardiology*. 7:637-647.
- Lorent, J.H., K.R. Levental, L. Ganesan, G. Rivera-Longworth, E. Sezgin, M. Doktorova, E. Lyman, and I. Levental. 2020. Plasma membranes are asymmetric in lipid unsaturation, packing and protein shape. *Nature Chemical Biology*. 16:644-652.
- Lorizate, M., T. Sachsenheimer, B. Glass, A. Habermann, M.J. Gerl, H.-G. Kräusslich, and B. Brügger. 2013. Comparative lipidomics analysis of HIV-1 particles and their producer cell membrane in different cell lines. *Cellular Microbiology*. 15:292-304.
- Lundström, S.L., J. Yang, J.D. Brannan, J.Z. Haeggström, B.D. Hammock, P. Nair, P. O'Byrne, S.E. Dahlén, and C.E. Wheelock. 2013. Lipid mediator serum profiles in asthmatics significantly shift following dietary supplementation with omega-3 fatty acids. *Molecular nutrition & food research*. 57:1378-1389.

- Machacek, M., L. Hodgson, C. Welch, H. Elliott, O. Pertz, P. Nalbant, A. Abell, G.L. Johnson, K.M. Hahn, and G. Danuser. 2009. Coordination of Rho GTPase activities during cell protrusion. *Nature*. 461:99-103.
- Maddugoda, Madhavi P., C. Stefani, D. Gonzalez-Rodriguez, J. Saarikangas, S. Torrino, S. Janel, P. Munro, A. Doye, F. Prodon, M. Aurrand-Lions, Pierre L. Goossens, F. Lafont, P. Bassereau, P. Lappalainen, F. Brochard, and E. Lemichez. 2011. cAMP Signaling by Anthrax Edema Toxin Induces Transendothelial Cell Tunnels, which Are Resealed by MIM via Arp2/3-Driven Actin Polymerization. *Cell Host & Microbe*. 10:464-474.
- Magdeleine, M., R. Gautier, P. Gounon, H. Barelli, S. Vanni, and B. Antonny. 2016. A filter at the entrance of the Golgi that selects vesicles according to size and bulk lipid composition. *eLife*. 5:e16988.
- Manni, M.M., M.L. Tiberti, S. Pagnotta, H. Barelli, R. Gautier, and B. Antonny. 2018. Acyl chain asymmetry and polyunsaturation of brain phospholipids facilitate membrane vesiculation without leakage. *eLife*. 7:e34394.
- Martin, R.E., M.H. Elliott, R.S. Brush, and R.E. Anderson. 2005. Detailed Characterization of the Lipid Composition of Detergent-Resistant Membranes from Photoreceptor Rod Outer Segment Membranes. *Investigative Ophthalmology & Visual Science*. 46:1147-1154.
- Mashek, D.G., and R.A. Coleman. 2006. Cellular fatty acid uptake: the contribution of metabolism. *Current opinion in lipidology*. 17:274-278.
- Mitchell, D.C., and B.J. Litman. 1998a. Effect of cholesterol on molecular order and dynamics in highly polyunsaturated phospholipid bilayers. *Biophysical journal*. 75:896-908.
- Mitchell, D.C., and B.J. Litman. 1998b. Molecular Order and Dynamics in Bilayers Consisting of Highly Polyunsaturated Phospholipids. *Biophysical Journal*. 74:879-891.
- Molinari, G., M. Rohde, C. Wilde, I. Just, K. Aktories, and G.S. Chhatwal. 2006. Localization of the C3-Like ADP-Ribosyltransferase from *Staphylococcus aureus* during Bacterial Invasion of Mammalian Cells. *Infection and Immunity*. 74:3673.
- Morita, Y., T. Sakaguchi, K. Ikegami, N. Goto-Inoue, T. Hayasaka, V.T. Hang, H. Tanaka, T. Harada, Y. Shibasaki, A. Suzuki, K. Fukumoto, K. Inaba, M. Murakami, M. Setou, and H. Konno. 2013. Lysophosphatidylcholine acyltransferase 1 altered phospholipid composition and regulated hepatoma progression. *Journal of Hepatology*. 59:292-299.
- Moy, A.B., J. Van Engelenhoven, J. Bodmer, J. Kamath, C. Keese, I. Giaever, S. Shasby, and D.M. Shasby. 1996. Histamine and thrombin modulate endothelial focal adhesion through centripetal and centrifugal forces. *J Clin Invest*. 97:1020-1027.
- Munro, P., M. Benchetrit, M.-A. Nahori, C. Stefani, R. Clément, J.-F. Michiels, L. Landraud, O. Dussurget, and E. Lemichez. 2010. The *Staphylococcus aureus* Epidermal Cell Differentiation Inhibitor Toxin Promotes Formation of Infection Foci in a Mouse Model of Bacteremia. *Infection and Immunity*. 78:3404-3411.
- Mysorekar, I.U., and S.J. Hultgren. 2006. Mechanisms of uropathogenic *Escherichia coli* persistence and eradication from the urinary tract. *Proceedings of the National Academy of Sciences*. 103:14170-14175.
- Nakanishi, H., H. Shindou, D. Hishikawa, T. Harayama, R. Ogasawara, A. Suwabe, R. Taguchi, and T. Shimizu. 2006. Cloning and Characterization of Mouse Lung-type Acyl-CoA:Lysophosphatidylcholine Acyltransferase 1 (LPCAT1): EXPRESSION IN ALVEOLAR TYPE II CELLS AND POSSIBLE INVOLVEMENT IN SURFACTANT PRODUCTION. *Journal of Biological Chemistry*. 281:20140-20147.

- Nelson, D.L., A.L. Lehninger, and M.M. Cox. 2008. *Lehninger principles of biochemistry*. W.H. Freeman, New York.
- Ng, W.P., K.D. Webster, C. Stefani, E.M. Schmid, E. Lemichez, P. Bassereau, and D.A. Fletcher. 2017. Force-induced transcellular tunnel formation in endothelial cells. *Molecular Biology of the Cell*. 28:2650-2660.
- Nguyen, L.N., D. Ma, G. Shui, P. Wong, A. Cazenave-Gassiot, X. Zhang, M.R. Wenk, E.L.K. Goh, and D.L. Silver. 2014. Mfsd2a is a transporter for the essential omega-3 fatty acid docosahexaenoic acid. *Nature*. 509:503-506.
- Nicolson, G.L. 2014. The Fluid—Mosaic Model of Membrane Structure: Still relevant to understanding the structure, function and dynamics of biological membranes after more than 40years. *Biochimica et Biophysica Acta (BBA) - Biomembranes*. 1838:1451-1466.
- Niko, Y., P. Didier, Y. Mely, G.-i. Konishi, and A.S. Klymchenko. 2016. Bright and photostable push-pull pyrene dye visualizes lipid order variation between plasma and intracellular membranes. *Scientific Reports*. 6:18870.
- Niu, S.-L., D.C. Mitchell, S.-Y. Lim, Z.-M. Wen, H.-Y. Kim, N. Salem, and B.J. Litman. 2004. Reduced G Protein-coupled Signaling Efficiency in Retinal Rod Outer Segments in Response to n-3 Fatty Acid Deficiency. *Journal of Biological Chemistry*. 279:31098-31104.
- Niu, S.-L., D.C. Mitchell, and B.J. Litman. 2001. Optimization of Receptor-G Protein Coupling by Bilayer Lipid Composition II: FORMATION OF METARHODOPSIN II-TRANSDUCIN COMPLEX. *Journal of Biological Chemistry*. 276:42807-42811.
- Nobes, C.D., and A. Hall. 1995. Rho, Rac, and Cdc42 GTPases regulate the assembly of multimolecular focal complexes associated with actin stress fibers, lamellipodia, and filopodia. *Cell*. 81:53-62.
- Nomura, T., C.G. Cranfield, E. Deplazes, D.M. Owen, A. Macmillan, A.R. Battle, M. Constantine, M. Sokabe, and B. Martinac. 2012. Differential effects of lipids and lysolipids on the mechanosensitivity of the mechanosensitive channels MscL and MscS. *Proceedings of the National Academy of Sciences*. 109:8770-8775.
- Noren, N.K., B.P. Liu, K. Burrige, and B. Kreft. 2000. P120 Catenin Regulates the Actin Cytoskeleton via Rho Family Gtpases. *Journal of Cell Biology*. 150:567-580.
- O'Brien, J.S., and E.L. Sampson. 1965. Fatty acid and fatty aldehyde composition of the major brain lipids in normal human gray matter, white matter, and myelin. *Journal of Lipid Research*. 6:545-551.
- Olbrich, K., W. Rawicz, D. Needham, and E. Evans. 2000. Water Permeability and Mechanical Strength of Polyunsaturated Lipid Bilayers. *Biophysical Journal*. 79:321-327.
- Peetla, C., S. Vijayaraghavalu, and V. Labhasetwar. 2013. Biophysics of cell membrane lipids in cancer drug resistance: Implications for drug transport and drug delivery with nanoparticles. *Advanced Drug Delivery Reviews*. 65:1686-1698.
- Pelaseyed, T., R. Viswanatha, C. Sauvanet, J.J. Filter, M.L. Goldberg, and A. Bretscher. 2017. Ezrin activation by LOK phosphorylation involves a PIP2-dependent wedge mechanism. *eLife*. 6:e22759.
- Pertz, O., L. Hodgson, R.L. Klemke, and K.M. Hahn. 2006. Spatiotemporal dynamics of RhoA activity in migrating cells. *Nature*. 440:1069-1072.
- Peter, B.J., H.M. Kent, I.G. Mills, Y. Vallis, P.J.G. Butler, P.R. Evans, and H.T. McMahon. 2004. BAR Domains as Sensors of Membrane Curvature: The Amphiphysin BAR Structure. *Science*. 303:495-499.

- Pezard, C., P. Berche, and M. Mock. 1991. Contribution of individual toxin components to virulence of *Bacillus anthracis*. *Infection and Immunity*. 59:3472.
- Pinot, M., S. Vanni, S. Pagnotta, S. Lacas-Gervais, L.-A. Payet, T. Ferreira, R. Gautier, B. Goud, B. Antony, and H. Barelli. 2014. Polyunsaturated phospholipids facilitate membrane deformation and fission by endocytic proteins. *Science*. 345:693-697.
- Pitman, M.C., A. Grossfield, F. Suits, and S.E. Feller. 2005. Role of Cholesterol and Polyunsaturated Chains in Lipid-Protein Interactions: Molecular Dynamics Simulation of Rhodopsin in a Realistic Membrane Environment. *Journal of the American Chemical Society*. 127:4576-4577.
- Prasad, S.S., A. Garg, and A.K. Agarwal. 2011. Enzymatic activities of the human AGPAT isoform 3 and isoform 5: localization of AGPAT5 to mitochondria. *Journal of Lipid Research*. 52:451-462.
- Qualmann, B., D. Koch, and M.M. Kessels. 2011. Let's go bananas: revisiting the endocytic BAR code. *The EMBO Journal*. 30:3501-3515.
- Rabiet, M.-J., J.-L. Plantier, Y. Rival, Y. Genoux, M.-G. Lampugnani, and E. Dejana. 1996. Thrombin-Induced Increase in Endothelial Permeability Is Associated With Changes in Cell-to-Cell Junction Organization. *Arteriosclerosis, Thrombosis, and Vascular Biology*. 16:488-496.
- Rajamoorthi, K., H.I. Petrache, T.J. McIntosh, and M.F. Brown. 2005. Packing and Viscoelasticity of Polyunsaturated ω -3 and ω -6 Lipid Bilayers as Seen by ²H NMR and X-ray Diffraction. *Journal of the American Chemical Society*. 127:1576-1588.
- Randall, A.S., C.-H. Liu, B. Chu, Q. Zhang, S.A. Dongre, M. Juusola, K. Franze, M.J.O. Wakelam, and R.C. Hardie. 2015. Speed and Sensitivity of Phototransduction in *Drosophila* Depend on Degree of Saturation of Membrane Phospholipids. *The Journal of Neuroscience*. 35:2731-2746.
- Rawicz, W., K.C. Olbrich, T. McIntosh, D. Needham, and E. Evans. 2000. Effect of chain length and unsaturation on elasticity of lipid bilayers. *Biophysical journal*. 79:328-339.
- Renaud, J.F., A.M. Scanu, T. Kazazoglou, A. Lombet, G. Romey, and M. Lazdunski. 1982. Normal serum and lipoprotein-deficient serum give different expressions of excitability, corresponding to different stages of differentiation, in chicken cardiac cells in culture. *Proc Natl Acad Sci U S A*. 79:7768-7772.
- Ridley, A.J., and A. Hall. 1992. The small GTP-binding protein rho regulates the assembly of focal adhesions and actin stress fibers in response to growth factors. *Cell*. 70:389-399.
- Ridley, A.J., H.F. Paterson, C.L. Johnston, D. Diekmann, and A. Hall. 1992. The small GTP-binding protein rac regulates growth factor-induced membrane ruffling. *Cell*. 70:401-410.
- Ridone, P., S.L. Grage, A. Patkunarajah, A.R. Battle, A.S. Ulrich, and B. Martinac. 2018. "Force-from-lipids" gating of mechanosensitive channels modulated by PUFAs. *Journal of the mechanical behavior of biomedical materials*. 79:158-167.
- Riento, K., and A.J. Ridley. 2003. ROCKs: multifunctional kinases in cell behaviour. *Nature Reviews Molecular Cell Biology*. 4:446-456.
- Robertson, R.M., J. Yao, S. Gajewski, G. Kumar, E.W. Martin, C.O. Rock, and S.W. White. 2017. A two-helix motif positions the lysophosphatidic acid acyltransferase active site for catalysis within the membrane bilayer. *Nature Structural & Molecular Biology*. 24:666-671.

- Rohrbeck, A., and I. Just. 2017. Cell Entry of C3 Exoenzyme from *Clostridium botulinum*. In *Uptake and Trafficking of Protein Toxins*. H. Barth, editor. Springer International Publishing, Cham. 97-118.
- Rohwedder, A., Q. Zhang, S.A. Rudge, and M.J.O. Wakelam. 2014. Lipid droplet formation in response to oleic acid in Huh-7 cells is mediated by the fatty acid receptor FFAR4. *Journal of Cell Science*. 127:3104-3115.
- Rolando, M., P. Munro, C. Stefani, P. Auberger, G. Flatau, and E. Lemichez. 2009. Injection of *Staphylococcus aureus* EDIN by the *Bacillus anthracis* Protective Antigen Machinery Induces Vascular Permeability. *Infection and Immunity*. 77:3596-3601.
- Rolli-Derkinderen, M., V. Sauzeau, L. Boyer, E. Lemichez, C. Baron, D. Henrion, G. Loirand, and P. Pacaud. 2005. Phosphorylation of Serine 188 Protects RhoA from Ubiquitin/Proteasome-Mediated Degradation in Vascular Smooth Muscle Cells. *Circulation Research*. 96:1152-1160.
- Römer, W., L. Berland, V. Chambon, K. Gaus, B. Windschiegl, D. Tenza, M.R.E. Aly, V. Fraissier, J.-C. Florent, D. Perrais, C. Lamaze, G. Raposo, C. Steinem, P. Sens, P. Bassereau, and L. Johannes. 2007. Shiga toxin induces tubular membrane invaginations for its uptake into cells. *Nature*. 450:670-675.
- Ronald, A. 2002. The etiology of urinary tract infection: traditional and emerging pathogens. *The American Journal of Medicine*. 113:14-19.
- Saarikangas, J., H. Zhao, A. Pykäläinen, P. Laurinmäki, P.K. Mattila, P.K.J. Kinnunen, S.J. Butcher, and P. Lappalainen. 2009. Molecular Mechanisms of Membrane Deformation by I-BAR Domain Proteins. *Current Biology*. 19:95-107.
- Salas-Estrada, L.A., N. Leioatts, T.D. Romo, and A. Grossfield. 2018. Lipids Alter Rhodopsin Function via Ligand-like and Solvent-like Interactions. *Biophysical Journal*. 114:355-367.
- Salmon, A., S.W. Dodd, G.D. Williams, J.M. Beach, and M.F. Brown. 1987. Configurational statistics of acyl chains in polyunsaturated lipid bilayers from deuterium NMR. *Journal of the American Chemical Society*. 109:2600-2609.
- Sandre, O., L. Moreaux, and F. Brochard-Wyart. 1999. Dynamics of transient pores in stretched vesicles. *Proceedings of the National Academy of Sciences*. 96:10591-10596.
- Sawada, N., S. Salomone, H.-H. Kim, J. Kwiatkowski David, and K. Liao James. 2008. Regulation of Endothelial Nitric Oxide Synthase and Postnatal Angiogenesis by Rac1. *Circulation Research*. 103:360-368.
- Sellin, M.E., P. Holmfeldt, S. Stenmark, and M. Gullberg. 2011. Microtubules support a disk-like septin arrangement at the plasma membrane of mammalian cells. *Mol Biol Cell*. 22:4588-4601.
- Sezgin, E., H.-J. Kaiser, T. Baumgart, P. Schwille, K. Simons, and I. Levental. 2012. Elucidating membrane structure and protein behavior using giant plasma membrane vesicles. *Nature Protocols*. 7:1042-1051.
- Shahidi, F., and P. Ambigaipalan. 2018. Omega-3 Polyunsaturated Fatty Acids and Their Health Benefits. *Annual Review of Food Science and Technology*. 9:345-381.
- Shindou, H., M. Eto, R. Morimoto, and T. Shimizu. 2009. Identification of membrane O-acyltransferase family motifs. *Biochem Biophys Res Commun*. 383:320-325.
- Shindou, H., D. Hishikawa, T. Harayama, M. Eto, and T. Shimizu. 2013. Generation of membrane diversity by lysophospholipid acyltransferases. *The Journal of Biochemistry*. 154:21-28.

- Shindou, H., D. Hishikawa, H. Nakanishi, T. Harayama, S. Ishii, R. Taguchi, and T. Shimizu. 2007. A Single Enzyme Catalyzes Both Platelet-activating Factor Production and Membrane Biogenesis of Inflammatory Cells: CLONING AND CHARACTERIZATION OF ACETYL-CoA:LYSO-PAF ACETYLTRANSFERASE. *Journal of Biological Chemistry*. 282:6532-6539.
- Shindou, H., H. Koso, J. Sasaki, H. Nakanishi, H. Sagara, K.M. Nakagawa, Y. Takahashi, D. Hishikawa, Y. Iizuka-Hishikawa, F. Tokumasu, H. Noguchi, S. Watanabe, T. Sasaki, and T. Shimizu. 2017. Docosahexaenoic acid preserves visual function by maintaining correct disc morphology in retinal photoreceptor cells. *Journal of Biological Chemistry*. 292:12054-12064.
- Shindou, H., and T. Shimizu. 2009. Acyl-CoA:Lysophospholipid Acyltransferases. *Journal of Biological Chemistry*. 284:1-5.
- Singer, S.J., and G.L. Nicolson. 1972. The fluid mosaic model of the structure of cell membranes. *Science*. 175:720-731.
- Soiné, J.R.D., C.A. Brand, J. Stricker, P.W. Oakes, M.L. Gardel, and U.S. Schwarz. 2015. Model-based Traction Force Microscopy Reveals Differential Tension in Cellular Actin Bundles. *PLOS Computational Biology*. 11:e1004076.
- Stefani, C., D. Gonzalez-Rodriguez, Y. Senju, A. Doye, N. Efimova, S. Janel, J. Lipuma, M.C. Tsai, D. Hamaoui, M.P. Maddugoda, O. Cochet-Escartin, C. Prévost, F. Lafont, T. Svitkina, P. Lappalainen, P. Bassereau, and E. Lemichez. 2017. Ezrin enhances line tension along transcellular tunnel edges via NMI1a driven actomyosin cable formation. *Nature Communications*. 8:15839.
- Stone, W.L., C.C. Farnsworth, and E.A. Dratz. 1979. A reinvestigation of the fatty acid content of bovine, rat and frog retinal rod outer segments. *Experimental Eye Research*. 28:387-397.
- Takamori, S., M. Holt, K. Stenius, E.A. Lemke, M. Grønborg, D. Riedel, H. Urlaub, S. Schenck, B. Brügger, P. Ringler, S.A. Müller, B. Rammner, F. Gräter, J.S. Hub, B.L. De Groot, G. Mieskes, Y. Moriyama, J. Klingauf, H. Grubmüller, J. Heuser, F. Wieland, and R. Jahn. 2006. Molecular Anatomy of a Trafficking Organelle. *Cell*. 127:831-846.
- Tan, W., T.R. Palmby, J. Gavard, P. Amornphimoltham, Y. Zheng, and J.S. Gui. 2008a. An essential role for Rac1 in endothelial cell function and vascular development. *The FASEB Journal*. 22:1829-1838.
- Tan, W., T.R. Palmby, J. Gavard, P. Amornphimoltham, Y. Zheng, and J.S. Gutkind. 2008b. An essential role for Rac1 in endothelial cell function and vascular development. *FASEB journal : official publication of the Federation of American Societies for Experimental Biology*. 22:1829-1838.
- Tanguy, E., P. Costé de Bagneaux, N. Kassas, M.-R. Ammar, Q. Wang, A.-M. Haeberlé, J. Raherindratsara, L. Fouillen, P.-Y. Renard, M. Montero-Hadjadje, S. Chasserot-Golaz, S. Ory, S. Gasman, M.-F. Bader, and N. Vitale. 2020. Mono- and Poly-unsaturated Phosphatidic Acid Regulate Distinct Steps of Regulated Exocytosis in Neuroendocrine Cells. *Cell Reports*. 32:108026.
- Tiberti, M.L., B. Antonny, and R. Gautier. 2020. The transbilayer distribution of polyunsaturated phospholipids determines their facilitating effect on membrane deformation. *Soft Matter*. 16:1722-1730.
- Tixier-Vidal, A., R. Picart, C. Loudes, and A.F. Bauman. 1986. Effects of polyunsaturated fatty acids and hormones on synaptogenesis in serum-free medium cultures of mouse fetal hypothalamic cells. *Neuroscience*. 17:115-132.

- Totsukawa, G., Y. Yamakita, S. Yamashiro, D.J. Hartshorne, Y. Sasaki, and F. Matsumura. 2000. Distinct roles of ROCK (Rho-kinase) and MLCK in spatial regulation of MLC phosphorylation for assembly of stress fibers and focal adhesions in 3T3 fibroblasts. *The Journal of cell biology*. 150:797-806.
- Tsai, F.-C., A. Bertin, H. Bousquet, J. Manzi, Y. Senju, M.-C. Tsai, L. Picas, S. Miserey-Lenkei, P. Lappalainen, E. Lemichez, E. Coudrier, and P. Bassereau. 2018. Ezrin enrichment on curved membranes requires a specific conformation or interaction with a curvature-sensitive partner. *eLife*. 7:e37262.
- van Meer, G., D.R. Voelker, and G.W. Feigenson. 2008. Membrane lipids: where they are and how they behave. *Nat Rev Mol Cell Biol*. 9:112-124.
- Vásquez, V., M. Krieg, D. Lockhead, and Miriam B. Goodman. 2014. Phospholipids that Contain Polyunsaturated Fatty Acids Enhance Neuronal Cell Mechanics and Touch Sensation. *Cell Reports*. 6:70-80.
- Vega, F.M., G. Fruhwirth, T. Ng, and A.J. Ridley. 2011. RhoA and RhoC have distinct roles in migration and invasion by acting through different targets. *Journal of Cell Biology*. 193:655-665.
- Verkleij, A.J., R.F. Zwaal, B. Roelofsen, P. Comfurius, D. Kastelijn, and L.L. van Deenen. 1973. The asymmetric distribution of phospholipids in the human red cell membrane. A combined study using phospholipases and freeze-etch electron microscopy. *Biochimica et biophysica acta*. 323:178-193.
- Vicente-Manzanares, M., X. Ma, R.S. Adelstein, and A.R. Horwitz. 2009. Non-muscle myosin II takes centre stage in cell adhesion and migration. *Nature Reviews Molecular Cell Biology*. 10:778-790.
- Villarroel, A., and T. Schwarz. 1996. Inhibition of the Kv4 (Shal) family of transient K⁺ currents by arachidonic acid. *The Journal of Neuroscience*. 16:1016-1025.
- Visvikis, O., L. Boyer, S. Torrino, A. Doye, M. Lemonnier, P. Lorès, M. Rolando, G. Flatau, A. Mettouchi, D. Bouvard, E. Veiga, G. Gacon, P. Cossart, and E. Lemichez. 2011. Escherichia coli Producing CNF1 Toxin Hijacks Tollip to Trigger Rac1-Dependent Cell Invasion. *Traffic*. 12:579-590.
- Vrablik, T.L., and J.L. Watts. 2013. Polyunsaturated fatty acid derived signaling in reproduction and development: Insights from *Caenorhabditis elegans* and *Drosophila melanogaster*. *Molecular Reproduction and Development*. 80:244-259.
- Wallis, J.G., J.L. Watts, and J. Browse. 2002. Polyunsaturated fatty acid synthesis: what will they think of next? *Trends in Biochemical Sciences*. 27:467-473.
- Wang, H.-R., Y. Zhang, B. Ozdamar, A.A. Ogunjimi, E. Alexandrova, G.H. Thomsen, and J.L. Wrana. 2003. Regulation of Cell Polarity and Protrusion Formation by Targeting RhoA for Degradation. *Science*. 302:1775.
- Watanabe, S., and E. Boucrot. 2017. Fast and ultrafast endocytosis. *Current Opinion in Cell Biology*. 47:64-71.
- Watanabe, S., Q. Liu, M.W. Davis, G. Hollopeter, N. Thomas, N.B. Jorgensen, and E.M. Jorgensen. 2013a. Ultrafast endocytosis at *Caenorhabditis elegans* neuromuscular junctions. *eLife*. 2:e00723.
- Watanabe, S., B.R. Rost, M. Camacho-Pérez, M.W. Davis, B. Söhl-Kielczynski, C. Rosenmund, and E.M. Jorgensen. 2013b. Ultrafast endocytosis at mouse hippocampal synapses. *Nature*. 504:242-247.

- Watanabe, S., T. Trimbuch, M. Camacho-Pérez, B.R. Rost, B. Brokowski, B. Söhl-Kielczynski, A. Felies, M.W. Davis, C. Rosenmund, and E.M. Jorgensen. 2014. Clathrin regenerates synaptic vesicles from endosomes. *Nature*. 515:228-233.
- Watkins, E.B., J. Majewski, E.Y. Chi, H. Gao, J.-C. Florent, and L. Johannes. 2019. Shiga Toxin Induces Lipid Compression: A Mechanism for Generating Membrane Curvature. *Nano Letters*. 19:7365-7369.
- Wells, C.M., M. Walmsley, S. Ooi, V. Tybulewicz, and A.J. Ridley. 2004. Rac1-deficient macrophages exhibit defects in cell spreading and membrane ruffling but not migration. *Journal of Cell Science*. 117:1259.
- Wilde, C., M. Vogelsgesang, and K. Aktories. 2003. Rho-Specific Bacillus cereus ADP-Ribosyltransferase C3cer Cloning and Characterization. *Biochemistry*. 42:9694-9702.
- Wildenberg, G.A., M.R. Dohn, R.H. Carnahan, M.A. Davis, N.A. Lobdell, J. Settleman, and A.B. Reynolds. 2006. p120-Catenin and p190RhoGAP Regulate Cell-Cell Adhesion by Coordinating Antagonism between Rac and Rho. *Cell*. 127:1027-1039.
- Wojciak-Stothard, B., and A.J. Ridley. 2002. Rho GTPases and the regulation of endothelial permeability. *Vascular Pharmacology*. 39:187-199.
- Wu, Y.I., D. Frey, O.I. Lungu, A. Jaehrig, I. Schlichting, B. Kuhlman, and K.M. Hahn. 2009. A genetically encoded photoactivatable Rac controls the motility of living cells. *Nature*. 461:104-108.
- Yabuuchi, H., and J.S. O'Brien. 1968. Positional distribution of fatty acids in glycerophosphatides of bovine gray matter. *Journal of Lipid Research*. 9:65-67.
- Yamashita, A., Y. Hayashi, N. Matsumoto, Y. Nemoto-Sasaki, S. Oka, T. Tanikawa, and T. Sugiura. 2014. Glycerophosphate/Acylglycerophosphate acyltransferases. *Biology (Basel)*. 3:801-830.
- Yang, H.-J., Y. Sugiura, K. Ikegami, Y. Konishi, and M. Setou. 2012. Axonal Gradient of Arachidonic Acid-containing Phosphatidylcholine and Its Dependence on Actin Dynamics. *Journal of Biological Chemistry*. 287:5290-5300.
- Yau, K.-W., and R.C. Hardie. 2009. Phototransduction Motifs and Variations. *Cell*. 139:246-264.
- Yeh, Y.-T., R. Serrano, J. François, J.-J. Chiu, Y.-S.J. Li, J.C. del Álamo, S. Chien, and J.C. Lasheras. 2018. Three-dimensional forces exerted by leukocytes and vascular endothelial cells dynamically facilitate diapedesis. *Proceedings of the National Academy of Sciences*. 115:133.
- Yuki, K., H. Shindou, D. Hishikawa, and T. Shimizu. 2009. Characterization of mouse lysophosphatidic acid acyltransferase 3: an enzyme with dual functions in the testis. *J Lipid Res*. 50:860-869.
- Zhang, B., Y.H. Koh, R.B. Beckstead, V. Budnik, B. Ganetzky, and H.J. Bellen. 1998. Synaptic Vesicle Size and Number Are Regulated by a Clathrin Adaptor Protein Required for Endocytosis. *Neuron*. 21:1465-1475.
- Zhao, H., A. Pykäläinen, and P. Lappalainen. 2011. I-BAR domain proteins: linking actin and plasma membrane dynamics. *Curr Opin Cell Biol*. 23:14-21.
- Zhukovsky, M.A., A. Filograna, A. Luini, D. Corda, and C. Valente. 2019. The Structure and Function of Acylglycerophosphate Acyltransferase 4/ Lysophosphatidic Acid Acyltransferase Delta (AGPAT4/LPAAT δ). *Front Cell Dev Biol*. 7:147.

Appendix

Author's list of publications

1. Bachelor internship topic
Tsai Meng-Chen, Tsai CL and Chen ME. (2014). cDNA cloning and transcriptional expression profiles of a hexamerin in the oriental fruit fly, *Bactrocera dorsalis*. *Arch. Insect Biochem. Physiol.* 86 (3):190-191
2. PhD side project
Stefani C, Gonzalez-Rodriguez D, Senju Y, Doye A, Efimova N, Janel S, Lipuma J, Tsai Meng-Chen, Hamaoui D, Maddugoda MP, Cochet-Escartin O, Prévost C, Lafont F, Svitkina T, Lappalainen P, Bassereau P & Lemichez E. (2017). Ezrin enhances line tension along transcellular tunnel edges via NMIIa driven actomyosin cable formation. *Nature Communication*.
3. PhD side project
Tsai FC, Bertin A, Bousquet H, Manzi J, Senju Y, Tsai Meng-Chen, Picas L, Miserey-Lenkei S, Lappalainen P, Lemichez E, Coudrier E, Bassereau, P. (2018). Ezrin enrichment on curved membranes requires a specific conformation or interaction with a curvature-sensitive partner. *eLife*, 7, e37262. doi:10.7554/eLife.37262
4. Master thesis
Chiang TS, Lin MC, Tsai Meng-Chen, Chen CH, Jang LT, & Lee FJS. (2018). ADP-ribosylation factor-like 4A interacts with Robo1 to promote cell migration by regulating Cdc42 activation. *Molecular Biology of the cell*, 30(1), 69-81.
5. PhD side project
Péresse T, Kovacs D, Subra M, Bigay J, Tsai Meng-Chen, Polidori J, Gautier R, Desrat S, Fleuriot L, Debayle Delphine, Litaudon M, Pham VC, Bignon J, Antony B, Roussi F and Mesmin B. (2020). Molecular and cellular dissection of the oxysterol-binding protein cycle through a fluorescent inhibitor. *Journal of biological chemistry*, doi:10.1074/jbc.RA119.012012
6. PhD main project
Tsai Meng-Chen, Fleuriot L, Janel S, Morel C, Dallongeville S, Debayle D, Mettouchi A, Olivo-Marin JC, Antony B, Ldfont F, Lemichez E, Barelli H. Docosaheptaenoic fatty acid-containing phospholipids affect plasma membrane susceptibility to disruption by bacterial toxin-induc, *BioRxiv*, doi: 10.1101/2020.12.23.424114

Docosahexaenoic fatty acid-containing phospholipids affect plasma membrane susceptibility to disruption by bacterial toxin-induced macroapertures

Meng-Chen TSAI¹⁻², Lucile FLEURIOT¹, Sébastien JANEL³, David GONZALEZ-RODRIGUEZ⁴, Camille MOREL^{2, 5}, Amel METTOUCHI^{2, 5}, Delphine DEBAYLE¹, Stéphane DALLONGEVILLE⁶, Jean-Christophe OLIVO-MARIN⁶, Bruno ANTONNY¹, Frank LAFONT⁴, Emmanuel LEMICHEZ^{2, 5*,#} and Hélène BARELLI^{1*,#}

¹ Institut de Pharmacologie Moléculaire et Cellulaire, UMR 7275, CNRS and Université Côte d'Azur, 06560, Valbonne, France

² Unité des Toxines Bactériennes, UMR CNRS 2001, Institut Pasteur, 25 rue du Dr Roux, 75724, Paris, France.

³ Université de Lille, CNRS, Inserm, CHU Lille, Institut Pasteur Lille, U1019 - UMR 9017 - CIIL - Center for Infection and Immunity of Lille, F-59000 Lille, France

⁴ Université de Lorraine, LCP-A2MC, F-57000 Metz, France

⁵ Université Paris Diderot, Sorbonne Paris Cité, Paris, France

⁶ Institut Pasteur, BioImage Analysis Unit, CNRS UMR 3691, Paris, France

*: co-last authors

#: co-corresponding authors:

barelli@ipmc.cnrs.fr and emmanuel.lemichez@pasteur.fr

Abstract

Metabolic studies and animal knockout models point to the critical role of polyunsaturated docosahexaenoic acid (22:6, DHA)-containing phospholipids (PLs) in physiology. Here, we study the impact of DHA-PLs on the dynamics of transendothelial cell macroapertures (TEMs) tunnels triggered by the RhoA GTPase inhibitory exotoxin C3 from *Clostridium botulinum*. Through lipidomic analyses, we show that primary human umbilical vein endothelial cells (HUVECs) subjected to DHA-diet undergo a 6-fold DHA-PLs enrichment in plasma membrane, mostly in phosphatidylcholine and phosphatidylethanolamine classes, at the expense of monounsaturated OA-PLs. In contrast, OA-diet had almost no effect on PLs composition. Consequently, DHA treatment increases the nucleation rate of TEMs by 2-fold that we ascribe to a reduction of cell thickness. We reveal that the global transcellular area of cells remains conserved through a reduction of the width and lifetime of TEMs. Altogether, we reveal a homeostasis between plasma membrane DHA-PLs content and large-scale membrane dynamics.

1 **Introduction**

2 The plasma membrane attached to the cortical cytoskeleton forms a composite material that
3 undergoes constant reshaping to perform essential cellular processes, including cell division,
4 migration, phagocytosis and epithelial or endothelial semipermeable barrier organization and
5 function (Levayer and Lecuit, 2012; Salbreux et al., 2012). Lipidomic approaches offer ways to
6 quantitatively decipher the impact of fine-tuned changes in the composition of lipid acyl chains on
7 membrane dynamics.

8 Phospholipids (PLs) often contain an unsaturated acyl chain at the sn-2 position that determines the
9 biophysical properties of cellular membranes. Fatty acids (FA) are classified as saturated (S),
10 monounsaturated (MU), and polyunsaturated (PU) by the number of double bonds present in the
11 hydrocarbon acyl chain. Several glycerophospholipid classes, including phosphatidylcholine (PC),
12 phosphatidylethanolamine (PE) and phosphatidylserine (PS), are the dominant constituents of the
13 plasma membrane in addition to cholesterol (van Meer et al., 2008). Notably, phosphatidylcholine
14 (PC) accounts for 40-50% of total phospholipids at the plasma membrane (van Meer et al., 2008).
15 Variations in the length and number of double bonds in acyl chains lead to a remarkably large
16 repertoire of phospholipid variants, such as PC(16:0/18:1, PE(18:0/20:4), and PS(18:0/22:6),
17 conferring different biophysical properties, i.e., fluidity, packing order and curvature (Barelli and
18 Antonny, 2016; Harayama and Riezman, 2018). The double bonds in polyunsaturated phospholipids
19 allow acyl chains to twist at various angles, thereby providing the membrane with remarkably flexible
20 properties (Manni et al., 2018). It is important to decode how the pattern of acyl chain variants in PLs
21 translates into variations in cellular membrane dynamics (Harayama and Riezman, 2018; Pinot et al.,
22 2014).

23 With 22 carbons and six double bonds, docosahexaenoic acid (DHA) is the most unsaturated form of
24 the omega-3 fatty acids. Given the limited synthesis of this FA from linolenic acid, a dietary supply
25 of DHA is essential to the functions of the retina and for spermatogenesis (Iizuka-Hishikawa et al.,
26 2017; Shindou et al., 2017) in addition to brain function (Bazinet and Layé, 2014). In particular,
27 animals fed with PUFA-free diets develop reduced visual functions paralleling the low DHA content
28 in their retinas, outcomes that indicate the critical requirement of attaining DHA from the diet for
29 visual function (Jeffrey and Neuringer, 2009). Lysophosphatidic acid acyltransferase 3 (LPAAT3),
30 which catalyzes the esterification of DHA to generate lysophosphatidic acid and form precursors of
31 PL, notably DHA-containing PC and PE, is particularly rich in the retina and testis (Yuki et al., 2009).
32 Mice with LPAAT3 knocked out display male infertility and show visual impairment due to structural
33 defects in the membranes of photoreceptors. Much remains to be learned on how DHA impacts the
34 architecture and dynamics of the plasma membrane.

35 Recent works have shown that polyunsaturated lipids facilitate membrane processes requiring
36 deformations at the nanometer scale. First, incorporation of polyunsaturated acyl chains into PLs
37 facilitates endocytosis in model cellular systems and makes the pure lipid bilayer more flexible and
38 prone to fission mediated by dynamin and endophilin (Pinot et al., 2014, Manni et al., 2018). These
39 effects might explain why polyunsaturated phospholipids are necessary for proper synaptic vesicle
40 formation (Tixier-Vidal et al., 1986). Second, polyunsaturated phosphatidic acid facilitates secretory
41 granule exocytosis in neuroendocrine chromaffin cells, probably by stabilizing intermediates that
42 contribute to a high-curvature membrane during fusion pore formation (Tanguy et al., 2020). Finally,
43 polyunsaturated PLs modulate the activity of several mechanosensitive ion channels, including TRP,
44 TRP-like and Piezo channels (Caires et al., 2017; Randall et al., 2015; Romero et al., 2019). Many of
45 these effects have been proposed to arise from a reduction in the energetic cost of membrane bending
46 and/or from a modulation of the energy required for protein conformational changes within the
47 membrane matrix. However, whether and how the enrichment of cellular membranes with PUPLs
48 modulates large-scale membrane dynamics remain to be elucidated.

49 Transcellular pores are observed in endothelial cell-lined vessels and form during the transcellular
50 diapedesis of leukocytes (Aird, 2007; Braakman et al., 2016; Schimmel et al., 2017). Several toxins
51 from pathogenic bacteria, such as RhoA-inhibitory exoenzymes from *Staphylococcus aureus* and
52 *Clostridium botulinum*, can induce transendothelial cell macroaperture (TEM) tunnels (Lemichez et
53 al., 2013). This TEM formation has been linked to increased vascular permeability and dissemination
54 of *S. aureus* in tissues via the hematogenous route (Boyer et al., 2006; Munro et al., 2010; Rolando
55 et al., 2009). Several bacteria secrete toxins that lower cell actomyosin contractility, thereby
56 promoting cell spreading, which favors close contact between the apical and basal membranes and
57 initiates their self-fusion (Boyer et al., 2006; Ng et al., 2017). The cellular dewetting physical model
58 is based on the premise that spreading cells generate enough membrane tension for TEM nucleation
59 and growth (Gonzalez-Rodriguez et al., 2012). Widening of TEMs is resisted by line tension, which
60 is partially explained by the membrane curvature generated by torus-like pores (Gonzalez-Rodriguez
61 et al., 2012; Stefani et al., 2017). After nucleation, an imbalance between the membrane and line
62 tension causes TEMs to passively expand up to the maximal equilibrium size, which is stabilized by
63 a newly formed stiff actomyosin cable that encircles TEMs (Stefani et al., 2017). TEMs are eventually
64 sealed by active cytoskeleton-based processes (e.g., lamellipodia formation or purse-string
65 contraction) (Maddugoda et al., 2011; Stefani et al., 2017). While considerable progress has been
66 made in understanding the interactions between the membrane and actin cytoskeleton regulatory
67 machinery in the control of TEMs, much remains to be known about the contribution of plasma
68 membrane mechanical properties.

69 We investigated these areas by analyzing TEM dynamics in primary human endothelial cells
70 subjected to polyunsaturated versus monounsaturated fatty acid diets. We show that membrane
71 enrichment in DHA-containing phospholipids increases the probability of TEM nucleation while
72 decreasing the width and the lifetime of transcellular tunnels.

73 **RESULTS**

74 **Comprehensive analysis of the phospholipids in HUVECs fed with fatty acid diets**

75 HUVECs represent a convenient endothelial cell model to study several aspects of TEM formation.
76 We first determined whether these cells are amenable to defined fatty acid diets aimed at changing
77 the acyl chain profile of their membrane phospholipids. We compared docosahexaenoic acid (DHA,
78 C22:6) with oleic acid (OA, C18:1) diets, i.e., the most polyunsaturated acyl chain *versus* the most
79 abundant monounsaturated acyl chain in PLs, respectively (Harayama and Riezman, 2018). HUVECs
80 were first subjected to medium with lipoprotein-depleted serum (LPDS) followed by a diet of LPDS
81 supplemented with bovine serum albumin (BSA) complexed either with docosahexaenoic acid (DHA,
82 C22:6) or oleic acid (OA, C18:1). A comprehensive analysis of the lipidome of HUVECs subjected
83 to the different diet conditions was conducted by comparing relative quantities of lipid species using
84 a Q Exactive mass spectrometer.

85 While lipid starvation conditions decreased the triglyceride (TG) storing form of acyl chains, we did
86 not detect significant changes in the relative distribution of phospholipid classes (Figure 1A and Sup.
87 Figure 1A). We monitored the cellular lipidome of HUVECs fed with FA diets for different times.
88 We recorded a massive increase in TG that peaked at 1 hour (Sup. Figure 2A). The incorporation of
89 fatty acids into phospholipids occurred with slower kinetics, reaching a plateau at 6 hours, most
90 notably for DHA incorporation into PC (Sup. Figure 2B). Importantly, the relative distribution of
91 phospholipid classes was conserved between conditions, except for PE, which was reduced by 25%
92 in the DHA-treated cells (Figure 1A).

93 As shown in Figure 1B and Sup1B, in contrast to OA, the DHA diet had an impact on the profile of
94 phospholipids, which show enrichment in DHA-containing PL species (Figure 1B and Sup. Figure
95 1B). Specifically, DHA was incorporated in large amounts in PC and PE, with a 4-fold increase in
96 PC(16:0/22:6) and a 2-fold increase in PE(18:0/22:6) (Figure 1B). In comparison, the remodeling of
97 the anionic lipids PS and PI was modest, although we recorded an increase in PI(18:0/22:6) at the
98 expense of PI(18:1/20:4), one of the major PI species. In sharp contrast, OA treatment had a narrow
99 and slight impact on the acyl chain profile of phospholipids, inducing a specific increase in
100 PL(18:1/18:1) at the cellular level, which was largely restricted to PC (Figure 1B). Overall, cells fed
101 with DHA displayed considerable enrichment with polyunsaturated phospholipids, which we

102 estimated as a polyunsaturated PC increase from 25% to 50%, at the expense of OA-containing PC
103 (Figure 1C and Sup. Figure 2D). Furthermore, the addition of OA to HUVECs had a minor impact
104 on the lipidome, which was already rich in OA-containing PLs and poor in DHA-containing lipids.

105 **Shifting the plasma membrane PL balance from the mono-unsaturated to the hexa-unsaturated** 106 **form**

107 The acyl chain profile of phospholipids varies according to subcellular localization (Antonny et al.,
108 2015). Thus, we determined the impact of both FA diet conditions on the composition of PLs at the
109 plasma membrane. For this experiment, we prepared giant plasma membrane vesicles (GPMVs)
110 corresponding to plasma membrane blebs (Figure 2A). We observed the expected enrichment of the
111 plasma membrane markers Annexin-V and Na⁺/K⁺ ATPase in the GPMV fractions (Figure 2B).
112 Markers of internal compartments were observed in the total cell membrane fractions but were largely
113 excluded from the GPMV fractions. The lipidomic analysis of the GPMVs compared to that of the
114 total membrane fractions showed an enrichment in PS and sphingomyelin (SM), which are known to
115 concentrate in the plasma membrane. In contrast, lipids characterizing membranes of internal
116 compartments, such as diglyceride (DG; ER and lipid droplets) and lysobisphosphatidic acid (LBPA;
117 late endosomes), were largely excluded from the GPMV fractions (Figure 2C). Moreover,
118 quantitative analysis of PL classes in the GPMV fraction established the conservation of PL class
119 distribution at the plasma membrane, including PE (Figure 2D).

120 We analyzed the changes in the acyl chain composition of PLs in the plasma membrane-derived
121 GPMVs prepared from cells subjected to the two fatty acid diets. As observed for the total membrane
122 fraction, the GPMV fraction from DHA-treated cells was enriched in DHA-containing PC, the
123 dominant PL class, by 10-fold (from 1.6% to 16.7%) and PE species by 2-fold (from 8.8% to 18.2%)
124 at the expense of monounsaturated species as compared to GPMV from OA-treated cells (Figure 2E).
125 Thus, the DHA diet triggered a 1.9-fold reduction in OA-containing PC compared to OA-treated cells.
126 Interestingly, these variations are accompanied by an increase in saturated PC species in agreement
127 with recent work by Levental et. al. (Levental et. al., 2020).

128 Our comprehensive analysis of the HUVEC lipidome establishes that these cells have a plasma
129 membrane intrinsically rich in OA-containing PLs, a profile that can be largely shifted to
130 polyunsaturated DHA-containing PLs upon exposure to a high-DHA fatty acid diet.

131 **The DHA diet leads to smaller pores in the TEM population**

132 Inhibition of the small GTPase RhoA by bacterial ExoC3-like toxins induces the nucleation and
133 expansion of TEMs (Boyer et al., 2006). This effect is triggered by a collapse of RhoA-driven

134 actomyosin contractility and leads to cell spreading and a reduction in cell thickness (Figure 3A)(Ng
135 et al., 2017). We first verified the absence of the impact of RhoA signaling shutdown on the proper
136 incorporation of OA or DHA into PLs. To this end, HUVECs were incubated in LPDS medium as
137 the sole treatment or in LPDS containing the RhoA-inhibitory C3-exoenzyme (ExoC3). Next, the
138 cells were incubated for 1 to 6 hours in LPDS medium supplemented with bovine serum albumin
139 (BSA) complexed with either OA or DHA fatty acids. We observed that ExoC3 treatment did not
140 interfere with the enrichment of DHA-PL or OA-PL species in cellular membranes (Sup. Figure 3),
141 suggesting that RhoA signaling did not impact the metabolism of OA/DHA acyl chains in a manner
142 that would interfere their proper incorporation into PLs species. In parallel, we measured similar level
143 of RhoA ADP-ribosylation in cells subjected to OA and DHA fatty acid diets (data not shown) and
144 verified the proper disruption of actin stress fibers due to ExoC3 action under the different diet
145 conditions (Figure 3B).

146 We analyzed the impact of OA or DHA treatment on the spreading of cells induced by ExoC3.
147 Measures of cell area showed no significant difference between the two diet conditions in non-
148 intoxicated cells (Figure 3C). When cells were treated with ExoC3, we recorded a 1.2-fold spreading
149 of both OA- and DHA-treated cells, indicating that cell enrichment in DHA-containing PL did not
150 significantly influence the extent of HUVECs spreading in response to the inhibition of RhoA.

151 Next, we analyzed TEM parameters on fixed cells stained with FITC-phalloidin to label filamentous
152 actin accumulating around TEMs. We observed that approximately 25% of cells displayed at least
153 one TEM with no significant difference between the cells cultured under the two fatty acid diet
154 conditions (Figure 3D). In this subpopulation, we recorded a net increase in the density of TEMs in
155 the DHA-treated cells of 3.5 ± 0.3 TEM/cell *versus* 2.5 ± 0.1 TEM/cell for the OA-fed cells (Figure
156 3E). In addition, we observed a 1.6-fold decrease in the TEM area in the DHA-treated cells compared
157 with the OA-treated cells, with $A_{\text{DHA}} = 5.6 \mu\text{m}^2$ *versus* $A_{\text{OA}} = 9.9 \mu\text{m}^2$, respectively (Figure 3F and
158 3G). Despite the moderate global effect of DHA on TEM median size, a thorough analysis of the
159 distribution of TEMs revealed that the DHA diet induced a major shift toward TEMs of small size
160 ($R < 1 \mu\text{m}$; 21% to 33%) at the expense of large TEMs ($R > 4 \mu\text{m}$; 24% to 14%) (Figure 3H). Altogether,
161 these results indicated that inhibition of RhoA and incorporation of DHA into phospholipids did not
162 interfere with each other, while DHA-PL enrichment in the plasma membrane led to an increase in
163 TEM density and a decrease in TEM size.

164 **The DHA diet increases TEM nucleation frequency**

165 TEM tunnels form labile openings (Figure 4A) (Video 1). After nucleation and growth, TEMs reach
166 a stable state in which they oscillate around a maximal area. After this period of latency, TEMs

167 undergo a phase of closure via actin-dependent processes involving either purse-string contraction or
168 membrane wave extension (Maddugoda et al., 2011). Here, we noticed that approximately 70% of
169 the TEMs resealed via a purse-string contraction phenomenon regardless of the fatty acid diet (not
170 shown).

171 To quantitatively analyze TEM dynamics, we recorded the cycles of TEM opening and closing by
172 time-lapse video in LifeAct-GFP-expressing cells, allowing us to determine the frequency of TEM
173 nucleation and their complete lifetime. Interestingly, this analysis revealed a critical impact of the
174 DHA fatty acid diet. Figure 4B shows that the DHA-fed cells had a higher frequency of opening
175 events during the recording period than OA-fed cells (Video 2 and 3). Mean values were $N=19.3$
176 events/h for the DHA-fed cells *versus* $N=8.9$ events/h for the OA-fed cells (Figure 4C). Moreover,
177 we measured that the lifetime for complete TEM opening and closing cycle was 1.7-fold shorter in
178 the DHA-fed cells than in OA-fed cells, i.e., mean values of 24.6 ± 1.8 min for the DHA-fed cells
179 *versus* 42.0 ± 4.0 min for the OA-fed cells (Figure 4D). TEM cycles encompass two dynamic phases
180 of opening and closure and a phase of latency where the TEM area oscillates within approximately
181 5% of its maximal size. While the time for TEM opening was not affected by DHA, we recorded a
182 decrease in the duration of both the latency and closure phases (Table 1). The probability of observing
183 a TEM in a cell depends on the product of TEM nucleation frequency by their lifetime. The net
184 consequences of reducing the TEM lifetime and increasing the nucleation rate in DHA-treated cells
185 explain the minimal difference in TEM density between the two conditions. We concluded that
186 membrane enrichment in DHA-PLs increases the nucleation rate of TEMs with short lifetimes.

187 **The DHA diet decreases cell thickness**

188 Using atomic force microscopy (AFM), we measured the elasticity of cells, which is mainly affected
189 by cortical actin (Figure 5A). RhoA inhibition greatly reduced cell elasticity, by 1.7-fold, as reported
190 (Ng et al., 2017). However, we measured similar elasticity in the cells subjected to the OA and DHA
191 treatments (5.1 ± 0.2 kPa *versus* 5.8 ± 0.3 kPa, respectively) (Figure 5B-C), suggesting negligible
192 impact of DHA enrichment on cortical elasticity.

193 On the other hand, we measured differences in the topology of the TEMs with AFM by scanning the
194 cell surface with zero force. Interestingly, DHA treatment decreased the cell thickness to 1.2-fold;
195 i.e., mean values for the DHA-fed cells was 164 ± 6 nm *versus* 190 ± 6 nm for the OA-fed cells
196 (Figure 5D). As previously reported, the TEM rim is elevated and forms a ridge structure (Maddugoda
197 et al., 2011). In accordance with the measures of cell thickness, the height of the TEM ridge was
198 decreased 1.2-fold in the DHA-enriched cells (Figure 5E). We concluded that DHA enrichment

199 decreases the thickness of TEMs without affecting the cell elasticity contributed by the cellular cortex
200 (Figure 5F).

201 **The impact of DHA-PL enrichment on TEM opening kinetics**

202 The maximal area reached by TEMs depends on two parameters: the relaxation of membrane tension
203 as TEMs open, which controls their opening speed, and the time required for a cell to encircle TEMs
204 with a stiff actomyosin cable that prevents further widening (Stefani et al., 2017). Dynamic
205 parameters were analyzed with a custom-made Icy-based program that automatically segments the
206 LifeAct-GFP-decorated actin-rich circumference of TEMs as a function of time (Figures 4A and 6A).
207 This analysis enabled us to determine the maximal area and opening and closing speeds.

208 Interestingly, we observed that, under LPDS conditions, approximately 11% of the TEMs in the OA-
209 treated cells *versus* 3% of the TEMs in the DHA-treated cells resumed their enlargement 104 ± 33
210 seconds after stabilization, i.e., after they had reached the first stable state (Sup. Figure 4), suggesting
211 that DHA-PL-rich membranes form pores with greater stability. In parallel, we performed a
212 comparative super-resolution stimulated emission depletion (STED) microscopy analysis of the actin
213 structures around the TEMs in the OA- and DHA-fed cells; i.e., we examined the typical actomyosin
214 belt and membrane wave-containing dendritic F-actin network (Stefani et al., 2017). No significant
215 difference in actin organization around the TEMs between the two conditions was recorded (Figure
216 6B). For the quantitative analysis, we focused on the first equilibrium state reached by the TEMs. We
217 recorded and defined the median size of the TEMs over the recording period (Figure 6C). We also
218 determined the initial speed of TEM opening, which correlates with membrane tension that drives the
219 opening of TEMs (Gonzalez-Rodriguez et al., 2012). A comparative analysis of the initial speeds of
220 opening between 10 and 20 seconds in the OA- and DHA-fed cells revealed no significant difference
221 between the DHA-fed cells ($V_{i-DHA} = 0.39 \mu\text{m}^2 \text{s}^{-1}$) and OA-fed cells ($V_{i-OA} = 0.47 \mu\text{m}^2 \text{s}^{-1}$) (Table 1).
222 In contrast, when we compared the median opening speed over the first 20-70 seconds, the values
223 were 1.4-fold lower for the DHA-fed cells ($V_{0-DHA} = 0.27 \mu\text{m}^2 \text{s}^{-1}$) than for the OA-fed cells ($V_{0-OA} =$
224 $0.38 \mu\text{m}^2 \text{s}^{-1}$) (Figure 6D). In parallel, we assessed the maximal size of the TEMs during the recording
225 periods. Consistent with measures of the fixed cells, the TEM maximal size was increased by
226 approximately 1.5-fold in the DHA-treated cells compared with the OA-treated cells, with $S_{\text{max-DHA}}$
227 $= 25 \pm 2 \mu\text{m}^2$ *versus* $S_{\text{max-OA}} = 37 \pm 7 \mu\text{m}^2$ (Figure 6E). In accordance with the TEM size of the fixed
228 cells, we recorded, in live cells, an increase in small ($R < 3 \mu\text{m}$) TEMs from 38% to 60% at the expense
229 of large ($R > 4 \mu\text{m}$) TEMs (from 42% to 20%) in the DHA-treated cells *vs* OA-treated cells (Figure
230 6F). Consistent with the significant decrease in TEM size and in the speed of opening recorded for
231 the DHA-fed cells, we observed no difference in the time to reach the maximal surface area, i.e., 179
232 ± 21 seconds for the OA-fed cells and 162 ± 23 seconds for the DHA-fed cells (Figure 6G). Taken

233 together, our data establish that, despite having no effect on the initial speed of opening, DHA-PLs
234 reduced the overall TEM opening speed, thereby impacting the maximal TEM size.

235 The cellular dewetting physical model, which describes TEM dynamics (Gonzalez-Rodriguez et al.,
236 2012; Stefani et al., 2017), indicates that the initial TEM opening speed (at the very first opening
237 stage) is proportional to the membrane tension. Because the initial speed was similar between the
238 OA- and DHA-treated cells, the average cell membrane tension is expected to be comparable between
239 the two conditions. This conclusion was supported by the observation of comparable spreading of the
240 OA- and DHA-fed cells because the cell spreading area correlates with cell membrane tension.

241 According to the physical model, an estimate of the global membrane bending rigidity is given by

$$242 \quad \kappa \approx \frac{k_B T A_{cell}}{8\pi N A_{max}},$$

243 where N is the number of TEMs simultaneously evident per cell, A_{max} is the maximum area of a TEM,
244 k_B is the Boltzmann constant, T is the temperature, and A_{cell} is the total cell spreading area. This
245 equation is based on the relaxation of membrane tension during TEM opening, as described by
246 Helfrich's law (Helfrich, 1973). Membrane relaxation is larger when the bending rigidity κ is larger.
247 In deriving this equation, we assume a joint effect of N , the number of simultaneous TEMs on
248 membrane, on tension relaxation, which affects each TEM. Because the cell spreading area A_{cell} is
249 the same in the OA- and DHA-fed conditions, this equation indicates that the global bending rigidity
250 κ is inversely proportional to the product $N \cdot A_{max}$. A comparison between the two conditions leads to

$$251 \quad \frac{\kappa_{DHA}}{\kappa_{OA}} \approx \frac{N_{OA} \cdot A_{max,OA}}{N_{DHA} \cdot A_{max,DHA}} = 1.05,$$

252 whose difference from 1 is not statistically significant. Thus, this calculation suggests that the average
253 bending rigidity at the cellular scale is similar between cells in the OA- and DHA-fed conditions.

254 Overall, the interpretation of the experimentally observed TEM dynamics in light of the physical
255 model suggests that average tension and bending rigidity of the membrane in association to cortex
256 composite material are unchanged in cells subjected to these OA and DHA treatments. This result
257 points to a regulation mechanism of global membrane dynamics controlling TEM opening that is
258 robust despite changes in membrane lipid composition, which dictate the TEM nucleation rate.

259 **Discussion**

260 Since the discovery of the cellular dewetting phenomenon, the contribution of plasma membrane
261 mechanical properties to the dynamics of TEMs remains to be elucidated. Here, we show that the

262 DHA fatty acid diet induces a shift in the acyl chain composition of phospholipids at the plasma
263 membrane of endothelial cells, with an increase in DHA-PLs, and greatly affects TEM dynamics.
264 Remarkably, DHA-PLs enrichment changes membrane dynamics, i.e., nucleation and lifetime of
265 TEMs, in a coordinated manner to ensure the relative conservation of the overall TEM width per cell,
266 and shifts the size range of the TEMs to a smaller range via reduction of opening speed. Moreover,
267 DHA-PL enrichment reduced uncontrolled resume TEM growth. Collectively, these findings indicate
268 that DHA-PL facilitates the nucleation of smaller TEMs displaying shorter lifetimes. Conversely,
269 deficient DHA-PLs may lead to the opening of unstable and wider TEMs.

270 DHA-PL enrichment at the plasma membrane leads to a decrease in TEM maximal size and an
271 increase in the number of simultaneous TEMs present in a cell. Strikingly, the total maximum TEM
272 area, obtained as the product of the maximum area per TEM by the number of TEMs, remains
273 constant between OA- and DHA-fed cells. Together with the physical interpretation provided by the
274 cell dewetting model (Boyer et al., 2006; Gonzalez-Rodriguez et al., 2012), this observation suggests
275 a conservation of the global membrane mechanical response at the scale of the entire cell. Therefore,
276 whereas DHA-PL enrichment promotes the frequency of TEM nucleation events by 2-fold, the
277 regulation of membrane mechanical characteristics at the scale of the whole cell appears sufficiently
278 robust for the cell to cope with these changes, leading to a conserved total TEM area over the cell.
279 To maintain the overall conservation of the TEM area, DHA-PL-enriched cells compensate for the
280 increase in the nucleation rate by reducing the TEM opening speed and thereby maximal size.
281 Moreover, we record a decrease of lifetime that is ascribed to a reduction in both the phase of latency
282 and closure without affecting the initial opening phase.

283 Enrichment of DHA-PLs at the plasma membrane decreases the speed of opening, while the time to
284 reach the maximal size is not affected. Consistent with the conserved time frame of TEM opening,
285 we observed that actin organization around TEMs formed in the DHA- and OA-fed cells showed no
286 significant difference. Nevertheless, we observed that TEMs were less stable in the OA-fed cells and
287 were more prone to resume their enlargement. Lower TEM stability may reflect defects in the
288 recruitment or activity of actin-crosslinking proteins around the edge of the TEMs that are yet to be
289 identified. Importantly, we previously reported that the absence of TEM stabilization is linked to
290 massive hemorrhage induced by an ExoC3-chimeric toxin derived from the *B. anthracis* lethal toxin
291 (Rolando et al., 2009). This provides additional evidence that DHA might play a key function in the
292 appropriate homeostasis of the endothelial barrier, pointing to a likely role in stabilizing large pore
293 structures that are observed along the vascular system (see for review) (Aird, 2007; Lemichez et al.,
294 2010).

295 Finally, we found a decrease in cell thickness in the DHA-PL-enriched cells. Applying force to the
296 apical part of the plasma membrane of normal growing cells is sufficient to bring membranes in close
297 apposition and trigger the nucleation and opening of transcellular pores (Ng et al., 2017). Consistent
298 with this idea, HUVECs intoxicated with ExoC3 were thinner than the control cells, i.e., with medians
299 near the edge of the cells at 332 nm *versus* 462 nm, respectively (Ng et al., 2017). It is therefore
300 reasonable to think that enriching DHA-PLs may enhance close plasma membrane apposition and
301 increase the probability of pore nucleation by reducing the energy cost to initiate a fusion event. As
302 discussed below, changes in the asymmetric distribution of polyunsaturated phospholipids in DHA-
303 PL-enriched cells might contribute to membrane apposition and fusion.

304 The plasma membrane is asymmetric in both lipid classes and lipid unsaturation (Lorent, et al., 2020).
305 The outer leaflet contains mostly PC and SM, whereas the inner leaflet contains 3 major PL classes,
306 namely, PC, PE and PS. Coarse-grained molecular dynamics simulations on asymmetric phospholipid
307 bilayers show that DHA-PLs facilitate membrane tubulation only when they are located on the convex
308 side of the deformation (Tiberti et al., 2020). This effect is due to the ability of DHA-PLs to switch
309 between several twisted conformations in a convex environment, notably to adopt a conformation in
310 which the polyunsaturated acyl chain occupies voids between polar heads and invades the water-lipid
311 interface. DHA-fed cells showed a 10-fold higher content of DHA-PC species at the plasma
312 membrane than was evident in the OA-fed cells (16.7 and 1.6%, respectively). In contrast, the amount
313 of DHA-PE and DHA-PS species was only approximately 2-fold higher in the DHA-fed HUVECs
314 (18.2% and 14.1%, respectively) than in OA-fed cells (8.8% and 9.5%, respectively). Consequently,
315 the DHA diet might not only increase the overall DHA-PL content of the plasma membrane but might
316 also reduce DHA asymmetry because PC is the most affected PL and is quite evenly distributed
317 between the two leaflets. Such a change coupled with the lack of contractile forces mediated by the
318 cytoskeleton, due to the ExoC3 effect, may favor large undulations in the plasma membrane. High
319 levels of polyunsaturated PLs on the inner and outer sides of the plasma membrane would be
320 beneficial for sustaining large membrane undulations, which are a series of convex and concave
321 deformations. As a prerequisite for hemifusion, the decrease in cell thickness in the DHA-fed cells
322 likely increases the probability of close apposition between the two undulating apical and basal
323 membranes, explaining the increase in the frequency and the number of TEMs. Further experimental
324 work on model membrane systems and coarse-grained simulations of TEM formation will help test
325 this idea.

326

327

328 **Materials and Methods**

329 **Reagents**

330 LifeAct-GFP-pCMV plasmid was purchased from Ibidi. Antibodies used in this study were mouse
331 anti-Na⁺/K⁺ ATPase (Santa Cruz), Annexin II (BD Transduction Laboratories), Calregulin (Santa
332 Cruz), ERGIC 54 (Santa Cruz), and LAMP1 (BD Transduction Laboratories), and sheep anti-TGN46
333 (BioRad). Secondary Alexa Fluor-conjugated antibodies were from ThermoFisher and secondary
334 peroxidase-conjugated antibodies were from Jackson ImmunoResearch. For immunofluorescence,
335 hoechst 33342 and Alexa-fluor conjugated FITC-phalloidin were purchased from ThermoFisher. For
336 STED imaging, Star635-phalloidin was purchased from Abberior. C3 toxin was purified as described
337 (Boyer et al., 2006).

338 OA and DHA fatty acids (Sigma-Aldrich) were conjugated with fatty acid-free BSA (Sigma-Aldrich).
339 Fatty acids were dissolved in warm (60°C) 200 mM NaOH and conjugated with BSA at the molar
340 ratio of 5:1. The FA-BSA was aliquoted and filled with argon to minimalized oxidation. Lipoprotein
341 depleted serum (LPDS) were prepared as described (Renaud et al., 1982). In brief, fetal bovine serum
342 was loaded with NaBr to increase density to 1.21 g/ml followed by ultracentrifugation at 220,000g at
343 10°C for 48 hours in a Beckman Ti70 rotor. After centrifugation, a greasy layer containing
344 lipoproteins appeared on the top of the tube was removed and the supernatant was centrifuged again
345 at 220,000g at 10°C for 24 hours to remove the remaining lipoprotein. Later the serum was dialyzed
346 intensively with Earle buffer (115 mM NaCl, 5.4 mM KCl, 1.8 mM CaCl₂, 0.8 mM MgSO₄, 5 mM
347 Hepes, pH 7.4) in 14 kD cut-off dialysis membrane (Spectrum) for 72 hours and the buffer was
348 refreshed for at least 5 times.

349 **Cell Culture, Treatment, and Transfection**

350 HUVECs were cultured and electroporated, as described in (Stefani et al., 2017). In brief, HUVECs
351 were trypsinized and suspended in Ingenio Solution (Mirus) containing the targeted DNA (10 g per
352 10⁶ cells) in a 4-mm cuvette (CellProjects). Then, cells were electroporated at 300 V, 450 μF, one
353 pulse by GenePulser electroporator (BioRad).

354 To enrich HUVECs with OA or DHA, cells were washed twice with PBS and lipid starved in LPDS
355 medium (Human endothelial SFM, 20% LPDS, 20 ng/ml FGF, 10 ng/ml EGF, 1 μg/ml Heparin, and
356 Zellshield) overnight with or without 50 μg/ml ExoC3 toxin prepared as described in (Boyer et al.,
357 2006) as indicated. Before experiments, cells were supplemented with 125 μM FA-BSA for 6 hr.

358 **Lipid extraction and Lipidomic**

359 A clear description of lipidomic analysis was in supplementary material. Briefly, a modified Bligh
360 and Dyer (Bligh and Dyer, 1959) extraction was carried out on cell pellets and purified cell
361 membranes in order to extract lipids, which were then separated by chromatography with a C18
362 column and an appropriate gradient of mobile phase. The mass spectrometry analyzes were done
363 using a Q-Exactive mass spectrometer (ThermoFisher) operating in data dependent MS/MS mode
364 (dd-MS2) and the data were then processed using LipidSearch software v4.1.16 (ThermoFisher) in
365 product search mode.

366 **Video Microscope**

367 HUVECs were electroporated with LifeAct-GFP-pCMV as described above and seeded on gelatin
368 coated polymer coverslip dish (Ibidi). After recovering for 24 hours from transfection, cells were lipid
369 starved as in LPDS containing medium overnight. OA-BSA and DHA-BSA were added to the cells
370 to the final concentration at 125 μ M for 6 hours prior to video recording. Cells were supplemented
371 with 25 mM Hepes (pH 7.4) and recorded on a 37°C heated stage of Nikon Ti inverted microscope
372 using Ultraview spinning disk confocal system (Perkin Elmer). For the TEM opening, images were
373 taken every 10 seconds for 1 hour. For TEM closure, images were taken every minute for 3 hour to
374 avoid phototoxicity and bleaching during the acquisition. Acquired videos were analyzed by an Icy
375 based automatic protocol. Acquired videos were analyzed by an Icy based automatic protocol.

376 **Image Analysis**

377 Time-lapse videos were analysed with the Icy software (de Chaumont et al., 2012) and segmentation
378 plugins (icy.bioimageanalysis.org/plugin). Each TEM was first manually identified as a region of
379 interest (ROI). Considering the gradual recruitment of LifeAct-GFP around TEMs, it was difficult to
380 properly identify the edge of TEMs. Indeed, the non-homogeneous contrast at the TEM border leads
381 to a difficult clipping process. To overcome this challenge, we used advanced image analysis methods
382 like the Active Contour plugin to properly track TEM over time. This allowed us in particular to
383 determine the surface of the TEMs at each time point. We then applied a post-processing analysis to
384 filter the TEMs and automatically eliminate remaining wrong segmentations. For instance we
385 discarded any TEMs that display excessive growing air. In the end this protocol allowed us to provide
386 precise statistics of the TEM dynamics, such as the evolution of the area, the diameters or the
387 sphericity of TEMs over time.

388 **GPMV purification**

389 Cells were enriched with OA or DHA as described above followed by induction of GPMV as
390 described (Sezgin et al., 2012). Cells were washed with GPMV buffer (10 mM HEPES, 150 mM

391 NaCl, 2 mM CaCl₂, pH 7.4) twice and incubated with GPMV buffer containing 25 mM PFA and 2
392 mM DTT for 1 hour. Blebs were formed and released as GPMVs. Supernatant was collected and
393 centrifuged at 100 g for 5 minutes to remove cell debris. Supernatant containing GPMVs was
394 centrifuged in Beckman Type 70 Ti rotor at 20,000 g at 4 °C for 1 hr. GPMVs appeared as a
395 transparent pellet and was collected for lipidomic analysis or western blot. For western blot, GPMV
396 was lysed in Leammli buffer (50 mM Tris pH 7.4, EDTA 5mM, 2% SDS) and protein concentration
397 was determined with BCA assay kit (Thermo Fisher) using BSA suspended in Leammli buffer as
398 standard. GPMV lysate was adjusted to the same protein quantity. Glycerol, β-mercaptoethanol, and
399 bromophenol blue were added to final concentration of 10%, 5% and 0.004%. Protein samples were
400 analyzed by SDS-PAGE western blot.

401 **STED**

402 Cells were grown on H1.5 glass coverslips coated with 10 μg/ml fibronectin. After treatment, cells
403 were fixed with 4% PFA/0.1% glutaraldehyde for 15 minutes at room temperature. Cells were washed
404 with PBS, quenched in 50 mM NH₄Cl for 15 minutes followed by permeabilizing in IF buffer
405 (PBS/0.05% saponin/0.2 % BSA) for 30 minutes. Later, the cells were stained with 1 μM Star635-
406 phalloidin (Abberior) for 1 hr followed by 3 washes with IF buffer for 5 minutes and a final wash in
407 H₂O. The cells were mounted in Mount Solid Antifade (Abberior) following manufacturer's
408 instruction. Stimulated Emission Depletion (STED) imaging was performed by TCS STED SP8
409 (Leica) using a APO 93X/1.3 motCORR lens. The excitation laser was at 633 nm and pulse depletion
410 laser at 775 nm. STED images were deconvolved using Huygens with 5 iterations.

411 **Atomic force microscope measurement of TEM topology**

412 AFM experiments were carried out on a JPK NanoWizardIII mounted on a Zeiss Axio Observer.Z1.
413 For elasticity measurements PFQNM-LC-A-Cal cantilevers (Bruker) were used with the SNAP
414 calibration method (Schillers et al., 2017). The AFM was operated in QI mode on the cytoplasmic
415 region of living cells to record a 10 μm , 20x20 pixels map of force curves with 2 μm ramp length,
416 200 pN force trigger and 50μm/s tip velocity. Force maps were computed using in-house software
417 (pyAF) for the fitting of the indentation up to 40 nm using Hertz model. For height measurements of
418 TEMs Olympus AC40 cantilevers were used with the SADER calibration method (Sader et al., 2016).
419 A QI map of 150x150 pixels bigger than the size of the TEM was recorded on 4 % PFA fixed cells
420 with an 800-nm ramp and 100 μm/s tip velocity. We then computed the zero-force topography by
421 determining the point of contact, and drew several profiles across the TEM to measure its diameter
422 and the height of the cell at the border. This was all performed on the JPK analysis software.

423

424 **Physical model of TEM opening**

425 In the physical model for TEM opening dynamics (Gonzalez-Rodriguez et al., 2012), the driving
426 force for opening is given by

$$427 \quad F_d = 2\sigma - \frac{\tilde{T}}{R},$$

428 where σ is the membrane tension, \tilde{T} is the line tension and R is the TEM radius. The membrane
429 tension σ depends on R through Helfrich's law, which here we write in a generalized form to account
430 for the coexistence of N simultaneous TEMs in the same cell:

$$431 \quad \sigma = \sigma_0 \exp\left[-\frac{(\sum_{i=1}^N R_i)^2}{NR_c^2}\right],$$

432 where $R_c^2 = (R_{\text{cell}}^2 k_B T)/(8\pi\kappa)$ is the so-called critical radius, with R_{cell} the total cell radius, k_B the
433 Boltzmann constant, T the temperature, and κ the membrane bending rigidity. Due to actin cable
434 polymerization around the TEM, the line tension is not a constant but rather it increases with time,
435 which can be represented by a linear increase $\tilde{T} \sim \alpha t$ (Stefani et al., 2017). The dynamics of TEM
436 opening are governed by a balance between driving force and cell-substrate friction, characterized by
437 a friction coefficient μ . For the case of N identical TEMs, this balance results in the following
438 differential equation:

$$439 \quad \mu R^2 \frac{dR}{dt} = 2\sigma_0 R \exp\left(-\frac{NR^2}{R_c^2}\right) - \alpha t.$$

440 This equation can be solved numerically. However, insight can be gained by analytical
441 approximations. First, in the limit of short time, when R is small, the equation can be approximated
442 as

$$443 \quad v_0 = \frac{dA}{dt} = \frac{4\pi\sigma_0}{\mu},$$

444 where $A = \pi R^2$ is the TEM area. Therefore, TEM opening speed at short time, v_0 , is proportional to the
445 undisturbed cell membrane tension σ_0 .

446 Second, the dependence of the maximum TEM area $A_{\text{max}} = \pi R_{\text{max}}^2$ on the membrane parameters σ_0
447 and κ can be estimated by the following approximation. Let us suppose that the initial opening speed
448 v_0 is an acceptable estimate of the average opening speed. Then, the opening time t_{max} is related to the
449 maximum TEM area by

450
$$t_{\max} \approx \frac{\mu A_{\max}}{4\pi\sigma_0}.$$

451 Moreover, at $t = t_{\max}$, the opening stops and $dR/dt=0$. By replacing these two results in the differential
452 equation, we obtain the following approximate relationship:

453
$$x \exp x^2 = \frac{8 N \sigma_0^2}{\mu \alpha R_c},$$

454 where we have defined $x = N R_{\max}/R_c$. The nondimensional parameter on the right-hand side of this
455 expression is slightly larger than 1, which requires x to be somewhat larger than 1. In this range of
456 values, small changes in x yield large changes of the exponential function, implying that x is weakly
457 dependent on the right-hand side. Therefore, x will remain approximately constant for moderate
458 changes of σ_0 , implying that $NR_{\max} \sim R_c \sim 1/\kappa^{1/2}$. This result shows that the maximum TEM size is
459 very sensitive to κ but rather insensitive to σ_0 . We thus obtain the following estimate of the membrane
460 bending rigidity:

461
$$\kappa \approx \frac{k_B T A_{cell}}{8\pi N A_{max}}.$$

462

463 **Statistical analysis.** Data are showed as the medium \pm s.e.m. unless otherwise indicated. Data were
464 analyzed with unpaired and two-tailed Mann-Whitney test unless otherwise indicated. P-value for
465 *P<0.05, **P<0.01, ***P<0.001 and ****P<0.0001 were considered statistically significant. The
466 statistical software used was Prism 8 (GraphPad Software, San Diego, CA, USA).

467

468 **Acknowledgments.** This work was supported by a grant from the Fondation pour la Recherche
469 Médicale (Convention DEQ20180339156 Equipes FRM 2018), the Agence Nationale de la
470 Recherche (ANR-11-LABX-0028-01, ANR-15-CE18-0016, ANR 10-EQPX-04-01, ANR- 10-
471 INBS- 04, and ANR- 10- LABX-62-IBEID) and FEDER 12,001,407. MCT was supported by a PhD
472 fellowship from the Labex Signallife PhD Programme and by the Fondation pour la Recherche
473 Médicale (Contrat FDT201904008135). We thank Blandine Madji Hounoum for pilot lipidomics
474 experiments. Frédéric Brau and Sophie Abelanet for support in light and STED microscopy. James
475 Muncey for its helps in time-lapse analyses with Icy software.

476

477 **References**

- 478 Aird, W.C. 2007. Vascular bed-specific thrombosis. *Journal of Thrombosis and Haemostasis*. 5:283-
479 291.
- 480 Antonny, B., S. Vanni, H. Shindou, and T. Ferreira. 2015. From zero to six double bonds:
481 phospholipid unsaturation and organelle function. *Trends in Cell Biology*. 25:427-436.
- 482 Barelli, H., and B. Antonny. 2016. Lipid unsaturation and organelle dynamics. *Current Opinion in*
483 *Cell Biology*. 41:25-32.
- 484 Baudin, B., A. Bruneel, N. Bosselut, and M. Vaubourdolle. 2007. A protocol for isolation and culture
485 of human umbilical vein endothelial cells. *Nature Protocols*. 2:481-485.
- 486 Bazinet, R.P., and S. Layé. 2014. Polyunsaturated fatty acids and their metabolites in brain function
487 and disease. *Nature Reviews Neuroscience*. 15:771-785.
- 488 Bligh, E.G., and W.J. Dyer. 1959. A RAPID METHOD OF TOTAL LIPID EXTRACTION AND
489 PURIFICATION. *Canadian Journal of Biochemistry and Physiology*. 37:911-917.
- 490 Boyer, L., A. Doye, M. Rolando, G. Flatau, P. Munro, P. Gounon, R. Clément, C. Pulcini, M.R.
491 Popoff, A. Mettouchi, L. Landraud, O. Dussurget, and E. Lemichez. 2006. Induction of transient
492 macroapertures in endothelial cells through RhoA inhibition by Staphylococcus aureus factors. *The*
493 *Journal of Cell Biology*. 173:809-819.
- 494 Braakman, S.T., J.E. Moore, C.R. Ethier, and D.R. Overby. 2016. Transport across Schlemm's canal
495 endothelium and the blood-aqueous barrier. *Experimental Eye Research*. 146:17-21.
- 496 Caires, R., F.J. Sierra-Valdez, J.R.M. Millet, J.D. Herwig, E. Roan, V. Vásquez, and J.F. Cordero-
497 Morales. 2017. Omega-3 Fatty Acids Modulate TRPV4 Function through Plasma Membrane
498 Remodeling. *Cell Reports*. 21:246-258.
- 499 de Chaumont, F., S. Dallongeville, N. Chenouard, N. Hervé, S. Pop, T. Provoost, V. Meas-Yedid, P.
500 Pankajakshan, T. Lecomte, Y. Le Montagner, T. Lagache, A. Dufour, and J.C. Olivo-Marin. 2012.
501 Icy: an open bioimage informatics platform for extended reproducible research. *Nature methods*.
502 9:690-696.
- 503 Gonzalez-Rodriguez, D., M.P. Maddugoda, C. Stefani, S. Janel, F. Lafont, D. Cuvelier, E. Lemichez,
504 and F. Brochard-Wyart. 2012. Cellular Dewetting: Opening of Macroapertures in Endothelial Cells.
505 *Physical Review Letters*. 108:218105.
- 506 Harayama, T., and H. Riezman. 2018. Understanding the diversity of membrane lipid composition.
507 *Nature Reviews Molecular Cell Biology*. 19:281-296.
- 508 Helfrich, W. 1973. Elastic properties of lipid bilayers: theory and possible experiments. *Zeitschrift*
509 *fur Naturforschung. Teil C: Biochemie, Biophysik, Biologie, Virologie*. 28:693-703.
- 510 Iizuka-Hishikawa, Y., D. Hishikawa, J. Sasaki, K. Takubo, M. Goto, K. Nagata, H. Nakanishi, H.
511 Shindou, T. Okamura, C. Ito, K. Toshimori, T. Sasaki, and T. Shimizu. 2017. Lysophosphatidic acid
512 acyltransferase 3 tunes the membrane status of germ cells by incorporating docosahexaenoic acid
513 during spermatogenesis. *J Biol Chem*. 292:12065-12076.
- 514 Jeffrey, B.G., and M. Neuringer. 2009. Age-Related Decline in Rod Phototransduction Sensitivity in
515 Rhesus Monkeys Fed an n-3 Fatty Acid–Deficient Diet. *Investigative Ophthalmology & Visual*
516 *Science*. 50:4360-4367.

- 517 Lemichez, E., M. Lecuit, X. Nassif, and S. Bourdoulous. 2010. Breaking the wall: targeting of the
518 endothelium by pathogenic bacteria. *Nat Rev Micro.* 8:93-104.
- 519 Lemichez, E., D. Gonzalez-Rodriguez, P. Bassereau, and F. Brochard-Wyart. 2013. Transcellular
520 tunnel dynamics: Control of cellular dewetting by actomyosin contractility and I-BAR proteins.
521 *Biology of the Cell.* 105:109-117.
- 522 Levayer, R., and T. Lecuit. 2012. Biomechanical regulation of contractility: spatial control and
523 dynamics. *Trends Cell Biol.* 22:61-81.
- 524 Levental, K.R., E. Malmberg, J.L. Symons, Y.-Y. Fan, R.S. Chapkin, R. Ernst, and I. Levental. 2020.
525 Lipidomic and biophysical homeostasis of mammalian membranes counteracts dietary lipid
526 perturbations to maintain cellular fitness. *Nature Communications.* 11:1339
- 527 Lorent, J.H., K.R. Levental, L. Ganesan, G. Rivera-Longsworth, E. Sezgin, M. Doktorova, E. Lyman,
528 and I. Levental. 2020. Plasma membranes are asymmetric in lipid unsaturation, packing and protein
529 shape. *Nature Chemical Biology.* 16:644-652.
- 530 Maddugoda, Madhavi P., C. Stefani, D. Gonzalez-Rodriguez, J. Saarikangas, S. Torrino, S. Janel, P.
531 Munro, A. Doye, F. Prodon, M. Aurrand-Lions, Pierre L. Goossens, F. Lafont, P. Bassereau, P.
532 Lappalainen, F. Brochard, and E. Lemichez. 2011. cAMP Signaling by Anthrax Edema Toxin Induces
533 Transendothelial Cell Tunnels, which Are Resealed by MIM via Arp2/3-Driven Actin Polymerization.
534 *Cell Host & Microbe.* 10:464-474.
- 535 Manni, M.M., M.L. Tiberti, S. Pagnotta, H. Barelli, R. Gautier, and B. Antonny. 2018. Acyl chain
536 asymmetry and polyunsaturation of brain phospholipids facilitate membrane vesiculation without
537 leakage. *eLife.* 7:e34394.
- 538 Munro, P., M. Benchetrit, M.-A. Nahori, C. Stefani, R. Clément, J.-F. Michiels, L. Landraud, O.
539 Dussurget, and E. Lemichez. 2010. The Staphylococcus aureus Epidermal Cell Differentiation
540 Inhibitor Toxin Promotes Formation of Infection Foci in a Mouse Model of Bacteremia. *Infection
541 and Immunity.* 78:3404-3411.
- 542 Ng, W.P., K.D. Webster, C. Stefani, E.M. Schmid, E. Lemichez, P. Bassereau, and D.A. Fletcher.
543 2017. Force-induced transcellular tunnel formation in endothelial cells. *Molecular Biology of the Cell.*
544 28:2650-2660.
- 545 Pinot, M., S. Vanni, S. Pagnotta, S. Lacas-Gervais, L.-A. Payet, T. Ferreira, R. Gautier, B. Goud, B.
546 Antonny, and H. Barelli. 2014. Polyunsaturated phospholipids facilitate membrane deformation and
547 fission by endocytic proteins. *Science.* 345:693-697.
- 548 Randall, A.S., C.-H. Liu, B. Chu, Q. Zhang, S.A. Dongre, M. Juusola, K. Franze, M.J.O. Wakelam,
549 and R.C. Hardie. 2015. Speed and Sensitivity of Phototransduction in Drosophila Depend on Degree
550 of Saturation of Membrane Phospholipids. *The Journal of Neuroscience.* 35:2731-2746.
- 551 Renaud, J.F., A.M. Scanu, T. Kazazoglou, A. Lombet, G. Romey, and M. Lazdunski. 1982. Normal
552 serum and lipoprotein-deficient serum give different expressions of excitability, corresponding to
553 different stages of differentiation, in chicken cardiac cells in culture. *Proc Natl Acad Sci U S A.*
554 79:7768-7772.
- 555 Rolando, M., P. Munro, C. Stefani, P. Auberger, G. Flatau, and E. Lemichez. 2009. Injection of
556 Staphylococcus aureus EDIN by the Bacillus anthracis Protective Antigen Machinery Induces
557 Vascular Permeability. *Infection and Immunity.* 77:3596-3601.

558 Romero, L.O., A.E. Massey, A.D. Mata-Daboin, F.J. Sierra-Valdez, S.C. Chauhan, J.F. Cordero-
559 Morales, and V. Vásquez. 2019. Dietary fatty acids fine-tune Piezo1 mechanical response. *Nature*
560 *Communications*. 10:1200.

561 Sader, J.E., R. Borgani, C.T. Gibson, D.B. Haviland, M.J. Higgins, J.I. Kilpatrick, J. Lu, P. Mulvaney,
562 C.J. Shearer, A.D. Slattery, P.-A. Thorén, J. Tran, H. Zhang, H. Zhang, and T. Zheng. 2016. A virtual
563 instrument to standardise the calibration of atomic force microscope cantilevers. *Review of Scientific*
564 *Instruments*. 87:093711.

565 Salbreux, G., G. Charras, and E. Paluch. 2012. Actin cortex mechanics and cellular morphogenesis.
566 *Trends Cell Biol*. 22:536-545.

567 Schillers, H., C. Rianna, J. Schäpe, T. Luque, H. Doschke, M. Wälte, J.J. Uriarte, N. Campillo, G.P.A.
568 Michanetzis, J. Bobrowska, A. Dumitru, E.T. Herruzo, S. Bovio, P. Parot, M. Galluzzi, A. Podestà,
569 L. Puricelli, S. Scheuring, Y. Missirlis, R. Garcia, M. Odorico, J.-M. Teulon, F. Lafont, M. Lekka, F.
570 Rico, A. Rigato, J.-L. Pellequer, H. Oberleithner, D. Navajas, and M. Radmacher. 2017. Standardized
571 Nanomechanical Atomic Force Microscopy Procedure (SNAP) for Measuring Soft and Biological
572 Samples. *Scientific Reports*. 7:5117.

573 Schimmel, L., N. Heemskerk, and J.D. van Buul. 2017. Leukocyte transendothelial migration: A local
574 affair. *Small GTPases*. 8:1-15.

575 Sezgin, E., H.-J. Kaiser, T. Baumgart, P. Schwille, K. Simons, and I. Levental. 2012. Elucidating
576 membrane structure and protein behavior using giant plasma membrane vesicles. *Nature Protocols*.
577 7:1042-1051.

578 Shindou, H., H. Koso, J. Sasaki, H. Nakanishi, H. Sagara, K.M. Nakagawa, Y. Takahashi, D.
579 Hishikawa, Y. Iizuka-Hishikawa, F. Tokumasu, H. Noguchi, S. Watanabe, T. Sasaki, and T. Shimizu.
580 2017. Docosahexaenoic acid preserves visual function by maintaining correct disc morphology in
581 retinal photoreceptor cells. *Journal of Biological Chemistry*. 292:12054-12064.

582 Stefani, C., D. Gonzalez-Rodriguez, Y. Senju, A. Doye, N. Efimova, S. Janel, J. Lipuma, M.C. Tsai,
583 D. Hamaoui, M.P. Maddugoda, O. Cochet-Escartin, C. Prévost, F. Lafont, T. Svitkina, P. Lappalainen,
584 P. Bassereau, and E. Lemichez. 2017. Ezrin enhances line tension along transcellular tunnel edges
585 via NMIIa driven actomyosin cable formation. *Nature Communications*. 8:15839.

586 Tanguy, E., P. Costé de Bagneaux, N. Kassas, M.-R. Ammar, Q. Wang, A.-M. Haeberlé, J.
587 Raherindratsara, L. Fouillen, P.-Y. Renard, M. Montero-Hadjadje, S. Chasserot-Golaz, S. Ory, S.
588 Gasman, M.-F. Bader, and N. Vitale. 2020. Mono- and Poly-unsaturated Phosphatidic Acid Regulate
589 Distinct Steps of Regulated Exocytosis in Neuroendocrine Cells. *Cell Reports*. 32:108026.

590 Tiberti, M.L., B. Antonny, and R. Gautier. 2020. The transbilayer distribution of polyunsaturated
591 phospholipids determines their facilitating effect on membrane deformation. *Soft Matter*. 16:1722-
592 1730.

593 Tixier-Vidal, A., R. Picart, C. Loudes, and A.F. Bauman. 1986. Effects of polyunsaturated fatty acids
594 and hormones on synaptogenesis in serum-free medium cultures of mouse fetal hypothalamic cells.
595 *Neuroscience*. 17:115-132.

596 van Meer, G., D.R. Voelker, and G.W. Feigenson. 2008. Membrane lipids: where they are and how
597 they behave. *Nat Rev Mol Cell Biol*. 9:112-124.

598 Yuki, K., H. Shindou, D. Hishikawa, and T. Shimizu. 2009. Characterization of mouse
599 lysophosphatidic acid acyltransferase 3: an enzyme with dual functions in the testis. *J Lipid Res*.
600 50:860-869.

602 **FIGURE LEGENDS**

603 **FIGURE 1. Analysis of phospholipid classes in HUVEC submitted to oleic acid (OA) versus**
604 **docosahexaenoic acid (DHA).**

605 (A) Global fold change of phosphatidyl choline (PC), ethanolamine (PE), serine (PS) and inositol (PI)
606 classes from HUVEC submitted to OA- or DHA-diet for 6 hours compared to FBS- or LPDS-cultured
607 HUVEC. (B) Lipidic profiles comparison of the different PL classes: PC, PE, PS and PI upon OA-
608 diet, DHA-diet compared to controls (FBS and LPDS). Values were normalized individually to the
609 sum of each PL classes. (C) PL species distribution regarding their number of double bond (level of
610 unsaturation): from zero to 6 double bonds as illustrated in figure 1B. AA and DHA contain 4 and 6
611 double bonds, respectively. LPDS = lipoprotein-depleted serum. (A-C) Data show means \pm SEM;
612 $n > 3$ / experiments; 3 biological replicates.

613 **FIGURE 2. Lipidomic analysis of phospholipids from Giant Plasma Membrane Vesicle**
614 **(GPMV).**

615 (A) 3D-projection of WGA-Alexa488 labeled GPMVs (left) and FM4-64 labelled GPMVs (right)
616 from HUVEC. Scale bars 10 μ m. (B) Western blot of total membrane (TM) and GPMV using
617 different organelles markers. Plasma membrane (PM) marker: Na⁺/K⁺ATPase and Annexin V,
618 Endoplasmic reticulum (ER) marker: Calregulin, ER-Golgi intermediate compartment (ERGIC)
619 marker: ERGIC53, Golgi complex marker: Trans-Golgi Network 46 (TGN46), Lysosome marker:
620 Lysosomal-associated membrane protein 1 (LAMP1). (C) Lipidomic analyses of GPMVs from OA-
621 or DHA-treated cells. Lipid classes enrichment in GPMVs was calculated by dividing the relative
622 content of each lipid class in GPMVs by those of total membranes. Value bigger than 1 indicate that
623 lipids were enriched in GPMVs, value smaller than 1 indicate that lipids were excluded from GPMVs.
624 SM, sphingomyelin; PC, phosphatidylcholine; PE, phosphatidylethanolamine; PS,
625 phosphatidylserine; PI, phosphatidylinositol; DG, diacylglycerol; LBPA, lysobisphosphatidic acid.
626 (D) Fold change of different PL classes in DHA-treated cells compared with OA-treated cells. (E)
627 PL species distribution regarding their number of double bond (level of unsaturation): from zero to 6
628 double bonds as illustrated in figure 1B. AA and DHA contain 4 and 6 double bonds, respectively.
629 (C-E) Data show means \pm SEM; $n > 3$ / experiments; 3 biological replicates.

630 **FIGURE 3. The impact of DHA on TEM parameters.**

631 (A) Schematic representations of liquid dewetting physics phenomenon and TransEndothelial cell
632 Macroaperture dynamics. Scale bar 20 μ m. (B-H) HUVEC were treated with C3 exoenzyme or
633 without (Mock) for 16 hours prior to 6-hours fatty acid diet (OA or DHA) as sole source of

634 exogenously added acyl chain. (B) FITC-phalloidin staining of HUVEC in Mock, OA or DHA
635 conditions. Scale bar 100 μm . (C) Cell area of cells on OA- or DHA-diet. Data show median \pm max
636 to min; cells > 450 / experiments; 2 biological replicates. (D) Percentage of HUVEC with at least one
637 TEM in the population in OA or DHA conditions. Data show means \pm SEM; cells > 200 / experiments;
638 3 biological replicates. (E) Number of TEMs per cell under OA- or DHA-diet. Data show median \pm
639 max to min of >150 cells from 3 independent experiments (> 50 cells / experiment). (F)
640 Representative FITC-phalloidin staining of OA or DHA-treated cells intoxicated with C3 toxins.
641 Scale bar 20 μm . (G) Graph shows median values of TEM area in fixed cells treated with either OA
642 or DHA. Data show median \pm max to min of > 450 TEMs from 3 independent experiments (>40 cells/
643 experiments). (H) Distribution of TEM sizes in HUVEC under OA- or DHA-diet. (C, D, E, G) Data
644 were analyzed with nonparametric Mann-Whitney statistical test. Data are significant with $p < 0.05$ (*),
645 $p < 0.0001$ (****) or not significant, ns.

646 **FIGURE 4. Impact of DHA-enriched membrane on TEM opening dynamics.**

647 Time-lapse images of TEM opening dynamics in OA- or DHA-fed cells using LifAct-GFP as label.
648 Scale bars 10 μm . (B-C) Frequency of TEM opening events per cell in cells treated with ExoC3 and
649 fed with either OA or DHA. (B) Each row on the Y-axis of the diagram pinpoints all opening events
650 of TEM in a single cell, each black bar is an individual opening event. (C) Graph shows total number
651 of TEM opening events per cell per hour. Data show are median \pm max to min; $n > 28$ cells from 28
652 independent experiments. (D) Graph shows the distribution of values of TEM opening lifetimes
653 measured for each TEM. Data are median \pm max to min, $n > 75$ TEMs from >8 independent
654 experiments. (C-D) Data were analyzed with nonparametric Mann-Whitney statistical test and are
655 significant with $p < 0.01$ (**) and $p < 0.0001$.

656 **FIGURE 5. Impact of DHA on cell geometry.**

657 (A) Atomic force microscopy (cantilever shape seen in foreground) is used to measure the mechanical
658 parameters of the cell (background in bright field). Scale bar 20 μm . (B) Heatmap of cell elasticity
659 on OA- and DHA-treated cells. Scale: 10 μm^2 per field of view. (C) Graph shows the elasticity of
660 Mock or C3-intoxicated cells treated with OA or DHA. Data show median \pm max to min; $n = 40$
661 TEMs. Data were analyzed with one-way ANOVA with Bonferroni correction and are significant
662 with **** $p < 0.0001$ or not significant, ns. Thickness of the cell at the periphery of TEM (D) and
663 thickness of TEM border (E) were measured by AFM using zero-force topology. (F) Graph shows
664 the curvature of TEMs derived from the TEM height measurements. (D-F) Data show median \pm max
665 to min; $n > 20$ TEMs. Data were analyzed with Mann-Whitney test and are significant with ** $p <$
666 0.01.

667 **FIGURE 6. Impact of DHA-enrichment on TEM opening parameters.**

668 (A) Experimental workflow. HUVEC cultivated in LPDS medium were transfected with LifeAct-
669 GFP, treated with C3 toxin, and fed with OA- or DHA-BSA for 6 hours. The dynamics of each TEM
670 was recorded by spinning disk confocal microscopy and was analyzed through custom made Icy-
671 based protocol. (B) Super-resolution stimulated emission depletion (STED) microscopy images of
672 phalloidin-StarRed in C3 intoxicated cells treated without any fatty diet (Mock) or with OA- or DHA-
673 diet. Scale bar 5 (upper) and 2 (lower) μm . (C) Graph shows median values of TEM area as a function
674 of time in cells treated with either OA (blue, n=71 TEMs) or DHA (pink, n=94 TEMs) as sole source
675 of exogenously added acyl chain. Values correspond to average surface of TEMs. Data show median
676 \pm 95% CI from 28 independent experiments. (D) Distribution of opening speed of TEM between 20-
677 70 seconds. (E) Graph shows median values of TEM maximum area in cells treated with either OA
678 or DHA. (F) Distribution of TEM sizes in HUVEC under OA- or DHA-diet. (G) Graph shows
679 distribution of time durations to reach 95% of maximum area. (D, E, G) Data show median \pm max to
680 min, n>70 TEMs for each condition from 28 independent experiments. Data were analyzed with
681 Mann-Whitney test and are significant with *p < 0.05 or not significant, ns.

682

683 SUPPLEMENTARY FILES

684 Supplementary Materials and Methods

685 A modified Bligh and Dyer (Bligh and Dyer 1959) was used for lipid extraction. One million cells
686 were collected and pelleted in an eppendorf and 200 μ L of water was added. After vortexing (30s),
687 the sample was transferred in a glass tube containing 500 μ L of methanol and 250 μ L of chloroform.
688 The mixture was vortexed for 30s and centrifuged (2500 rpm, 4°C, 10 minutes). Then, 300 μ L of the
689 organic phase was collected in a new glass tube and dried under a stream of nitrogen. The dried
690 extract was resuspended in 60 μ L of methanol/chloroform 1:1 (v/v) and transferred in an injection
691 vial. The extraction protocol for purified cell pellet is the same as the one aforementioned in which
692 every volume is divided by two.

693 Reverse phase liquid chromatography was selected for separation with an UPLC system (Ultimate
694 3000, ThermoFisher). Lipid extracts were separated on an Accucore C18 (150x2.1, 2.5 μ m) column
695 (ThermoFisher) operated at 400 μ l/ minutes flow rate. The injection volume was 3 μ L. Eluent
696 solutions were ACN/H₂O 50/50 (V/V) containing 10mM ammonium formate and 0.1% formic acid
697 (solvent A) and IPA/ACN/H₂O 88/10/2 (V/V) containing 2mM ammonium formate and 0.02%
698 formic acid (solvent B). The step gradient of elution was in %B : 0.0 min, 35%; 0.0-4.0 min, 35 to
699 60%; 4.0-8.0 min, 60 to 70%; 8.0-16.0 min, 70 to 85%; 16.0-25.0 min, 85 to 97%; 25-25.1 min 97 to
700 100% B, 25.1-31 min 100% B and finally the column was reconditioned at 35% B for 4 min. The
701 UPLC system was coupled with a Q-exactive Mass Spectrometer (thermofisher, CA); equipped with
702 a heated electrospray ionization (HESI) probe. This spectrometer was controlled by Xcalibur software
703 (version 4.1.31.9.) and operated in electrospray positive mode.

704 Data were acquired with dd-MS² mode at a resolution of 70 000 for MS and 35 000 for MS² (at 200
705 m/z) and a normalized collision energy (NCE) of 25 and 30 eV. Data were reprocessed using Lipid
706 Search 4.1.16 (ThermoFisher). The product search mode was used and the identification was based
707 on the accurate mass of precursor ions and MS² spectral pattern.

708

709 **Supplementary Figures**

710 **SUP. FIGURE 1. Modification of neutral lipids during OA- or DHA-diet.**

711 (A) Fold change of neutral lipids compare to normal-cultured condition (FBS). TG triacylglycerol,
712 DG diacylglycerol, Cer ceramide, SM sphingomyosine, ChE cholesterol ester. Data show means \pm
713 SEM; $n > 3$ / experiments; 3 biological replicates. (B) The MS counts of each PC species normalized
714 to total PC counts. (C) PI species distribution regarding their number of double bond (level of
715 unsaturation): from zero to 6 double bonds as illustrated in figure 1B. AA and DHA contain 4 and 6
716 double bonds, respectively. LPDS: lipoprotein-depleted serum.

717 **SUP. FIGURE 2. Kinetics of OA and DHA-incorporation in HUVECs.**

718 (A) Kinetics of TG(18:1/18:1/18:1) formation in OA-treated cells (blue line). Kinetics of
719 TG(22:6/22:6/22:6) formation in DHA-treated cells (pink line). (B) Kinetics of PUPL (orange line)
720 and non PUPL (blue line) into the indicated lipid classes (PC, PE, PS, and PI) during OA treatment.
721 (C) Kinetics of PUPL (orange line) and non PUPL (blue line) into PC, PE, PS, and PI during OA
722 treatment. (B-C) PUPL contains at least one FA with at least 2 double bonds. Non-PUPL contains
723 either SFA or MUFA on both acyl chains. (A-D) Data show means \pm SEM; $n > 3$ / experiments; 3
724 biological replicates.

725 **SUP. FIGURE 3. Impacts of C3 toxin on cellular lipidome.**

726 (A) PL species distribution regarding their number of double bond (level of unsaturation): from zero
727 to 6 double bonds as illustrated in figure 1B. AA and DHA contain respectively 4 and 6 double bonds.
728 (B) Kinetics of DHA (red or pink line) and OA (blue or light blue line) incorporation into different
729 lipid classes (PC, PE, PS, and PI) in the absence or presence of C3 toxin. Data show means \pm SEM;
730 $n > 3$ / experiments; 1 biological replicates.

731 **SUP. FIGURE 4. Resume opening shows instability of TEM.**

732 (A) Scheme of resume opening. TEM breaks locally and undergoes a second phase of opening. (B)
733 Time-lapse images of TEM resume opening dynamics in OA- or DHA-fed cells using LifAct-GFP
734 as label. (C-D) The evolution of TEM size over the period of recording in OA- (C) or DHA- (D)
735 treated cells. (E) Correlation of TEM radius before (R_0) and after resume opening (R_{eq}). (F)
736 Percentage TEM that undergo resume opening. (G) Difference in TEM radius (ΔR) before and after
737 resume opening. (H) Speed of resume opening. (G-H) Data show median \pm max to min of > 5 TEMs.
738 Data were analyzed with Mann-Whitney test and are not significant, ns.

739 **VIDEO 1. TEM tunnels have labile openings.** Video of LifeAct-GFP expressing HUVEC cells
740 intoxicated with C3 exotoxin. The video was taken with spinning disk confocal at 1 frame per 10
741 seconds over the duration of 50 minutes. Scale bar, 20 μm .

742 **VIDEO 2. TEM tunnels in OA-treated cells.** Video of C3 intoxicated HUVEC cells treated with
743 OA for 6 hours. LifeAct-GFP was transgenically expressed in HUVEC and the video was taken with
744 a spinning disk confocal at 1 frame per 10 seconds over the duration of 50 minutes. Scale bar, 20 μm .

745 **VIDEO 3. TEM tunnels in DHA-treated cells.** Video of C3 intoxicated HUVEC cells treated with
746 DHA for 6 hours. LifeAct-GFP was transgenically expressed in HUVEC and the video was taken
747 with a spinning disk confocal at 1 frame per 10 seconds over the duration of 50 minutes. Scale bar,
748 20 μm .

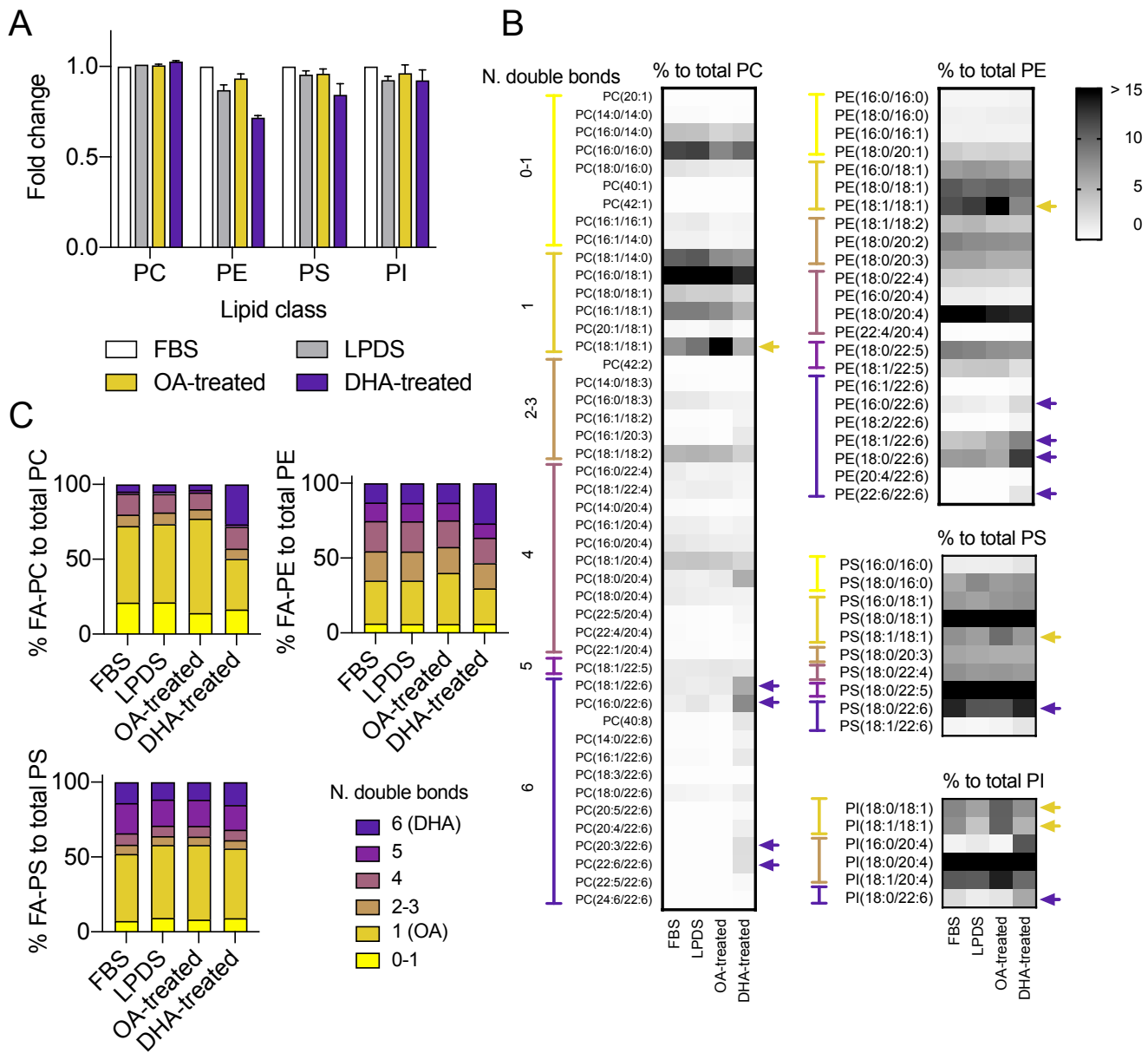


Figure 1.

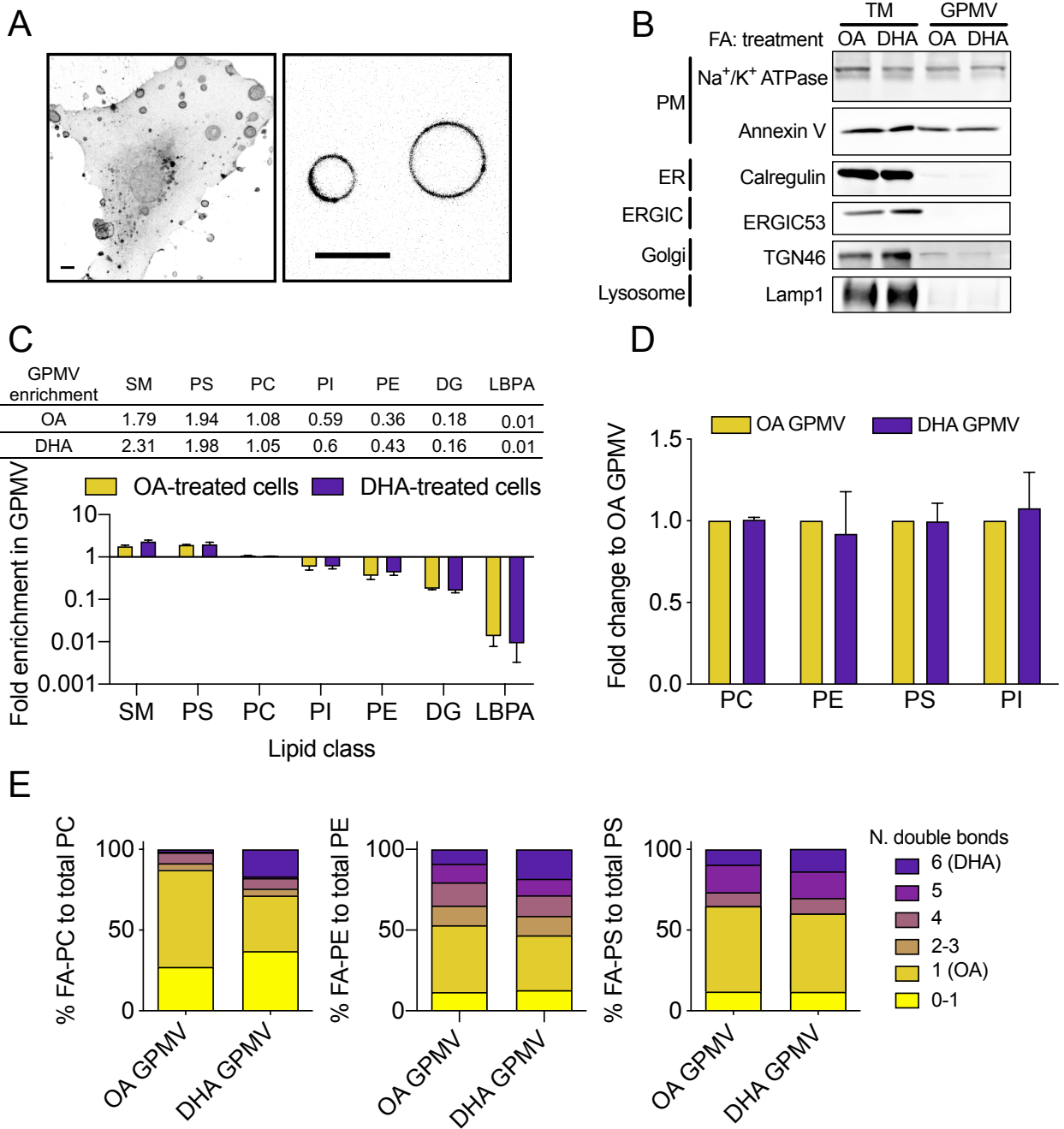
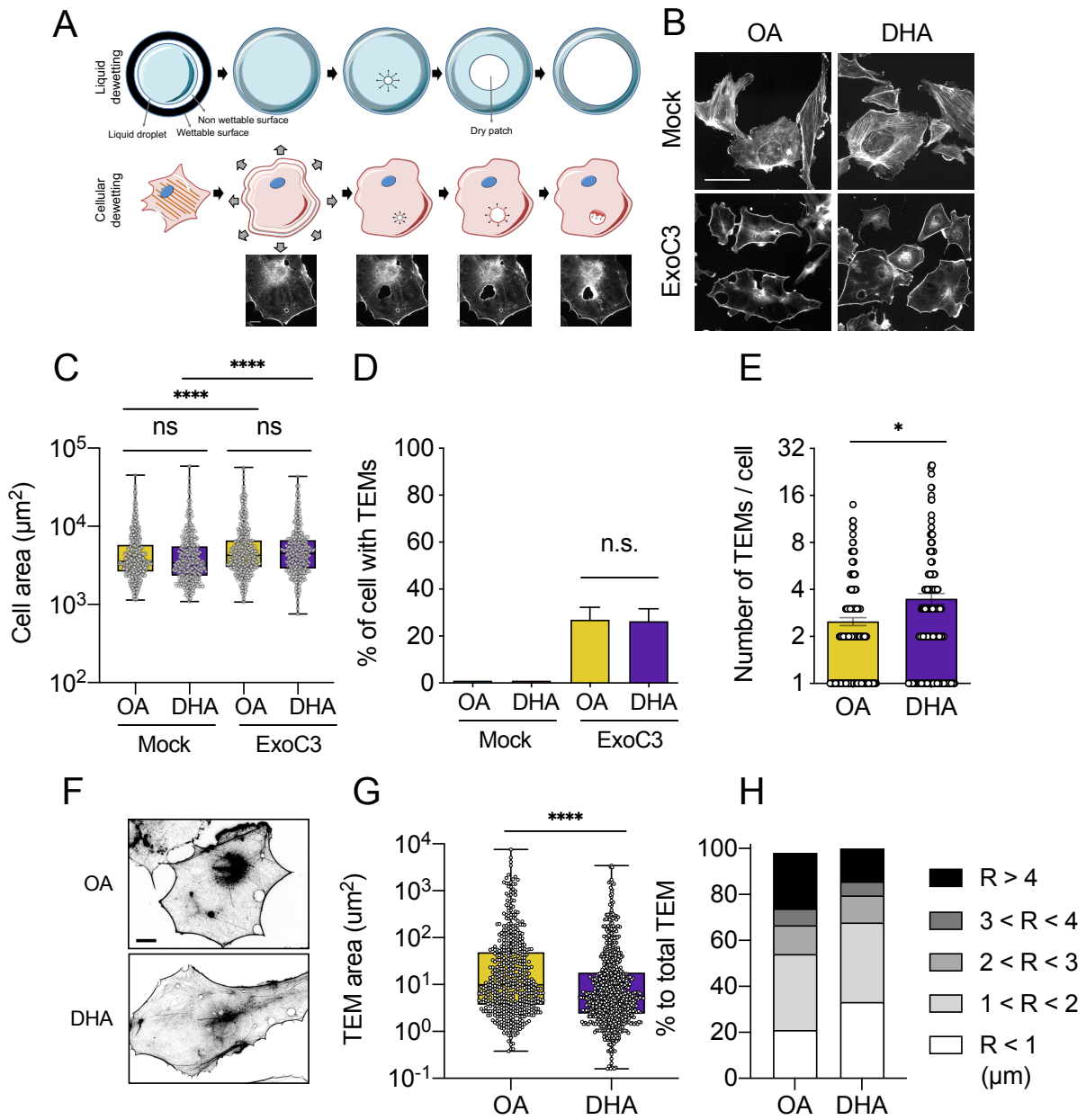


Figure 2.



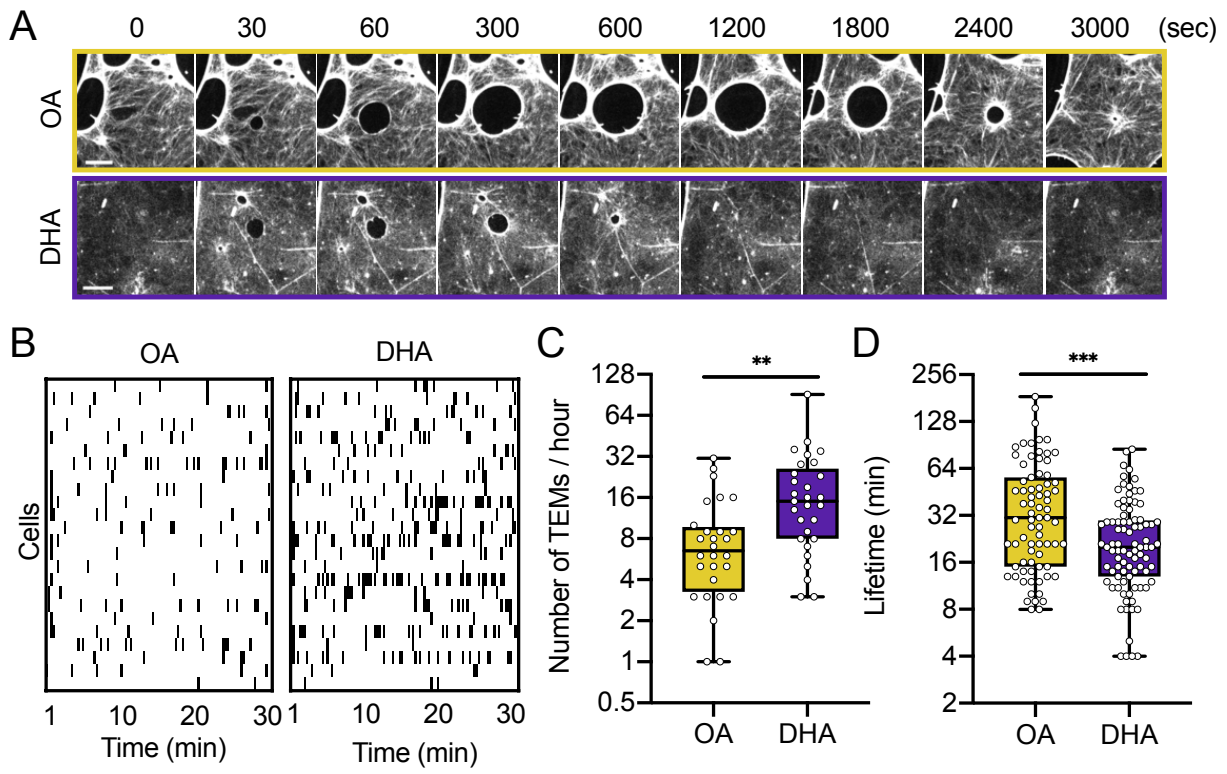


Figure 4.

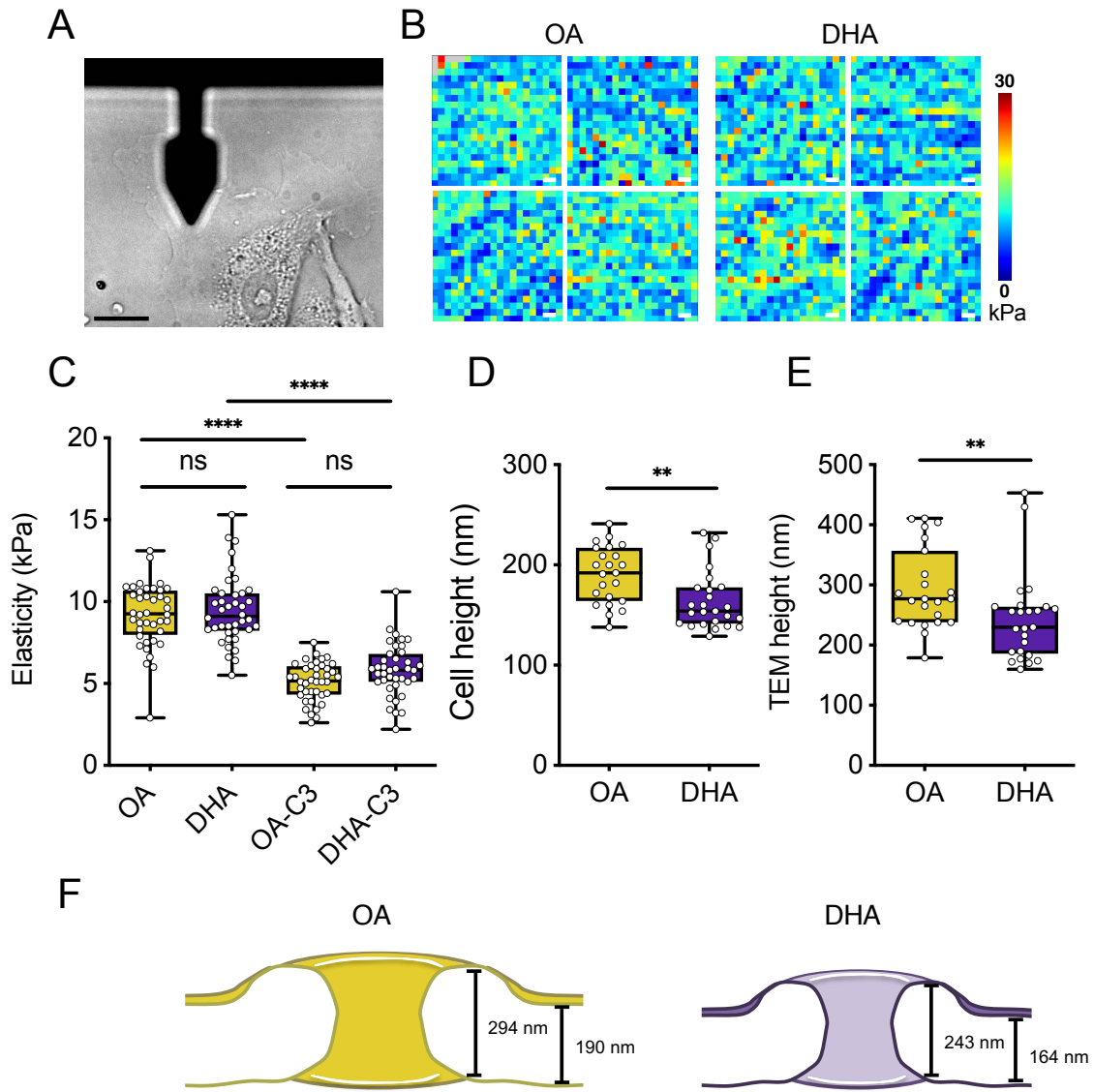


Figure 5.

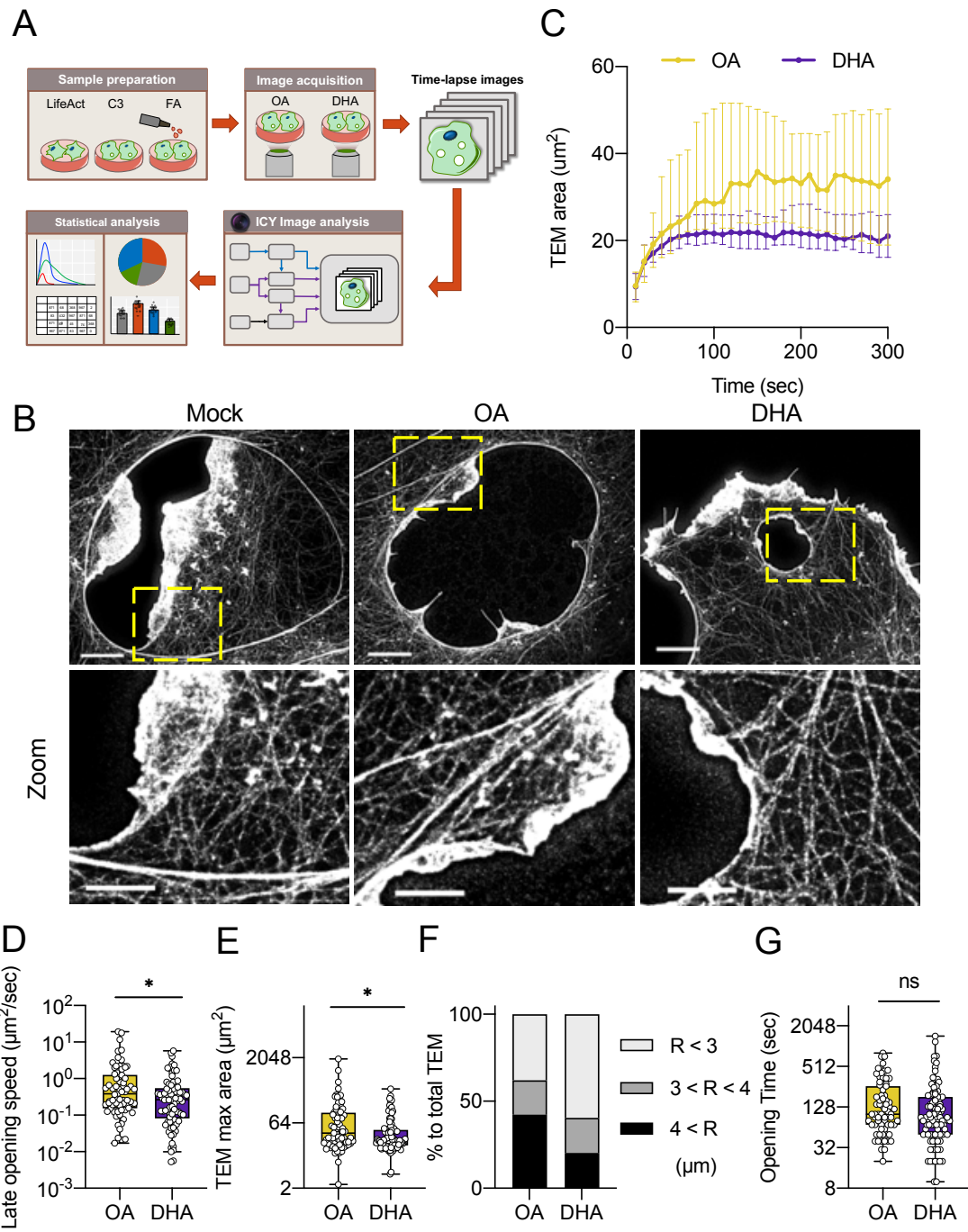


Figure 6.

Table 1. Effect of FA diet on TEM parameters

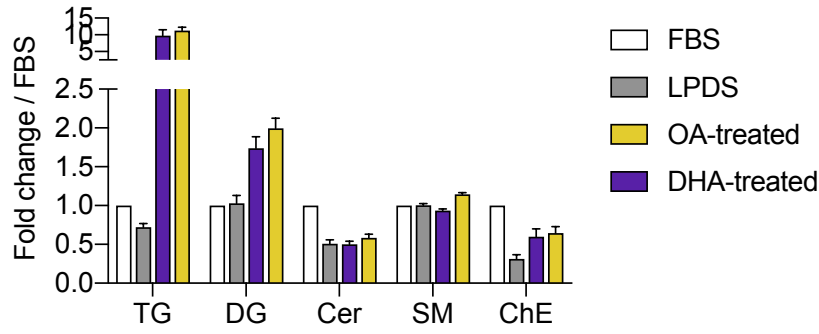
	OA	DHA	Statistics
Cell area (μm^2)	6330 \pm 271	6003 \pm 251	ns
Cell thickness (nm)	190 \pm 6	164 \pm 6	**
% of cells with TEMs	27 \pm 3	26 \pm 3	ns
Number of TEMs/cell	2.5 \pm 0.1	3.5 \pm 0.3	*
TEM frequency (TEMs/hour)	8.9 \pm 1.4	19.3 \pm 3.2	**
TEM max size (μm^2) ^a	37.4 (27.6-59.4)	25.4 (21.2-28.6)	*
Opening time (sec)	179 \pm 21	162 \pm 23	ns
Initial opening speed ($\mu\text{m}^2/\text{sec}$) ^a	0.47 (0.35-0.95)	0.39 (0.29-0.54)	ns
Late opening speed ($\mu\text{m}^2/\text{sec}$) ^a	0.38 (0.22-0.61)	0.27 (0.14-0.37)	*
Latency phase (min)	7.3 \pm 0.6	5.3 \pm 0.4	*
Closure time (min)	16.3 \pm 1.4	11.1 \pm 0.8	**
Closure speed ($\mu\text{m}^2/\text{sec}$) ^a	4.3 (3.4-6.1)	2.7 (2.1-3.3)	***
Life time (min)	42.0 \pm 4.0	24.6 \pm 1.8	***

Data show the means \pm SEM; data were analyzed by Mann-Whitney test

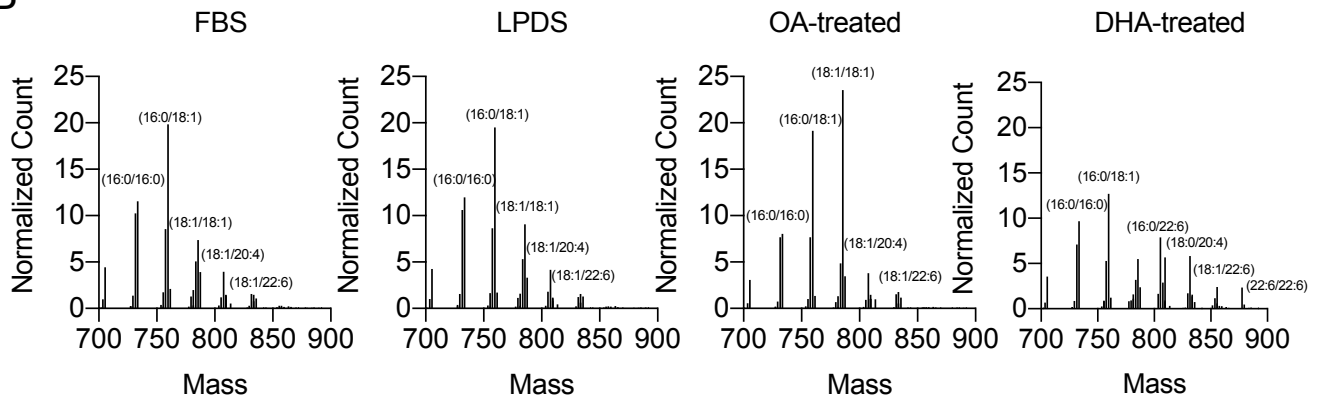
^a data show the median (95% CI, upper-lower)

ns, not significant; * p <0.05, ** p <0.01, *** p <0.001

A



B



C

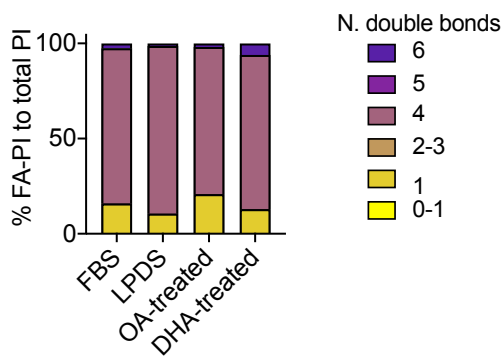
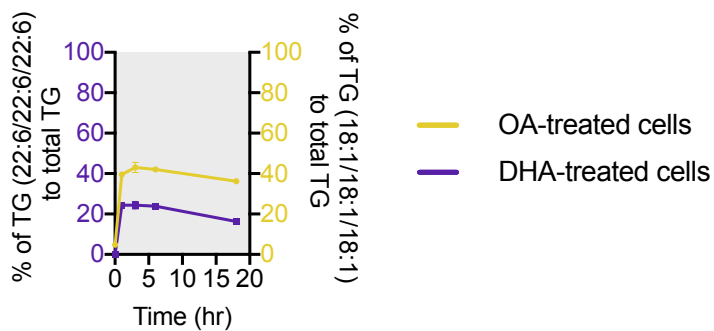
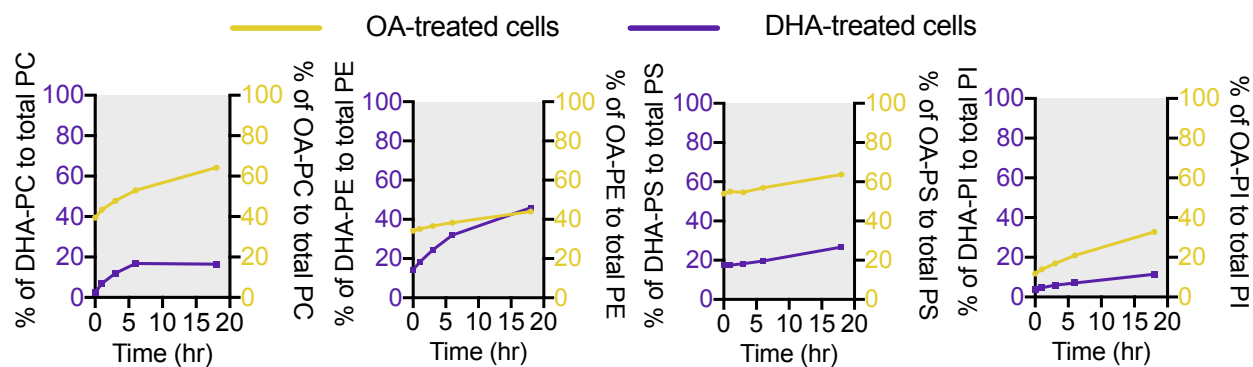


Figure S1

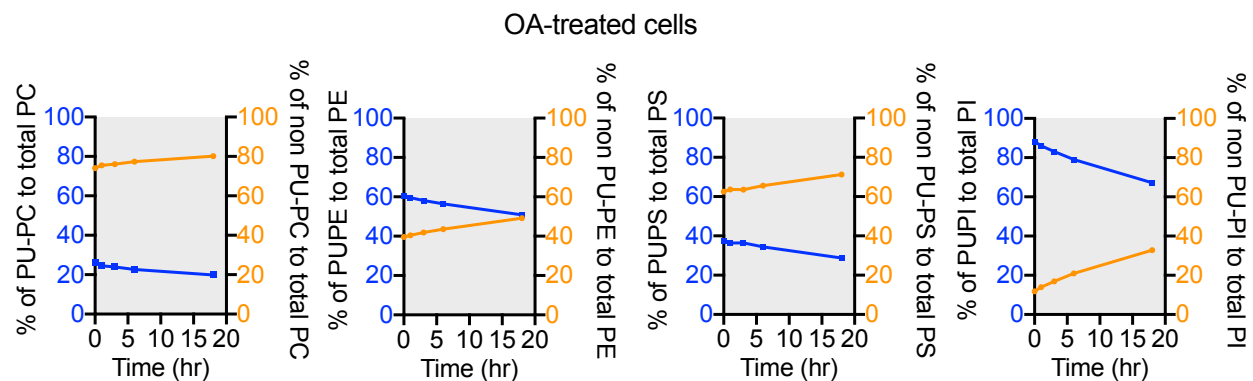
A



B



C



D

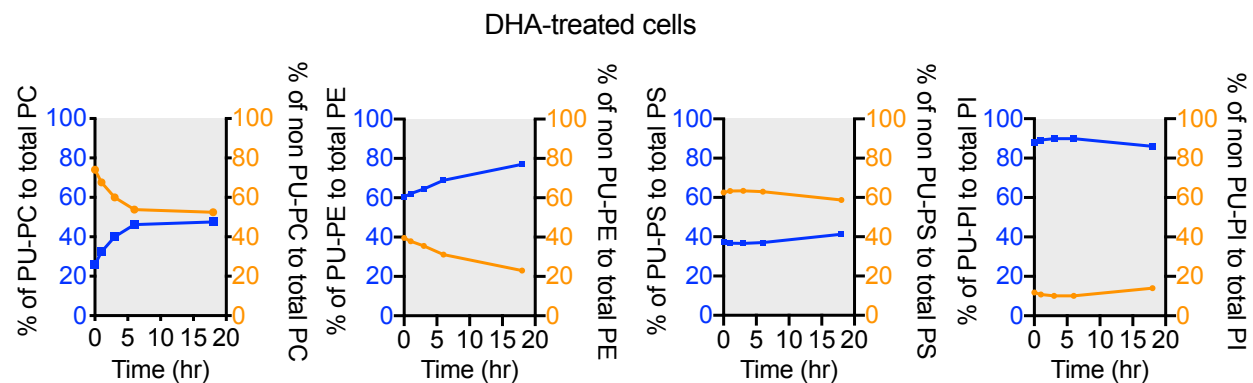
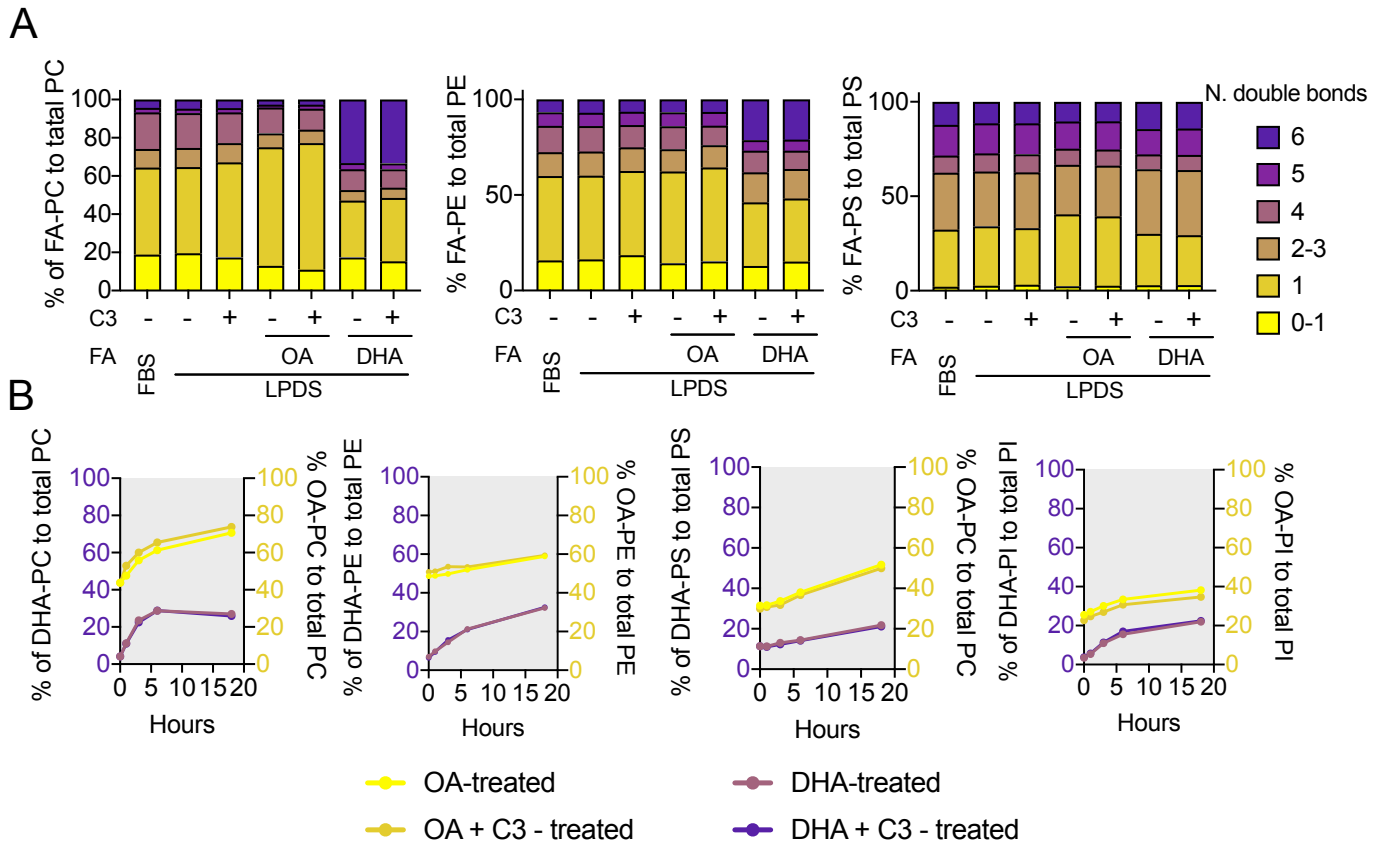


Figure S2.



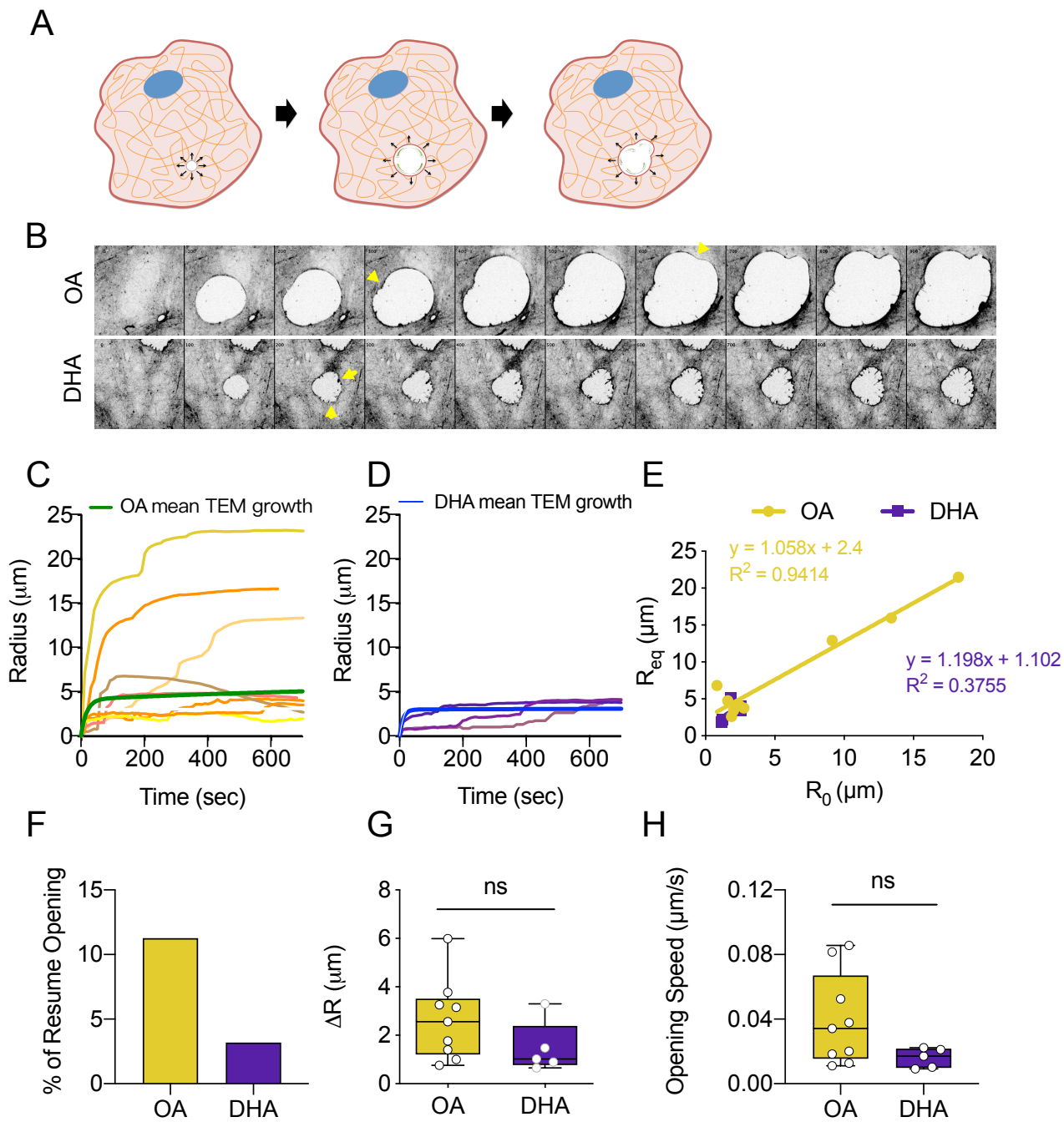


Figure S4.